

Attenuation of the scintillation light
in liquid argon and
investigation of the double beta decay of
 ^{76}Ge into excited states of ^{76}Se
in the GERDA experiment

DISSERTATION

zur Erlangung des akademischen Grades

Doctor rerum naturalium

(Dr. rer. nat.)

vorgelegt der

Fakultät Physik

der Technischen Universität Dresden

von

Dipl.-Phys. Birgit Zatschler (geb. Schneider)

geboren am 21.08.1989 in Pirna

Gutachter: Prof. Dr. Kai Zuber
Prof. Dr. Stefan Schönert

Abgabe: 29. Juni 2020
Disputation: 29. September 2020

For my lovely husband.

Abstract

The GERDA experiment searches for the neutrinoless double beta ($0\nu\beta\beta$) decay of ^{76}Ge . The observation of this decay would prove the Majorana character of the neutrino, i.e. that it is its own antiparticle. This would clarify the question which neutrino mass ordering is realized in nature and give a hint of the effective Majorana neutrino mass. Furthermore, the existence of the $0\nu\beta\beta$ decay would imply the violation of lepton number conservation which is a key feature in some theories explaining the asymmetry of matter and antimatter in the universe.

The effective Majorana neutrino mass is connected with the half life of the $0\nu\beta\beta$ decay via a nuclear matrix element (NME), which is predicted by various theoretical models that are afflicted by large uncertainties. The accuracy of the different NMEs and their internal model assumptions can be increased by considering experimental investigations. While the NMEs for the $0\nu\beta\beta$ decay and the neutrino accompanied double beta ($2\nu\beta\beta$) decay are numerically different, they rely on similar model assumptions. Thus, experimental constraints can be given by the $2\nu\beta\beta$ decay into the ground state, which has been already measured by GERDA with unprecedented precision for ^{76}Ge , but also by the investigation of the $2\nu\beta\beta$ decay into excited states, which has not yet been observed for ^{76}Ge .

GERDA operates enriched germanium detectors in liquid argon (LAr) which serves as an additional background veto using the scintillation light that is created when energy is deposited in LAr. The signal signature of the decay into excited states can be enhanced with the application of the LAr veto, however, for that the efficiency of the LAr veto needs to be determined. One of the key parameters of the LAr efficiency is the attenuation of the scintillation light in LAr, which is dependent on the impurity composition and concentration in LAr. Therefore, the attenuation length of the scintillation light in LAr has been measured in GERDA with a dedicated setup in the course of this work. The analysis of the acquired data required intense computer simulations in order to describe the background for the measurement sufficiently. This also involved the measurement of the steel reflectivity in the visible and the UV region, where LAr scintillates.

Therewith, the search for excited states has been performed in this work for the data accumulated in GERDA Phase I, Phase II and Phase II+ including the LAr veto for the latter two data sets. New limits have been set on the investigated excited states decay modes and some of the corresponding theoretical half life predictions could be disfavored, i.e. the underlying NMEs models can be constrained.

The successor experiment LEGEND will continue searching for the $0\nu\beta\beta$ decay of ^{76}Ge using more germanium detectors together with an improved LAr veto. The investigation of the decay of ^{76}Ge into excited states will also be further pursued in LEGEND.

Kurzdarstellung

Das GERDA Experiment sucht nach dem neutrinolosen doppelten Betazerfall ($0\nu\beta\beta$) von ^{76}Ge . Die Beobachtung dieses Zerfalls wäre ein Nachweis dafür, dass das Neutrino sein eigenes Antiteilchen ist, d.h. ein sogenanntes Majorana-Teilchen. Dies würde einen Rückschluss auf die effektive Majorana-Neutrinomasse liefern und könnte die Frage klären, welche Neutrinomassenordnung in der Natur realisiert ist. Weiterhin würde die Existenz des $0\nu\beta\beta$ Zerfalls die Verletzung der Leptonenzahlerhaltung implizieren. Diese wiederum spielt eine Schlüsselrolle in einigen Theorien, die die Asymmetrie zwischen Materie und Antimaterie im Universum erklären könnten.

Die effektive Majorana-Neutrinomasse und die Halbwertszeit des $0\nu\beta\beta$ Zerfalls sind über ein Kernmatrixelement miteinander verbunden. Das Kernmatrixelement wird von verschiedenen theoretischen Modellen vorhergesagt, die allerdings große Unsicherheiten mit sich bringen. Die Genauigkeit der Modelle inklusive ihrer internen Annahmen können verbessert werden indem man experimentelle Untersuchungen einfließen lässt. Die Kernmatrixelemente des $0\nu\beta\beta$ Zerfalls und des neutrinobegleiteten doppelten Betazerfalls ($2\nu\beta\beta$) sind zwar numerisch unterschiedlich, beruhen aber auf ähnlichen Modellannahmen. Daher kann der $2\nu\beta\beta$ Zerfall in den Grundzustand, der von GERDA bereits mit bisher beispielloser Genauigkeit für ^{76}Ge gemessen wurde, aber auch die Untersuchung des $2\nu\beta\beta$ Zerfall in angeregte Zustände, der bisher noch nicht für ^{76}Ge beobachtet wurde, experimentelle Restriktionen liefern.

GERDA betreibt angereicherte Germaniumdetektoren in flüssigem Argon, welches, unter Ausnutzung seiner Szintillationseigenschaften, als zusätzliches Untergrundveto fungiert. Die Signalsignatur des Zerfalls in angeregte Zustände kann durch die Anwendung des Argonvetos verbessert werden, allerdings ist es dafür notwendig die Effizienz des Argonvetos zu bestimmen. Einer der wichtigsten Parameter ist dabei die Abschwächung des Szintillationslichts im Argon, welches von der Zusammensetzung und Konzentration von Verunreinigungen im Argon abhängt. Daher wurde im Rahmen dieser Arbeit die Abschwächungslänge des Szintillationslichts in Argon mit einem eigens dafür entwickelten Setup in GERDA gemessen. Die Analyse der gewonnenen Daten erforderte umfangreiche Computersimulationen um den Untergrund für die Messung ausreichend zu beschreiben. Dies schließt auch die Messung der Stahlreflektivität im sichtbaren und UV Bereich, in welchem Argon szintilliert, mit ein.

In dieser Arbeit wurde damit die Suche nach angeregten Zuständen für die akkumulierten Daten in GERDA Phase I, Phase II und Phase II+ fortgeführt, und das Argonveto für die letzteren beiden Datensätze implementiert. Neue Limits wurden auf die untersuchten Zerfallskanäle gesetzt, wodurch einige der theoretischen Vorhersagen für die jeweiligen Halbwertszeiten ausgeschlossen werden konnten und folglich die zu Grunde liegenden Kernmatrixelemente weiter eingegrenzt wurden.

Das Nachfolgerexperiment LEGEND wird die Suche nach dem $0\nu\beta\beta$ Zerfall von ^{76}Ge mit einer größeren Anzahl an Germaniumdetektoren fortsetzen und ein verbessertes Argonveto verwenden. Auch die Untersuchung des Zerfalls von ^{76}Ge in angeregte Zustände wird in LEGEND weiter verfolgt.

Contents

1	Introduction to neutrinos physics and double beta decay	11
1.1	Neutrino oscillations	11
1.2	Standard Model of particle physics	13
1.2.1	Extension of the Standard Model with sterile neutrinos	14
1.3	Direct neutrino mass measurements	16
1.4	Present neutrino mass limits	16
1.5	Double beta decay	18
1.5.1	Nuclear matrix elements	20
1.5.2	Experimental considerations	22
2	The GERDA experiment	25
2.1	Laboratori Nazionali del Gran Sasso	25
2.2	GERDA Phase I and II	26
2.2.1	Water Cherenkov veto	27
2.2.2	LAr veto	27
2.2.3	Germanium detector array	30
2.3	Results	32
2.4	Successor experiment LEGEND	33
3	Scintillation properties of liquid argon	35
3.1	Scintillation mechanism	35
3.2	Impurities and their influences on LAr properties	38
3.2.1	Singlet and triplet lifetime	40
3.2.2	Scintillation light yield	40
3.2.3	Absorption and attenuation length	41
3.2.4	Rayleigh scattering	43
4	Reflectivity measurement of steel in the visible and VUV region	45
4.1	Specular and diffuse reflection	45
4.2	Reflection properties of various materials	46
4.3	Reflectivity measuring device in Münster	47
4.4	Measurement of the steel reflectivity in the visible region	49
4.4.1	Spectrophotometer	49
4.4.2	Data taking	50
4.4.3	Interpretation of the measurement	52
4.5	Measurement of the steel reflectivity in the VUV region	54
4.5.1	Reflectometer	54
4.5.2	Homogeneity of the reflectance	55

4.5.3	Angular measurements of the reflectivity	56
4.6	Combination of the reflectivity measurements	57
5	Implementation of optical properties in Monte Carlo simulations	59
5.1	Simulation framework MaGe	59
5.1.1	DECAY0	60
5.2	Liquid argon	60
5.2.1	LAr scintillation spectrum	60
5.2.2	LAr absorption length	60
5.2.3	LAr scintillation light yield	61
5.2.4	LAr singlet and triplet lifetime	61
5.2.5	LAr refractive index	61
5.2.6	LAr scattering length	62
5.2.7	Cherenkov light	62
5.3	Steel reflectivity	63
5.3.1	GEANT4 surface modeling	63
5.3.2	Extrapolation to the VUV region	65
5.4	Wavelength shifter TPB	65
5.4.1	TPB absorption length	66
5.4.2	TPB emission spectrum	66
5.4.3	TPB light yield	66
5.5	PMT efficiency	67
5.6	Discussion	67
6	Measurement of the scintillation light attenuation in LAr in GERDA	69
6.1	Development of a dedicated setup	69
6.1.1	Stepper motor	70
6.1.2	Material of the setup	71
6.1.3	Source	72
6.1.4	Scintillation light detection	74
6.1.5	Background expectation from argon and steel	75
6.2	Measuring points	76
6.3	Data taking	76
6.3.1	Signal reconstruction	76
7	Analysis of the attenuation measurement	81
7.1	Measuring data	81
7.2	Simulation of the attenuation setup	83
7.3	Simulation with the IPF reflectivity	84
7.3.1	Solid angle correction	84
7.3.2	Cherenkov background	86
7.3.3	Analysis procedure	87
7.3.4	Determination of the best matching simulation input parameters	89
7.3.5	Comparison of simulation and experimental data	91
7.3.6	Systematic uncertainties	92
7.3.7	Result	94
7.4	Simulation with the combined reflectivity	95
7.4.1	Solid angle correction, Cherenkov background and data analysis	95
7.4.2	Determination of the best matching simulation input parameters	95
7.4.3	Comparison of simulation and experimental data	96

7.4.4	Systematic uncertainties	96
7.4.5	Result	97
7.5	Discussion	98
8	Determination of the triplet lifetime of LAr in GERDA	101
8.1	Event reconstruction	101
8.2	Simulation studies of the triplet lifetime	102
8.2.1	Systematic uncertainties	105
8.3	Data analysis	106
8.3.1	Systematic uncertainties	106
8.4	Discussion	106
9	$2\nu\beta\beta$ decay of ^{76}Ge into excited states of ^{76}Se	109
9.1	Motivation	109
9.2	Decay modes	110
9.2.1	Angular correlation of de-excitation γ rays	111
9.3	Implementation of the LAr veto	113
9.3.1	Creation of scintillation light in GEANT4	113
9.3.2	LAr photon detection probability map	114
9.4	Monte Carlo simulation of the signal signature	117
9.4.1	Detector size and position in the array	117
9.4.2	Signal signature of the decay modes	121
9.5	Data sets	125
9.6	Analysis	126
9.6.1	Background model	126
9.6.2	Signal cuts and optimization	128
9.6.3	Signal cut efficiencies	130
9.7	Data count results	131
9.8	Statistical analysis	135
9.8.1	Likelihood function	135
9.8.2	Prior and posterior probability density distribution	136
9.8.3	Systematical uncertainties	136
9.8.4	Limit extraction	136
9.9	Discussion	137
10	Conclusions	139
	Appendices	141
A	Simulation and analysis of the scintillation light attenuation in LAr	141
A.1	Low energy fits of the attenuation spectra	141
A.2	Attenuation simulation and analysis with IPF reflectivity	144
A.3	Attenuation simulation and analysis with the combined reflectivity	158
B	Simulation and analysis of the $2\nu\beta\beta$ decay into excited states	163
B.1	Energy depositions in LAr	163
B.2	M2 fractions of each detector	164
B.3	Background model for M2 data in Phase II	167
B.4	Events in ROI and SBs surviving all cuts	170
B.5	List of events in ROI surviving all cuts	174
B.6	Marginalized posterior probability density distributions	181

List of Figures	183
List of Tables	186
List of Acronyms	189
Bibliography	193
Acknowledgements	203

Chapter 1

Introduction to neutrinos physics and double beta decay

The neutrino was first postulated by Pauli in 1930 and introduced by Fermi in 1934 as an explanation of the continuous electron spectrum where the neutrinos carries away the missing energy from the detector [Fer34]. Much later, in 1956, the first evidence of the neutrino was observed in the experiment developed by Cowan and Reines [RC56].

Nowadays, it is known that neutrinos are fermions, carry no electric charge and participate only in gravitational and weak interactions, which makes them very challenging to detect. Neutrinos can be produced by weak charged-current interactions and are classified in three flavors according to the corresponding charged lepton that is created or destroyed alongside the neutrino [Gou16].

Neutrinos are produced in weak interactions, such as radioactive decays and nuclear fusions occurring inside stars. The measurement of neutrinos from the sun proved the solar model of the underlying fusion processes and the resulting energy production. Neutrinos also play a dominant role in core-collapse supernovae causing the main energy loss in the end of the life cycle of a star and carrying away the main energy in the supernova explosion. The detection of about 20 neutrinos from the supernova 1987A [BBB+87, HKK+87] confirmed the rough knowledge of the processes causing the supernova explosion. Similar to the cosmic microwave background it is expected that a cosmic neutrino background as a relic of the big bang exists, although it has not yet been observed due to the low cross section of the neutrinos. Its detection could give an insight in the time before the universe became transparent for photons, which is so far the earliest achievable picture of the universe. Consequently, neutrinos participated significantly in shaping the universe known today and their investigation can shed light on processes not yet understood [Gou16].

1.1 Neutrino oscillations

Experiments measuring solar neutrinos were initially confronted with the issue that the measured flux was much lower than expected, which is also known as the solar neutrino problem. It has been solved by Super-Kamiokande and the SNO (Sudbury Neutrino Observatory) experiment [SK02, SNO02] which confirmed the assumption that neutrinos are oscillating, i.e. that the flavor is not conserved in the propagation. This causes the electron neutrinos emitted by the sun to transform into muon or tau neutrinos, resulting in a lower measured electron neutrino flux on the earth. The flavor eigenstate ν_α is a linear combination of the mass eigenstates ν_i with the mixing matrix U , also called PMNS (Pontecorvo-Maki-Nakagawa-Sakata) matrix [PDG19].

$$|\nu_\alpha\rangle = \sum_i U_{\alpha i}^* |\nu_i\rangle \quad \text{with} \quad \alpha = e, \mu, \tau \quad \text{and} \quad i = 1, 2, 3 \quad (1.1)$$

This state is actually evolving in time, i.e. $|\nu_\alpha\rangle \rightarrow |\nu_\alpha(t)\rangle$ and $|\nu_i\rangle \rightarrow |\nu_i(t)\rangle$. The probability that a neutrino is emitted with flavor α and detected with flavor β after a traveled distance L is given by [PDG19]:

$$P_{\alpha\beta} = |\langle \nu_\beta | \nu_\alpha(t) \rangle|^2 = \left| \sum_{i=1}^n \sum_{j=1}^n U_{\alpha i}^* U_{\beta j} \langle \nu_j | \nu_i(t) \rangle \right|^2 \quad (1.2)$$

The neutrino propagation can be described as a plane wave $|\nu_i(t)\rangle = e^{-iE_i t} |\nu_i(0)\rangle$ with the energy $E_i = \sqrt{p_i^2 + m_i^2}$ and the mass m_i of the neutrino mass eigenstate ν_i . Additionally, neutrinos are highly relativistic, i.e. $p_i \gg m_i$ and $p_i \approx p_j \equiv p \approx E$, leading to the following relation [PDG19].

$$E_i = \sqrt{p_i^2 + m_i^2} \approx E + \frac{m_i^2}{2E} \quad (1.3)$$

The oscillation probability can then be expressed with the following formula with the squared mass difference $\Delta m_{ij}^2 = m_i^2 - m_j^2$ of the corresponding mass eigenstates [PDG19].

$$P_{\alpha\beta} = \delta_{\alpha\beta} - 4 \sum_{i<j}^n \text{Re} (U_{\alpha i} U_{\beta i}^* U_{\alpha j}^* U_{\beta j}) \sin^2 \left(\frac{\Delta m_{ij}^2 L}{4E} \right) + 2 \sum_{i<j}^n \text{Im} (U_{\alpha i} U_{\beta i}^* U_{\alpha j}^* U_{\beta j}) \sin \left(\frac{\Delta m_{ij}^2 L}{2E} \right) \quad (1.4)$$

Consequently, neutrino oscillation requires a non-zero difference of the mass eigenstates as well as a non vanishing mixing of the flavor and mass eigenstates which is given by the related entries in the mixing matrix U [PDG19].

$$U = \begin{pmatrix} 1 & 0 & 0 \\ 0 & c_{23} & s_{23} \\ 0 & -s_{23} & c_{23} \end{pmatrix} \begin{pmatrix} c_{13} & 0 & s_{13} e^{-i\delta_{\text{CP}}} \\ 0 & 1 & 0 \\ -s_{13} e^{i\delta_{\text{CP}}} & 0 & c_{13} \end{pmatrix} \begin{pmatrix} c_{12} & s_{12} & 0 \\ -s_{12} & c_{12} & 0 \\ 0 & 0 & 0 \end{pmatrix} \begin{pmatrix} e^{i\eta_1} & 0 & 0 \\ 0 & e^{i\eta_2} & 0 \\ 0 & 0 & 1 \end{pmatrix} \quad (1.5)$$

The mixing angles θ_{ij} are covered by the short notations $c_{ij} \equiv \cos \theta_{ij}$ and $s_{ij} \equiv \sin \theta_{ij}$. The phase factor δ_{CP} is only non-zero if neutrino oscillation is not invariant under CP (charge conjugation parity) transformation. For Dirac neutrinos, the phases η_1 and η_2 are zero, i.e. the last matrix in equation 1.5 is an identity matrix. In the case neutrinos are Majorana particles, the phases η_1 and η_2 are non-zero, altering the mixing matrix U as indicated in equation 1.5 [PDG19].

The Majorana phases η_1 and η_2 cancel each other in the oscillation probability (see eq. 1.4), thus the existence of Majorana neutrinos cannot be proved with oscillation experiments. The current values of the mass differences and mixing angles obtained from global fits of several measurements reveal that all entries in the PMNS matrix U are non-zero, i.e. all three known neutrino mass eigenstates are mixing [PDG19].

$$\begin{aligned} \Delta m_{21}^2 &\sim 7.4 \cdot 10^{-5} \text{eV}^2 & \theta_{12} &\sim 34^\circ \\ |\Delta m_{32}^2| &\sim 2.5 \cdot 10^{-3} \text{eV}^2 & \theta_{23} &\sim 48^\circ \\ & & \theta_{13} &\sim 8.6^\circ \end{aligned} \quad (1.6)$$

Various neutrino sources are observed in order to obtain the quoted oscillation parameters in equation 1.6. This includes the sun, which emits electron neutrinos in its fusion processes as well as electron and muon neutrinos and their antiparticles produced by the decays of kaons, pions and muons created by cosmic rays interacting with nucleons in the earth's atmosphere.

In accelerator experiments high energy protons collide with matter, producing kaons and pions, creating a neutrino beam composed mainly of muon neutrinos or antineutrinos. In nuclear reactor neutron rich nuclides decay under the emission of electron antineutrinos [PDG19].

In contrast to experiments observing solar and atmospheric neutrinos, in accelerator and reactor experiments the distance of the detector measuring the neutrinos can be chosen more or less freely. The traveled distance and the energy of the neutrinos need to be in a certain relation (see eq. 1.4) in order to be able to observe the appearance of a different neutrino flavor or the disappearance of the originally emitted neutrino flavor [PDG19].

While appearance experiments are sensitive on the sign of the investigated mass difference Δm_{ij}^2 , disappearance experiments can only measure the absolute value $|\Delta m_{ij}^2|$. Thus, the measured oscillation parameters compiled in equation 1.6 allow the possibility of two mass orderings, normal (NMO) and inverted (IMO), as depicted in figure 1.1 [BK18].

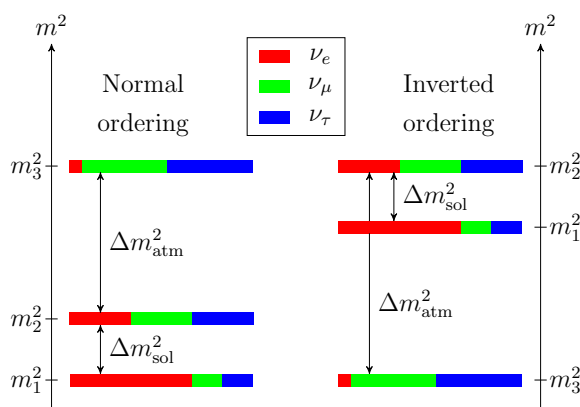


Figure 1.1: Possible mass orderings of the neutrino mass eigenstates resulting from the measured oscillation parameters. While solar neutrino experiments are sensitive on the sign of the mass difference $\Delta m_{sol}^2 \equiv \Delta m_{21}^2$, atmospheric neutrinos are investigated with disappearance experiments, thus they are only sensitive on the absolute of the mass difference $\Delta m_{atm}^2 \equiv |\Delta m_{32}^2|$. Adapted from [MAB⁺04].

Neutrino oscillation experiments are only sensitive on the mass differences, but not on the absolute neutrino masses. Additionally, the question which mass ordering is realized in nature could not be answered so far. Dedicated appearance experiments are already investigating this topic, however, they have not been conclusive yet [NOv19]. Furthermore, they cannot indicate if neutrinos are Dirac or Majorana particles. However, the observation of neutrino oscillation is a clear evidence for massive neutrinos or strictly speaking that at least two of the neutrino masses are non-zero. Theoretical models of physics processes leading to non-vanishing neutrino masses exist, although non of them have been proven so far [Gou16, PDG19].

1.2 Standard Model of particle physics

The SM (Standard Model of particle physics) is a renormalizable, Lorentz-invariant QFT (quantum field theory) describing the interactions of the known matter fields via gauge symmetries. The gauge groups of the SM connect the strong, weak and electromagnetic interactions by $SU(3)_C \times SU(2)_L \times U(1)_Y$, where C stands for color, L for left-handed and Y for hypercharge. The SM gauge symmetry is spontaneously broken due to the Higgs mechanism, where the particles coupling to the Higgs field become massive. This includes W^\pm and Z^0 bosons as well as all electrically charged fermions [Gou16, PDG19].

In the SM, fermion masses are generated by the Yukawa coupling Y of the Higgs doublet ϕ with a left-handed fermion doublet and a right-handed fermion singlet. In the case of leptons, the corresponding Lagrangian term can be written as follows with the left-handed lepton doublet ψ_L and the right-handed charged lepton field ψ_R [PDG19]:

$$\mathcal{L}_Y = -Y_{ij}^l \bar{\psi}_{Li} \phi \psi_{Rj} + \text{h.c.} \quad (1.7)$$

$$\phi = \frac{1}{\sqrt{2}} \begin{pmatrix} 0 \\ v + h \end{pmatrix} \quad \psi_L = \begin{pmatrix} \nu_l \\ l \end{pmatrix}_L \quad \psi_R = l_R \quad (1.8)$$

After symmetry breaking, these Lagrangian terms lead to the mass terms of the charged leptons $l = e, \mu, \tau$ with the vacuum expectation value v of the Higgs field.

$$\mathcal{L}_m = -m_{ij}^l \bar{\psi}_{Li} \psi_{Rj} + \text{h.c.} \quad \text{with} \quad m_{ij}^l = Y_{ij}^l \frac{v}{\sqrt{2}} \quad (1.9)$$

Since the SM does not contain right-handed neutrinos, these terms cannot be built for neutrinos. As a consequence, neutrinos remain massless in the SM.

The described minimal SM predicts that all known neutrinos are massless contradictory to the observations of neutrino oscillations which require that at least two neutrino mass eigenstates are non-zero. Consequently, massive neutrinos imply physics beyond the SM and the SM needs to be extended to introduce massive neutrinos [Gou16, PDG19].

Neutrinos participate only in the weak interaction in the SM, corresponding to two possible interactions: CC (charged current) between the left-handed neutrino and its corresponding left-handed charged lepton as well as NC (neutral current) among neutrinos themselves. CC and NC refer to the respective charge of the exchanged boson, i.e. W^\pm and Z^0 . Neutrinos taking part in these interactions are referred to as active neutrinos. The Lagrangians can be expressed accordingly with the coupling constant g , the Weinberg angle θ_W , the gamma matrices γ^μ , the left-handed neutrino field ν_{Li} and the respective left-handed charged lepton field l_L^- of the same flavor l [PDG19].

$$\mathcal{L}_{\text{CC}} = -\frac{g}{\sqrt{2}} \sum_l \bar{\nu}_{Li} \gamma^\mu l_L^- W_\mu^+ + \text{h.c.} \quad (1.10)$$

$$\mathcal{L}_{\text{NC}} = -\frac{g}{2 \cos \theta_W} \sum_l \bar{\nu}_{Li} \gamma^\mu \nu_{Li} Z_\mu^0 \quad (1.11)$$

The Lagrangians in equations 1.10 and 1.11 cover all interactions of neutrinos within the SM. Equation 1.11 also describes the decay of the Z^0 boson into light left-handed neutrinos with a mass of $m_\nu \leq m_{Z^0}/2$. Measurements of the total decay width of the Z^0 can determine the number of neutrino states N_ν in which the Z^0 decays. Currently, these measurements result in $N_\nu = 2.984 \pm 0.008$. Consequently, extensions of the SM need to contain exactly three light active neutrinos [BK18, PDG19].

Any extra neutrinos must be heavier or sterile, i.e. do not couple to Z^0 and W^\pm bosons, but can receive their mass by the Yukawa coupling. They do not interact in the SM at all and are singlets of the SM gauge group. There is no evidence for sterile neutrinos yet, however, if they exist it is expected that they mix with active neutrinos altering the oscillation probabilities [BK18, MS06, PDG19].

1.2.1 Extension of the Standard Model with sterile neutrinos

Proceeding from equation 1.7 the following Lagrangians are introduced by adding a number of m right-handed sterile neutrinos ν_{si} ($i = 1, \dots, m$) that couple to Yukawa interactions [PDG19].

$$\mathcal{L}_Y = -Y_{ij}^\nu \bar{\nu}_{si} \phi \nu_{Lj} - \frac{1}{2} Y_{ij}^\nu \bar{\nu}_{si} \phi \nu_{sj}^c + \text{h.c.} \quad (1.12)$$

Here, ν^c is the charged conjugated field of the corresponding neutrino field ν . After symmetry breaking this leads to the following mass terms [PDG19].

$$\mathcal{L}_{M_\nu} = -M_{Dij} \bar{\nu}_{si} \nu_{Lj} - \frac{1}{2} M_{Nij} \bar{\nu}_{si} \nu_{sj}^c + \text{h.c.} \quad (1.13)$$

M_D is a complex matrix of the dimension $m \times 3$ containing the three known active neutrinos and M_N is a symmetric $m \times m$ matrix covering the m sterile neutrinos [PDG19].

Dirac neutrinos

The first term in the Lagrangian in equation 1.13 is similar to equation 1.9 for the charged fermions [PDG19].

$$M_{Dij} = Y_{ij}^\nu \frac{v}{\sqrt{2}} \quad (1.14)$$

Accordingly, this is called the Dirac mass term. Assuming $M_N = 0$, the second term in equation 1.13 vanishes, which leads to $m = 3$ sterile neutrinos. These would then be of Dirac character, i.e. the neutrino is distinct from its antiparticle. The lepton carries the lepton number $L = +1$, while the antilepton has $L = -1$, thus particle and antiparticle are distinguished by their opposite values of L [BK18, PDG19]. For Dirac neutrinos lepton number is conserved, which is an accidental global symmetry in the SM, but lepton flavor symmetry can be violated, allowing neutrinos to oscillate between the flavors. However, since they receive their mass via the Yukawa coupling equivalent to the charged fermions, this case does not explain why neutrinos masses are so tiny compared to the other fermions [PDG19].

Majorana neutrinos

Majorana particles are identical to their antiparticles, i.e. the neutrino field ν is equivalent to its charged conjugated field ν^c . Consequently, lepton number is violated by Majorana neutrinos. Thus, the second term in equation 1.13 is denoted as Majorana mass term which contains two right-handed neutrino fields. By introducing the $(3 + m)$ -dimensional vector $\vec{\nu} = (\vec{\nu}_L, \vec{\nu}_s^c)^T$ equation 1.13 can be rewritten as follows [BK18, PDG19].

$$\mathcal{L}_{M_\nu} = -\frac{1}{2} (\overline{\vec{\nu}}_L^c, \overline{\vec{\nu}}_s) \begin{pmatrix} 0 & M_D^T \\ M_D & M_N \end{pmatrix} \begin{pmatrix} \vec{\nu}_L \\ \vec{\nu}_s^c \end{pmatrix} + \text{h.c.} \equiv \overline{\vec{\nu}}^c M_\nu \vec{\nu} + \text{h.c.} \quad (1.15)$$

The mass matrix M_ν is complex and symmetric and can be diagonalized as expressed in equation 1.16 [PDG19].

$$M_\nu \simeq \begin{pmatrix} M_D^T M_N^{-1} M_D & 0 \\ 0 & M_N \end{pmatrix} \quad (1.16)$$

If the mass eigenvalues of M_N are much larger than for M_D , this leads to three light neutrinos with masses proportional to $M_D^T M_N^{-1} M_D$ and m heavy neutrinos with masses proportional to M_N . Thus, the larger the masses of the heavy neutrinos get, the smaller are the masses of the three light neutrinos, which is referred to as see-saw mechanism. Both, the three active light neutrinos and the heavy sterile neutrinos, are Majorana particles. Very large values of M_N provide a natural explanation why the masses of the three active neutrinos are so tiny while at the same time the neutrino Yukawa couplings are of the same order as for the other fermions [Gou16, PDG19].

1.3 Direct neutrino mass measurements

Due to the energy-momentum conservation the absolute neutrino mass can be extracted by investigating interactions involving neutrinos or antineutrinos. This includes ordinary beta decays since the available energy of the known Q -value is used to generate the mass and the kinetic energy of the emitted particles, i.e. electron and neutrino. The endpoint of the beta spectra is therefore distorted and shifted to lower energies according to the neutrino mass. Historically, the achieved limits of the neutrino mass are denoted as the neutrino flavor with respect to the corresponding flavor of the charged lepton also emitted in the decay [PDG19].

The leading experiment in this field is KATRIN (Karlsruhe Tritium Neutrino experiment) measuring the decay of tritium ${}^3\text{H} \rightarrow {}^3\text{He} + e^- + \bar{\nu}_e$. Tritium has a very low Q -value, $Q = 18.6\text{ keV}$ [CEF99], which makes it more sensitive on beta spectra distortions caused by a massive neutrino. The current limit on the effective electron antineutrino mass is $m_\beta < 1.1\text{ eV}$ at 90% C.L. [KAT19]. The neutrino mass derived from beta decay experiments is given by the following formula [PDG19].

$$m_\beta^2 = \sum_i |U_{ei}|^2 m_i^2 \quad (1.17)$$

The KATRIN experiment continues accumulating data with a sensitivity estimation of about 0.2 eV . The Project 8 experiment will also measure the decay of ${}^3\text{H}$, but follows a different concept [Pro17]. Other experiments using various approaches are aiming for measuring the neutrino mass or lowering the current limit and are expected to publish results in the near future. This includes ECHo, HOLMES as well as the NuMECS experiment investigating the EC (electron capture) of ${}^{163}\text{Ho}$ [ECH14, HOL15, NuM16].

1.4 Present neutrino mass limits

While the absolute masses of the neutrinos are still unknown, they have been measured very precisely for the other fermions, i.e. quarks and charged leptons. The current upper limit on the electron neutrino mass raises the question why the neutrino masses are so tiny and also why they are so different from the other fermion masses since there are no known fermions in the region between 1 eV and 511 keV as illustrated in figure 1.2 [Gou16].

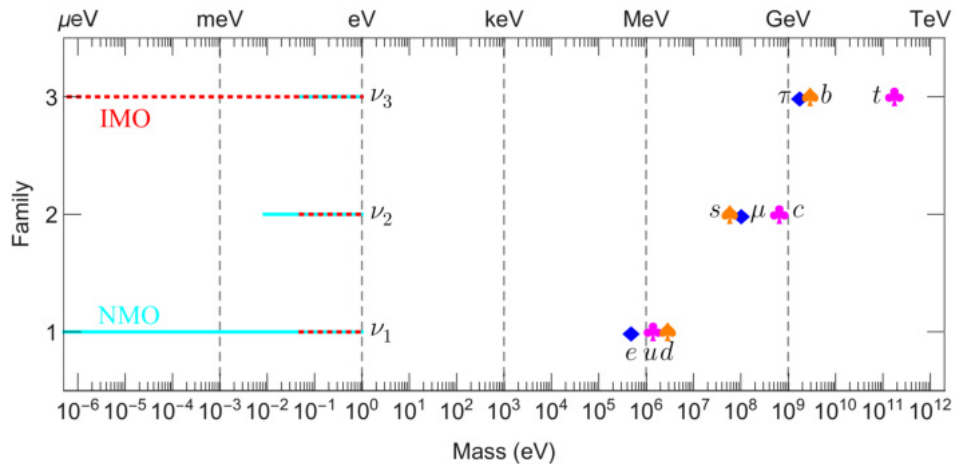


Figure 1.2: Fermion masses of quarks and charged leptons as well as the current allowed mass regions of neutrino mass eigenstates ν_1, ν_2 and ν_3 . The red dashed lines stand for NMO and the cyan lines for IMO. The lower limit of m_1 in the NMO and of m_3 in the IMO can be extended to zero (see also fig. 1.1) [XZ17].

As shown in figure 1.2 the masses of quarks and charged leptons follow an ordering according to their family, sometimes also referred to as generation. Thus it was expected that neutrino masses behave similarly. However, as achieved from oscillation measurements, it is nowadays known that neutrinos mix. While the quark mixing matrix is very structured with diagonal elements being larger than off-diagonal elements and the latter are ordered, the lepton mixing matrix elements are all about one with the exception of U_{e3} . It is argued that the very different mixing behavior causes the neutrino masses to be qualitatively different from the other fermion masses [Gou16].

A summary of the current allowed parameter space of the neutrino masses is depicted in figure 1.3. The effective Majorana neutrino mass is derived from experiments searching for the neutrinoless double beta ($0\nu\beta\beta$) decay, which is discussed in more detail in section 1.5. Cosmology constrains the sum of the three light neutrino masses $\Sigma = \sum m_i$ and clearly disfavors a degenerated mass ordering. The direct neutrino mass measurements exclude values larger than 1.1 eV for the effective electron neutrino mass [BK18, Gou16, MS06].

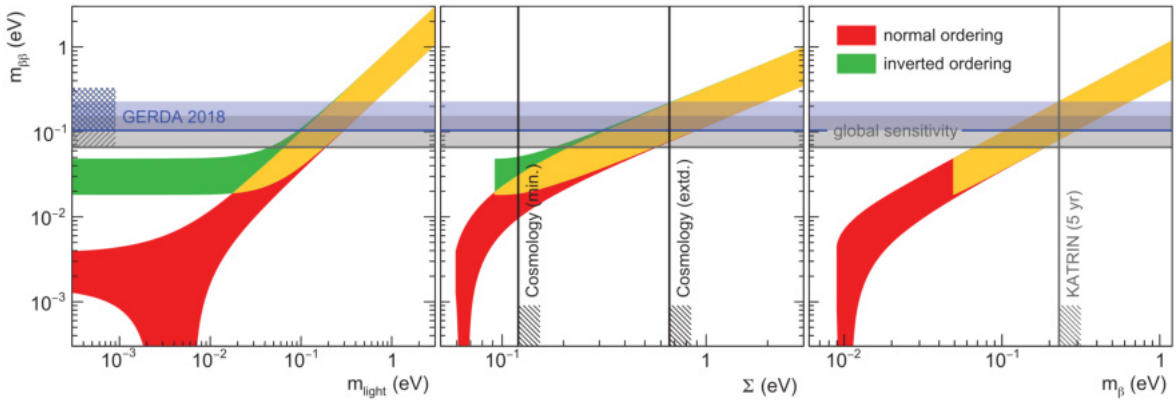


Figure 1.3: Constraints on the parameter space of the effective Majorana neutrino mass $m_{\beta\beta}$ with three light Majorana neutrinos as a function of the lightest neutrino mass m_{light} (left), the sum of the neutrino masses Σ (middle) and the effective electron neutrino mass m_β (right). The red and green bands indicate the allowed values for the NMO and the IMO, respectively. The overlapping region (yellow), where the mass differences are small compared to the absolute masses, is denoted as degenerated mass ordering. In the NMO it is possible that $m_{\beta\beta}$ is zero, while for the IMO oscillation measurements result in a lower bound of $m_{\beta\beta} > 0.016$ eV [PDG19]. The horizontal blue band marks the current upper limit of $m_{\beta\beta}$ achieved by GERDA and the horizontal gray band shows the combined sensitivities of the leading experiments in the search for $0\nu\beta\beta$ decay. The vertical lines in the middle plot denote the limits derived from cosmology with a stringent limit $\Sigma < 0.12$ eV and an extended model bound $\Sigma < 0.66$ eV. The vertical line in the right plot shows the 5-year sensitivity of KATRIN of 0.2 eV. The hatched areas mark the excluded parameter space. From [GER19].

1.5 Double beta decay

In the SM a nucleus (A, Z) is allowed to decay via a $\beta\beta$ decay if the daughter nucleus $(A, Z + 2)$ is energetically low enough. As depicted in figure 1.4 this is possible for even and odd mass numbers A , however is it experimentally accessible solely in the case the first-order β -decay is energetically prohibited. This can only be true for nuclei with even numbers of both neutrons and protons, N and Z , respectively [BK18, DMVV16].

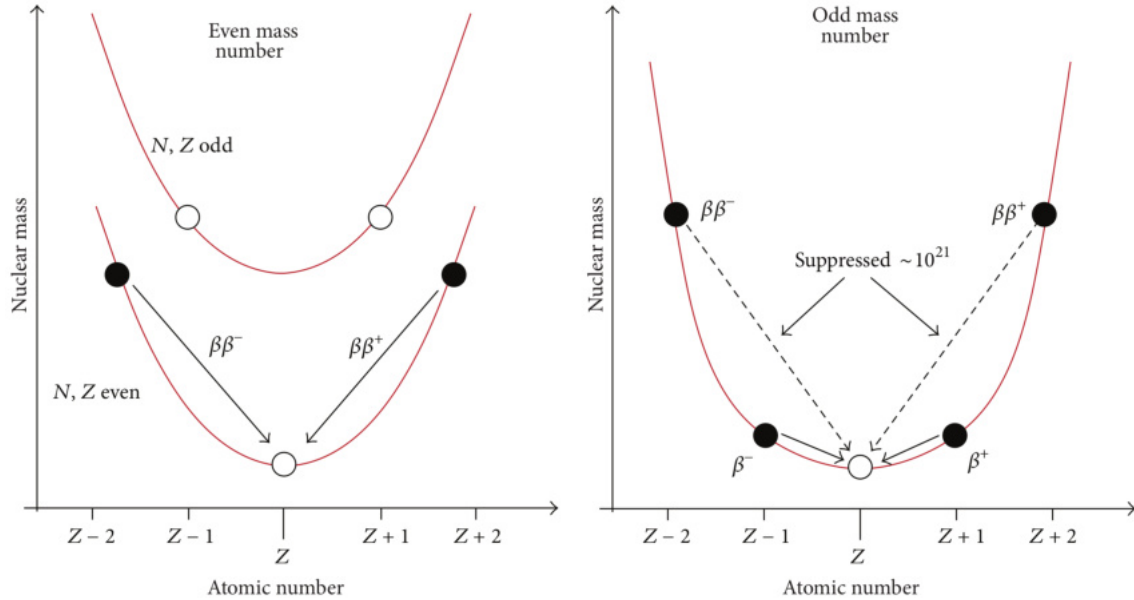


Figure 1.4: Masses of nuclei with an even (left) and an odd (right) mass number A and the respective mass parabolas. For an even A the β -decay is energetically forbidden for some nuclei with N and Z both even, while the $\beta\beta$ decay is possible, allowing for the observation of the latter. For an odd A the $\beta\beta$ decay is always overlaid by the β -decay, making an observation almost impossible [DMVV16].

The neutrino accompanied double beta ($2\nu\beta\beta$) decay can occur in four different modes, which are summarized in equation 1.18. In total there are 35 nuclides known to be capable of undergoing a $\beta^-\beta^-$ (double beta minus) decay and for several of these it has been already observed [PDG19].

$$\begin{aligned}
 \beta^-\beta^- &: (A, Z) \rightarrow (A, Z + 2) + 2e^- + 2\bar{\nu}_e \\
 \beta^+\beta^+ &: (A, Z) \rightarrow (A, Z - 2) + 2e^+ + 2\nu_e \\
 \text{ECEC} &: (A, Z) + 2e^- \rightarrow (A, Z - 2) + 2\nu_e \\
 \text{EC}\beta^+ &: (A, Z) + e^- \rightarrow (A, Z - 2) + e^+ + 2\nu_e
 \end{aligned} \tag{1.18}$$

If neutrinos are Majorana particles, the $\beta\beta$ decay can also occur without the emission of neutrinos, which is called neutrinoless double beta ($0\nu\beta\beta$) decay. This is exemplarily expressed for the $\beta^-\beta^-$ -decay mode as follows [BK18].

$$2\nu\beta\beta : (A, Z) \rightarrow (A, Z + 2) + 2e^- + 2\bar{\nu}_e \tag{1.19}$$

$$0\nu\beta\beta : (A, Z) \rightarrow (A, Z + 2) + 2e^- \tag{1.20}$$

The corresponding feynman graphs of the $2\nu\beta\beta$ decay and the $0\nu\beta\beta$ decay are depicted in figure 1.5. In some references, the $0\nu\beta\beta$ decay is interpreted in such a way that the Majorana neutrino ν_M is emitted by one nucleon and absorbed by another [BK18].

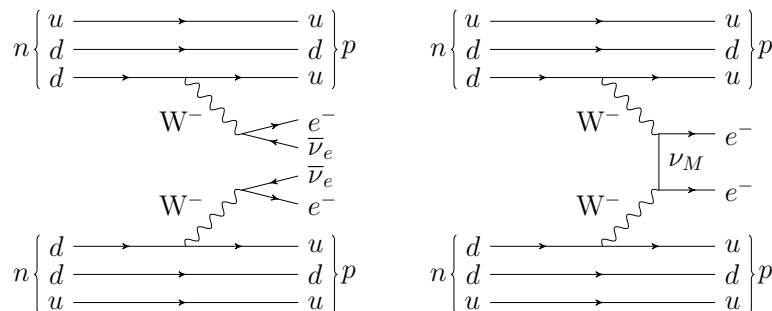


Figure 1.5: Feynman graphs of the $2\nu\beta\beta$ decay (left) and $0\nu\beta\beta$ decay (right). In the $2\nu\beta\beta$ decay the neutrinos are emitted along with the electrons, in the $0\nu\beta\beta$ decay only the two electrons are in the final state.

The $0\nu\beta\beta$ decay has not been observed yet. While light Majorana neutrino exchange is one possible explanation of the $0\nu\beta\beta$ decay, the observation of this transition is neither able to identify the underlying mechanism, nor determining the dominant process. Nevertheless, the detection of $0\nu\beta\beta$ decay would prove that lepton number violating interactions exist and neutrinos are Majorana particles, also known as the Schechter-Valle theorem [SV82]. At the same time, an observation of the $0\nu\beta\beta$ decay would imply that neutrinos cannot be of Dirac character. Consequently, the $0\nu\beta\beta$ decay is the most sensitive probe whether neutrinos are Dirac or Majorana particles. Other mechanisms capable of inducing the $0\nu\beta\beta$ decay, such as the exchange of heavy neutrinos are discussed in [BK18, DPR19, DMVV16, PDG19].

Assuming that light Majorana neutrino exchange is the only contributing process, the half life of the $0\nu\beta\beta$ decay depends on the effective Majorana neutrinos mass $m_{\beta\beta}$ and is connected with the phase space factor $G^{0\nu}$, the NME (nuclear matrix element) $M^{0\nu}$ of the transition and the electron mass m_e as a reference value [PDG19].

$$\left(T_{1/2}^{0\nu}\right)^{-1} = G^{0\nu} |M^{0\nu}|^2 \left(\frac{m_{\beta\beta}}{m_e}\right)^2 \quad (1.21)$$

The effective Majorana neutrino mass $m_{\beta\beta}$, sometimes also denoted with m_{ee} , is the sum of the three light neutrinos weighted by the mixing matrix U including the Majorana phases η_1 and η_2 (see eq. 1.5) [DMVV16, PDG19].

$$m_{\beta\beta} = \left| \sum_i U_{ei}^2 m_i \right| \quad (1.22)$$

Since $m_{\beta\beta}$ depends on the neutrino masses and not their squares, the observation or limitation of $0\nu\beta\beta$ decay is sensitive to the neutrino mass ordering as shown in figure 1.3. The half life of the $0\nu\beta\beta$ decay depends also on the Majorana phases in the mixing matrix, on which oscillation experiments are not sensitive. This also includes additional phases induced by possible sterile neutrinos [BK18].

The theoretical calculations of the phase space factor $G^{0\nu}$ are nowadays very precisely for both, single and double beta decay. Relativistic corrections, the finite nuclear size and the effect of atomic screening on the emitted electrons are taken into account solving the Thomas-Fermi equation [DMVV16]. For the NME $M^{0\nu}$ the situation is much more complicated and will be discussed in more detail in the next section.

1.5.1 Nuclear matrix elements

The calculation of the NME requires exact knowledge of the nuclear structure details of the considered nuclide. Different models and approaches result in varying NMEs. A compilation of some selected calculations is depicted in figure 1.6. The results vary depending on the selected model and the individual assumptions concerning the nucleon interactions within the nuclei.

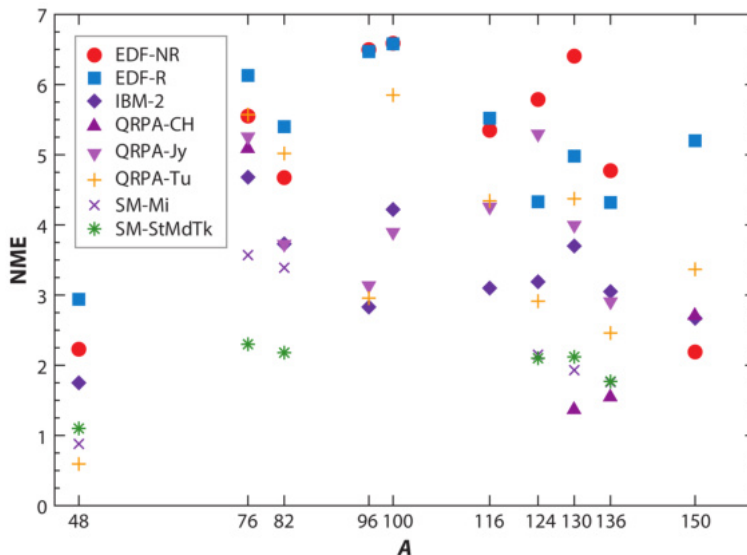


Figure 1.6: Compilation of NMEs calculated with various models assuming an unquenched $g_A = 1.27$ for nuclides of different mass numbers A . Considered models are energy density functional theory (EDF), interacting boson model (IBM-2), quasiparticle random-phase approximation (QRPA) and shell model (SM). The letters after the hyphen label the group or collaboration which calculated the NMEs. From [DPR19], originally published in [EM17] with references to the individual calculations.

For the NME calculations the nuclear wave functions of the initial and the final state of the considered nucleus need to be known leading to a multi-dimensional problem [DPR19]. The NME can be parametrized as follows [DMVV16].

$$M^{0\nu} = g_A^2 \left(M_{\text{GT}}^{0\nu} - \left(\frac{g_V}{g_A} \right)^2 M_{\text{F}}^{0\nu} + M_{\text{T}}^{0\nu} \right) \quad (1.23)$$

Here, g_V and g_A are the vector and axial vector coupling constants, respectively, $M_{\text{GT}}^{0\nu}$ is the Gamow-Teller matrix element between the initial and the final states describing spin-spin interactions, $M_{\text{F}}^{0\nu}$ is the Fermi matrix element covering spin independent interactions and $M_{\text{T}}^{0\nu}$ is the tensor matrix element. In the case of light Majorana neutrino exchange, the Gamow-Teller matrix element dominates, thus the NME is proportional to g_A^2 , i.e. $T_{1/2}^{0\nu} \sim g_A^4$ [DMVV16, DPR19].

There are hints from measurements of forbidden β -decays, that g_A might be quenched, leading to a much smaller NME and significantly longer $T_{1/2}^{0\nu}$. A quenched g_A would affect all NME models equally. If another mechanism is dominating the $0\nu\beta\beta$ decay, it could be influenced by quenching as well, although it may be not as crucial in the case $M_{\text{GT}}^{0\nu}$ is not the dominant term [DMVV16, DPR19].

Even if the quenching of g_A can be determined by precise $2\nu\beta\beta$ decay measurements, it is not clear yet if the quenching for $2\nu\beta\beta$ and $0\nu\beta\beta$ decay is the same since the $2\nu\beta\beta$ decay can only occur through Gamow-Teller 1^+ transitions of the intermediate nucleus while $0\nu\beta\beta$ decay can happen through all intermediate states [DMVV16, DPR19].

To be more precise, for the NMEs calculations of the $2\nu\beta\beta$ and the $0\nu\beta\beta$ decay virtual intermediate states of the nucleus $(A, Z + 1)$ for $\beta^-\beta^-$ or $(A, Z - 1)$ for $\beta^+\beta^+$ (see eq. 1.18) need to be taken into account [BK18].

In the case of the $2\nu\beta\beta$ decay two neutrinos are emitted, thus the virtual momentum transfers are comparatively small. The ground states of the initial and the final nuclei have both spin parity 0^+ since neutron and proton numbers are both even (see fig. 1.4). Therefore it is sufficient to consider only the 1^+ states of the intermediate nucleus up to $Q_{\beta\beta}$ [BK18, DPR19].

In the $0\nu\beta\beta$ decay no neutrinos are emitted, i.e. they are virtual, resulting in virtual momentum transfers up to a few hundred MeV. Hence, most of the excitation levels of the intermediate nucleus must be considered, which leads to a much more complicated calculation. Consequently, the NMEs of the $2\nu\beta\beta$ and $0\nu\beta\beta$ decay are significantly different even if the calculations are based on the same model and internal assumptions [BK18].

The different models are briefly described in the following.

Nuclear shell model (NSM)

The NSM is based on the following assumptions. The nucleons fill nuclear shells. Heavy nuclei typically have an excess of neutrons and the last filled shell near the Fermi level is most important for low-energy properties of the nucleus. Thus, only the correlations between these nucleons are taken into account solving the Schrödinger equation. Consequently, instead of the full Hilbert space, only a limited space near the Fermi surface, the valence space, is considered. Pairing correlations in the valence space are treated precisely, while these of the low-level states might not be fully covered, leading to an underestimation of the NME as it can be seen in figure 1.6 [BK18, DMVV16, DPR19, EM17].

Interacting boson model (IBM)

In the IBM the nucleon pairs in low-energy states are treated as bosons. More shells are taken into account compared to the NSM, but fewer correlations are considered. The $0\nu\beta\beta$ decay is then restricted to 0^+ and 2^+ neutron pairs that are transferred into two protons. The IBM is a more phenomenological approach of the nuclear structure and relies on determining the Hamiltonians and effective operators by fits to the data. Hence, the model parameters are adjusted to be compatible with present limits of the $0\nu\beta\beta$ decay [DMVV16, DPR19, EM17].

Quasiparticle random-phase approximation (QRPA)

The QRPA covers a large valence space including most of the orbitals up to the Fermi surface, but contains only few correlations. Single particles states in a Woods-Saxon potential and the proton-proton as well as the neutron-neutron pairings are considered. The QRPA calculations are adjusted to reproduce the measured $2\nu\beta\beta$ decay half-lives [DMVV16, DPR19, EM17].

Energy density functional theory (EDF)

While the other models use simple mean fields which states and orbitals feel, the EDF mixes many mean fields with various properties. Many single-particle states and their collective motion are considered, but only a few correlations are used. This might lead to an overestimation of the NME as shown in figure 1.6 [DMVV16, DPR19].

1.5.2 Experimental considerations

Within the last decades an extensive $0\nu\beta\beta$ search with multiple isotopes has been developed, which will help clarifying the open questions regarding the Majorana or Dirac nature of the neutrino as well as the theoretical aspects concerning NME calculations and possible g_A quenching.

In the $2\nu\beta\beta$ decay the released energy, i.e. the Q -value, is distributed uniformly on the electrons and antineutrinos resulting in a continuous electron energy spectrum observed by the detector as depicted in figure 1.7. On the contrary, in the $0\nu\beta\beta$ decay only two electrons are emitted. In total they receive the complete energy released in the decay, since the recoil of the nucleus is negligible. Thus, a tiny peak at the Q -value is expected in the detector.

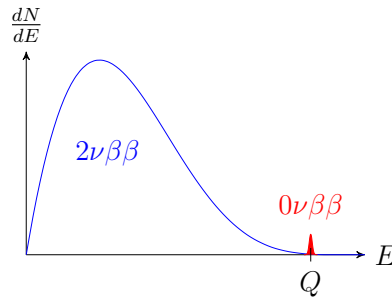


Figure 1.7: Typical spectral shape of a $\beta\beta$ decay. The neutrinos emitted in the $2\nu\beta\beta$ decay leave the detector unseen, thus a continuous electron energy spectrum is observed. In the $0\nu\beta\beta$ decay no neutrinos are released and the two electrons receive in sum the full Q -value causing a peak at this energy. This peak is expected to be very tiny compared to the $2\nu\beta\beta$ spectrum, since the probability of the $0\nu\beta\beta$ decay is much lower.

In the case a $0\nu\beta\beta$ peak is observed, the half life $T_{1/2}^{0\nu}$ of the corresponding isotope can be determined with the number of counts N_{peak} in the peak, the number of nuclei $N_{\beta\beta}$ that are available for the $\beta\beta$ decay, the measuring time t and the detection efficiency ε [BCD19].

$$T_{1/2}^{0\nu} = \ln 2 \cdot t \cdot \varepsilon \cdot \frac{N_{\beta\beta}}{N_{\text{peak}}} \quad (1.24)$$

If no peak is observed in the ROI (region of interest), i.e. the energy region around the Q -value, usually a lower limit on the half life is quoted. Additionally, the sensitivity $S^{0\nu}$ can be derived, which is the minimum half life that is compatible with the background fluctuation at a desired C.L. (confidence level) given by the number of sigmas n_σ . The corresponding background level B , also denoted as BI (background index) is defined as the number of expected background events in the ROI per mass, energy and time. The energy resolution at the Q -value is ΔE [BCD19].

$$S^{0\nu} = \ln 2 \cdot \varepsilon \cdot \frac{1}{n_\sigma} \cdot \frac{x \cdot a \cdot N_A}{M} \cdot \sqrt{\frac{m \cdot t}{B \cdot \Delta E}} \quad (1.25)$$

Here, x is the number of nuclei of the element containing the $\beta\beta$ isotope per molecule, a the isotopic abundance of the $\beta\beta$ nuclide, N_A the Avogadro constant, M the molar mass of the compound and m the total mass of the compound containing the $\beta\beta$ isotope [BCD19].

Equation 1.25 assumes Gaussian distributed uncertainties, hence it is not accurate for very low counts. In order to be able to observe the $0\nu\beta\beta$, i.e. increase the sensitivity, an experiment has to maximize the detection efficiency ε , the available number of $\beta\beta$ isotopes and the measuring time t while at the same time keeping the background level B in the ROI as low as possible and achieving a sufficiently well energy resolution at $Q_{\beta\beta}$ [BCD19].

In the case that the background level becomes so low, that the expected number of background events in the ROI is below one, equation 1.25 is modified using the maximum number of counts n_L compatible with the expected background within a certain C.L. [BCD19].

$$S_{0\text{bkg}}^{0\nu} = \ln 2 \cdot \varepsilon \cdot \frac{x \cdot a \cdot N_A}{M} \cdot \frac{m \cdot t}{n_L} \quad (1.26)$$

Comparing equations 1.25 and 1.26 it gets obvious to aim for a background free experiment since in this case the sensitivity scales linearly with the exposure, which is defined as the product of the active $\beta\beta$ mass multiplied with the measuring time [BCD19].

The sensitivity formulas also indicate that a high isotopic abundance a is most desirable. At the same time the selected isotope should have a sufficiently high Q -value since the phase space factor $G^{0\nu}$ (see eq. 1.21) scales with $Q_{\beta\beta}^5$ [DPR19], leading to a significantly larger decay rate. Additionally, Q -values above the highest prominent natural occurring γ -line at 2614 keV emitted by ^{208}Tl [IAE20] are favored, because a very low background can be achieved due to the absence of any Compton continuum at $Q_{\beta\beta}$ [BCD19].

A compilation of selected isotopes that are interesting for the search of $0\nu\beta\beta$ decay are listed in table 1.1 together with corresponding experiments setting limits on the $0\nu\beta\beta$ decay, but also measuring the half life of the $2\nu\beta\beta$ very precisely.

Table 1.1: List of selected isotopes with $Q_{\beta\beta} > 2 \text{ MeV}$. The natural abundances a_{nat} are taken from [IAE20]. If $T_{1/2}^{2\nu}$ is not included in the given reference, it is taken from the corresponding latest measurement quoted in [Bar19]. The limits on $T_{1/2}^{0\nu}$ list the results of the currently leading experiments for the respective isotope.

isotope	a_{nat} [%]	$Q_{\beta\beta}$ [keV]	$T_{1/2}^{2\nu}$ [yr]	$T_{1/2}^{0\nu}$ [yr]	experiment	ref.
^{48}Ca	0.187	4268	$6.4 \cdot 10^{19}$	$> 5.8 \cdot 10^{22}$	ELEGANT-IV	[UKO+08]
				$> 1.3 \cdot 10^{22}$	NEMO-3	[NEM11]
^{76}Ge	7.73	2039	$1.92 \cdot 10^{21}$	$> 0.9 \cdot 10^{26}$	GERDA	[GER19]
				$> 2.7 \cdot 10^{25}$	MAJORANA	[MAJ19a]
^{82}Se	8.73	3517	$9.39 \cdot 10^{19}$	$> 2.4 \cdot 10^{24}$	CUPID-0	[CUP18]
^{96}Zr	2.80	3350	$2.35 \cdot 10^{19}$	$> 9.2 \cdot 10^{21}$	NEMO-3	[NEM11]
^{100}Mo	9.82	3034	$7.11 \cdot 10^{18}$	$> 1.1 \cdot 10^{24}$	NEMO-3	[NEM11]
^{116}Cd	7.49	2813	$2.63 \cdot 10^{19}$	$> 2.2 \cdot 10^{23}$	Aurora	[BBB+18]
^{130}Te	34.08	2527	$7.9 \cdot 10^{20}$	$> 1.5 \cdot 10^{25}$	CUORE	[CUO18]
^{136}Xe	8.86	2458	$2.21 \cdot 10^{21}$	$> 1.07 \cdot 10^{26}$	KamLAND-Zen	[KLZ16]
				$> 1.8 \cdot 10^{25}$	EXO-200	[EXO18]
^{150}Nd	5.638	3371	$9.34 \cdot 10^{18}$	$> 2.0 \cdot 10^{22}$	NEMO-3	[NEM16]

Due to its already high natural abundance, ^{130}Te is a good candidate in order to reach a large sensitivity. Furthermore, materials can be enriched in the desired isotope, increasing the abundance of the $\beta\beta$ isotope to much larger values than provided by nature. However, the lower the natural abundance, the higher are the costs of the enrichment [DPR19].

The detection efficiency ε can be increased significantly by integrating the $\beta\beta$ isotope in the detector material. Obviously, the detection technique has to be suitable for this. Typical examples are semiconductor detectors made of germanium, which are enriched in ^{76}Ge or scintillation detectors with xenon containing ^{136}Xe . A detailed discussion of various detection techniques with examples of corresponding successful realized experiments can be found in [BCD19, DMVV16, DPR19].

Chapter 2

The GERDA experiment

The GERDA (Germanium Detector Array) experiment is located in the underground laboratory LNGS (Laboratori Nazionali del Gran Sasso) in Italy and searches for the $0\nu\beta\beta$ decay in ^{76}Ge . The following section will provide a brief insight into the LNGS. The various phases of GERDA and the latest upgrade are discussed as well as the current results. The successor experiment LEGEND (Large Enriched Germanium Experiment for $0\nu\beta\beta$ Decay) which will use the existing infrastructure of GERDA is shortly described at the end of this chapter.

2.1 Laboratori Nazionali del Gran Sasso

The LNGS is one of the largest underground laboratories in the world. It is funded by the INFN (Istituto Nazionale di Fisica Nucleare) and devoted to experiments looking for new insights into neutrino and astroparticle physics as well as dark matter searches. The LNGS is located 120 km east of Rome and can be accessed from a 10 km long highway tunnel going from Teramo to L'Aquila. The tunnel is crossing the Gran Sasso massif providing 1400 m of rock overburden, which is equal to about 3400 m.w.e. (meters of water equivalent). The cosmic muon flux is reduced by a factor of 10^6 and the neutron flux by 1000 [LNG20]. The reduction of the muon flux is depicted in comparison to other underground laboratories of various depths in figure 2.1.

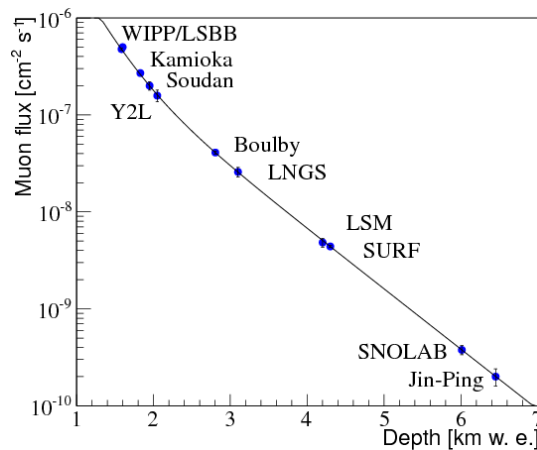


Figure 2.1: Muon flux depending on the depth of several underground laboratories. While the LNGS was the largest and SNOLAB the deepest of these facilities for a long time, Jin-Ping is now claiming both titles for itself and has a lower muon flux than achieved in any other underground laboratory before [UR16].

The LNGS underground facility consists of three main halls, which are about 100 m long, 20 m wide and 18 m high providing enough room for several large experiments. Less space consuming experiments are housed in the smaller connecting tunnels. A map of the main halls, the highway tunnel and connecting tunnels is shown in figure 2.2 [LNG20].

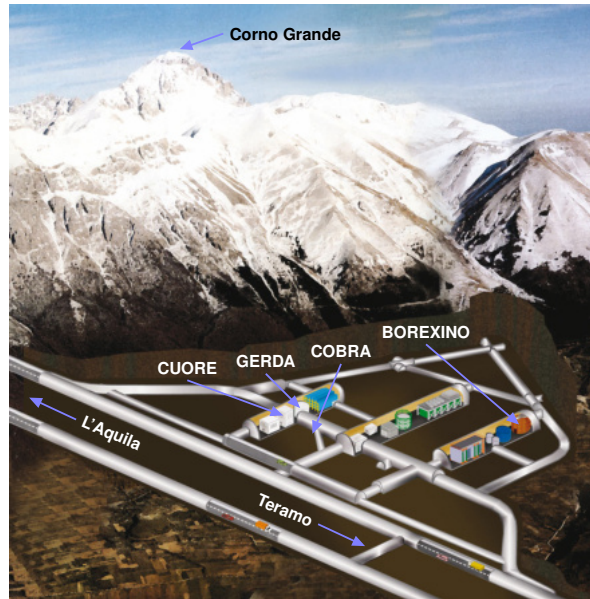


Figure 2.2: Sketch of the LNGS underground laboratory with the three main halls. The positions of some selected experiments as well as the directions of the highway tunnels are indicated. The rumor says, that the highest mountain in the Gran Sasso massif “Corno Grande” peaks right above Hall A, where the GERDA experiment is located [App14].

The outside facility consists of more than 23 laboratories, workshops and the computing center. Currently about 1100 scientists from 29 countries are involved in the research activities at the LNGS. At the moment four of the many experiments housed in the LNGS are dedicated to the $0\nu\beta\beta$ decay search within different isotopes. This includes COBRA (Cadmium Zinc Telluride 0-Neutrino Double-Beta Research Apparatus) and GERDA operating semiconductor detectors as well as CUORE (Cryogenic Underground Laboratory for Rare Events) and CUPID (CUORE Upgrade with Particle Identification) using a crystal bolometer approach [LNG20].

2.2 GERDA Phase I and II

The GERDA experiment uses germanium detectors which are enriched in the $\beta\beta$ candidate ^{76}Ge pursuing the approach that the source equals the detector. The detectors are operated bare in liquid argon which serves as a cooling for the detectors and a shielding against external radiation. The LAr (liquid argon) cryostat is surrounded by a water tank acting as a muon veto and an additional shield. The current setup is depicted in figure 2.3.

The experiment was planned in different phases with successive upgrades adding more detector mass while decreasing the background at the same time. Phase I was running from November 2011 until June 2013 without any indication of a signal. The exposure was $21.6 \text{ kg} \cdot \text{yr}$ and a BI of $10^{-2} \text{ counts}/(\text{keV} \cdot \text{kg} \cdot \text{yr})$ could be achieved. Phase II started in December 2015 with the aim of $100 \text{ kg} \cdot \text{yr}$ exposure and a design goal of a BI of $10^{-3} \text{ counts}/\text{keV} \cdot \text{kg} \cdot \text{yr}$, thus decreasing the BI by a factor of 10 compared to the previous phase [GER18a, GER18b]. An additional upgrade within Phase II was done in the time between April and June 2018, adding more enriched detectors to the already existing ones. The subsequent data taking period is denoted as Phase II+. Several changes of the setup were necessary in order to reach the design goals, which is explained in more detail in the following sections.

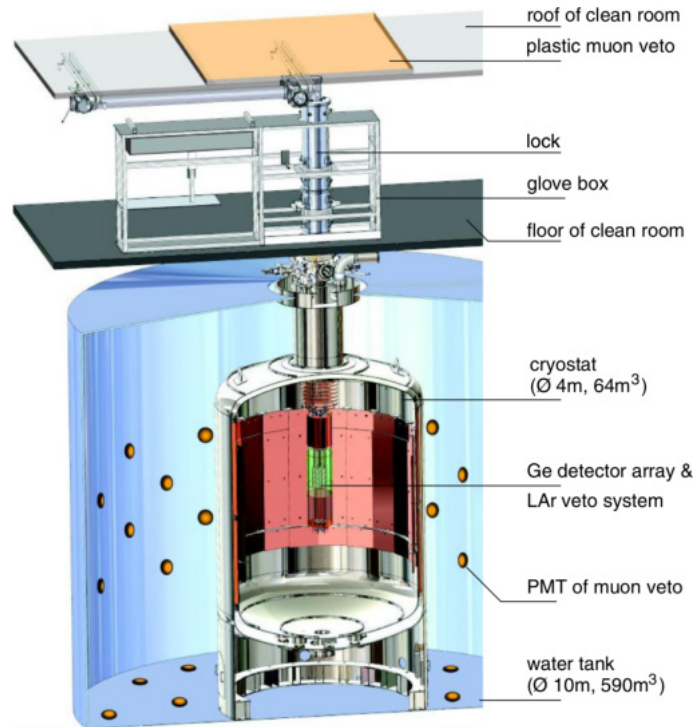


Figure 2.3: The setup of the GERDA experiment in phase II. The germanium detectors are operated in the LAr which acts as a coolant of the detectors and shields them from external radiation. The detector array is surrounded by the LAr veto which rejects background events depositing energy into LAr. The LAr cryostat is enclosed by a water tank serving as a Cherenkov muon veto. On top of the water tank is the clean room providing access to the LAr cryostat via a lock system. An additional muon veto is mounted on the roof of the clean room which observes muons crossing the detector array vertically which are unseen by the water tank [GER18b].

2.2.1 Water Cherenkov veto

A tank filled with 590 m^3 ultra-pure water encloses the LAr cryostat. It serves as a shielding for external γ -radiation and as a moderator for neutrons which can be created by (α, n) reactions from decays of isotopes of the natural radioactive chains in the rock surrounding the underground laboratory [GER18b].

The water is instrumented with 66 PMTs (photomultiplier tubes) facing inward in order to observe Cherenkov light created by muons crossing the water tank. In the case this muon veto triggers coincidentally with a germanium detector, the event will be rejected since it is likely muon induced background. After Phase I the water tank was emptied and two of four broken PMTs have been replaced by spare ones, since these were within reach without scaffolding. At the start of Phase II, three PMTs were not working and until the end of Phase II four more broke [GER18b].

A plastic scintillator panel on the roof of the clean room facility is complementing the muon veto by observing muons which cross the GERDA setup vertically through the lock of the cryostat and are invisible to the water Cherenkov veto [GER18b].

2.2.2 LAr veto

In Phase I of GERDA the LAr was solely used as a cooling for the detectors and as a shielding against external radiation. If ionizing particles deposit energy in LAr, it scintillates (see also ch. 3 for more details), which can be used as an additional background veto [GER19].

While the electrons emitted in the $\beta\beta$ decay can travel only a few millimeters in germanium, thus almost always remain in the detector and do not deposit energy in the LAr, background events, especially γ -rays, usually deposit energy in the germanium detectors as well as the LAr. Therefore, events coincidentally occurring in the germanium detectors and the LAr veto are rejected for the $0\nu\beta\beta$ analysis [GER19, GER18b].

For Phase II the LAr veto was added, i.e. the LAr has been instrumented in order to read out its scintillation light. A schematic sketch of the LAr is depicted in figure 2.4. The dimensions of the instrumentation are constrained by the lock system to a diameter of 50 cm and a height of 2.6 m. PMTs at the top and bottom of the setup are coated with WLS (wavelength shifter) in order to convert the scintillation light at 128 nm to the PMT's sensitive region around 400 nm (see ch. 5.5). Scintillation fibers with a coverage of about 50% surround the detector array. They are read out by SiPMs (Silicon photomultipliers). Copper cylinders above and below the curtain of scintillation fibers serve as a light guide to the PMTs via reflections. The fibers as well as the inner walls of the copper cylinders are coated with WLS in order to maximize the efficiency of the veto system since light shifted to the visible region has a much longer range in LAr compared to the scintillation light (see ch. 3) [GER18b].

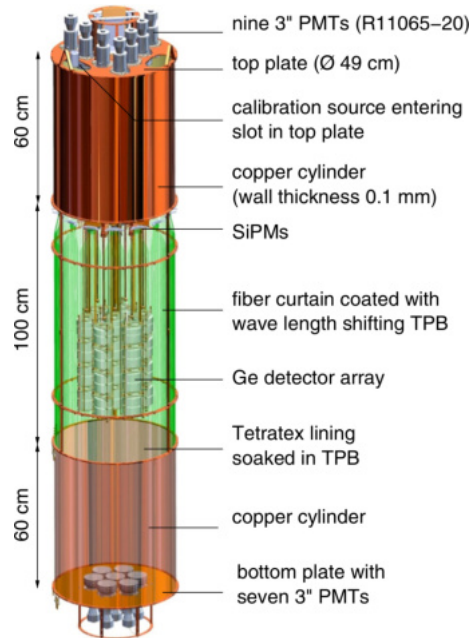


Figure 2.4: LAr veto for Phase II of GERDA. The hybrid system is composed of PMTs at top and bottom of the setup as well as a curtain of scintillation fibers that surrounds the detector array and is read out by SiPMs [GER18b].

Since the amount of material near to the germanium detectors is larger than in Phase I due to the LAr instrumentation, the restrictions for the radiopurity of each part entering the LAr became more stringent in Phase II in order to achieve the aimed BI. Thus, all materials and parts used for the detector array and the LAr veto were screened for radioactive contaminations before deploying them in the LAr cryostat [GER18b].

In order to monitor the LAr veto performance and the LAr quality, two parameters are recorded permanently during Phase II, which are depicted in figure 2.5. The triplet lifetime is an indication of the impurity level of LAr, which is discussed in more detail in chapter 3.2.1. It was stable around $1\ \mu\text{s}$ during Phase II and shortly after the upgrade to Phase II+, however, after a valve exchange in the cryostat in September 2018 it slightly dropped which suggests that some impurities were injected during the maintenance procedure.

The survival probability is the percentage of events in the energy window 200 – 400 keV which did not trigger the LAr veto. Events in this energy region are mainly originated by the pure β -emitter ^{39}Ar , which is an intrinsic impurity in LAr. Thus, the emitted electrons are expected to trigger almost always scintillation light giving a good indication of the LAr veto efficiency.

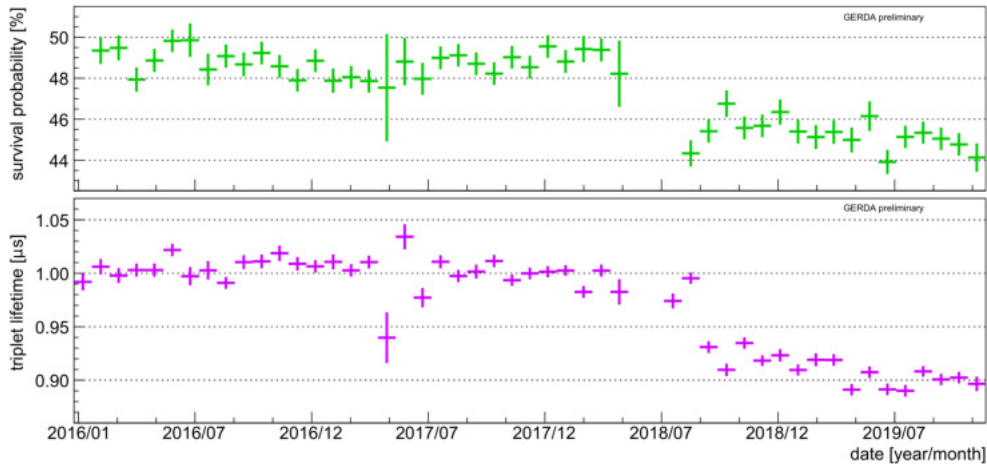


Figure 2.5: Monitoring of the survival probability of ^{39}Ar events (top) and triplet lifetime of LAr (bottom) in GERDA Phase II. The survival probability gives the percentage of events in the energy region of 200 – 400 keV which are mostly induced by ^{39}Ar and are not rejected by the LAr veto cut. The triplet lifetime is stable around $1\ \mu\text{s}$. During the upgrade to Phase II+ from April to June 2018 the purity level of the LAr have been maintained since the triplet lifetime stayed unchanged. The survival probability of ^{39}Ar is reduced after the upgrade due to a improved light collection of the LAr instrumentation. In September 2018 a safety valve in the cryostat was exchanged leading to a small contamination of the LAr which is expressed in a slight increase of the survival probability and a shorter triplet lifetime [Wie].

During the upgrade to Phase II+ the LAr veto was extended by adding more scintillation fibers between the detector strings as shown in figure 2.6. In this way the less efficient light collection between the detector strings has been improved which results in a lower survival probability of ^{39}Ar events as depicted in figure 2.5. Figure 2.6 also shows the nylon shrouds enclosing each detector string. They prevent ionized ^{42}K from the decay of ^{42}Ar in LAr to drift to the germanium detectors due to their electric field. Otherwise ^{42}K would attach to the contacts and thus inducing more background events. Since nylon is opaque for the LAr scintillation light, the mini-shrouds are coated on both sides with WLS, enabling the photon transport through them and increasing the LAr veto detection probability [GER18b].

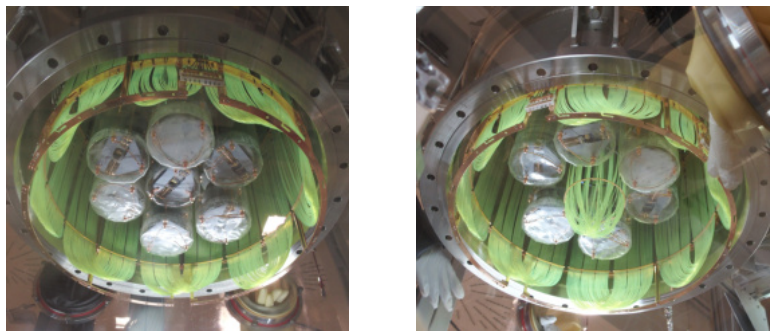


Figure 2.6: View on the bottom of the 7 germanium detector strings hanging in the lock. The scintillation fibers (light greenish color) surround the detector array. From Phase II (left) to Phase II+ (right) scintillation fibers enclosing the middle detector string were added to the existing setup. Pictures taken by GERDA collaborators during the Phase II upgrade in May 2018.

2.2.3 Germanium detector array

The GERDA semiconductor detectors are produced from HPGe (High Purity Germanium) (99.9999% Ge) which is enriched in ^{76}Ge . In Phase I the detector array consisted of 4 strings with 8 enriched (85.5–88.3% ^{76}Ge) semi-coaxial Ge detectors (ANG, RG) with a total mass of 15.6 kg. These detectors were reused from the predecessor experiments Heidelberg-Moscow and IGEX. Additionally, 3 natural (7.8% ^{76}Ge) semi-coaxial Ge detectors (GTF) were operated for crosscheck purposes regarding the enriched detectors. The string holding the natural detectors was replaced in July 2012 by 5 BEGe (Broad Energy Germanium) detectors with a total mass of 3.6 kg [GER19, GER18a, GER18b].

Since the BEGe prototypes operated in Phase I were performing excellently, they became the main detector type in Phase II. 30 BEGe detectors with a total mass of 20.0 kg and an enrichment factor of 87.8% as well as 7 of the enriched and 3 natural coaxial detectors from Phase I are used in Phase II [GER19, GER18a, GER18b]. During the upgrade to Phase II+ the natural and one of the enriched coaxial detectors have been replaced by 5 new enriched detectors of an inverted coaxial (IC) design with a mass of about 1.8 kg each [Wie19]. In Phase II and II+ the detectors are arranged in 7 strings within an array as shown in figure 2.7.

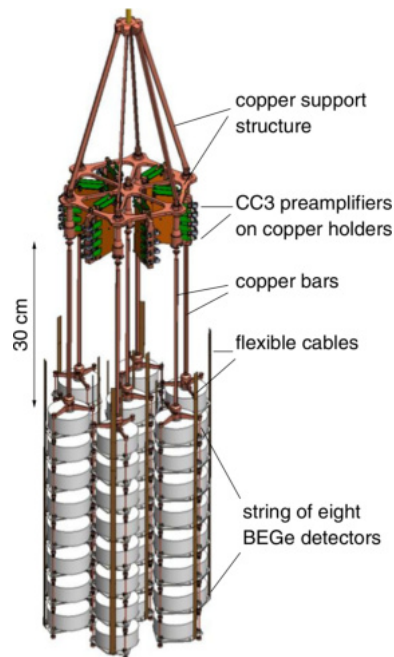


Figure 2.7: Sketch of the detector array for Phase II and II+. The detectors are arranged in 7 strings. In Phase II the middle string consisted of the natural GTF detectors, which were replaced by the inverted coaxial detectors in Phase II+ [GER18b].

The material of the detector holders has been significantly reduced from Phase I to II in order to minimize the background originated by radioactive impurities close to the detectors. CAD drawings of the detectors holders used in Phase II and II+ are depicted in figure 2.8. Initially, the BEGe detectors were arranged in pairs operating one detector upside down. However, during the commissioning of Phase II the detectors with the groove pointing upward featured a worse performance including biasing and leakage currents due to microscopic particles that had fallen into the groove during the detector installation. Thus, the respective detectors have been turned around pursuing a single detector mounting. During the upgrade to Phase II+ it was decided to split the remaining detector pairs to the single detector design as well [GER18b].

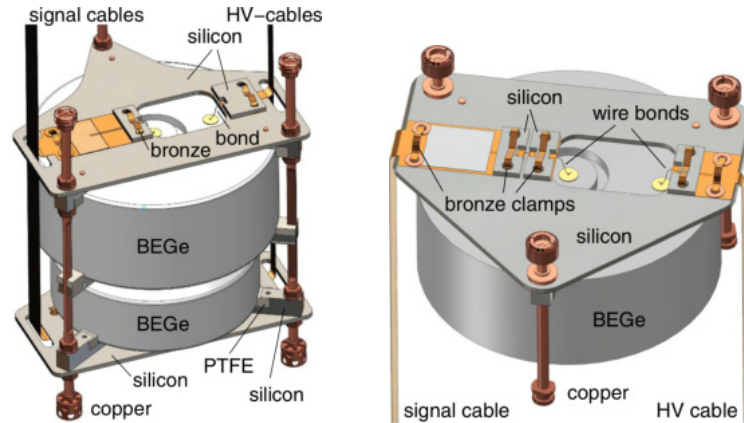


Figure 2.8: Detector holder structure in Phase II and II+ of GERDA. The detector holder material is minimized in order to decrease the background from intrinsic impurities in the materials near the detectors. The holder plates are composed of mono-crystalline silicon which has an intrinsically high radiopurity [GER18b].

The string configuration of the detectors is depicted in figure 2.9 for Phase II and in figure 2.10 for Phase II+. Depending on the location where the detector was cut from the ingot, various shapes occur. Detectors from the middle of an ingot are cylindrical while detectors from the top and bottom feature a conical shape. Since the latter perform equally well, the shape was accepted in order to maximize the number of detectors obtained from one ingot [GER18b].

Compared to Phase I the array is more densely packed including more detectors leading to a significantly larger efficiency for detector-detector coincident events. Since the $\beta\beta$ signal is almost always contained by one single detector, an event which triggers two detectors at the same time can be rejected as background. This procedure is also denoted as the detector anti-coincidence veto [GER18b].

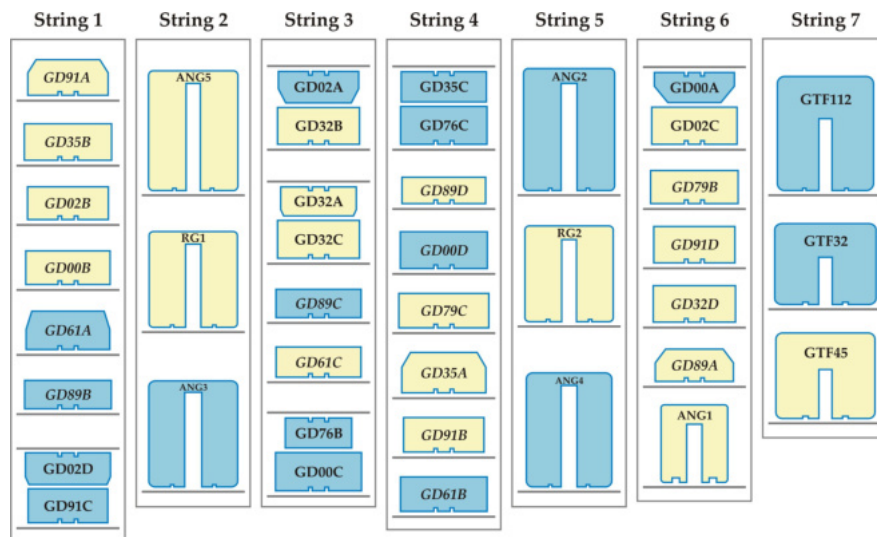


Figure 2.9: String configuration in Phase II. The BEGe detectors (GDxxx) are partly paired with the top detector operated upside down. The horizontal gray lines mark the position of the silicon plates (see fig.2.8). 6 of the semi-coaxial detectors (RGx and ANGx) are located in the two opposite strings 2 and 5 (see also fig. 2.7). The natural detectors (GTFxx) are in the middle string 7. The detector numbering indicates the specific ingot from which the detector was cut and the last letter denotes the corresponding cut position, i.e. A–D from the top to bottom. Detectors colored blue have the original manufacturer’s passivation layer on the insulating groove between p^+ and n^+ contact, for the yellow colored detector this layer is removed [GER18b].

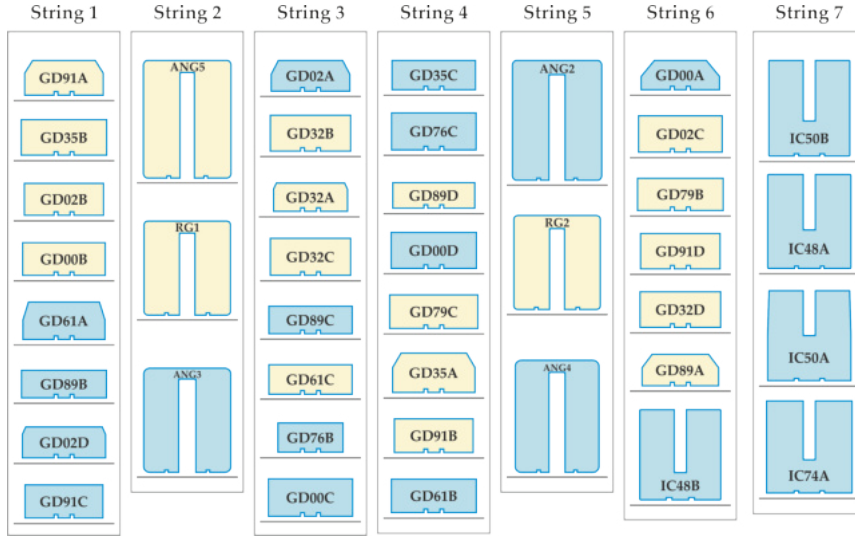


Figure 2.10: String configuration in Phase II+. See also figure 2.9 for more details. The inverted coaxial detectors (ICxxx) replace the natural detectors in the middle string 7 and one semi-coaxial detector in string 6 [Gus18].

2.3 Results

The analysis is performed blinded, i.e. the events in the energy range of $Q_{\beta\beta} \pm 25$ keV are revealed only after all analysis steps are fixed in order to prevent a human bias in the choice of analysis parameters. The Ge detector signals are recorded with a sampling rate of 100 MHz allowing for a complex offline analysis. Calibrations are performed weekly with ^{228}Th sources for the monitoring of the energy scale and resolution. Additionally, the analysis cuts are also tested with the calibration data. The Ge detectors feature an excellent energy resolution with a FWHM (full width at half maximum) at $Q_{\beta\beta}$ of 3.6 ± 0.1 keV for the coaxial detectors and 3.0 ± 0.1 keV for the BEGe detectors [GER19].

If at least one Ge detector triggers, all Ge and LAr channels are read out. Events are rejected if the water Cherenkov veto or the LAr veto trigger simultaneously. Multiple Ge detector hits are discarded by the anti-coincidence cut for the $0\nu\beta\beta$ analysis. With the help of PSD (pulse shape discrimination), events occurring in single or in multiple positions in the detector, and also surface events, can be distinguished. Since the range of the electrons emitted in the $\beta\beta$ decay is only a few millimeters, a signal-like event deposits energy within a very localized single site in the detector. On the contrary, multi-site events are background-like and are rejected by the PSD for the $0\nu\beta\beta$ analysis.

Figure 2.11 shows the GERDA Phase II spectra before analysis cuts as well as after PSD and LAr veto. Below 500 keV the spectrum is dominated by ^{39}Ar events. Between 500 keV and 1800 keV the main contributions come from the $2\nu\beta\beta$ decay of ^{76}Ge and the Compton continua from ^{40}K and ^{42}K . Above the ^{208}Tl line the spectrum is dominated by α decays, which are mainly from ^{210}Po at the p^+ contact or in the insulating groove between the p^+ and n^+ electrodes. The γ line emitted by ^{40}K is originated from a preceding EC, thus if the full γ energy is observed in a Ge detector, no energy is deposited in LAr and the event is not vetoed. Still, such events can be rejected by the PSD cut. Since the γ line from ^{42}K is accompanied by a β decay depositing up to 2 MeV in LAr, these events are effectively discarded by the LAr veto. In the ROI of the $0\nu\beta\beta$ decay the energy spectrum is populated by α decays from ^{210}Po and β decays from ^{42}K at the detector surface as well as Compton scattered γ rays from ^{214}Bi and ^{208}Tl [GER18a].

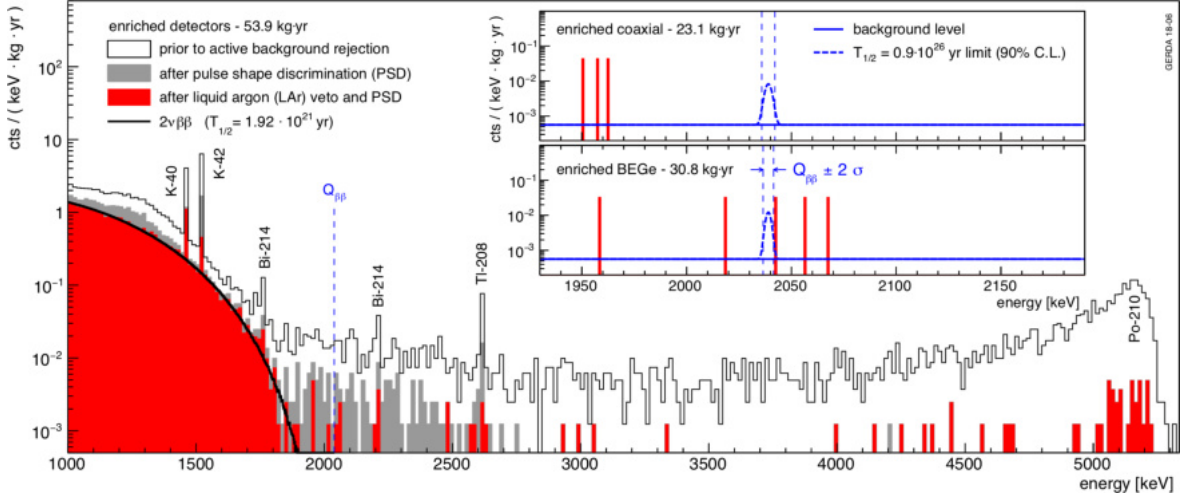


Figure 2.11: Combined energy spectra of GERDA Phase II enriched detectors for an exposure of 53.9 kg · yr. After LAr veto and PSD the spectrum at low energies is dominated by the $2\nu\beta\beta$ decay. The insets show the ROI for the two enriched detector types used in Phase II with the BI and 90% C.L. limit for a signal of $T_{1/2}^{0\nu} > 0.9 \cdot 10^{26}$ yr derived from the likelihood fit of the combined data sets. No events are observed within $Q_{\beta\beta} \pm 2\sigma$ after all analysis cuts [GER19].

GERDA is quasi background-free after applying all analysis cuts, i.e. within the planned exposure of 100 kg · yr the expected background counts within $Q_{\beta\beta} \pm 2\sigma$ is less than one. More precisely, the predicted background rate is $5.7^{+4.1}_{-2.6} \cdot 10^{-4}$ counts/(keV · kg · yr) for the coaxial detectors and of $5.6^{+3.4}_{-2.4} \cdot 10^{-4}$ counts/(keV · kg · yr) for the BEGe detectors. No signal for the $0\nu\beta\beta$ decay has been observed after an exposure of 53.9 kg · yr. A lower half life limit of $T_{1/2}^{0\nu} > 0.9 \cdot 10^{26}$ yr (90% C.L.) has been derived. This limit is compatible with a sensitivity of $1.1 \cdot 10^{26}$ yr assuming no signal [GER19].

2.4 Successor experiment LEGEND

After the GERDA experiment is concluded, the existing infrastructure will be overtaken by the LEGEND experiment, which is a joint collaboration of GERDA and MAJORANA members.

The first phase, LEGEND-200, aims for 200 kg of ^{76}Ge pursuing a similar approach as GERDA. The preliminary design of the extended lock of the LAr cryostat and a potential string configuration with the LAr veto is depicted in figure 2.12 [GER19]. The lock will be broadened in order to be able to house more and longer detector strings. Currently, it is planned to arrange 14 strings in a circle with scintillation fibers covering the inner and the outer mantle of the resulting cylinder for a maximum light collection probability, i.e. LAr veto efficiency. At the same time, the rate of multi-detector hits will be decreased compared to GERDA due to the less denser packed detector array.

The LEGEND experiment aims for an exposure of 1 t · yr while at the same time lowering the BI to 0.6 counts/(FWHM · t · yr), i.e. the goal sensitivity will be increased by factor of about 10 [LEG17].

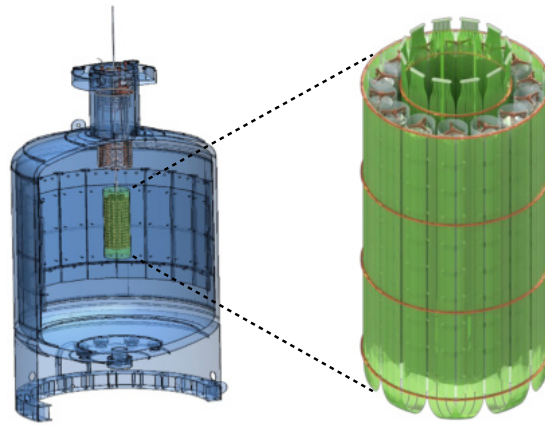


Figure 2.12: Lock design for the LAr cryostat and LAr veto for the LEGEND experiment. The lock will be extended in order to be able to house a LAr veto with a larger diameter and length. The detector strings are planned to be arranged in a circular design with scintillation fibers on the outer and the inner sides for a maximal LAr veto efficiency [Zsi19].

Chapter 3

Scintillation properties of liquid argon

Liquid noble gases such as argon and xenon are suitable detection media for WIMPs (weakly interacting massive particles), which are currently the most promising candidates for dark matter. Both argon and xenon have high scintillation yields and low ionization potentials which make them also ideal for charge detection [ABB⁺08]. While some detectors use only the scintillation light [DEA19], others are built as two phase TPCs (time projection chambers), additionally collecting the induced charge [Dar18, XEN17]. Purified liquid noble gases are commercially available, but argon is much cheaper compared to xenon, making it the preferred choice for larger volumes. On the counterside, argon that is extracted from air in the atmosphere contains the natural contaminations ^{39}Ar ($T_{1/2} = 269$ yr, $Q_{\beta} = 565$ keV) and ^{42}Ar ($T_{1/2} = 32.9$ yr, $Q_{\beta} = 599$ keV) [CEF99], which are produced by cosmic rays interacting in the atmosphere [PPS⁺08]. However, ^{39}Ar can be removed by constantly cleaning the argon with an active purification plant connected to the detector [DEA19].

3.1 Scintillation mechanism

Particles depositing energy along their propagation in LAr can excite (Ar^*) or ionize (Ar^+) argon atoms, which form excited (Ar_2^*) or ionized (Ar_2^+) argon molecules by collisions with argon atoms in the ground state. This process is pictured in figure 3.1. These so called excimer molecules are built in singlet ($^1\Sigma_u$) or triplet ($^3\Sigma_u$) states, depending on the previous spin orientation of the excited electron in the predecessor state of the excimer molecule [HDH⁺13]. The ionized argon molecule (charged excimer) gets neutralized by the recombination with a thermalized electron. In both ways the resulting excited argon molecule (neutral excimer) decays radiatively into two unbound argon atoms in the ground state.

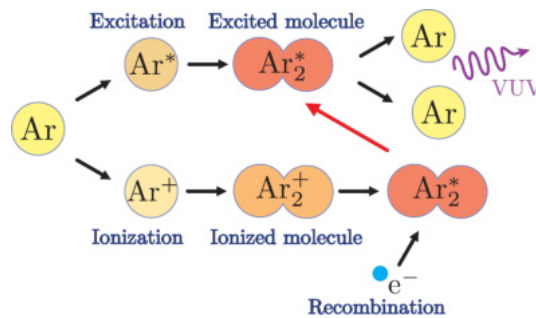


Figure 3.1: Sketch of the LAr scintillation mechanism. Particles depositing energy in LAr lead to excited (Ar^*) or ionized (Ar^+) argon atoms, which form molecules with atoms in the ground state. The ionized molecule Ar_2^+ recombines with a free electron to the excited molecule Ar_2^* . This decays into two ground state argon atoms under the emission of a vacuum ultraviolet (VUV) photon [ABB⁺08].

The described processes occur in noble gases in their liquid and gaseous appearance. In GAr (gaseous argon) both mechanisms are strongly dependent on the pressure and density.

While excitation dominates for GAR at room temperature and normal pressure, ionization becomes more relevant at higher pressures or in liquid [ABB⁺08].

Figure 3.2 shows the excitation scheme of an argon atom. The 1P_1 and 3P_1 states have lifetimes in the order of $10^{-5} - 10^{-6}$ s and the resulting de-excitation gammas are highly absorbed in argon, hence these are trapped within the argon and cannot be observed. The transition from the 3P_2 and 3P_0 states are dipole forbidden and have therefore longer lifetimes. All of these four states can be reached either by direct excitation from the ground state 1S_0 or by de-excitation cascades from higher states. The 3P_1 and 3P_2 states can form molecules by the collision with argon atoms in the ground state 1S_0 , which the 1P_1 and 3P_0 states do not do [GJR⁺72]. The scintillation light emitted from the molecular states $^1\Sigma_u$ and $^3\Sigma_u$ peaks around 128 nm and is not absorbed by atomic argon, hence it propagates in argon and can be detected [ABB⁺08].

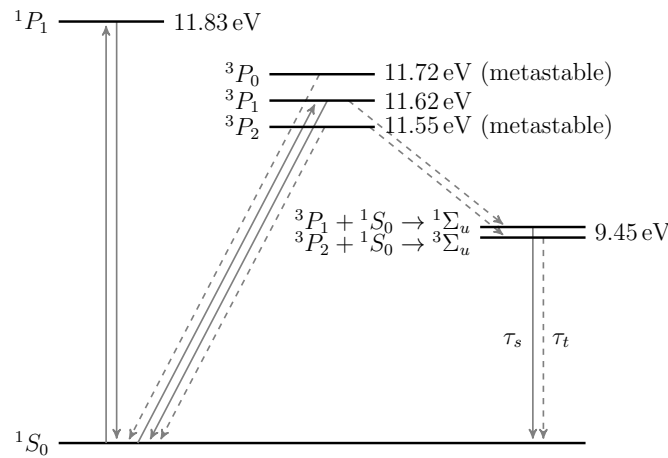


Figure 3.2: LAr energy scheme of the four lowest excited states. The de-excitation gammas of the 1P_1 and 3P_1 states are heavily reabsorbed in argon, while the 3P_0 and 3P_2 states are dipole forbidden. An argon in the 3P_1 or 3P_2 state can form the molecular state $^1\Sigma_u$ or $^3\Sigma_u$ when colliding with an argon atom in the ground state 1S_0 . The mechanism occurs similarly in xenon and krypton. Adapted from [GJR⁺72].

The kind of particle depositing energy in LAr strongly changes the production time (recombination time) of the excimer molecules $^1\Sigma_u$ and $^3\Sigma_u$ (see table 3.1), but does not affect the emitted scintillation wavelength [HDH⁺13].

Table 3.1: Production times of the excimer molecules for different particle beams depositing energy in LAr.

particle	production time [ns]	reference
e^-	0.80 ± 0.25 (108 K)	[KGS79]
e^-	1.00 ± 0.20 (120 K)	[KGS79]
p	7.7 ± 0.1	[HDH ⁺ 13]
sulfur	37.4 ± 0.2	[HDH ⁺ 13]

The lifetimes (decay times) of the singlet $^1\Sigma_u$ and the triplet $^3\Sigma_u$ state are independent of the temperature and density of argon as well as the emitted scintillation wavelength. While in one reference the decay time of the singlet state varies with the kind of particle beam used to excite the argon [HDH⁺13], in another it was found that the singlet and triplet decay times are independent of the ionizing particle [ABB⁺08].

The ratio of the singlet to triplet intensity is found to be larger for higher energies of the ionizing particle and is also dependent on the particle type [HDH⁺13, HTF⁺83, KGS79]. Additionally, for shorter wavelengths the contribution of singlet states gets larger [HDH⁺13]. Both are summarized in table 3.2.

Since γ -rays create electrons via photoelectric effect, Compton scattering and pair production in LAr, the values in table 3.2 are similar for both particles. It should be noted, that in one reference the authors include the recombination time of the molecules in the fit of the decay times of the singlet and triplet states, which changes the result of the fast singlet decay time greatly [HDH⁺13]. A unique property of argon is the much longer triplet lifetime compared to other noble gases [ABB⁺08]. Xenon, for instance, has a triplet lifetime around 21 – 34 ns [HTF⁺83].

Table 3.2: Compilation of selected measurements of singlet τ_s and triplet τ_t lifetimes as well as the singlet to triplet intensity ratio I_s/I_t in pure LAr. The acronym f.f. stands for fission fragments.

particle	τ_s [ns]	τ_t [ns]	I_s/I_t	reference
e^-	6.3 ± 0.2	1020 ± 60	0.083	[KHR78]
	4.6	1540	0.26	[CK79]
	6.5	1100	0.086	[KHSR82]
	6 ± 2	1590 ± 100	0.3	[HTF ⁺ 83]
	< 6.2	1300 ± 60	0.51 ± 0.05	[HDH ⁺ 10], [Hei11]
γ	10 ± 5	1280 ± 20	0.30 ± 0.01	[PPS ⁺ 08]
α	4.4	1100	3.3	[CK79]
	7.1 ± 1.0	1660 ± 100	1.3	[HTF ⁺ 83]
	10 ± 5	1280 ± 20	2.6 ± 0.1	[PPS ⁺ 08]
n	10 ± 5	1280 ± 20	3.5 ± 0.2	[PPS ⁺ 08]
p	3.20 ± 0.02	1355.8 ± 5.8	0.28 ± 0.01	[HDH ⁺ 13]
f.f.	6.8 ± 1.0	1550 ± 100	3	[HTF ⁺ 83]
	6.47 ± 0.09	1224.0 ± 17.9	2.19 ± 0.07	[HDH ⁺ 13]

A measurement of the scintillation spectrum of LAr is shown in figure 3.3. The light emission in LAr is dominated by the lowest molecular states $^1\Sigma_u$ and $^3\Sigma_u$, which is also called the second excimer continuum and peaks around 128 nm [GJR⁺72, HDH⁺10]. Since both states emit photons in a broad range, they cannot be separated by variations in the spectrum [HTF⁺83]. However, the large difference between the two time constants τ_s and τ_t allows more detailed studies regarding the composition of the emitted spectrum by LAr. The second excimer continuum is dominated by the slow component and comprises 99.9% of the emitted light. The 3rd continuum around 160 – 300 nm mostly contains the fast component [ABB⁺08, HDH⁺13].

Various measurements result in different values for the position as well as the width of the scintillation peak of the 2nd excimer continuum. While some references quote 128 nm [HTF⁺83, ABB⁺08], others result in 126.5 nm [GVBB97] and 126.8 nm (FWHM 7.8 nm) [HDH⁺10]. Some authors performed measurements with different incident particles, which indicate a dependence on the peak position as shown in table 3.3. In comparison to that, the 2nd excimer continuum of xenon peaks around 172 – 178 nm [DHK⁺02, GBMN17, HTF⁺83].

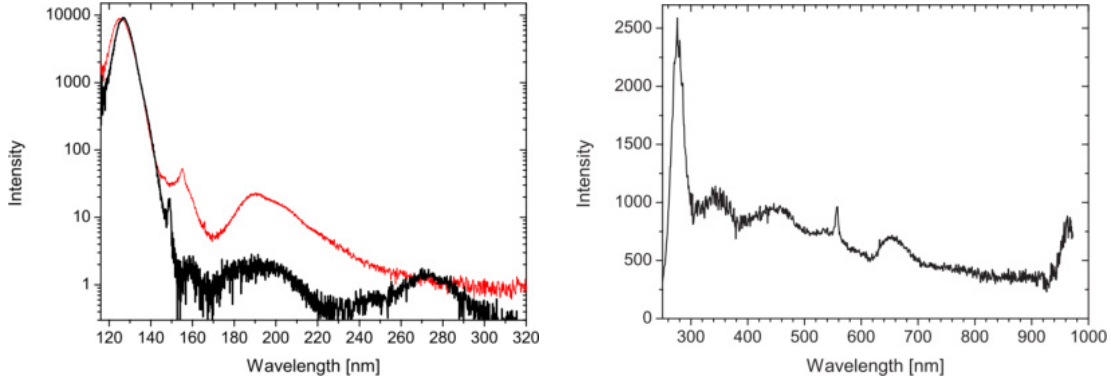


Figure 3.3: Argon scintillation emission spectrum. Left: The black line indicates LAr and the red line GAr. The peak at 149.1 nm is an emission line from oxygen. The 2nd continuum at 278 nm has by far the highest intensity in the whole spectrum. The 3rd emission continuum is visible around 270 nm in LAr. Right: The emission probability in the optical region is significantly smaller compared to the VUV peak. The argon was excited with a 12 keV electron beam [HDH⁺10].

Table 3.3: Measurements of the peak position of the 2nd excimer continuum in LAr. The slightly different values indicate a dependence on the incident particle beam.

particle	peak position [nm]	reference
α	129.5	[JMRW65]
p	126.8 ± 0.1	[HDH ⁺ 13]
S	126.4 ± 0.1	[HDH ⁺ 13]
Au	125.8 ± 0.2	[HDH ⁺ 13]

The average energy to produce one photon in LAr is $W_{\gamma(\max)} = 19.5 \pm 1.0$ eV [DHK⁺02], resulting in an ideal photon yield of $5.1 \cdot 10^4 \gamma/\text{MeV}$ [DMS90]. It was found that this value is quenched differently for various particles depending on their energy. The quenching factor is $Q_\alpha = 0.85 \pm 0.03$ (7.68 MeV) and $Q_\alpha = 0.88 \pm 0.03$ for low energy α particles. Additionally, the singlet to triplet ratio is lower for high energy alphas [PPS⁺08]. Other measurements result in $Q_\alpha = 0.71$ and $Q_e = 0.78$ (1 MeV) with a photon yield of $4.0 \cdot 10^4$ for 1 MeV electrons [DMS90].

3.2 Impurities and their influences on LAr properties

While perfectly pure LAr has a high light yield and is transparent for its own scintillation light, impurities can affect these properties dramatically by quenching and absorption [NHO⁺12, JCC⁺13]. The excited argon molecule decays to two ground state argon atoms under the emission of a 128 nm photon [WAr10a]:



Depending on the type and concentration of the impurity, several effects can occur. Quenching leads to a significant reduction of the Ar_2^* molecules by the non-radiative decay in two-body collisions with impurity molecules such as N_2 or O_2 [WAr10a, WAr10b]:



This process decreases the amount of excited argon molecules, while the impurity concentration stays constant. The slow component has a longer lifetime, hence it is more likely to collide with an impurity molecule before decaying under the emission of a scintillation photon. Thus, quenching affects the slow component much more which is expressed in a reduction of the triplet lifetime and the light yield [WAr10a, WAr10b, JCC⁺13].

Additionally, the emitted scintillation light can be absorbed during its propagation through LAr by impurities which decreases the light yield even more but does not change the singlet and triplet lifetime [WAr10a, WAr10b, JCC⁺13]. In the case of oxygen, the absorption can lead to atomic metastable states:



In liquids the excitation energy of these states is mostly converted to heat [WAr10b].

It has also been observed, that the absorption of LAr scintillation light results in the emission of characteristic energies of the corresponding impurity. In a spectral investigation, narrow peaks at 130 nm [NHO⁺12] and at 557 nm [HDH⁺10] are originated by oxygen. An emission peak in the range of 147–149 nm is visible by the direct transition ($^3P_2 \rightarrow ^1S_0$, see fig. 3.2) of excited xenon atoms to the ground state [HDH⁺10, NHO⁺12, NDH⁺15]. Furthermore, absorption features have been reported in literature, as for instance absorption bands below 180 nm from water [NHO⁺12] and around 126.5 nm from xenon [NHO⁺12, NDH⁺15], which coincides with the LAr scintillation peak. It was found that a concentration above 0.1 ppm of xenon makes LAr opaque to its own scintillation light [NDH⁺15].

With a wavelength resolved measurement of the transmission and the emission spectra of LAr it is possible to identify impurities due to characteristic absorption and emission bands or peaks. In contrast to that, it is not possible to disentangle any impurities with a wavelength integrated measurement [NHO⁺12].

A part of the scintillation light is produced by the recombination of ionized argon molecules with free electrons as shown in figure 3.1. Electro-negative molecules such as O₂ can attach these free electrons, thus reducing their availability for the recombination process in the scintillation mechanism and consequently decreasing the light yield [WAr10b]:



However, the production time of the excimer molecules is in the order of nanoseconds as summarized in table 3.1, while the electron attachment is a rather slow process with roughly a few milliseconds. Hence, this process is expected to be negligible for oxygen in LAr [WAr10b]. Due to the lower electro-negativity, electron attachment is not relevant for nitrogen [JCC⁺13].

Typically, LAr is gained commercially from air and can contain the following impurities: N₂, O₂, Xe, H₂O, CO, CO₂ [WAr10a, HDH⁺10, JCC⁺13, NHO⁺12]. While the extraction from air is a comparatively cheap source, it has the disadvantage that argon in air contains traces of the isotope ³⁹Ar (100% β⁻, Q_β = 565 keV, T_{1/2} = 269 yr [CEF99]). New generation of ultra low background experiments would be limited by such an intrinsic background, hence much purer argon is required. A new approach is to extract argon from underground CO₂ wells which consist of 96% CO₂, 2% N₂, 5700 ppm CH₄ and 600 ppm Ar [JAB⁺13]. Since this is a relatively new procedure, studies of the effects of CH₄ in LAr concerning the optical properties are still in the early stages of development.

3.2.1 Singlet and triplet lifetime

Due to the longer lifetime it is more probable for the triplet state to interact with impurities, which destroys the excited argon molecule without the emission of a scintillation photon. Thus it is affected stronger than the singlet state which results in a reduction of the time constant. In GAR the optical properties are dependent on the pressure, i.e. the triplet lifetime is smaller and the light yield is lower for higher pressure [WAr10a, WAr10b, ABB⁺08, JCC⁺13].

The effect of impurities on the time constants is investigated by doping pure LAr with known impurity concentrations and measuring the respective time constants. In some references an additional intermediate component (~ 40 ns) has been found, whose origin is so far unsolved [HTF⁺83]. It has been discussed in literature whether this is a physical effect or an instrumental artifact [WAr10a].

Figure 3.4 shows the effects on the time constants by N_2 and O_2 in LAr. The triplet lifetime decreases drastically in a similar level for higher impurity concentrations in both cases, although the investigated concentration ranges are quite differently for N_2 and O_2 .

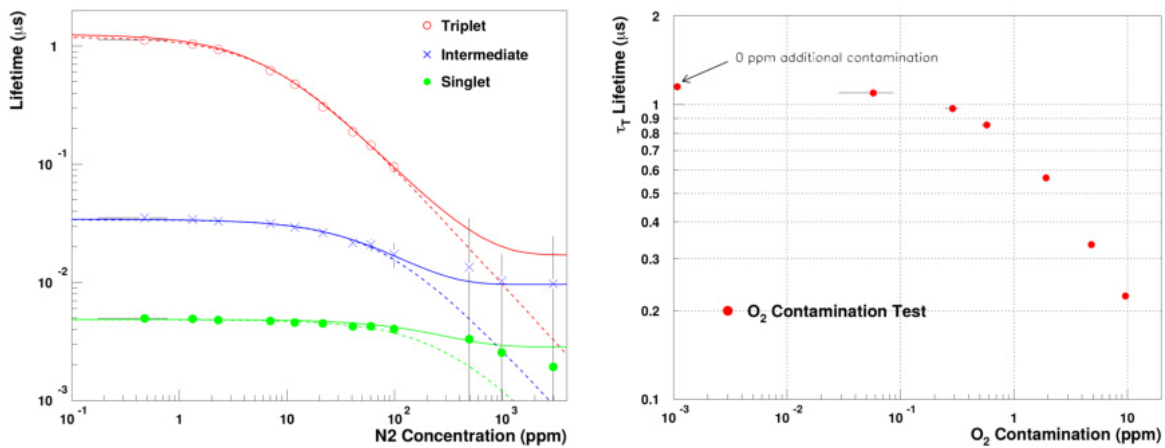


Figure 3.4: Investigation of the time constants of the LAr scintillation mechanism with various concentrations of N_2 (left) and O_2 (right). The triplet lifetime decreases rapidly with higher impurity concentrations in LAr while the singlet lifetime is mostly unaffected [WAr10a, WAr10b].

The quantitative description of the decreasing behavior of the triplet lifetime is quoted by the rate constant k_Q of the quenching process and is listed for two different impurities in table 3.4. According to these measurements, oxygen is already in tiny concentrations much more dangerous for the triplet lifetime than nitrogen.

Table 3.4: The rate constant k_Q of the light quenching process of the triplet state derived from doping LAr with various impurities. Different concentration ranges are investigated.

k_Q [$\mu s^{-1} ppm^{-1}$]	impurity	concentration [ppm]	reference
0.11 ± 0.01	N_2	$10^{-1} - 10^3$	[WAr10a]
0.54 ± 0.03	O_2	$10^{-3} - 10$	[WAr10b]

3.2.2 Scintillation light yield

Quenching of the excited argon molecules as well as absorption of the emitted scintillation photons by impurities in LAr both contribute to the reduction of the scintillation light yield.

Additionally, an intrinsic mechanism, the bi-excitonic quenching exists that is able to change the light yield even in the absence of impurities [HDH⁺13]:



This effect only decreases the light yield by reducing the amount of excited argon atoms, but does not affect the lifetime of the excited molecules.

The quantitative expression of the light yield reduction is quoted by the surviving fraction S_F , which is the ratio of the intensity of the scintillation light emitted for a known impurity concentration versus pure LAr. For the distinction of the processes reducing the light yield, a light quenching factor Q_F is defined, which gives the fraction of the surviving excimer molecules that emit a scintillation photon rather than decaying non-radiatively due to collisions with impurities. The difference between Q_F and S_F indicates that, besides quenching, also other mechanisms decrease the light yield, e.g. absorption of the scintillation photons [WAr10a, WAr10b].

Figure 3.5 shows measurements of the light yield reduction for N₂ and O₂ at various impurity concentrations. In the case of O₂ the surviving fraction is plotted as well, which shows that the absorption process is also relevant for O₂ in LAr.

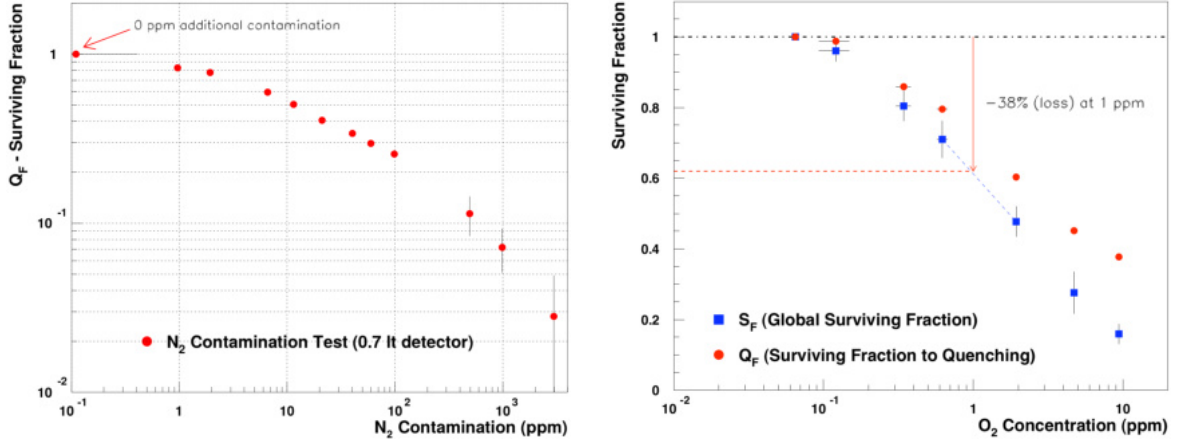


Figure 3.5: Dependence of the quenching factor Q_F and surviving fraction S_F of the scintillation light in LAr for N₂ (left) and O₂ (right). While quenching is the dominant process for N₂, the light reduction is also induced by absorption from O₂ in LAr, which is indicated by the difference between Q_F and S_F [WAr10a, WAr10b].

3.2.3 Absorption and attenuation length

Since detectors using LAr for its scintillation properties get larger and larger, the scintillation light has to travel longer paths. It is therefore essential to investigate the transmission and the attenuation of the scintillation light in LAr [NHO⁺12]. The attenuation coefficient μ_{att} denotes the total loss of the light intensity and is the sum of the absorption and scattering coefficients, which only describe the light loss due to the corresponding process:

$$\mu_{\text{att}} = \mu_{\text{abs}} + \mu_{\text{scat}} \quad (3.6)$$

The attenuation length α_{att} is the inverse of the attenuation coefficient μ_{att} and the light intensity I follows a Beer-Lambert-Law, where I_0 denotes the initial intensity and d the traveled path of the light:

$$I(d) = I_0 \cdot e^{-d/\alpha_{\text{att}}} \quad \text{with} \quad \frac{1}{\alpha_{\text{att}}} = \frac{1}{\alpha_{\text{abs}}} + \frac{1}{\alpha_{\text{scat}}} \quad (3.7)$$

It has been found, that even in chemically cleaned and distilled LAr the transmission below 130 nm decreases due to the absorption by the first excimer continuum [NHO⁺12]. Consequently, the attenuation length is significantly smaller for lower wavelengths as shown in figure 3.6. This results simultaneously in a redshift of the scintillation spectrum and a reduction of the observed light for longer path lengths.

Since the attenuation length changes strongly over the wavelength range of the scintillation emission spectrum of LAr shown in figure 3.3, an universal attenuation length cannot be derived for LAr. Instead a wavelength dependent measurement of the attenuation length would be much more appropriate [NHO⁺12]. Nonetheless, wavelength resolved measurements are performed rarely due to their complicated realization in cryogenic liquids in the VUV light region. Wavelength integrated measurements are only capable of measuring a combination of transmission and emission and it has also been found that the Lambert-Beer-Law does not fit well anymore when deriving the attenuation length in a wavelength integrated measurement [NHO⁺12].

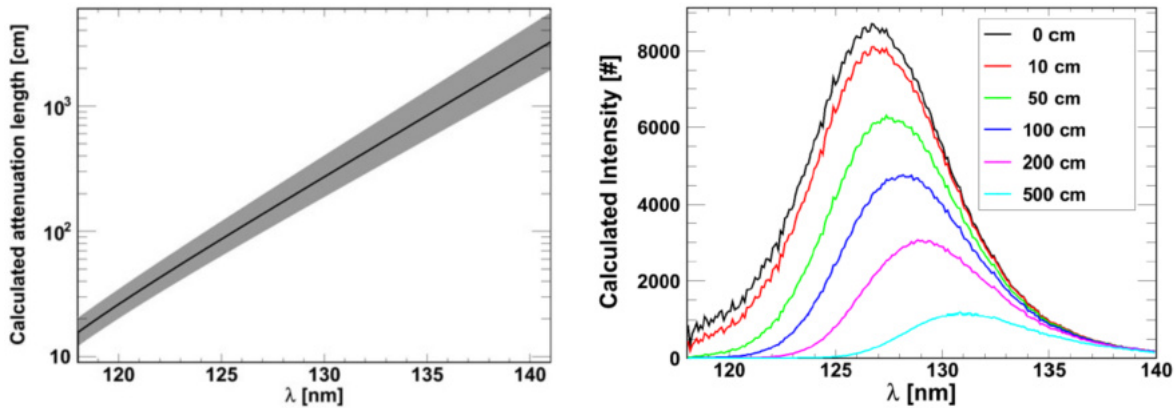


Figure 3.6: (Left) Wavelength-dependent attenuation length derived from the calculation from a transmission measurement in very pure LAr. (Right) A redshift of the scintillation peak is observed due to the shortening of the attenuation length for smaller wavelengths [NHO⁺12].

The attenuation length drops even more in the presence of impurities, however, various impurities absorb light in different ways, which makes a measurement of the attenuation length hardly comparable for different impurity compositions. A summary of attenuation lengths measured for very pure argon and known impurity compositions is listed in table 3.5. It is obvious that some measurements are not consistent with others, which applies especially to the values reported in [JCC⁺13]. An interplay of different impurities and the consequences for the attenuation length in LAr has not been investigated on a broader extent yet.

The attenuation lengths reported in [NHO⁺12, NDH⁺15] have been derived from wavelength resolved measurements, while the other values listed in table 3.5 are determined in wavelength integrated measurements.

The absorption has been measured for known impurity compositions by doping very pure LAr. A list of these measurements is compiled in table 3.6. The values for the absorption by N₂ are in the same order of magnitude, while the absorption by O₂ and CH₄ is much smaller. In contrast to that, N₂ is only relevant for larger concentrations in the ppm level or in very large volumes, whereas O₂ and CH₄ are already dangerous in small concentrations. In all these measurements the absorption coefficient is averaged over the width of the LAr scintillation peak [WAr10a, WAr10b].

Table 3.5: Compilation of attenuation length measurements performed in very pure LAr and for known impurity compositions. The authors in [ICD⁺97] conclude that their measurement is an effect of attenuation, but other references interpret this result as a scattering length [SLY02].

α_{att}	impurity	concentration	Reference
50 cm	H ₂ O	500 ppb	[CCC ⁺ 18]
	O ₂ , H ₂ , CO, CO ₂	100 ppb	
	N ₂	300 ppb	
163 cm	O ₂ , Xe	–	[NHO ⁺ 12]
>110 cm	Xe	0.1 ppm	[NDH ⁺ 15]
66 ± 3 cm	–	–	[ICD ⁺ 97]
170 ± 23 cm	Xe	3%	
118 ± 10 cm	Xe	3%	
1790 ± 160 m	N ₂	37 ppb	[JCC ⁺ 13]
30 ± 3 m	N ₂	2 ppm	

Table 3.6: Measurements of the absorption coefficient k_A for various impurities in LAr investigated in different concentration ranges

k_A [cm ⁻¹ ppm ⁻¹]	impurity	concentration [ppm]	reference
$(1.51 \pm 0.15) \cdot 10^{-4}$	N ₂	0 – 50	[JCC ⁺ 13]
$< 1 \cdot 10^{-4}$	N ₂	0.1 – 10 ³	[WAr10a]
0.034 ± 0.016	O ₂	10 ⁻³ – 10	[WAr10b]
0.3	CH ₄	0.01 – 1	[JAB ⁺ 13]

3.2.4 Rayleigh scattering

Rayleigh scattering describes the process of elastically scattered photons by particles which are much smaller than the wavelength of the photons. Since photons are scattered at atoms or molecules, impurities in LAr do not affect the cross section of the Rayleigh scattering due to their similar size. Nevertheless, Rayleigh scattering is inversely proportional to the fourth power of the photon wavelength and therefore changes strongly over the width of the LAr scintillation peak. This can be an additional reason for the redshift for photons traveling long distances in LAr as reported in figure 3.6 [GBMN17, SLY02].

LAr detectors are becoming much larger in the future and the LAr can be purified to high degrees nowadays, hence Rayleigh scattering gets more and more important. The scattering length is dependent on optical properties of the material, such as the refractive index and the dielectric constant [GBMN17, SLY02].

A calculation of the Rayleigh scattering length is performed in [SLY02] in the UV (ultra-violet) region for the scintillation wavelengths of noble gas liquids. The dielectric constants are measured in [BGAJ81] in the UV region in the gas phase and extrapolated to the VUV region. It is assumed that the dielectric constants of the noble gas liquids can be derived from the ones determined in gas [SLY02].

The scattering is calculated to be 90 cm with an uncertainty of 35% for argon [SLY02]. The calculation is compared to a measurement of the attenuation length, which resulted in 66 ± 3 cm [ICD⁺97]. The authors in [SLY02] interpret the agreement as a suggestion, that the measured attenuation length is due to Rayleigh scattering and not a result of absorption by impurities in LAr.

Another calculation is described in [GBMN17]. They include the temperature dependence of the scattering length, which is not the case in [SLY02]. Since the density varies with the temperature which also affects the refractive index, the scattering length is dependent on the temperature as well. Two measurements of the scattering length at 90 K result in 60 ± 6 cm and 55 ± 5 cm, which is consistent within the uncertainties of the values quoted above.

It was also investigated how xenon impurities in LAr affect the scattering. For a mixture of Ar doped with 3% Xe, the scattering was calculated to be 280 cm [SLY02]. Measurements of the same mixture result in 170 ± 23 cm and 118 ± 10 cm [ICD⁺97]. The disagreement of these measurements remains unclear. Since xenon shifts the scintillation to longer wavelengths as discussed in section 3.2, the scattering length increases for small amounts of xenon in LAr [SLY02].

Chapter 4

Reflectivity measurement of steel in the visible and VUV region

For the analysis of the attenuation measurement, which is described in chapter 7, it is necessary to perform a detailed simulation of the propagation of the photons within the measuring setup. The correct modeling of such a simulation requires a good knowledge of the reflection properties of the setup, which consists of stainless steel. Therefore the reflectivity of the used steel has been measured in the visible region down to the UV and VUV region. The reflectivity measurement devices are in the following distinguished by their locations: University of Münster, IPF (Leibniz Institute of Polymer Research) in Dresden and PTB (Physikalisch-Technische Bundesanstalt) in Berlin. Spare steel rings used for the collimation of the light in the attenuation setup (see ch. 6) have been sent to the IPF and the PTB for reflectivity measurements in the visible and the VUV range, respectively.

4.1 Specular and diffuse reflection

In general, reflection properties of materials can be divided into specular and diffuse, whereby the sum of both is the total reflectivity. A perfect specular reflector is a mirror, where the emergent angle of the light equals the incident angle as indicated in figure 4.1. On the contrary, a perfectly diffuse reflecting surface appears matte to the observer. The so called Lambertian reflection of such a surface follows Lambert's cosine law, i.e. the brightness is uniform in all directions. Frequently, optical surfaces feature a combination of specular and diffuse reflection.

Diffuse reflection can be caused by a rough surface, where the light is reflected at microfacets with many varying surface normals. Alternatively, in many materials reflection happens beneath the surface at the interfaces of the microscopic substructure. As a result, surfaces can be perfectly smooth, yet reflecting diffusely.

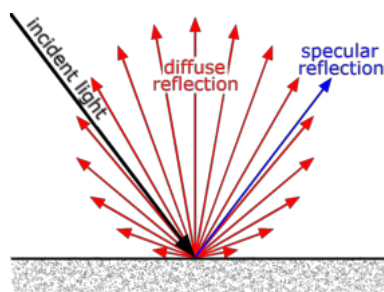


Figure 4.1: Schematical depiction of the specular and diffuse reflection at a surface. For the specular reflection the emergent and the incident angle are equal, while the diffuse reflection scatters the light at many angles [Gia10].

4.2 Reflection properties of various materials

In recent years, steel is investigated as a potential specular reflectance standard due to its suitable high reflectivity in the visible region. In figure 4.2 a measurement of the specular reflectance is depicted. The samples were mechanically polished with 0.3 μm alumina and water. After an aging of 10 months a small decrease of the reflectivity can be observed, which is stronger in the UV region. In comparison the specular reflectance measurement of aluminum is shown, which was polished with a diamond paste. Equally to steel, aluminum features a slightly lower reflectivity in the visible region after aging for 16 months. This can be a result of building up aluminum oxide on the surface over time. The oxide has a lower reflectivity, thus it decreases the reflectivity when the aluminum ages. Additionally, aluminum features a lower reflectivity between 800 and 900 nm which is due to an absorption band of aluminum in this region [ZND94]. Other metals like gold and silver have similar absorption bands, though these are much stronger, hence the reflectivity decreases to much lower values as shown in figure 4.3 for freshly prepared samples. In the case of silver, the reflectivity even drops to almost 0% between 300 and 400 nm [Mel05].

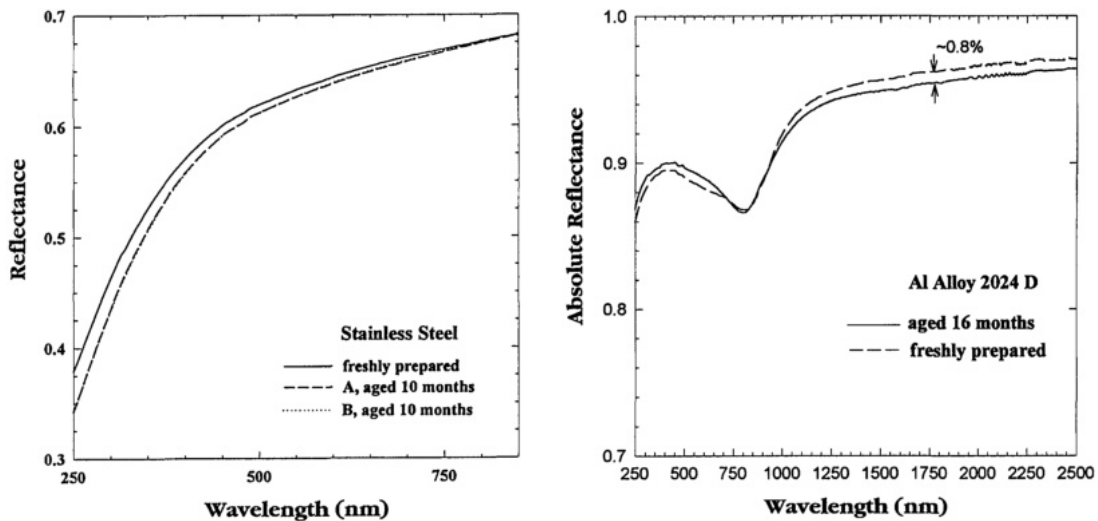


Figure 4.2: Measurements of the specular reflectance of stainless steel (left) and aluminum (right). Both were mechanically polished and examined right away as well as after several months of aging [ZND94].

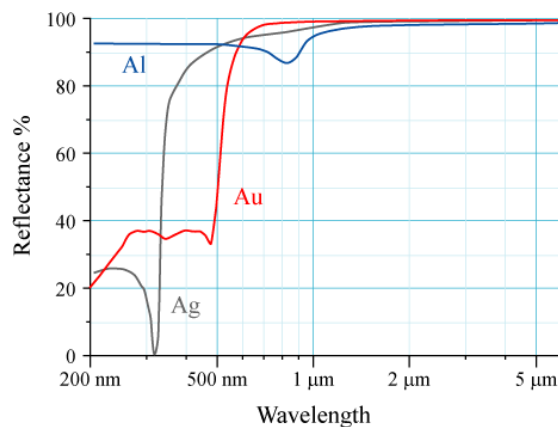


Figure 4.3: Reflectance of aluminum, gold and silver, which are typically used as mirror coatings. All three of them feature absorption bands resulting in regions with lower reflectivity [Mel05].

The steel used for the construction of the attenuation measuring setup was electropolished in order to clean all parts before submerging the setup in LAr (see ch. 6.1.2). It has been found, that the time as well as the current density of the electropolishing process affect the specular reflectivity of stainless steel [JSV⁺00]. The spare steel samples that were used for the reflectivity measurements are thin rings as described in chapter 6.1.2. Electropolishing removes a few micrometers of the surface. Consequently they would not fit precisely into the attenuation setup anymore if the electropolishing lasts too long. Hence, the thin steel rings are electropolished for a shorter time than other parts of the setup.

For a complete reflectance measurement it is necessary to investigate the reflectivity for various angles of incidence as well as *s*- and *p*-polarized light¹. Such measurements are usually performed relatively to a reference, thus the used reflectance standard must have been measured at all desired incident angles and both polarizations [ZND94].

PTFE (polytetrafluorethylen), also known as Teflon, is commonly used as a reflectance standard due to its high reflectivity over a wide wavelength range. For visible light, it is an almost perfect diffuser, since the specular reflection accounts for only about 3.4% of the total reflected light. However, the contribution of the specular reflection increases for lower wavelengths, thus PTFE loses its quality as a diffuser in the UV region and shows a clear specular peak [SPP⁺10].

Additionally, it has been found, that the specular reflection intensity is dependent on the incident angle and increases for larger angles [SPP⁺10]. Furthermore, PTFE has a porous surface, i.e. detergents like xenon can fill these holes and dissolve impurities on the surface. This affects the reflection properties of PTFE and can produce different outcomes depending on the gas or liquid that surrounds the PTFE surface [Lev14].

4.3 Reflectivity measuring device in Münster

The reflectivity measuring device in the nuclear physics department of the University of Münster has been developed for the measurement of the reflection of PTFE in LXe (liquid xenon) for the XENON100 experiment searching for dark matter [Lev14]. The XENON100 TPC consists of PTFE due to its high reflectivity in the UV region, which maximizes the light collection in the experiment. A schematic drawing of the reflectivity measuring device in Münster is depicted in figure 4.4.

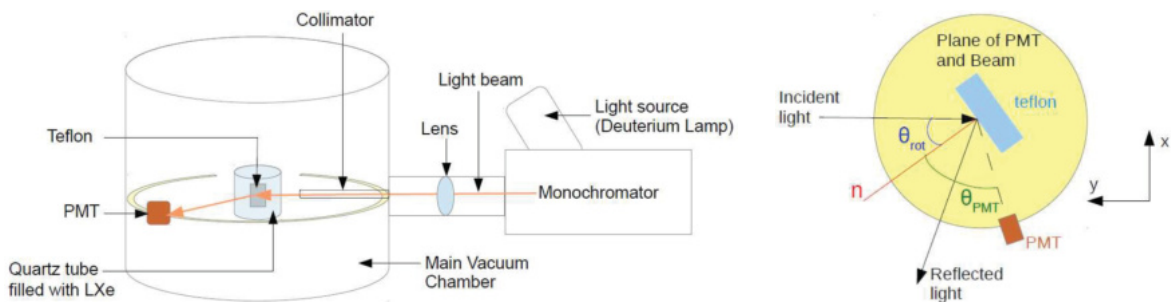


Figure 4.4: Reflectivity measuring device in Münster. (Left) The light of the deuterium lamp is selected by a monochromator. It is then focussed as well as collimated and hits the PTFE (Teflon) sample at a predefined angle. The sample is submerged in a LXe filled quartz tube. A PMT collects the light at various viewing angles. (Right) The incident angle of the light and the viewing angle of the PMT can be adjusted independently of each other [Lev14].

¹With respect to the plane in which the light propagates before and after the reflection, if the electric field is solely parallel to this plane, the light is *p*-polarized, while an electric field completely perpendicular to the plane is *s*-polarized.

The emitted light of a deuterium lamp is selected at 178 nm by a monochromator and focussed before entering the vacuum chamber. To suppress any attenuation by air, the vacuum chamber is operated at $2.5 \cdot 10^{-5}$ mbar. Inside the vacuum chamber the light is further collimated. The PTFE sample is fixed in a quartz tube filled with LXe. The quartz tube with the PTFE sample can be moved and rotated in order to investigate different spots of the sample and measure the reflectivity at various incident angles. The reflected light is detected by a PMT, which can be moved to different viewing angles. Hence, the specular and the diffuse reflected light can be measured by this device.

It is in principle unproblematic to exchange the LXe by LAr to serve the needs of a reflectivity measurement of steel in LAr. The challenge of this exchange is to ensure that no xenon traces are left in the apparatus, which would falsify the measurement.

The PMT could be exchanged by a model which is sensitive to VUV light or coated with a WLS to convert the 128 nm light to its sensitive region. The disadvantage of a WLS is that the shifted light is emitted isotropically, hence also away from the PMT into the vacuum chamber, where it can be reflected at the inner walls of the chamber. This would certainly falsify the measurement.

The emission spectrum of the deuterium lamp used in this device is shown in figure 4.5. In the region of the xenon scintillation peak at 178 nm the deuterium lamp has a mostly constant emission intensity, thus it is well suited for reflectivity measurements in this region. At the LAr emission peak around 128 nm the intensity of the deuterium lamp is much higher, but also unsteady. A proper reference measurement would be necessary to achieve trustable results.

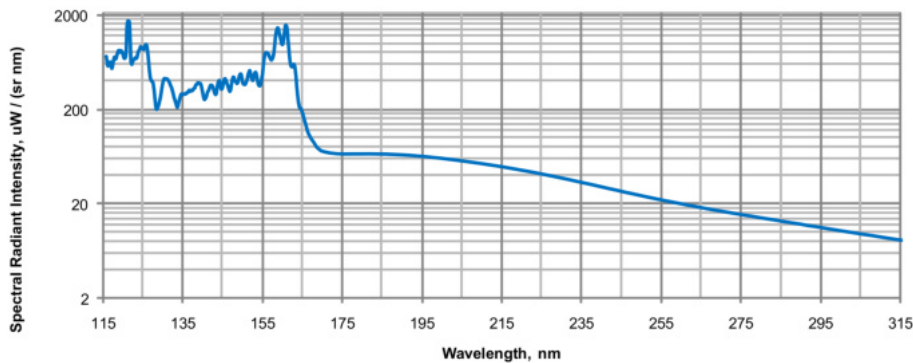


Figure 4.5: Emission spectrum of the deuterium lamp McPherson Model 632 [McP17].

One component that would be necessary to exchange for a reflectivity measurement at 128 nm is the quartz glass tube which is housing the sample with the desired liquid, i.e. LAr or LXe. The quartz glass is made of fused silica and is opaque for light below 160 nm as shown in figure 4.6. Therefore, a measurement at 128 nm would be impossible. A substitute of the quartz glass tube needs to have a high transmission in the VUV region. Additionally, it needs to withstand several orders of pressure gradient due to the operation in vacuum. Unfortunately, no material which meets these requirements could be found.

Therefore, a reflectivity measurement of steel in LAr is not feasible with this device. However, the measurement could be performed with steel samples in vacuum, leaving off the LAr and the quartz glass tube. Unlike PTFE, steel is not porous, hence it is not expected that LAr fills microscopic holes which changes the reflectivity. In this case, a PMT needs to be found that is sensitive in the VUV region in order to circumvent the problems arising with the usage of a WLS. Technically such PMTs are commercially available, though expensive.

Unfortunately, the costs of a suitable PMT as well as a two-week shift for two people, which are required for the operation of this device, could not be raised at that time, hence the reflectivity measurement of steel was not realized in Münster.

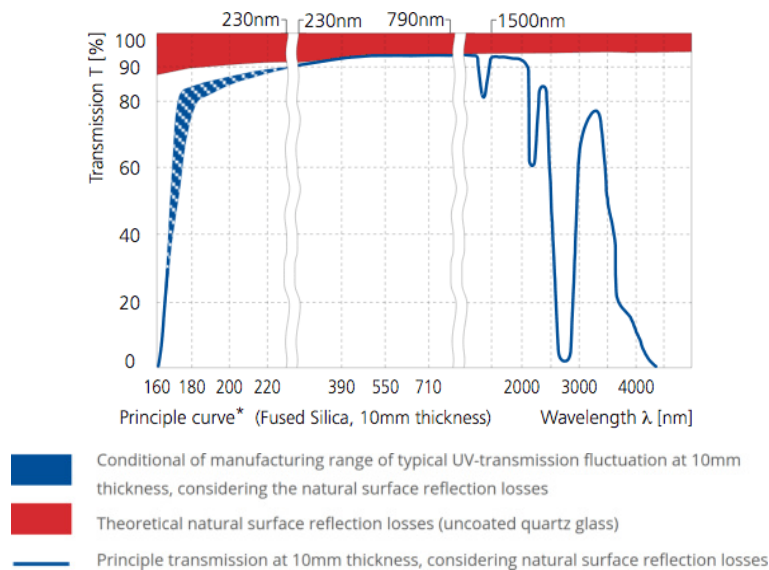


Figure 4.6: Transmission spectrum of fused silica [PGO19].

4.4 Measurement of the steel reflectivity in the visible region

The IPF in Dresden operates a spectrophotometer for regular reflectivity measurements in the visible and NIR (near infrared) region. This device is also able to perform measurements down to 200 nm. The IPF provided the device at no charge for reflectivity measurements of steel samples of the attenuation setup.

4.4.1 Spectrophotometer

The used spectrophotometer is the model Cary 5000 of the company Agilent [Agi19]. A schematic drawing of the device is depicted in figure 4.7. The Cary 5000 is equipped with a deuterium lamp for the UV region and a mercury lamp for the visible and the NIR region. A precise wavelength is selected with a monochromator.

PTFE is used as a reference for the relative reflectivity measurement. The reflectivity of PTFE is shown in figure 4.8. The inner wall of the integrating sphere (see fig. 4.7) consists nearly completely of PTFE with the exceptions of the small entrances of the light beams, the PMT at the bottom of the sphere and the mounted sample that is investigated. In this way the light collection efficiency is maximized independent of the reflected angle of the sample.

A light trap is available at the position where the emergent angle equals the incident angle on the sample. This light trap can be closed with a PTFE wall, i.e. all reflected light is detected by the PMT. In the case the light trap is opened, the specular reflected light is trapped inside it, thus only the diffuse reflected light is collected by the integrating sphere.

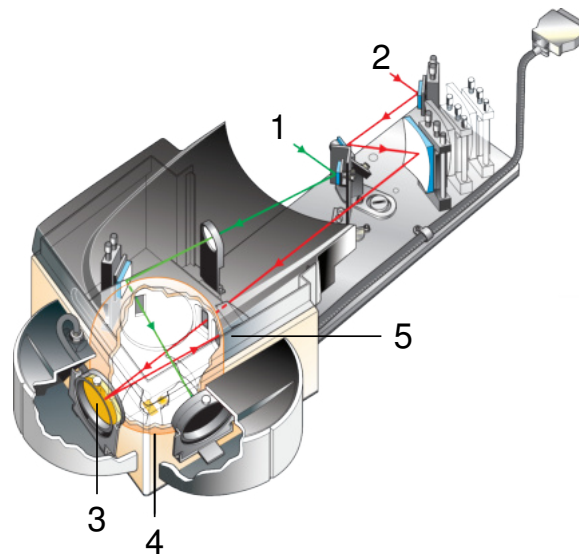


Figure 4.7: Sketch of the spectrophotometer Cary 5000 of Agilent. (1) reference beam, (2) sample beam, (3) sample, (4) integrating sphere, (5) light trap. A PMT is mounted in the bottom of the integrating sphere [Agi19].

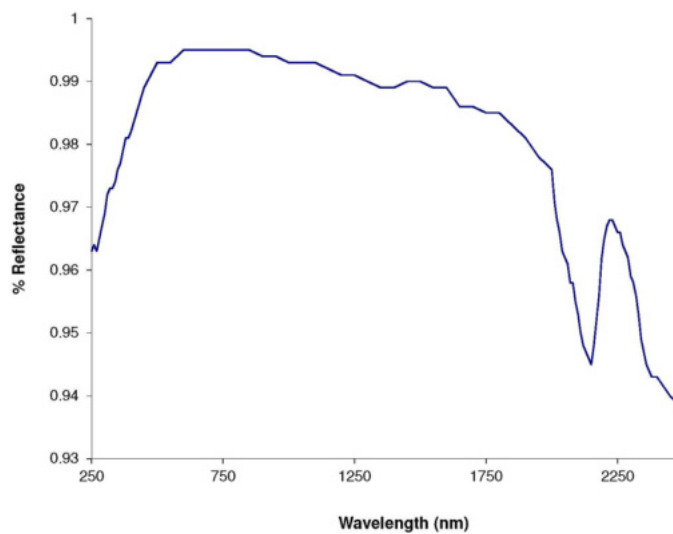


Figure 4.8: Reflectance of PTFE which is commonly used as a diffuse reflectance standard in the visible and NIR region [Spe19].

4.4.2 Data taking

The reflectivity measurements in the visible region have been performed relative to the reflectance standard PTFE. Therefore the reference beam hits the PTFE in the integrating sphere (fig. 4.7). These measurements are indicated as background in the following. The background measurements have been run without and with the light trap opened as shown in figure 4.9 on the left. The reflectivity is slightly higher with the light trap opened which is strange since some of the light should be lost in the light trap, hence it is expected that the reflectivity must be slightly lower. Nonetheless, the variance is within the measuring uncertainty and is not expected to greatly influence the resulting reflectivity.

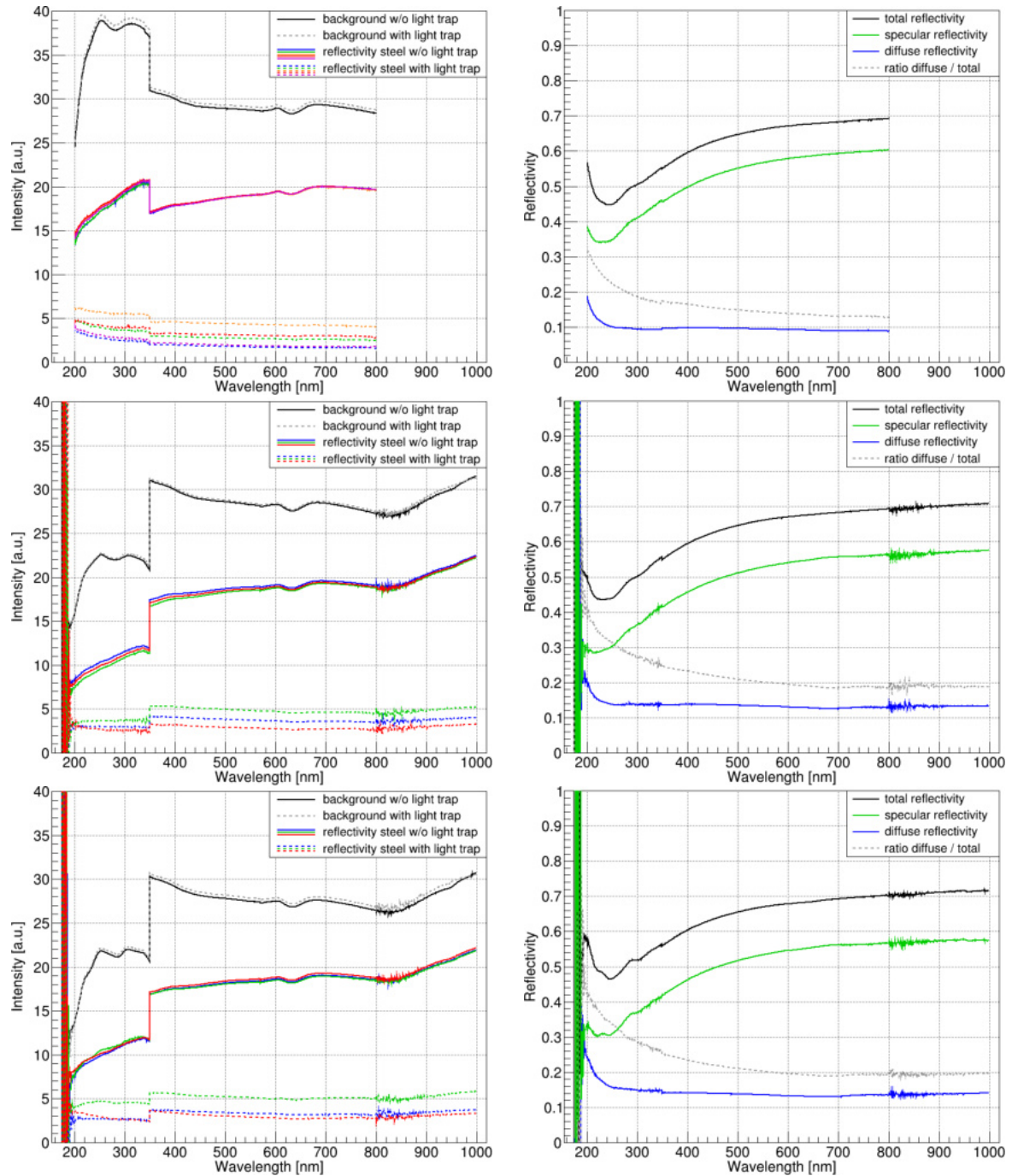


Figure 4.9: Reflectivity measurements in the visible region. (Left) The absolute reflectivity is measured without and with the light trap opened. The background corresponds to the measurement with the reference beam on PTFE. The reflectivity of various spots on the sample has been measured which is indicated by the different colors. (Right) The average reflectivities determined of the raw measurements on the left side. (Top, Middle) Measurements are done without nitrogen flushing. (Bottom) The integrating sphere is flushed with nitrogen.

The raw measurements depicted on the left in figure 4.9 also feature a kink at 350 nm which is due to the change of the light source from the visible to the UV region. This kink changes from the measurement at the top to the two below because the device has been repaired between these measurements due to a blown connector. The replacement of the broken parts caused the intensity of the deuterium lamp to be lower.

All measurements have been performed with a spectral band width of 5 nm. The first measurement shown on the top was done between 200 and 800 nm, while the other two were performed from 175 to 1000 nm. It can be seen, that below 200 nm a lot of absorption lines are visible and a proper measurement is not possible anymore. This can be a consequence of oxygen absorption in the setup as discussed in section 4.4.3. To circumvent this problem, the integrating sphere has been flushed with nitrogen and the measurement has been repeated as shown on the bottom in figure 4.9. However, the nitrogen flushing did not improve the measurement, hence the reflectivity measurements of the IPF can only be used down to 200 nm.

The steel sample has been moved to measure different spots in order to investigate the influence of surface scratches on the reflectivity. While the reflectivity without the light trap is mostly unaffected, the reflectivity changes significantly when the light trap is opened. This means that the total reflectivity is mainly independent of the chosen spot while the diffuse and the specular reflectivity change vastly as shown in figure 4.10.

The total reflectivity is determined as the ratio of the sample versus the background measurement without the light trap. The diffuse reflectivity is the sample to background ratio with the light trap opened. The specular reflectivity can be calculated as the difference between total and diffuse reflectivity. The ratio of the diffuse versus the total component is needed for the implementation into the simulation as described in chapter 5.3.

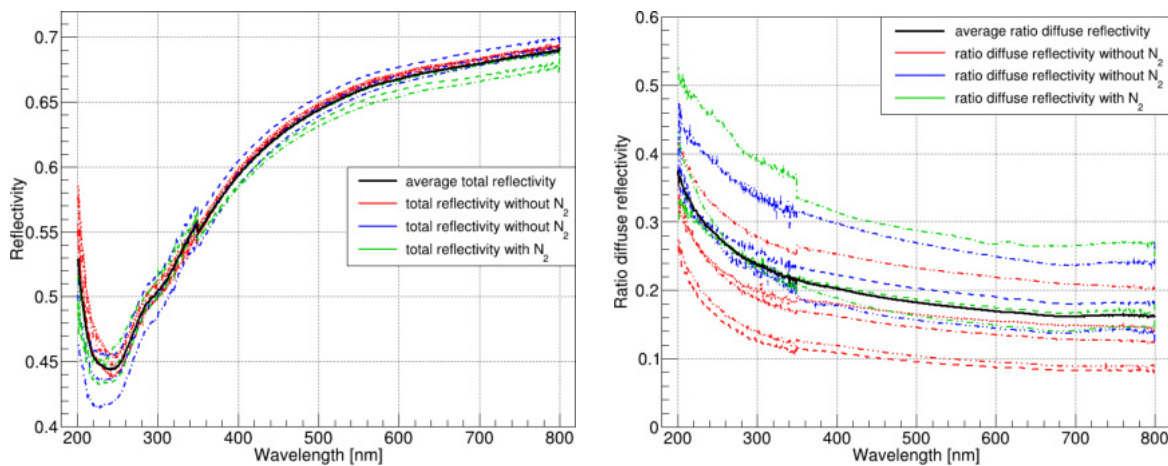


Figure 4.10: Reflectivity dependence on the chosen spot of the steel sample. The total reflectivity (left) changes only slightly, while the ratio of the diffuse versus total reflectivity (right) varies greatly. Both seem to be unaffected by the nitrogen flushing.

An average of all measured spots has been calculated as depicted in figure 4.11. The uncertainty is calculated as the standard deviation of the different measurements. All measurements have been taken into account, i.e. with and without nitrogen flushing and each investigated spot on the steel sample.

4.4.3 Interpretation of the measurement

According to [Agi16] the device should be flushed with nitrogen to suppress absorption bands of oxygen below 200 nm. The absorption cross section of oxygen in the UV and VUV region is depicted in figure 4.12. The Schumann-Runge-bands between 175 and 195 nm [SP06] can be very well the reason for the absorption lines visible in figure 4.9. However, the nitrogen flushing did not remove these lines. Since it is only possible to flush the integrating sphere (see fig. 4.7) with nitrogen, but not the whole device, the light beams still have to travel through air.

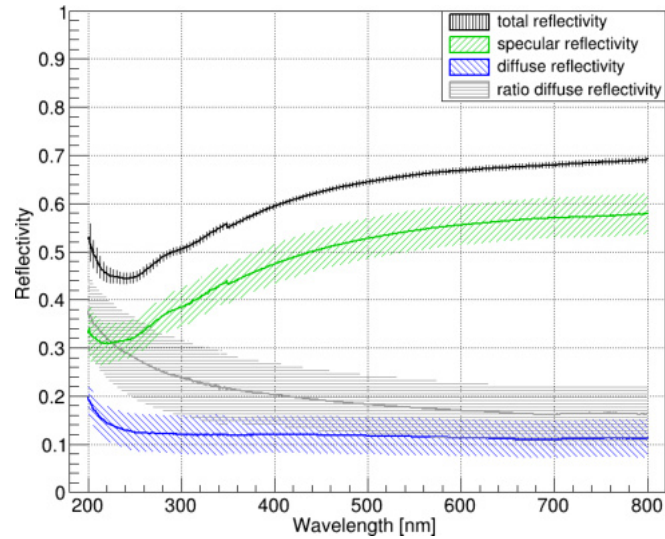


Figure 4.11: Average steel reflectivity of the measurement performed in the IPF. The uncertainty bands are calculated from the standard deviation of the various investigated spots.

A possible solution of this problem could be to operate the entire spectrophotometer in a closed chamber which is flushed with nitrogen. In this way, the measurements below 200 nm could have been used as well.

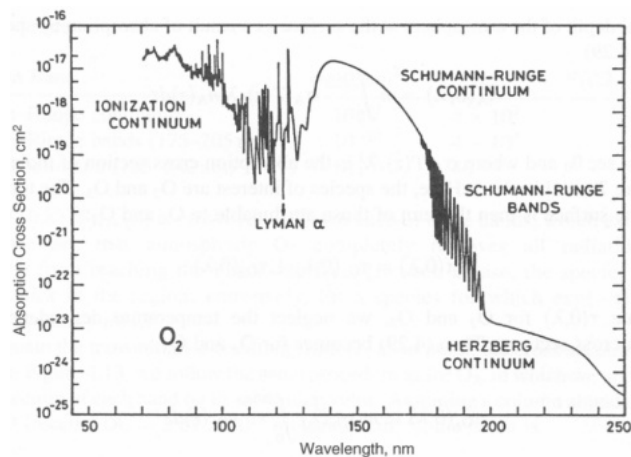


Figure 4.12: Absorption cross section of oxygen in the UV and VUV region. The absorption increases slightly below 250 nm and even stronger with a lot of absorption lines below 200 nm [SP06].

As depicted in figure 4.7 the light trap is located at the position where the emergent angle equals the incident angle of the sample. This corresponds only to the sample beam and not to the reference beam, since PTFE is assumed to be a perfect diffuser. Hence, the background measurements at lower wavelength with the opened light trap may be falsified since the specular reflectance of PTFE increases in this region. This could also be a reason why the background measurements in figure 4.9 feature a higher reflectivity with the opened light trap. An additional light trap at the specular reflected angle of the reference beam, which can be opened independently of the light trap for the sample beam, could provide a remedy.

The measured reflectivity of the steel samples has a minimum around 250 nm as shown in figure 4.11. While this can be a result of absorption bands of iron, nickel or chromium in this region, it has been discussed that the measurement presents several flaws for the lower wavelength. Hence, the UV reflectivity needs to be investigated with a different approach, which is described in the following section.

4.5 Measurement of the steel reflectivity in the VUV region

The PTB in Berlin offers services to measure the reflectance of optical materials between 40 nm and 400 nm. To minimize the costs of such a measurement, several parameters need to be constrained. Different optical configurations are used for the various spectral regions which have to be calibrated separately. Thus, the wavelength range was limited to 120 – 400 nm. Moreover, the reflectivity is measured for only one selected incident angle at 45° to keep the measuring time low. In contrary to the IPF measurement, the reflectivity of just a single spot on the steel sample has been measured in the entire wavelength range. These constraints reduced the measuring costs to an affordable amount provided by the granted application.

4.5.1 Reflectometer

The principle of the reflectometer used by the PTB is very similar to the device in Münster (fig. 4.4). The sample can be turned and the detector can be rotated to adjust the incident and emergent angle as desired. A picture of the reflectometer is shown in figure 4.13.

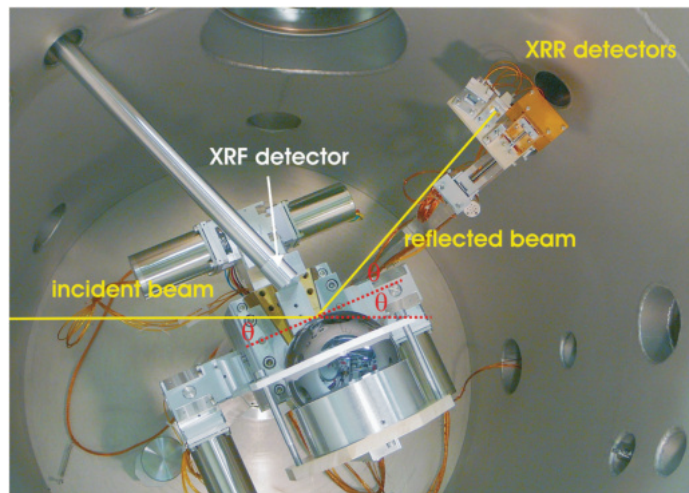


Figure 4.13: Reflectometer of the PTB. The sample, which is a silicon sphere in the picture, and the x-ray reflectometry (XRR) detector can be rotated to adjust the incident and the emergent angle. The x-ray fluorescence (XRF) detector can be used to analyze fluorescence of the sample surface [KCF⁺14].

The PTB uses monochromatic synchrotron radiation, which is highly polarized and has a spectral band width of 1.6 nm. For the determination of the reflectivity for unpolarized radiation two measurements with reflection planes turned by 90° have been performed, of which the average reflectivity has been calculated. The reflected light is measured by the GaAsP-Schottky-photodiode Hamamatsu G2119. The intensity of the incident beam is determined by removing the sample and rotating the detector into the direct beam light. Temporal changes of the light intensity are monitored and are normalized separately in each spectral range. All the following measurements have been performed in high vacuum at a pressure of 10^{-5} Pa and at room temperature.

4.5.2 Homogeneity of the reflectance

For the investigation of the homogeneity of the reflectance of the steel sample a spot appearing visual homogeneous has been chosen in the middle of a steel ring segment. This position has been verified by horizontal and vertical scans at three selected wavelengths. These measurements are depicted in figure 4.14 and are performed for *s*- and *p*-polarized light, respectively.

Since the reflection planes are turned by 90° for the two polarizations, the allocation of horizontal and vertical to radial and tangential is switched. The steel sample has a width of 10 mm, hence limiting the radial and tangential scans accordingly. The spot in the middle is taken as a reference and the relative intensity of the reflectance is plotted. While the reflectance decreases only slightly in some points, it increases significantly near the edges of the steel ring. This effect has no consistent explanation and is even stronger for lower wavelengths, where the reflectivity itself is lower.

Figure 4.14 also shows, that the reflectivity is almost equal for the different light polarizations. Hence, the reflectivity is independent of the polarization plane and can be determined as the average of *s*- and *p*-polarized light.

The selected spot in the middle has been used in all following measurements. The systematic uncertainty of the reflectance is determined conservatively with the maximum and minimum variation measured in the homogeneity measurements (fig. 4.14) and added to the statistical uncertainty. The uncertainty is extrapolated below 160 nm and above 350 nm as well as interpolated between the investigated wavelengths from these measurements.

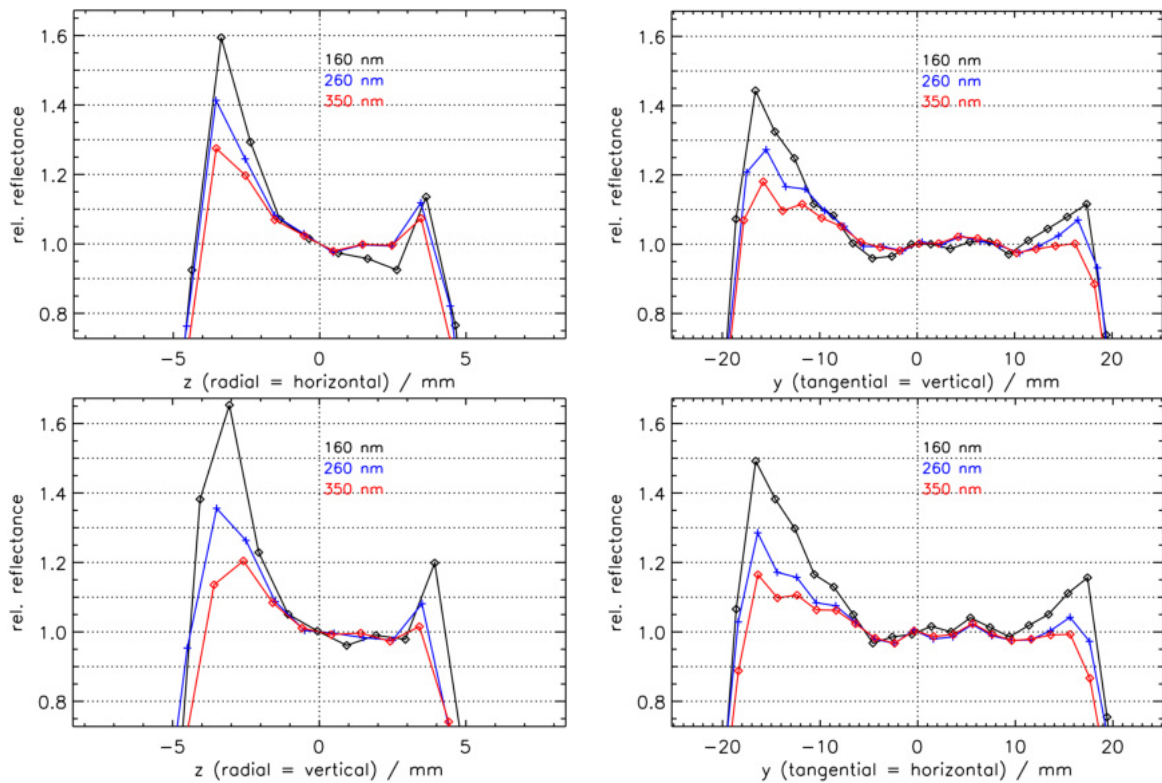


Figure 4.14: Measurements of the homogeneity of the reflectance of the steel sample. A homogeneous spot in the middle is verified by radial (left) and tangential (right) scans with *s*- (top) and *p*- (bottom) polarized light.

4.5.3 Angular measurements of the reflectivity

For the measurement of the specular and the diffuse component of the reflectivity of the steel sample, a fixed incident angle at 45° has been chosen. The detector has been rotated from 70° to 110° to scan the entire specular reflex and capture some of the diffuse reflected light.

The angular measurements are performed for selected wavelengths and are depicted in figure 4.15 on the left side. The specular peak increases with the wavelength, while the diffuse component is very low in all angular scans.

The detector has a distance of (200 ± 2) mm to the sample and an active area of (97.2 ± 0.2) mm². Thus, the covered solid angle of the detector is $(2.43 \pm 0.03) \cdot 10^{-3}$ sr, which is equivalent to an angular resolution of 2.81° . This is smaller than the width of the specular reflected peak. Consequently, the peak is smeared by the detector and has to be unfolded with the angular resolution of the detector to achieve the correct specular reflectivity.

The procedure of this unfolding is shown in figure 4.15 on the right. The angular scans were performed in steps of 0.5° and have been fit with a gaussian approximation. Since the contribution of the tail is negligible, it has not been taken into account. The fit is unfolded with the angular resolution of the detector. A homogeneous active area of the detector has been assumed in this case. The uncertainty of the angular resolution is propagated on the systematic uncertainty of the unfolding. It can be seen in figure 4.15 that the unfolded specular peak is sharper than the measurement of the detector. As a cross-check the unfolded peak has been smeared with the angular resolution which is consistent with the measurement.

The total reflectivity is determined by the numerical integration of the three-dimensionally modeled angular reflectivity, which is obtained from the rotation of the measured two-dimensional curve. The assumption of a spatial isotropic reflectivity has been verified with test measurements by the PTB.

The difference of the total and the specular reflectivity yields the diffuse component, whereas the statistical and systematic uncertainties are propagated from both sides, resulting in a very large uncertainty of the diffuse versus total reflectivity ratio.

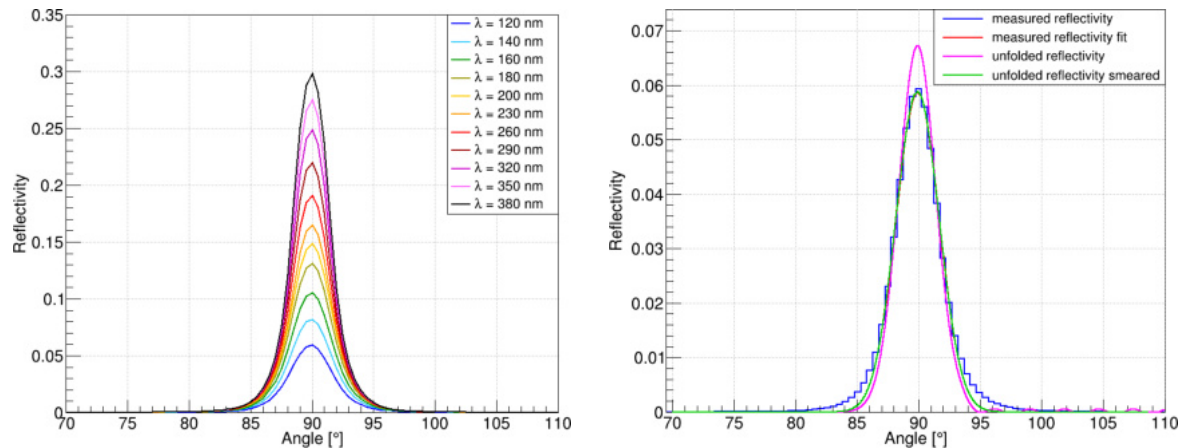


Figure 4.15: (Left) Angular measurement of the reflectivity for various wavelengths. (Right) Unfolding of the specular peak due to the small solid angle covered by the detector compared to the width of the reflection peak.

4.6 Combination of the reflectivity measurements

The measurements in the visible region performed in the IPF and in the VUV region done by the PTB will be combined for the implementation in the simulation of the attenuation setup.

The integrating sphere of the spectrophotometer of the IPF is much better suited for the measurement of diffuse reflected light due to the high light collection efficiency in the visible region. However, in the UV region the specular reflectivity of the PTFE increases, which can falsify the measurement of the diffuse light. On the other side, the reflectometer of the PTB scans systematically each angle, which leads to large uncertainties for small reflectivities like the diffuse component. But the conditions stay unchanged over the entire investigated wavelength range.

Due to oxygen in the spectrophotometer and the changing specular reflectivity of PTFE, the measurements of the IPF could be falsified at the lower wavelengths. The PTB operates their reflectometer in high vacuum without the use of a reflectance standard, thus eliminating both problems.

Consequently it was chosen to use the measurements of the PTB in the full measured region and the values of the IPF in the visible range only. The combined reflectivities are shown in figure 4.16. The kink in the reflectivity curves at 400 nm is not an issue in the simulation. Such discontinuities in the optical properties are propagated to the observed photons and are expressed in similar kinks in the resulting simulation spectra.

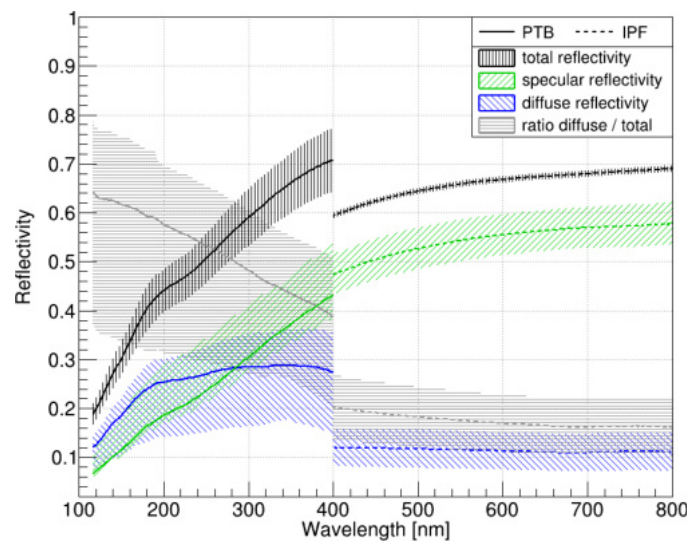


Figure 4.16: Combination of the reflectivity measurements of the PTB in the VUV and the IPF in the visible region.

While the specular reflectivity shown in figure 4.16 in the visible region agrees within the uncertainties with those depicted in figure 4.2, there are no publications with which the measurements below 250 nm can be compared. A reason for this lack of references is certainly the complexity of the measurement as well as the extremely time-consuming scanning of all incident and emergent angles. However, an appropriate integrating sphere for the UV region cannot be built, since no sufficiently well diffuser material in the UV region exists yet, which leaves the scanning of all angles the only feasible method for now.

If one additionally desires to measure the reflectivity of a material in LAr, the LAr container need to be transparent in the UV region while at the same time withstand cryogenic temperatures and vacuum. Unfortunately, a material meeting all these requirements is not known yet.

Chapter 5

Implementation of optical properties in Monte Carlo simulations

Background and signal events of the GERDA experiment are reproduced with simulations to investigate, understand and verify the detector response as well as determine the experimental sensitivity. In the case of the LAr veto, which is described in chapter 2.2.2, optical processes need to be simulated. This requires to specify all relevant optical properties of every interface optical photons can reach. The following sections give an introduction to the MaGe (MAJORANA/GERDA) simulation framework and the implementation of the considered optical properties partitioned in the corresponding materials. The corresponding simulation to the performed scintillation light attenuation measurement in LAr will be shortly labeled attenuation simulation in the following.

5.1 Simulation framework MaGe

MaGe is a MC (Monte Carlo) simulation software which is based on the GEANT4 (GEometry ANd Tracking) toolkit [BCD⁺11]. It is jointly developed between the MAJORANA and GERDA collaborations in order to simplify the conjunction to LEGEND, which was planned on a very early state of both experiments.

Since MAJORANA and GERDA use very similar detectors and physics processes, the joint development of MaGe is more efficient since relevant geometries, characteristics and processes can be shared. More generally, the MaGe framework contains commonly used materials, objects and their properties as well as prototypes, test stands, smaller experiments such as the attenuation setup described in chapter 6.1 and the entire MAJORANA and GERDA experiments. The desired experimental setup is selected with macro commands [BCD⁺11].

GEANT4 simulations are performed event-by-event, meaning that each event starts with the release of the initial particle(s) and ends as soon as all primary and secondary particles have deposited their full energy or stopped by a predefined condition such as leaving the relevant volume or not interacting for a certain period of time. This allows for a complete tracking of each single particle including the deposited energy in every step, the underlying processes and the creation of secondary particles [BCD⁺11].

The usual physics list used in MaGe is *Low Energy Electromagnetic Physics – Livermore* provided by GEANT4 and particularly developed for low-energy electromagnetic processes such as the interactions of electrons and photons with matter down to 250 eV. The Livermore library consists of interpolated data tables from EPDL (Photon Interaction Data), EADL (Atomic Relaxation Data) and EEDL (Electron Interaction Data) [Gea19].

5.1.1 DECAy0

The primary particles can be generated by GEANT4 itself or initialized from an input created by other programs. DECAy0 is a Fortran (FORmula TRANslation) based particle generator, which is in particular used for double beta decays and other nuclear decays.

DECAy0 also takes into account the angular correlation between γ -rays in de-excitation cascades, which is not done in the GEANT4 particle gun [BCD⁺11]. Data of nuclear and atomic decay schemes from the database libraries ENSDF (Evaluated Nuclear Structure Data File) and EADL are considered as well. DECAy0 takes the half life, energy distribution and angular correlation of the potential initial particles and generates the number and kind of emitted particles with their initial energy, the three-dimensional momentum and the emission time [PTZ00]. The number of generated events can be selected by the user. This information is saved into an ASCII (American Standard Code for Information Interchange) file, which can be used by MaGe. For each event the position of the primary particle(s) is randomly chosen in a predefined volume in MaGe and initialized with the start values given by DECAy0.

5.2 Liquid argon

As discussed in chapter 3 the optical properties of LAr are dependent on the impurity content. Since the LAr purity in the GERDA cryostat is unknown, the optical properties are implemented in a way to scale them to the desired values with macro commands.

5.2.1 LAr scintillation spectrum

A measurement of the scintillation spectrum of LAr is shown in figure 3.3. In chapter 3.1 it was discussed that the scintillation peak at 128 nm comprises 99.9% of the emitted light. Thus, only the peak is taken into account in the simulation and the other parts of the emission spectrum are neglected. The emission probability is approximated by a gaussian function [Pom09]:

$$f(\lambda) = \exp\left(-\frac{(\lambda - \lambda_{\text{peak}})^2}{2\sigma^2}\right) \quad \text{with} \quad \lambda_{\text{peak}} = 128 \text{ nm}, \quad \sigma = 2.929 \text{ nm} \quad (5.1)$$

The emission probability peak is shown in figure 5.1. It is important that the emission probability for the lowest and the largest wavelength is set to zero in the simulation, otherwise MaGe assumes a non-vanishing emission probability for all wavelengths below and above the actual scintillation peak according to the values implemented for the lowest and the largest wavelength.

5.2.2 LAr absorption length

The absorption length is implemented by fitting the attenuation measurement data shown in figure 3.6 under the assumption that the contribution of the scattering is negligible. A macro command is available to scale the achieved absorption length function to a desired value at 128 nm. Figure 5.1 shows the implemented absorption curve scaled to 15 cm at 128 nm superimposed with the scintillation emission peak. The absorption length changes drastically over the width of the peak, resulting in a redshift of the peak depending on the distance the scintillation photons traveled as discussed in chapter 3.2.3.

To avoid large values, the absorption length cannot exceed 1000 m in the simulation. For the attenuation simulation another macro command can be set to switch off absorption in LAr by setting the absorption to a large value, i.e. 1000 m for all wavelengths. This is used in order to investigate geometrical effects on the light propagation inside the attenuation setup.

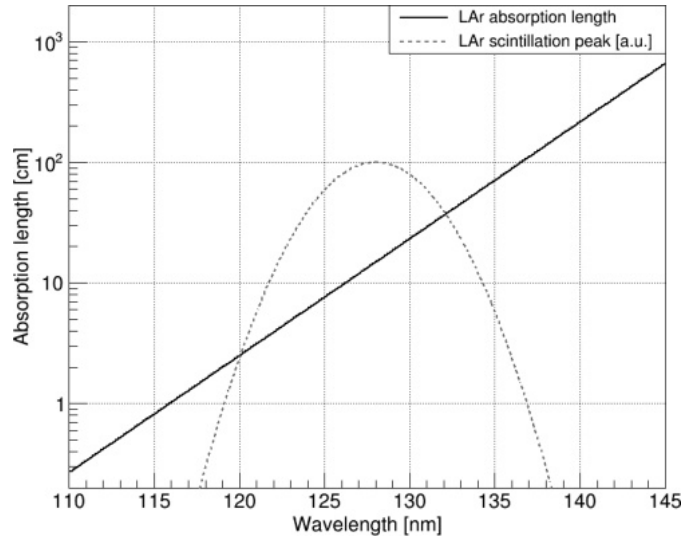


Figure 5.1: Absorption length and scintillation peak of LAr as implemented in the simulation. The absorption length is scaled to 15 cm at 128 nm.

5.2.3 LAr scintillation light yield

The light yield is quenched differently for various kinds of particles. The attenuation measurement is performed with a pure electron emitter, hence only one kind of particle has to be taken into account. The light yield can be set to any value by a macro command. For the LAr veto the situation is more difficult since also α -particles can deposit energy in LAr. The light yield is chosen by a macro command and at the same time MaGe considers the different quenching factors (see ch. 3.1) for electrons and alpha particles. This ensures that the ratio of the quenching factors remains the same for all selected light yields.

5.2.4 LAr singlet and triplet lifetime

In 2012, the triplet lifetime has been measured in GERDA to be $\tau_t = (922 \pm 31)$ ns [Weg17]. The triplet lifetime can be also retrieved of the data taken in the attenuation measurement, which results in $\tau_t = 1087.5 \pm 2.8(\text{stat.}) \pm 15.2(\text{syst.})$ ns as discussed in chapter 8. The fluctuation in the triplet lifetime showed that it can vary over time and may not be stable during the complete run-time. This caused a constant monitoring of the triplet lifetime in GERDA Phase II as shown in figure 2.5. For the simulations of the LAr veto a triplet life time of 1000 ns was chosen in order to reflect the monitored values in Phase II of GERDA.

A singlet lifetime of 6 ns has been implemented in MaGe, which is consistent with the values reported in table 3.2. The ratio of the singlet component to the total scintillation yield is set to 0.23 for electrons and 0.75 for nuclear recoils in MaGe (see tab. 3.2).

5.2.5 LAr refractive index

The refractive indices of rare gases have been measured in [BGJ81]. These values can be converted to the corresponding liquid by a correction of the density ratio of the liquid versus the gaseous form. In the case of LAr the refractive index has been measured down to 140 nm and has to be extrapolated for lower wavelengths. The resulting refractive index is shown in figure 5.2 on the left side.

Xenon has its first resonance line at 146.9 nm leading to a discontinuity in the refractive index curve at this wavelength. A measurement shows that the refractive index drops to very low values and rises sharply for lower wavelengths [BGAJ81]. Argon has the first resonance lines at 104.8 nm and 106.6 nm, thus it is expected, that the refractive index behaves continuous for larger wavelengths, which allows the extrapolation down to 110 nm.

The refractive index curve is implemented as a fit function of the data measured in [BGAJ81] as proposed in [Pom09] for wavelengths between 115 nm and 650 nm. The lower limit is bound to the resonance line of argon, where a measurement of the refractive index would be necessary for a implementation at lower wavelengths. The upper limit is chosen due to the sensitivity of the PMT which drops to zero for larger wavelengths, thus photons with wavelengths larger than 650 nm cannot be detected anymore. Consequently, they are not tracked to save computing time. These wavelength limits are consistently used for all other optical properties.

5.2.6 LAr scattering length

The scattering length implementation uses the wavelength dependency from calculations in [GBMN17] and [SLY02] with the extrapolated refractive index from [BGAJ81]. The curve is then scaled by multiplying a wavelength independent factor to fit the measurement at 128 nm in [ICD⁺97].

The implemented scattering length is shown in figure 5.2 on the right side. It is superimposed with the LAr scintillation emission peak to indicate the drastic change of the scattering length over the width of the scintillation peak. This can lead to an additional redshift of the scintillation peak as discussed in chapter 3.2.4.

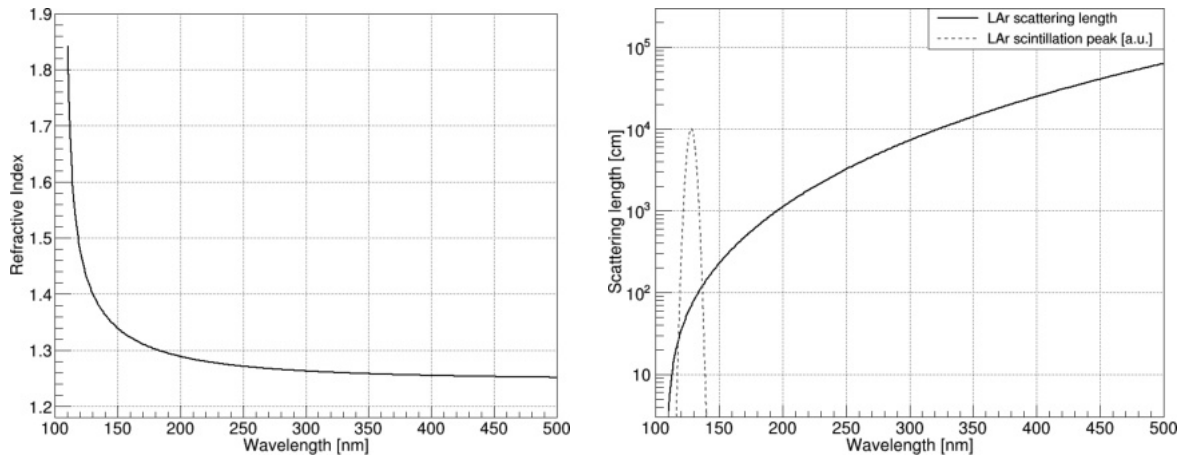


Figure 5.2: Refractive index (left) and scattering length (right) of LAr as implemented in MaGe.

5.2.7 Cherenkov light

The spectral distribution, i.e. the number N of emitted Cherenkov photons per path length dx and wavelength differential $d\lambda$ of the photon is given by the Frank-Tamm-formula with the charge z and the velocity $\beta = v/c$ of the particle, the fine structure constant α and the refractive index n of the traversed material [Die16]:

$$\frac{d^2N}{dx d\lambda} = \frac{2\pi\alpha z^2}{\lambda^2} \left(1 - \frac{1}{\beta^2 n^2(\lambda)} \right) \quad (5.2)$$

Consequently more photons with shorter wavelengths are emitted, explaining the bluish appearance of the visible Cherenkov light. The Cherenkov emission spectrum is revisited in section 5.6 and depicted in figure 5.7 for the attenuation simulation.

As measured in [BGJ81], the refractive index n changes with the wavelength in such a way that the Cherenkov emission cannot increase infinitely to shorter wavelengths. In fact, the refractive index becomes less than one in the X-ray region, prohibiting any Cherenkov light emission. However, the Cherenkov emission is not limited by MaGe, i.e. it can in principle also occur in other energy regions. Therefore the refractive index is only defined in the relevant wavelength region (115 nm – 650 nm) to prevent a Cherenkov emission at other wavelengths.

5.3 Steel reflectivity

The steel reflectivity curves are implemented as shown in figure 4.11 for the IPF measurement and in figure 4.16 for the combination of the IPF and PTB measurement. Since the PTB measurement was performed much later, the analysis of the attenuation data has been done with a simulation of the IPF data only and later on with the combination of both reflectivity measurements. This leads to two different analysis approaches, which are both described in chapter 7. The desired reflectivity curves can be selected via macro commands in MaGe. They are provided as data tables per wavelength, i.e. MaGe interpolates the reflectivity between the given values.

5.3.1 GEANT4 surface modeling

For the modeling of the steel reflectivity, the surface boundary of steel and LAr has to be defined precisely. When an optical photon reaches a boundary between two media, it can undergo various processes depending on the defined surface boundary. In the following only the properties concerning steel in LAr will be discussed. A complete overview including all surface options can be found in [CBPJ14, GA02, Gea19].

In table 5.1 the surface settings for the boundary between steel and LAr are summarized. The GEANT4 *unified* model is chosen, which allows the implementation of a wavelength dependent diffuse reflectivity that is not available in the *glisur* model. Since the diffuse reflectivity varies significantly over the measured wavelength range, the *glisur* model, which allows only for an approximation with just a single value for the diffuse reflectivity for all wavelengths, would introduce a large systematic uncertainty.

Table 5.1: Optical surface settings for the surface boundary of steel and LAr.

optical surface preference	setting
MODEL	unified
TYPE	dielectric_metal
FINISH	ground
SIGMAALPHA	0.02 rad

The type of interface is set to *dielectric_metal* which supports reflection and absorption (i.e. detection) at the metal surface. The surface finish is chosen to be *ground*, which describes rough surfaces composed of micro facets as depicted in figure 5.3 on the right. The reflected angle of an optical photon is calculated using the parameter SIGMAALPHA. The *unified* model describes the *ground* surface as a combination of micro facets, whose normals are calculated as a Gaussian distribution with the standard deviation σ_α around the average surface normal.

Assuming that the Gaussian shape of the unfolded specular reflected peak (see fig. 4.15) corresponds directly to the GEANT4 modeling of the micro facets, SIGMAALPHA has been set to 0.02rad, which results in the best agreement.

An optical photon reaching a *dielectric-metal* surface can be reflected in several processes. In GEANT4, the specular reflection is divided in spike and lobe reflection, describing the reflection concentrated along the emergent angle and distributed around it, respectively (see fig. 5.3). The specular spike reflection occurs at the average surface normal. When specular lobe reflection is happening, a micro-facet normal is randomly chosen based on SIGMAALPHA and the reflection is calculated for the incident angle on this surface. On very rough surfaces the reflection can occur in the direction where the optical photon came from, which is covered by the definition of a non-vanishing backscattering. The diffuse reflection is described by a lambertian cosine function (see ch. 4.1) around the average surface normal.

The measured reflectivities discussed in chapter 4 are implemented in the simulation as listed in table 5.2. The total reflectivity of the surface can be defined by the parameter REFLECTIVITY for each wavelength. The individual processes are given by the probability of occurrence of the respective process. These probabilities sum up to 100%. As a consequence, LAMBERTIAN is not defined directly, but is calculated implicitly from the values of SPECULARSPIKECONSTANT, SPECULARLOBECONSTANT and BACKSCATTERCONSTANT. The EFFICIENCY can be used if the metal surface is at the same time a detection medium, which is not the case in the attenuation simulation, thus it is set to be zero.

Figure 5.3 depicts a schematic drawing of the possible reflection processes summarized in table 5.2. If the probability of the process is set to zero, it does not occur in the simulation.

Table 5.2: Optical surface properties of the steel surface in LAr and the implemented measured data sets of the steel reflectivity.

optical surface property	implemented measured data
REFLECTIVITY	total reflectivity
SPECULARSPIKECONSTANT	0
SPECULARLOBECONSTANT	specular reflectivity
BACKSCATTERCONSTANT	0
LAMBERTIAN	diffuse reflectivity
EFFICIENCY	0

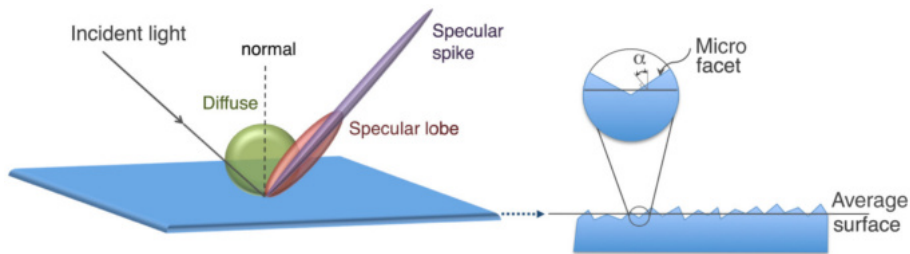


Figure 5.3: Schematic visualization of the possible reflection processes in GEANT4 with the *unified* model. The average surface normal is used for the specular spike reflection, while the angle α between the micro facet and surface normal defines the specular lobe reflection angle [CBPJ14].

5.3.2 Extrapolation to the VUV region

For the simulation with the reflectivity measurement performed in the IPF, no data is available below 200 nm. But since the scintillation light of LAr peaks at 128 nm, it is crucial to model the reflectivity in the VUV region as well. For this, several assumptions of the reflectivity curves in the VUV region have been made, which are shown in figure 5.4.

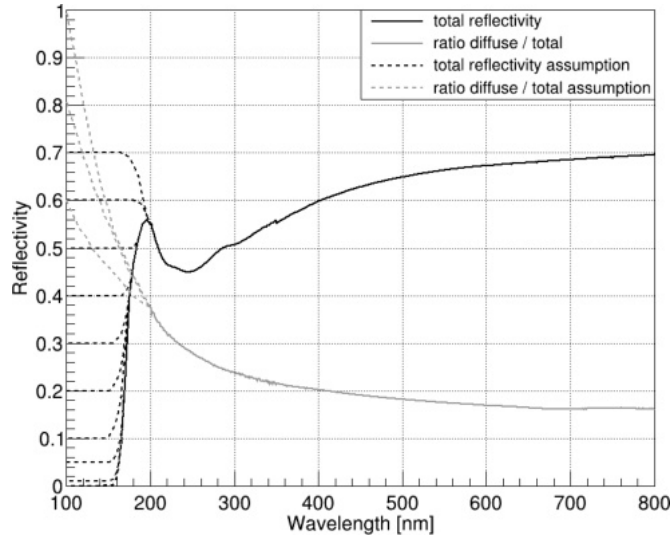


Figure 5.4: Average steel reflectivities measured in the IPF and assumptions of the total and diffuse reflectivity for the wavelengths below 200 nm for the simulations.

Due to the known absorption bands of other metals and their reflectivity behavior at wavelengths below these regions (see fig. 4.3), it is not expected that the reflectivity of the steel gets larger at wavelengths below 200 nm. At this time it was assumed, that steel features an absorption band around 250 nm causing the lower reflectivity in this region. This assumption was later disproved by the reflectivity measurements performed by the PTB.

5.4 Wavelength shifter TPB

TPB (tetraphenyl butadiene) is the chemical compound $C_{28}H_{22}$ and is used as a WLS dye to convert VUV light into the visible region. It is evaporated or painted on PMTs in order to shift the argon scintillation light to the PMT's sensitive region.

The most important property settings for TPB implemented in MaGe are summarized in table 5.3. The refractive index (RINDEX) quoted in [Mol20] is set to 1.635 for all wavelengths, since no wavelength resolved measurements exist yet. The life time of the WLS excitation state (WLSTIMECONSTANT) is chosen to be 0.01 ns as proposed in [Pom09].

Table 5.3: Optical property settings of the WLS TPB and the implemented values in MaGe.

optical property	implemented value	reference
RINDEX	1.635	[Mol20]
WLSTIMECONSTANT	0.01 ns	[Pom09]
WLSABSLLENGTH	TPB absorption length	[BOG18]
WLSCOMPONENT	TPB emission spectrum	[FMN ⁺ 13]
WLSMEANNUMBERPHOTONS	1.2	[GSR ⁺ 11]

5.4.1 TPB absorption length

The absorption length (WLSABSLLENGTH) of the WLS is implemented wavelength dependent as shown in figure 5.5. TPB has a short absorption length in the VUV region, thus it absorbs light in this region very efficiently. The absorption length grows for larger wavelengths, making TPB transparent for visible light.

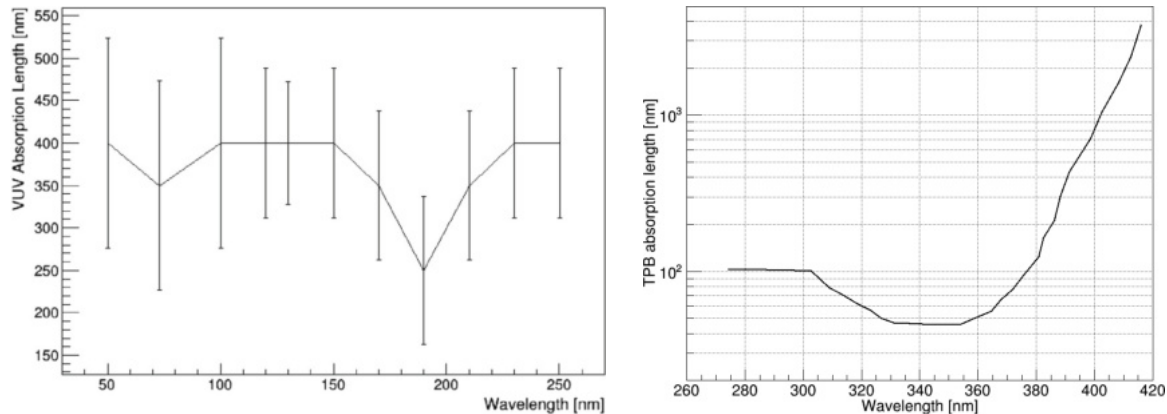


Figure 5.5: Absorption length measurements of TPB taken from [BOG18].

5.4.2 TPB emission spectrum

The parameter WLSCOMPONENT covers the wavelength resolved emission spectrum of the WLS. Several measurements exist indicating that the spectral shape depends on the excitation wavelength [GSR⁺11, FMN⁺13]. Additionally the thickness of the TPB layer and the specific composition of the WLS affect the shape of the emission spectrum [BOG18, FMN⁺13]. It has been found that the TPB emission peak shifts to larger wavelengths for a higher TPB layer density [FMN⁺13]. Also, the support material on which the WLS is evaporated can change the spectral shape [FMN⁺13].

The PMT used for the attenuation measurement was evaporated with PS (polystyrene) and TPB with a mixing ratio of 10:1. The WLS layer thickness was estimated to be 5 μ s on the PMT glass. Summarized, the measured emission spectrum in [FMN⁺13] of a compound of TPB in PS on glass with 10% TPB excited at 128 nm has been implemented in MaGe. The emission spectrum is depicted in figure 5.7.

5.4.3 TPB light yield

The parameter value of WLSMEANNUMBEROFPHOTONS is the average light yield of the WLS. It has been measured to be 1.2 at 128 nm in [GSR⁺11] and 1.5 ± 0.11 for a PS+TPB ratio of 10:1 [BBD⁺15]. It has also been found that the light yield gets larger for shorter excitation wavelengths [GSR⁺11]. Concluding a WLS light yield of 1.2 has been implemented in MaGe and the other values serve for systematic uncertainty investigations.

5.5 PMT efficiency

The PMT model R11065 provided by Hamamatsu has been used in the attenuation measurement [Ham15]. In the LAr veto in GERDA PMTs of the same model have been mounted with a modified VD (voltage divider). Other experiments are using the same PMT model due to its specific development for the operation in cryogenic temperatures and its extremely low radioactivity [LNG20, WAr12]. The measured PMT efficiencies of Hamamatsu, the WArP (WIMP Argon Programme) collaboration and the PMTs mounted in the LAr veto in GERDA are depicted in figure 5.6.

Since the PMT used in the attenuation measurement had an unmodified VD, the efficiency provided by Hamamatsu is implemented in the simulation with the option to use the other values for systematic uncertainty investigations.

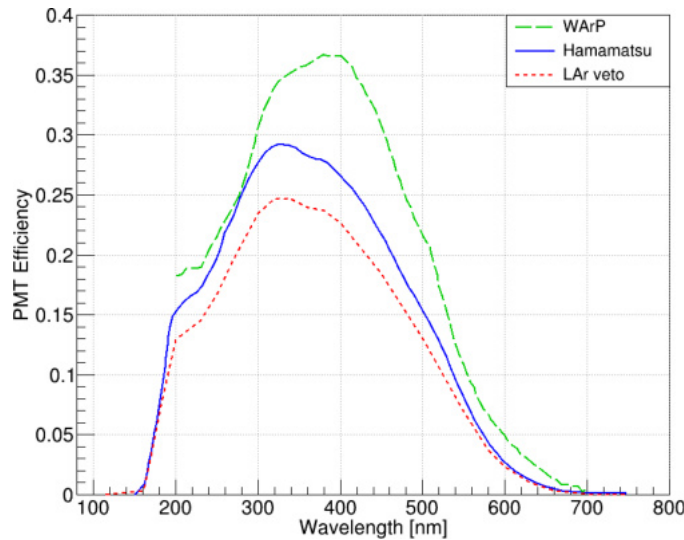


Figure 5.6: PMT efficiencies measured for the model R11065 by the WArP collaboration [WAr12], Hamamatsu [Ham15] and for the LAr veto in GERDA.

5.6 Discussion

In figure 5.7 a selected compilation of the discussed optical properties implemented for the attenuation setup is depicted. Depending on the LAr light yield the intensity of the LAr scintillation peak compared to the Cherenkov emission spectrum can vary. Consequently, the contribution of Cherenkov light is small for a high LAr light yield and vice versa. Thus, an investigation of the background caused by Cherenkov light is essential for a small LAr light yield.

As shown in figure 5.5 the absorption length of TPB is short in the VUV region, hence the LAr scintillation light gets shifted to the visible efficiently. This is also true for the Cherenkov light emitted in the VUV and UV region. In the end the origin of the shifted light – scintillation or Cherenkov – cannot be distinguished anymore. The analysis technique concerning the background contribution of the Cherenkov light is explained in chapter 7.3.2.

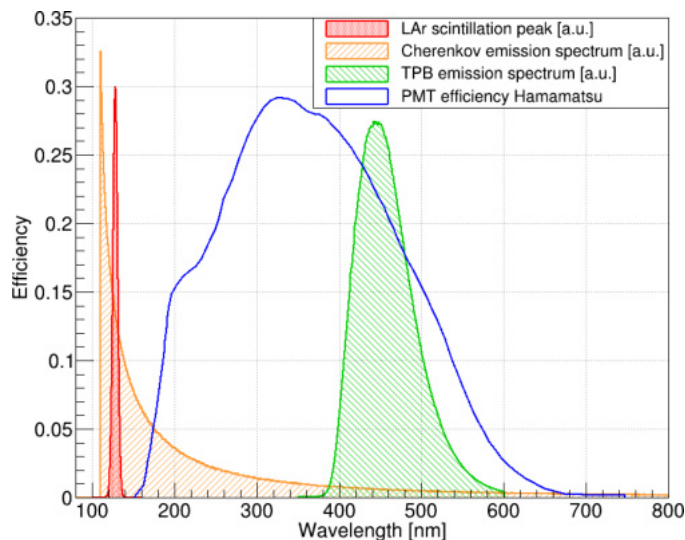


Figure 5.7: Compilation of the LAr scintillation peak and the Cherenkov emission spectrum for a ^{90}Sr source (see fig. 6.4 and 6.5) as well as the WLS emission spectrum [FMN⁺13] and the quantum efficiency of the PMT [Ham15] as implemented in MaGe for the attenuation setup.

Since the absorption length of TPB grows in the visible region, the WLS evaporated on the PMT gets transparent for the visible light. This applies not only to the Cherenkov light emitted in the visible, thus it can be detected directly, but also to the shifted light by the WLS itself. Since TPB emits light isotropically, the shifted light can be reflected at the steel of the attenuation setup and get back to the WLS, transmitting through it and triggering the PMT. Together with the fact, that the reflectivity of steel is much higher in the visible region than in the VUV region and the attenuation length is much longer for visible photons, this leads to the conclusion, that Cherenkov light is a non-trivial background for the attenuation measurement.

The PMT is sensitive in the visible and UV region, enabling the detection of the shifted light by the WLS as well as the Cherenkov light in the region where the WLS is transparent to it.

In summary the light propagation in the attenuation setup is a complex compilation of many parameters leading to a multidimensional problem. The data of the attenuation measurement is reconstructed with MC simulations in order to better understand the processes occurring in the measurement.

Chapter 6

Measurement of the scintillation light attenuation in LAr in GERDA

For the measurement of the attenuation of the scintillation light in LAr in GERDA a dedicated setup was developed that has been directly submerged into the LAr cryostat of the GERDA experiment in the LNGS. The almost final stage of the setup is described in [Sch14]. However, some changes were applied after the submission, which will be covered in this chapter. A description of the final setup as used in the measurement is given and suggestions of alternative options for specific parts are discussed. There, the main focus lies on a suitable source to create the scintillation light in LAr. The DAQ (data acquisition), the measured data and cleaning cuts for the preparation of the analysis are explained in the second part of this chapter. Some of the work has already been published in [BDL⁺20].

6.1 Development of a dedicated setup

The attenuation of the scintillation light is determined from the light intensity measured at various distances between the creation of the scintillation light and its detection. Therefore it is crucial to investigate all possible backgrounds that can contribute to the observed light. Consequently, all parts of the measuring setup have to be selected carefully to minimize the background from radiogenic impurities.

A CAD (computer-aided design) drawing of the setup is depicted in figure 6.1. The setup is composed completely of stainless steel with the exception of the PMT holder which is made of PTFE. The setup is 1 m long and the radioactive source can be moved in a range of 0.6 cm to 55.6 cm distance to the PMT. Considering the results from other attenuation measurements compiled in table 3.5, these dimensions were chosen in order to observe a clear attenuation of the light intensity for the various possible measuring distances.

The setup length is constrained by the opening of the LAr cryostat lock of GERDA. The length of 1 m can be mounted inside the lock without disassembling the construction, but only opening the main lock entry. Additionally, the weight of roughly 15 kg of the setup can be easily handled by a single person. Since the stepper motor requires a minimum weight of 20 kg to work reliable¹ and the minimum weight has not been achieved due the other constraints already discussed, additional weight was mounted above the setup by hanging copper plates on the string carrying the setup inside the lock.

A radioactive source to create the scintillation light is carried by a source holder, which is attached to steel rods as shown in figure 6.1. The source holder has no additional window at the side where the active sample of the source is located, hence the emitted particles only need to pass the steel window of 50 μm of the source itself. The source movement is controlled by a stepper motor which is connected via cogwheels to the steel rods (fig. 6.2).

¹If the weight is too low, the chain holding the weight is sagging and it can happen that the motor omits steps which leads to the problem that the exact position of the setup inside the lock becomes uncertain.

Figure 6.1 also shows collimator rings which serve as light absorbers. They are arranged in a way that light reflected at the inner steel wall of the setup cannot reach the PMT directly.

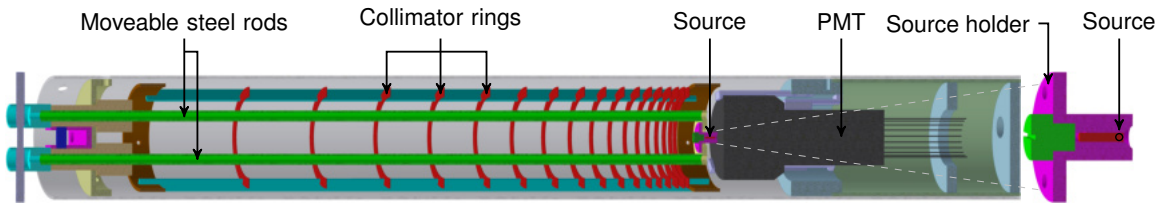


Figure 6.1: CAD drawing of the setup for the attenuation measurement. The source can be moved by the steel rods to adjust the distance to the PMT. The stepper motor (not shown) will be connected on the left end of the setup to the steel rods via cogwheels to control the movement of the source. The collimator rings absorb reflected light from the inner steel wall. The initial CAD drawing was drafted by Alexander Domula and finalized by Martin Siegel. Originally published in [BDL⁺20].

6.1.1 Stepper motor

The stepper motor controlling the source movement is depicted in figure 6.2. On the left side is shown a CAD drawing of the connection to the steel rods via cogwheels. On the right side a picture of the assembled motor can be seen. A copper contact is arranged in a PTFE holder to get an electrical signal when the source is moved to the nearest possible position with regard to the PMT. This is done in order to prevent the motor from unnecessarily pushing the source further, when it has already reached its final position. Since the setup is operated in a cryogenic liquid at 87 K, too much force could easily break parts of the setup.

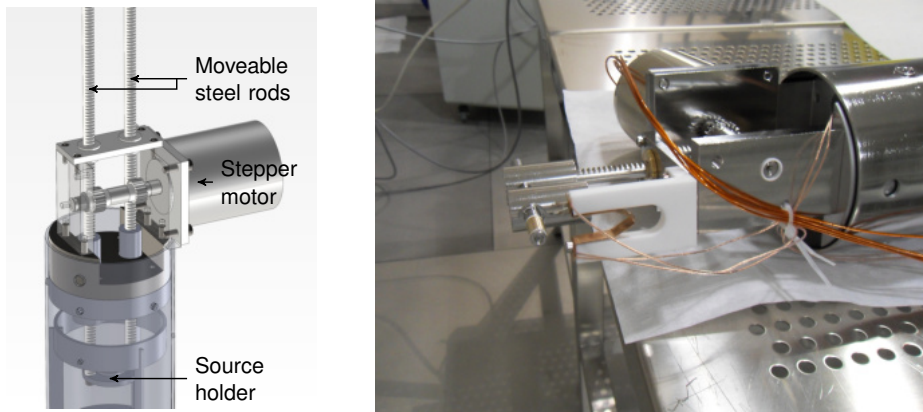


Figure 6.2: (Left) CAD drawing of the motor attached to the steel rods via cogwheels. Image made by Martin Siegel. (Right) Picture of the assembled motor. The copper contact signals that the source has reached the nearest possible position with respect to the PMT.

The stepper motor is the type [VSS 57.200.2,5-UHVC](#) of the company *Phytron* [Phy20] and is particularly designed for the operation in cryogenic temperatures.

Despite the LAr density of 1.4 g/cm^3 , the source holder would sink as soon as the motor is switched off, due to its weight and the weight of the steel rods. As a consequence the motor has been run with a holding torque in order to keep the source at its desired position during the measurements. This caused electromagnetic interferences on the PMT signal which is discussed in section 6.3.1.

Unfortunately, a mechanical switch to hold the source while the stepper motor is switched off during data taking had not been installed. This would have prevented an extensive data cleaning in the first place.

6.1.2 Material of the setup

Almost all parts of the setup for the attenuation measurement are made of stainless steel (SAE 304). It is advantageous to construct the setup mainly of one single material since different thermal expansions would cause tensions in the setup when submerging it into LAr, i.e. cooling it from room temperature to 87 K. In [Sch14] alternative materials, i.e. copper and aluminum were discussed. Steel combines the advantages of both. It is comparatively cheap, stable at cryogenic temperatures, has a high radiopurity and shrinks only about 0.3% from room temperature to 87 K [NIST20].

Additionally, steel can be electropolished, which cleans the surface entirely by removing a few micrometers from it. This prevents any impurities on the steel surface from dissolving in LAr, i.e. keeping the LAr in GERDA at its purity level. All steel parts of the setup underwent an electropolishing procedure. The collimator rings (fig. 6.1) are electropolished for a shorter time. They are only 0.5 mm thick and would not sit tightly in their designed position if too much material is removed. Due to concerns that these steel rings could break easily during the assembling of the setup, spare rings were crafted. These spare rings were used in the reflectivity measurements discussed in chapter 4.

Although radiogenic surface impurities were removed by the electropolishing, intrinsic impurities can deposit energy in LAr generating scintillation light and thus contributing to the background of the attenuation measurement. For an evaluation of the impurity content of stainless steel SAE 304 a compilation of relevant possible intrinsic isotopes is given in table 6.1. Of all measurements the respective highest values were chosen for a conservative estimation, which does not exceed 550 mBq/kg. The attenuation setup consists of roughly 13 kg of steel leading to a maximum overall background of roughly 7 Bq.

Table 6.1: Compilation of relevant possible intrinsic impurities in stainless steel SAE 304, measurements of their activities A [LCC⁺16], their dominant decay modes, Q -values and most prominent γ -lines including their emission probabilities [IAE20].

isotope	A [mBq/kg]	decay mode	Q [keV]	γ -line(s) [keV]
²²⁸ Ac	70 ± 10	100% β^-	2124	338 (11%), 911 (26%), 969 (16%)
²¹⁴ Bi	< 25	99.979% β^-	3269	609 (45%), 1120 (15%), 1764 (15%)
⁶⁰ Co	230 ± 40	100% β^-	2823	1173 (99.85%), 1332 (99.98%)
⁴⁰ K	< 60	89% β^-	1311	–
		11% EC, β^+	1504	1461 (11%)
²¹² Pb	70 ± 10	100% β^-	569	239 (44%)
²¹⁴ Pb	< 25	100% β^-	1018	295(18%), 352 (36%)
²⁰⁸ Tl	70 ± 10	100% β^-	4999	511 (23%), 583 (85%), 2615 (99.8%)

MC simulations were performed to estimate to what extent the isotopes listed in table 6.1 contribute to the expected background of the attenuation measurement. For this purpose the isotopes with the highest activities, Q -values and gamma energies were chosen, which are ²²⁸Ac, ⁶⁰Co and ²⁰⁸Tl. For each isotope 10^6 events were generated within the steel parts of the attenuation setup. The respective contribution to the scintillation light is weighted with the maximum expected activities given in table 6.1.

The results are summarized in table 6.2. The background contribution from radiogenic contaminations in steel is negligible compared to the overall detected light created by a 7 kBq ⁹⁰Sr source. Thus, it is not included in the background consideration for the analysis of the attenuation data.

6.1.3 Source

For the attenuation measurement the deposition of energy and consequently the origin of the scintillation light needs to be as point-like as possible in order to minimize uncertainties emerging from the distance the scintillation photons travel until hitting the PMT. Additionally the deposited energy in LAr should be sufficiently high to achieve a clear signal, i.e. many scintillation photons and a low background are desired. Hence, a suitable radioactive source should emit particles which have high energies and at the same time a short range in LAr. Therefore, a pure α -source would be ideal.

α -source

Since α -decays are often followed by a subsequent γ -emission, a suitable α -source needs to have either low energy γ -lines or a negligible γ -emission probability. The latter is true for the isotope ^{210}Po whose decay scheme is depicted in figure 6.3.

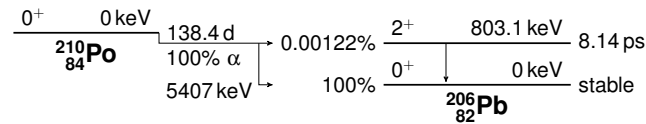


Figure 6.3: Decay scheme of ^{210}Po . Values are taken from [CEF99].

The CSDA (continuous-slowng-down approximation) range of a 5407 keV α -particle in LAr is about $50\ \mu\text{m}$ [NIST19a] which is perfectly suitable for the point-like source of scintillation light in LAr. Additionally, α -particles need a kinetic energy of more than 1100 MeV in order to create Cherenkov light in LAr, which is much higher than the Q -value of any known α -emitters. Thus, there is no Cherenkov light background created by α -particles.

Commercially available α -sources are open sources to reduce self-absorption of the α -particles due to their low range. However, the GERDA collaboration prohibits open sources inside the LAr cryostat, since the radioactive sample could dissolve in LAr, which would cause a large background for the experiment. Thus, an α -source cannot be used for the attenuation measurement inside the GERDA LAr cryostat.

β -source

Several contemplable β -sources were discussed in [Sch14], of which a ^{90}Sr -source turned out to be the best choice. The desired source was provided by *Eckert & Ziegler* at the LNGS and already tested as well as confirmed to be stable in LAr and therefore approved by the GERDA collaboration. It is only 2 mm in diameter and 10 mm long. The active sample is located at one end of the small cylinder and has the shape of a sphere with a diameter of 1 mm. The source has a steel window of $50\ \mu\text{m}$, which allows the β -particles to pass through it.

The decay chain of ^{90}Sr is shown in figure 6.4. It should be noted, that the ^{90}Sr -source is in equilibrium with its daughter ^{90}Y and the certified activity is for ^{90}Sr only. Thus, the beta emission rate of this source is twice as high as the given activity. The emission probabilities of the γ -rays from the decay of ^{90}Y are negligibly small. Nevertheless, they are taken into account by DECAY0 and are therefore also simulated with MaGe. The generated emission spectra of ^{90}Sr and ^{90}Y with $2 \cdot 10^6$ simulated events per isotope are shown in figure 6.5. An extremely small γ -peak is visible at 1761 keV.

As discussed in chapter 5.6 Cherenkov light causes a non-trivial and non-constant background for the attenuation measurement. Thus, it needs to be modeled with MC simulation to estimate its contribution to the overall detected light.

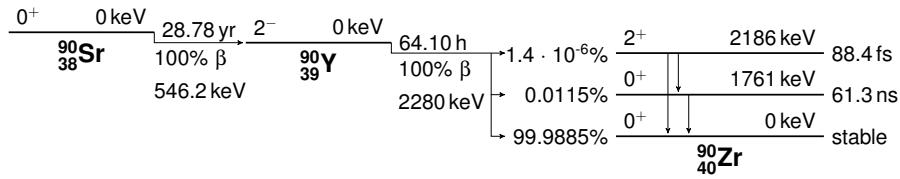


Figure 6.4: Decay chain of ^{90}Sr . Values are taken from [CEF99].

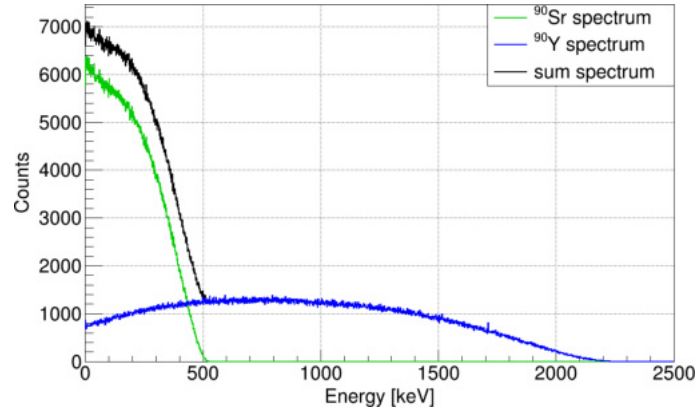


Figure 6.5: With DECAy0 generated electron emission spectrum of ^{90}Sr and ^{90}Y . The tiny peak at 1761 keV is originated by a low probable γ -emission of ^{90}Y .

As shown in figure 5.2, the refractive index of LAr is about 1.25 in the visible region and roughly 1.57 for 115 nm. This means, that an electron needs to have a kinetic energy of at least 340 keV to create Cherenkov light in the visible region, but for the creation of a 115 nm photon, an electron with a minimum kinetic energy of 150 keV is already sufficient. The emission spectra depicted in figure 6.5 reveals that higher energetic electrons from ^{90}Sr as well as most of the electrons emitted by ^{90}Y are able to create Cherenkov light in LAr.

The range of electrons in LAr can be determined by folding the ^{90}Sr and ^{90}Y spectra shown in figure 6.5 with the respective CSDA range of the corresponding energy. This results in an average range of 2.2 mm with a maximum of 10.4 mm [NIST19b]. However, the emitted electrons can also create bremsstrahlung photons inside the source holder and the source itself. These can produce electrons in the LAr much farther away from the actual ^{90}Sr source. Thus, the creation of scintillation photons is not point-like, but looks as depicted in figure 6.7 on the left.

γ -source

Since the range of γ -rays in LAr is much larger than for electrons and α -particles, γ -sources were not taken into account initially for the creation of the scintillation light in the attenuation measurement. However, the attenuation measurement triggered the development of a constant monitoring of the LAr scintillation light attenuation for the LEGEND experiment.

In this case an ^{241}Am source was chosen to circumvent the Cherenkov background created by electrons in the attenuation measurement. The decay scheme of ^{241}Am is depicted in figure 6.6. Only the energy levels populated dominantly and the most prominent transitions are shown. The energies of the most probable γ -rays of ^{241}Am are too low to produce electrons with a kinetic energy of more than 150 keV, and the population of higher energetic levels is negligible. Additionally, the energy of Auger and conversion electrons emitted by ^{241}Am is below 100 keV.

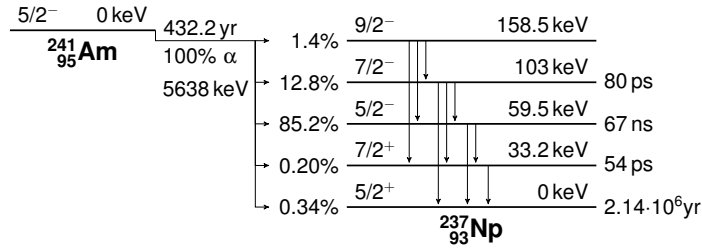


Figure 6.6: Decay scheme of ^{241}Am . Only the most prominent energy levels and γ -lines are shown. Values are taken from [CEF99].

The downside of γ -sources is the longer range in LAr causing a wider spread of the position of the creation of scintillation light as shown in figure 6.7 on the right side. On average the origin of the scintillation photons created by ^{241}Am is 7.8 mm away from the source, while for ^{90}Sr it is only 1.4 mm. Thus, the creation of the scintillation photons is more point-like for the almost pure β -emitter ^{90}Sr than for the low energy γ -emitter ^{241}Am . Additionally, the number of produced scintillation photons is more than a factor 10 higher for the ^{90}Sr source. These two important facts support the choice of the ^{90}Sr source for the attenuation measurement.

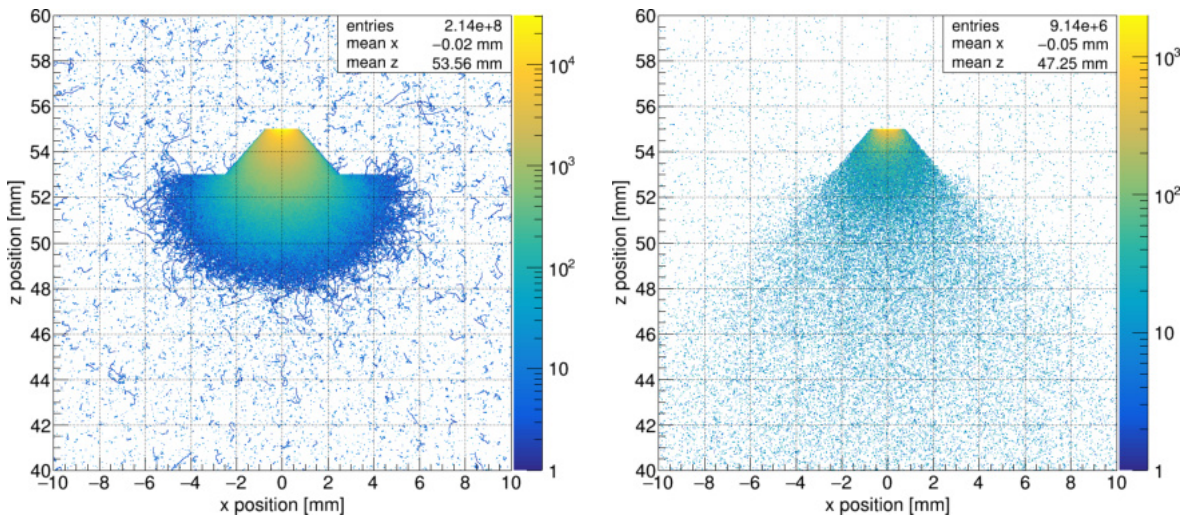


Figure 6.7: Origin positions of scintillation photons created in LAr with 10⁶ simulated events of ^{90}Sr and ^{90}Y each (left) and 10⁶ events of ^{241}Am (right). The source emits particles at $z = 55$ mm with a diameter of 1 mm in the x, y -plane. The origin positions are projected on the x -plane. The entries are the number of created scintillation photons and the mean gives the average value of the origin position of the created scintillation photons.

6.1.4 Scintillation light detection

The 3" PMT R11065-10 [Ham09] provided by Hamamatsu was chosen for the scintillation light detection in the attenuation measurement. At the time of the measurement several PMTs of this particular model were tested for the long-term operation in the LAr veto designed for Phase II of GERDA. Thus, a spare PMT that was already known to perform stable in LAr have been used for the attenuation measurement. This PMT model is specifically designed for the operation in cryogenic temperatures and has a low intrinsic radioactivity. Hamamatsu quotes an activity of 16 mBq [Ham15] for this PMT model, which is dominated by ^{40}K and additionally composed of ^{226}Ra and ^{228}Th . Since the PMT activity is even lower than the intrinsic impurities in steel (tab. 6.1), it is neglected.

The PMT is coated with the WLS TPB in order to convert the scintillation light to its sensitive region (see fig. 5.7). Unfortunately, no measurements of the radiogenic purity of the WLS coating exist so far.

6.1.5 Background expectation from argon and steel

Argon extracted from air contains the contaminations ^{39}Ar ($T_{1/2} = 269$ yr, $Q_{\beta} = 565$ keV) and ^{42}Ar ($T_{1/2} = 32.9$ yr, $Q_{\beta} = 599$ keV) [CEF99]), which are both pure β -emitters and can trigger scintillation light anywhere in the LAr. The other radioactive isotopes of argon are short-lived and have completely decayed in the LAr in GERDA. The activity of ^{39}Ar is measured to be 1.4 Bq/l in LAr and 85 mBq/l for ^{42}Ar [BCC⁺07], thus only the background contribution of ^{39}Ar is pursued.

The CSDA range of electrons emitted by ^{39}Ar is at maximum 2 mm in LAr and 0.4 mm in steel² [NIST19b]. The thickness of the steel housing of the setup is 2.6 mm, consequently only ^{39}Ar in the LAr volume inside the setup can contribute to the background of the light detection. The setup contains roughly 71 l of LAr, resulting in about 10 Bq of ^{39}Ar inside the setup.

For the background estimation MC simulations were performed with 10^7 decays of ^{39}Ar inside and surrounding the attenuation setup. Table 6.2 shows the expected number of detected events per second for ^{39}Ar and other investigated isotopes.

For the comparison, decays of ^{90}Sr and ^{90}Y have been simulated at the measured source positions with respect to the PMT. While the number of detected events per second of ^{90}Sr decreases with the distance due to the attenuation of the scintillation light, it is constant for ^{39}Ar for all ^{90}Sr source positions as expected. For the largest distance, the contribution of ^{39}Ar is only 3% to the detected light from the ^{90}Sr and even lower for the shorter distances. Consequently, the background originating from ^{39}Ar can be neglected in the attenuation measurement.

Table 6.2: Number of detected events estimated with MC simulations. Emitted particles of ^{90}Sr and ^{90}Y are started in the source (see fig. 6.1) at the distance d with respect to the PMT. ^{39}Ar is simulated in the argon volume within and surrounding the attenuation setup. The remaining isotopes are intrinsic contaminations in steel.

d [cm]	detected events [1/s]				
	$^{90}\text{Sr}+^{90}\text{Y}$	^{39}Ar	^{228}Ac	^{60}Co	^{208}Tl
5.5	28991.7	6.01	0.299	2.43	0.954
7.1	17731.3	5.97	0.300	2.42	0.965
8.7	11802.8	6.22	0.302	2.37	0.961
10.2	8464.3	6.20	0.300	2.44	0.972
11.8	6170.0	6.34	0.301	2.43	0.970
13.4	4574.6	6.27	0.304	2.40	0.979
15.0	3533.9	6.15	0.301	2.46	0.951
19.7	1828.3	6.24	0.301	2.37	0.956
24.4	1084.5	6.09	0.300	2.41	0.965
33.8	491.5	6.17	0.296	2.40	0.966
43.3	297.1	6.37	0.305	2.37	0.964
52.7	193.8	5.97	0.298	2.42	0.970

²Since the material stainless steel (SAE 304) is not available in the ESTAR program, a compound was defined using 72% iron, 19% chromium and 9% nickel.

The number of detected events is also listed for the investigated steel contaminations in table 6.2. It is also independent of the source position, since the weight of the source holder is small compared to the whole steel setup. Summarized, also the background contribution originated by steel contaminations can be neglected.

6.2 Measuring points

For the attenuation measurement the light intensity produced by a ^{90}Sr source was measured at 12 various distances with different step lengths in the range from 0.6 cm to 55.6 cm between PMT and source. Several uncertainties of the distance of the measuring points are taken into account. At room temperature the smallest adjustable distance was measured with an uncertainty of 0.1 cm. After submerging the attenuation setup in LAr the stepper motor moved the source up and down over the full range several times. The deduced standard deviation of the motor steps is determined to be 0.127 cm. Taking into account the shrinking of the setup due to the operation in cryogenic temperatures, an uncertainty of 0.3% for each distance is introduced, which causes the distance to be smaller. In summary the uncertainty of distance d is given by equation 6.1.

$$\Delta d = \pm 0.1 \text{ cm} \pm 0.127 \text{ cm} - 0.003 \cdot d[\text{cm}] \quad (6.1)$$

Consequently, the mechanical adjustment of the measuring points has a similar order of magnitude of the uncertainty as caused by the different points of origin of the scintillation light created by ^{90}Sr as discussed in section 6.1.3. The path length traveled by a scintillation photon from its origin until its detection is taken into account in the analysis, which is discussed in chapter 7.2. The uncertainty of the distance adjustment is contained in the systematic uncertainties in chapter 7.3.6.

6.3 Data taking

The signal of the PMT VD is converted with a MPMK-II shaper and afterwards processed by a 14-bit FADC (Fast Analog to Digital Converter) board SIS3301 provided by *Struck*. It has a maximum sampling frequency of 100 MHz and two memory banks of 128k samples each. The pulse traces were recorded with a trace length of 131072 samples, i.e. about 1.3 ms with 100 MHz and 16384 ADC channels.

The online trigger condition to save a pulse trace is constructed by the comparison of the sum of two consecutive samples with the sum of the following two samples. If the latter is larger by at least 80 ADC samples, the trigger condition is fulfilled.

It will be referred to as hardware trigger in order to prevent confusion to the later defined software trigger in the offline analysis. The hardware trigger has been chosen to be sufficiently high in order to not trigger on the interference created by the stepper motor. The pulse that exceeds this hardware trigger is located exactly in the middle of every pulse trace, i.e. at sample 65536. All pulse traces were saved for each measuring point to allow for a complex offline analysis.

6.3.1 Signal reconstruction

Signal events created by just a few photons cannot exceed the hardware trigger, thus the event associated with the hardware trigger is always composed of at least a couple of photons. Consequently, the hardware trigger is flagged in every pulse trace and not used for the later-on analysis to prevent a systematic bias.

For the reconstruction of very long pulse traces the FADC saves pulse traces which are overlapping with the previous one. However, this feature is not used here, thus the overlapping samples are kept in the previous trace, but discarded in the following trace in order to prevent a bias by analyzing twice the part of the pulse trace with the identical samples. The fraction of the overlapping pulse traces is listed for all measuring points in table 6.3. It is decreasing for larger distances due to the lower signal rate.

An example of a pulse trace is shown in figure 6.8. The periodic interference created by the stepper motor is visible with a frequency of about 20 kHz. Since it would falsify the event reconstruction, it is discarded for the analysis. For this purpose it is flagged in order to prevent the software trigger from finding signal events overlaid by the motor interference.

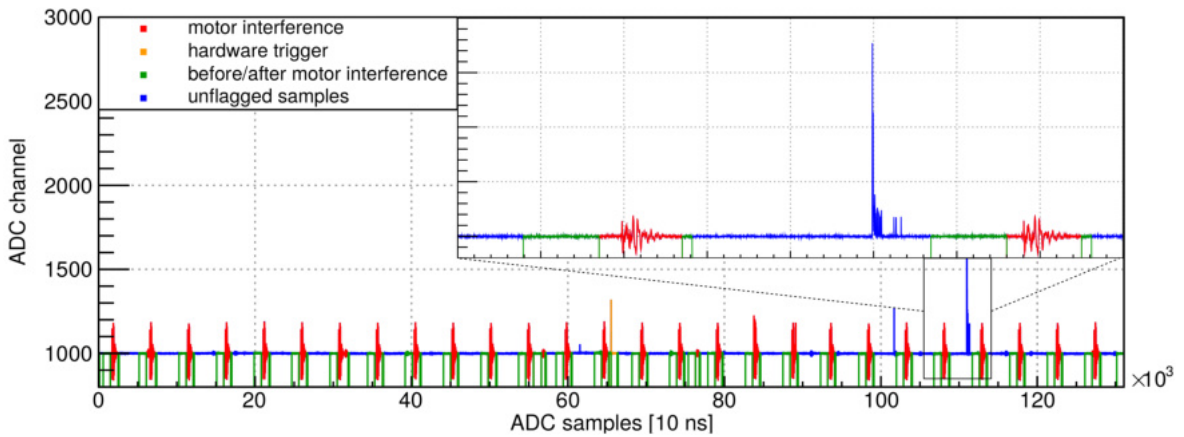


Figure 6.8: Pulse trace with flagged samples. The motor interference occurs with 20 kHz. The corresponding samples are not used for the further analysis. The hardware trigger is discarded as well. The samples before and after the motor interference can be used for the baseline determination and the signal event reconstruction. The software trigger can find signal events in the unflagged area. Originally published in [BDL⁺20].

The software trigger searches solely for signal events within the unflagged region. It is coded similarly to the hardware trigger and calculates the sum of two consecutive samples subtracted from the sum of the previous two samples. The trigger condition is fulfilled if the calculated difference is larger than 20 ADC channels. The software trigger is sensitive to single p.e. (photoelectron) events. The number of identified physical events N_{phys} by the software trigger is used for a correction of the signal efficiency in chapter 7.1.

The maximum length of the event window is chosen to be $8 \mu\text{s}$ which corresponds to 4.7 – 8 triplet lifetimes of LAr (see tab. 3.2). The cropping of events that are longer than $8 \mu\text{s}$ causes a reduction of the signal by 0.03 – 0.9%. The length of the event window is adjusted if the event is shorter than $8 \mu\text{s}$. The baseline is determined before and after the event for the length of $1 \mu\text{s}$. Two events can be differentiated if they are more than $1 \mu\text{s}$ apart, i.e. the last pulse of the predecessor event occurs at least $1 \mu\text{s}$ before the first pulse of the successor event.

The samples before each motor interference are flagged in order to prevent that long physical events start in the unflagged region and run into the motor interference, since such events have to be discarded. This happens more often for long signal events leading to a systematic bias of rejecting long events more frequently.

Therefore the flagged region before each motor interference is $9 \mu\text{s}$ long which is split into $8 \mu\text{s}$ for the event reconstruction and $1 \mu\text{s}$ for the baseline determination after a preceding event. The flagged region after each motor interference is $1 \mu\text{s}$ long which can be used for the baseline determination before the start of an event. Examples illustrating various cases are depicted in figure 6.9. With this method the fraction of events rejected due to running into a motor interference is below 0.2% as shown in table 6.3.

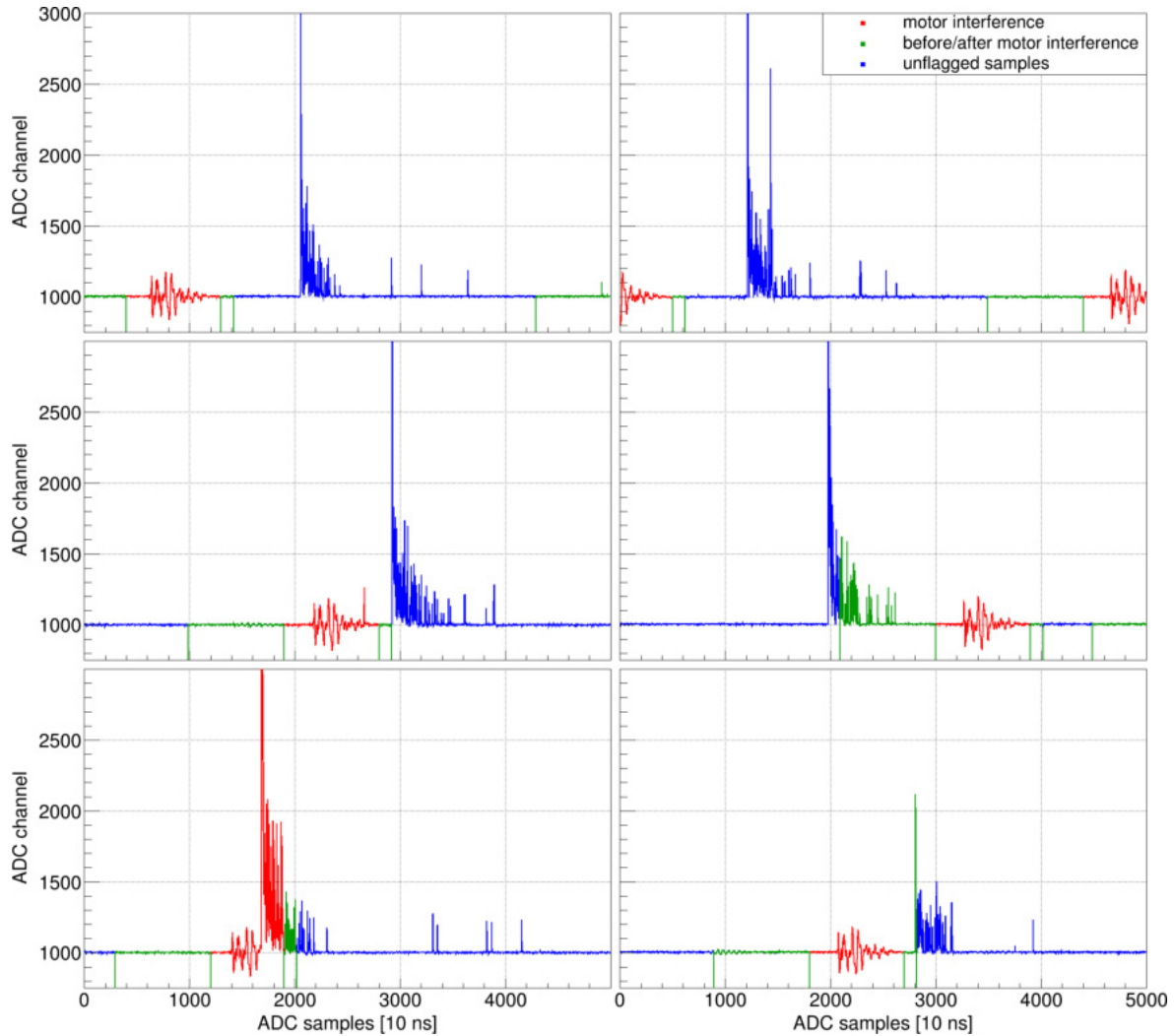


Figure 6.9: Examples of physical events that can be identified by the software trigger. (Top left) A long event with enough time before and after the event for the baseline determination. The three small events can be identified separately since they are more than $1\ \mu\text{s}$ apart. (Top right) Two long events starting shortly after each other. Since there is no space for the baseline determination in between, the two events are treated as one. (Middle left) The event starts right after the flagged area which provides enough space for the baseline determination, thus the event is accepted for the further analysis. (Middle right) The event starts in the unflagged region and runs into the flagged region before the motor interference, but not the flagged area of the motor interference itself. The space before the motor interference starts can be used for the baseline determination and the event is accepted for the analysis. (Bottom left) The events starts in the motor interference and runs into the unflagged region where it can be identified. It is discarded because it is overlaid with the motor interference. (Bottom right) The event starts in the flagged region after the motor interference and runs into the unflagged region. It is identified but discarded since there is not enough space for the baseline determination between the motor interference and the start of the event.

The position of the baseline determination before an event is fixed to be directly before the event. The baseline determination after an event can be shifted by a maximum of $10\ \mu\text{s}$ in cases where the baseline is not sufficiently smooth in the area directly after an event. The length of $1\ \mu\text{s}$ for the baseline determination stays unchanged in these cases. This method increases the fraction of the accepted events for the subsequent analysis. The ratio of discarded events due to a high variance of the baseline before or after an event is listed in table 6.3.

If the variance of the baseline before and after the identified physical event as well as their combination is sufficiently small, the pulse trace in the event window is integrated and the baseline level is subtracted. The number of the integrated events, i.e. the accepted events N_{acc} divided by the number of identified physical events N_{phys} is used for a correction of the signal efficiency in chapter 7.1. The correction factor $c = N_{\text{acc}}/N_{\text{phys}}$ is stable for all measuring points as shown in table 6.3. The resulting pulse integral enters a histogram which is created per measuring point as depicted in figure 7.1. The analysis of these histograms is described in chapter 7.

Table 6.3: For each measuring distance d the fraction of the overlapping pulse traces and the correction factor c is listed. The fraction of the discarded events is given separated by the rejection reason: (1) event and/or baseline is partly in a flagged area, (2) variance of baseline previous to the event is too high, (3) variance of baseline after the event is too high, (4) combined baseline is too high.

d [cm]	overlap [%]	c [%]	discarded events [%]			
			(1)	(2)	(3)	(4)
5.5	94.5	92.4	0.19	7.1	0.007	0.36
7.1	89.7	91.8	0.16	7.5	0.003	0.57
8.7	83.7	91.1	0.11	8.3	0.011	0.40
10.2	79.8	90.6	0.12	8.7	0.002	0.53
11.8	75.7	90.3	0.09	9.2	0.002	0.40
13.4	71.7	89.2	0.09	10.2	0.002	0.51
15.0	67.9	89.7	0.09	9.8	0.001	0.41
19.7	60.9	88.5	0.08	10.9	0.002	0.49
24.4	53.9	89.5	0.08	10.0	0.002	0.38
33.8	39.7	90.4	0.08	9.3	0.001	0.25
43.3	27.9	91.9	0.07	7.7	0.000	0.33
52.7	22.0	91.1	0.04	8.5	0.000	0.32

Chapter 7

Analysis of the attenuation measurement

The acquired data of the attenuation measurement is analyzed with the help of MC simulations. Therefore, a sophisticated simulation was developed in order to determine the solid angle correction as well as the background for the attenuation measurement. As described in chapter 4 and 5.3, the reflectivity of the steel of the attenuation setup is implemented in two different ways into the simulation. The initial analysis approach has been performed with the reflectivity of the IPF measurement and an extrapolation to the VUV region. The alternative analysis technique has been accomplished with the reflectivity derived from the combined measurements of IPF and PTB. Both versions are described in the following. They are denoted corresponding to the reflectivity used in the analysis, i.e. IPF and combined reflectivity. The analysis procedure with the IPF reflectivity has already been published in [BDL⁺20].

7.1 Measuring data

The data has been processed as described in chapter 6.3.1. The scintillation pulses have been integrated and entered a histogram for each measuring point as shown in figure 7.1. The constructed histograms are divided by the live time of each measuring point and corrected for the rejected events, respectively. The applied correction factor is the number of accepted events N_{acc} for the further analysis divided by the number of identified physical events N_{phys} by the software trigger: $c = N_{\text{acc}}/N_{\text{phys}}$.

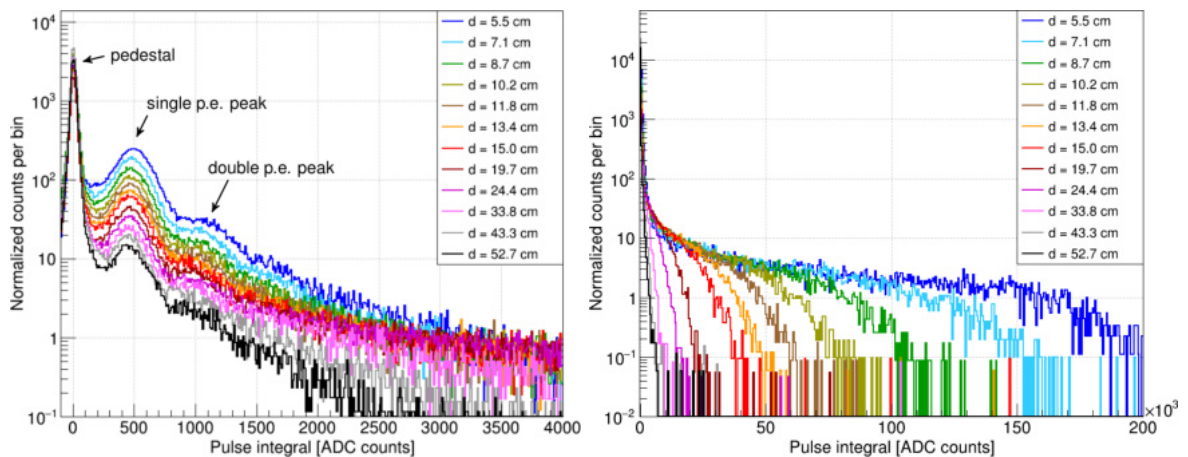


Figure 7.1: Pulse integral spectra of the attenuation measurement for various measuring points, normalized by the live time of the detection system and the ratio of accepted vs. identified physical events. The intensities of the single and double p.e. peaks drop with the distance (left) and the endpoints of the spectra shift to the left for larger distances (right). Originally published in [BDL⁺20].

With larger distances between ^{90}Sr source and PMT the endpoints of the spectra shift to lower values. Also the intensity of the single and double p.e. peaks drops. The height of the pedestal remains equal for all measuring distances, since it is caused by electronic noise triggers.

The light intensity for each measuring point is determined by integrating the spectra shown in figure 7.1. In order to correct the integral for pedestal effects, an understanding of the related noise source is necessary.

Noise sources in a PMT can have their origins in thermoelectron emission from the photocathode and the dynode system, leakage currents in the PMT anode circuit, electron autoemission by the electrodes, photon and ion feedbacks as well as external and internal radioactivity. Spurious signals with small amplitudes can occur in the PMT due to the incident photon flux on the photocathode. They can be caused by photoemission from the focusing electrodes and dynodes as well as p.e.s missing the first dynode [BBB⁺94].

These background processes can be assigned to two groups with different distribution functions. The first group shows a Gaussian distribution and covers the low charge processes (e.g. the leakage current) where no p.e. was emitted by the photocathode. Moreover, those effects are the reason for the non-zero width of the pedestal. The second group can be described by an exponential function and contains the discrete processes (e.g. thermoemission) which accompany the measured signal with a non-zero probability [BBB⁺94].

To correct for the noise that forms the pedestal, the low energy part of each spectrum is fit by a combination of two Gaussian functions for the single and double p.e. peak, respectively, and an exponential and a Gaussian function describing the pedestal. This procedure follows the description given in [BBB⁺94].

The corresponding formula of the combined fit is expressed in equation 7.1.

$$f(x) = \underbrace{e^{p_0+p_1 \cdot x} + p_2 \cdot e^{-\frac{(x-p_3)^2}{2 \cdot p_4^2}}}_{\text{pedestal}} + \underbrace{p_5 \cdot e^{-\frac{(x-p_6)^2}{2 \cdot p_7^2}}}_{\text{single p.e. peak}} + \underbrace{p_8 \cdot e^{-\frac{(x-2 \cdot p_6)^2}{2 \cdot p_9^2}}}_{\text{double p.e. peak}} \quad (7.1)$$

The fit is constrained by forcing the mean of the double p.e. peak to be exactly the mean value of the single p.e. peak multiplied by a factor of two. Its application to an example spectrum is depicted in figure 7.2. The local minimum of the valley between the pedestal and the single p.e. peak is determined with the help of the combined fit following equation 7.1. This minimum serves as a cut position, above which signals created by real light dominate. The measured light intensity per distance is calculated by integrating the histogram weighted by the respective p.e. value of each bin. The exponential part of the pedestal on the right side of this cut is subtracted from the integral and the Gaussian part of the single p.e. peak on the left side of this cut is added to the integral. The corrected integral is proportional to the number of photons that hit the PMT, i.e. the light intensity at the measuring point.

The measured light intensity I at the distance d between source and PMT is dependent on the initial light intensity and follows a Beer-Lambert law as discussed in chapter 3.2.3. Due to the unknown initial light intensity the data is analyzed relative to the nearest measuring point as expressed in equation 7.2. Therefore, the light intensity of the selected measuring point is divided by the reference point to achieve the distance difference Δd .

$$\frac{I(d)}{I(d_{\text{ref}})} = e^{-\Delta d / \alpha_{\text{att}}} \quad \text{with} \quad \frac{1}{\alpha_{\text{att}}} = \frac{1}{\alpha_{\text{abs}}} + \frac{1}{\alpha_{\text{scat}}} \quad (7.2)$$

Equation 7.2 does not include any background light source, hence an additional term must be added to account for the Cherenkov light created by the electrons emitted by the ^{90}Sr source. The background originated by Cherenkov light is determined with MC simulation studies of the setup developed for the attenuation measurement.

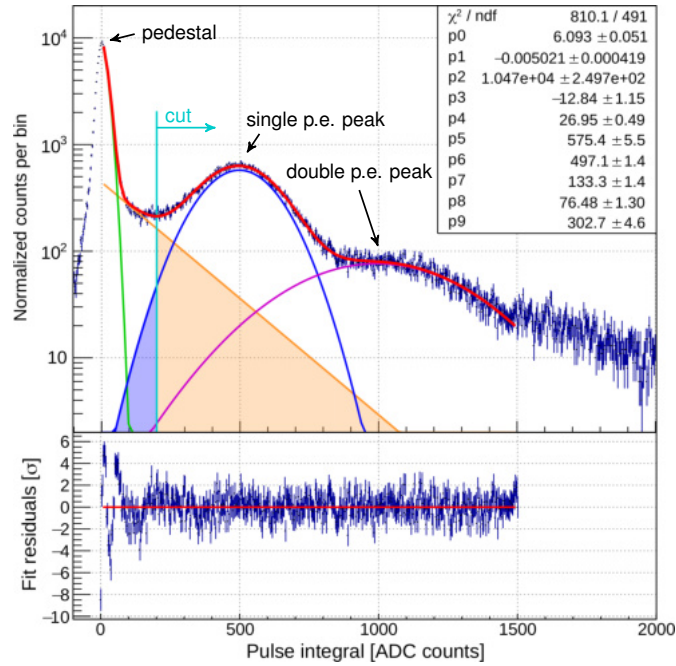


Figure 7.2: Example of a pulse integral spectrum with the combined fit (red) of the pedestal, single p.e. and double p.e. peak. The vertical line (light blue) marks the cut at the minimum of the valley between pedestal and single p.e. peak. The spectrum is integrated on the right side of this cut. This integral is corrected by subtracting the exponential part (orange) of the pedestal on the right side of the cut and adding the missing Gaussian part (dark blue) of the single p.e. peak on the left side. The fits of the spectra of the other measuring points are to be found in appendix A.1. Originally published in [BDL⁺20].

7.2 Simulation of the attenuation setup

The geometry of the attenuation setup is implemented in the simulation as indicated in figure 7.3. The length of the steel tube is reduced from its actual size to the range of the source movement, since the parts outside of the LAr volume filling the tube do not affect the propagation of the light inside the setup. Thus, the stepper motor and equivalent other parts are omitted in the simulation. For the PMT the photocathode is implemented as a 3.4 mm thick glass plate with the diameter corresponding to the active area of the PMT. The WLS is coated with a thickness of 5 μs directly on the photocathode glass. The other PMT parts are not considered in the simulation. The steel rings serving as light collimators as well as the source holder and the source with the active sample are implemented according to their real geometries. The vertical bars fixing the positions of the rings are omitted in the simulation. The steel rods which are connected to the source holder for the movement of the source are not taken into account as well. Since these parts are comparatively thin, their effect on the light propagation is expected to be negligible.

Figure 7.3 shows also the light propagation for two examples. The shape of the source holder constrains the light to expand in a certain direction. Most of the light is absorbed or reflected by the collimator rings or at the inner steel wall of the setup. The light that reaches the PMT is mainly direct light that was not scattered in the LAr or reflected at the steel of the setup. Still, the light propagation in the setup is investigated with MC simulations in detail to determine the solid angle correction per measuring point for the analysis of the attenuation data.

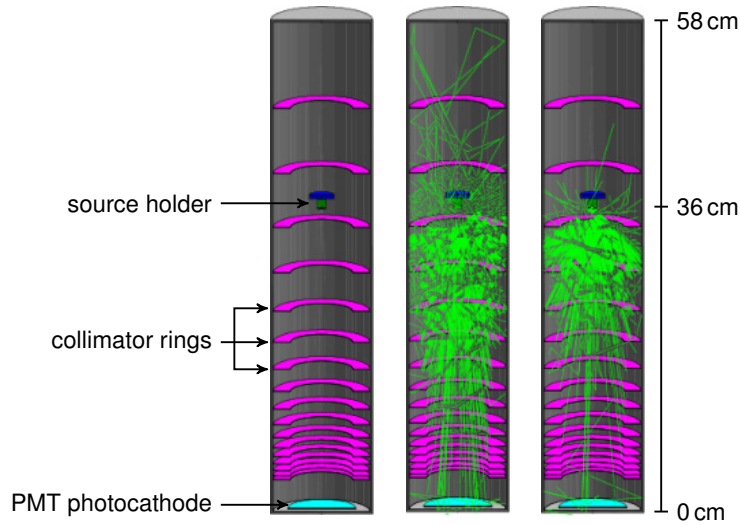


Figure 7.3: Schematic drawing of the setup as it is implemented in MaGe. The length of the steel tube is set to the actual adjustable distance range. The steel rods for the source movement are omitted. The source holder and the active sample are implemented according to their known geometries. The PMT is reduced to the photocathode on the bottom of the setup. The light propagation of two example events is shown. Most of the reflected light is absorbed by the collimator rings and mainly direct light hits the PMT.

7.3 Simulation with the IPF reflectivity

The IPF reflectivity is implemented as discussed in chapter 5.3.2. In the following the reflectivity value at 128 nm determines the reflectivity assumption curve (see fig. 5.4) chosen for the respective simulation study. The same applies to the diffuse reflectivity and its value at 100 nm is quoted. In the following sections the solid angle correction and Cherenkov background are determined dependent on the chosen reflectivity. The generated simulations for each reflectivity assumption are analyzed with the aim of reproducing the input value of the absorption length. In the analysis the reflectivity at 128 nm is treated as a free parameter that will be derived from comparisons between simulation and measured data.

7.3.1 Solid angle correction

To fit the attenuation data from equation 7.2, a solid angle correction has to be applied for each measured intensity. This solid angle correction is dependent on the distance between source and PMT since for larger distances the irradiated solid angle of the PMT decreases. MC simulations were performed to investigate the influence of other effects and take them into account for the determination of the solid angle correction making it non-trivial.

As discussed in chapter 6.1.3, the electrons emitted by the ^{90}Sr source can travel a few millimeters in LAr producing the scintillation light along their path. This reduces the effective distance scintillation and Cherenkov photons need to travel to reach the PMT on a straight path. Even more critical, bremsstrahlung photons created by the electrons inside the source holder or the source itself can travel much farther in the setup. They trigger further electrons anywhere in the setup which can in turn create scintillation light far away from the actual ^{90}Sr source. This leads to an extended virtual source of scintillation photons that is anything but point-like. Even if the contribution of this effect is not large as shown in figure 6.7, it does alter the length of the traveled path of the scintillation photon from its origin position until hitting the PMT.

The path length traveled by the scintillation photon can be elongated when the photon Rayleigh scatters inside the LAr or is reflected at the steel surface. This is also true for Cherenkov photons and especially important since the reflection probability is much higher in the visible region. All these processes increase the uncertainty of the distance which the scintillation photon traveled before it gets detected by the PMT.

Additionally, the emission of the WLS is isotropically and the shifted photons have a much longer range in LAr as well as a higher probability to get reflected at steel. Thus, wavelength shifted photons can reach the PMT via scatterings in the LAr or reflections at the steel surface. These photons contribute to the overall detected light, thus altering the solid angle correction.

With the help of MC simulations the solid angle correction factor is determined for each measuring point taking into account all these effects. To remove the influence of the absorption of light in LAr and only investigate geometrical effects, the absorption length has been set to 1 km for these simulations. Consequently, the effect of the scattering is covered by the solid angle correction and the absorption length can be directly retrieved from a fit of the solid angle corrected light intensity with a formula similar to equation 7.2.

The effective distance a scintillation photon traveled from its point of origin until hitting the WLS is determined for each scintillation photon that triggered the PMT. This is also true for the case when the wavelength shifted photon is emitted back into the LAr but nevertheless finally triggered the PMT.

As shown in figure 7.4 on the left the effective distance and its uncertainty increase with the reflectivity assumption at 128 nm as expected from the effects discussed above. Various simulation parameters have been altered to investigate their influence on the solid angle correction. Figure 7.4 shows two examples. While the solid angle correction factor depends on the reflectivity assumption at 128 nm, it is not affected by the LAr scintillation light yield. The influence of other investigated parameters is shown in the appendix A.2, figures A.4 – A.11. As a result, the further analysis is performed dependent on the reflectivity at 128 nm.

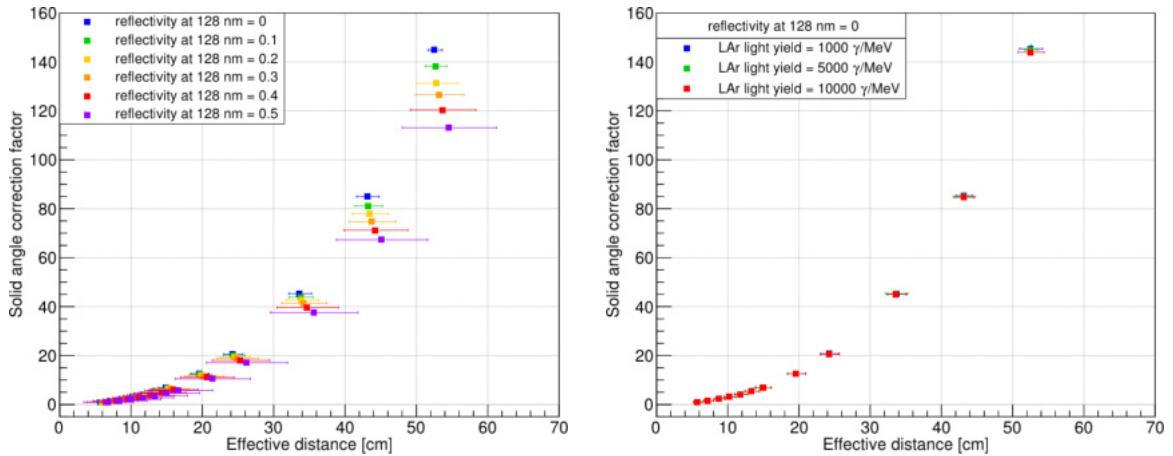


Figure 7.4: Solid angle correction factors for various reflectivity assumptions and LAr light yields. The solid angle correction varies with the chosen reflectivity and the distance and its uncertainty grows with the reflectivity since more photons can travel longer paths in LAr due to the higher reflection probability. The solid angle correction is independent of the LAr light yield for 0% reflectivity at 128 nm. The corresponding plots for other investigated parameters are shown in figures A.4 – A.11. Originally published in [BDL⁺20].

7.3.2 Cherenkov background

In the experimental data it cannot be distinguished if a PMT hit was caused by a scintillation photon or a Cherenkov photon. Consequently, all PMT hits will be solid angle corrected regardless of their origin. The background contribution of the Cherenkov light is investigated similarly to the determination of the solid angle. However, in this case only photons that were created by the Cherenkov effect and triggered the PMT are taken into account. This also includes Cherenkov photons that are converted by the WLS to the visible region and trigger the PMT after being reflected or scattered inside the setup.

Figure 7.5 depicts the already solid angle corrected Cherenkov background relative to the nearest measuring point. The distance difference Δd is calculated by subtracting the distance of the reference measuring point from the others, respectively. On the left side the influence of varying reflectivities at 128 nm can be seen, while the right side shows that the Cherenkov background is independent on the chosen LAr light yield. After applying the solid angle correction it can happen that the observed dependence of the solid angle correction can be strengthened or mitigated in the relative Cherenkov background. For instance, the relative Cherenkov background reveals an even wider spread for the different reflectivity values at 128 nm than the applied solid angle correction factor. The other investigated parameters are shown in figures A.4 – A.11.

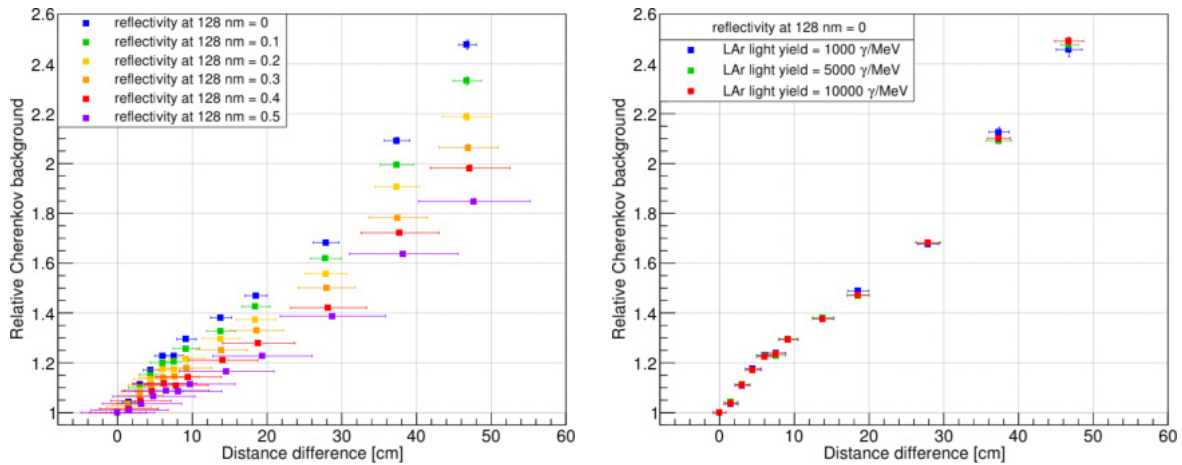


Figure 7.5: Relative Cherenkov background for various reflectivity assumptions and LAr light yields. It is dependent on the selected reflectivity, but not affected by the chosen LAr light yield. The relative Cherenkov background increases with the distance due to the high reflectivity of the steel in the visible region. The corresponding plots for other investigated parameters are shown in figures A.4 – A.11. Originally published in [BDL⁺20].

An analytical description of the Cherenkov background is necessary to include it in equation 7.2 and construct a combined fit of signal and background in the attenuation data. It was found that the expression in formula 7.3 describes the relative Cherenkov background $b(\Delta d)$ well for any reflectivity assumption at 128 nm. In figure 7.6 an example for the application of this fit is depicted.

$$b(\Delta d) = p_0 + p_1 \cdot \Delta d + p_2 \cdot (\Delta d)^2 + p_3 \cdot (\Delta d)^3 \quad (7.3)$$

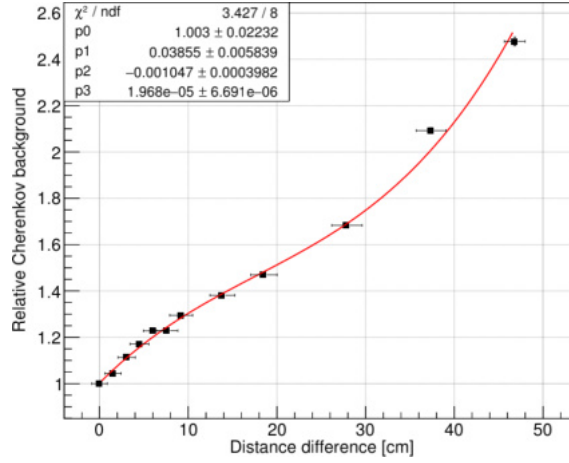


Figure 7.6: Polynomial fit of the relative Cherenkov background with the already applied solid angle correction for a reflectivity of 0% at 128 nm. The Cherenkov background is normalized by the first measuring point and plotted versus the distance difference Δd between the first and the other measuring points. Originally published in [BDL⁺20].

7.3.3 Analysis procedure

The combined fit $f(\Delta d)$ includes the signal s from the scintillation photons and the background b caused by the Cherenkov light. At first, the fit of the Cherenkov background (eq. 7.3) is performed which enters the combined fit with its resulting parameters fixed. Afterwards the combined fit is applied to the relative light intensity which is already corrected by the solid angle. The combined fit formula is expressed in equation 7.4 and its application is depicted in figure 7.7 for simulation data.

$$f(\Delta d) = s_{\text{rel}} \cdot s(\Delta d) + (1 - s_{\text{rel}}) \cdot b(\Delta d) \quad (7.4)$$

$$s(\Delta d) = e^{-\Delta d / \alpha_{\text{abs}}} \quad (7.5)$$

The fit parameter s_{rel} denotes the signal strength relative to the overall detected light intensity of signal and background. It gives an indication of the LAr scintillation light yield, i.e. a high value of s_{rel} is associated with a high LAr light yield. Physical results of s_{rel} need to be within 0 and 1, whereas $s_{\text{rel}} = 0$ would be interpreted as no observed signal, i.e. only Cherenkov light was detected, and $s_{\text{rel}} = 1$ would mean, that the measured light intensity would be solely composed of scintillation light. The fit parameter α_{abs} gives the resulting value for the absorption length in cm.

Simulation analysis

To probe the analysis technique a series of MC simulations was generated with varying combinations of input parameter values. For this purpose the absorption length was varied within 10 – 30 cm and the LAr light yield between 1000 – 10000 γ/MeV for each reflectivity assumption shown in figure 5.4. These simulations are analyzed with the same algorithms used for the measuring data aiming to retrieve the original input parameter values.

As depicted in figure 7.7 the influence of the Cherenkov light is clearly visible in case of a low LAr light yield and a short absorption length. It is expressed as an increase of the relative light intensity for larger distances. On the contrary, the absorption causes the decrease of the relative light intensity. Hence, if the contribution of the Cherenkov light is very small, the light intensity drops to ever lower values for larger distances and does not rise again.

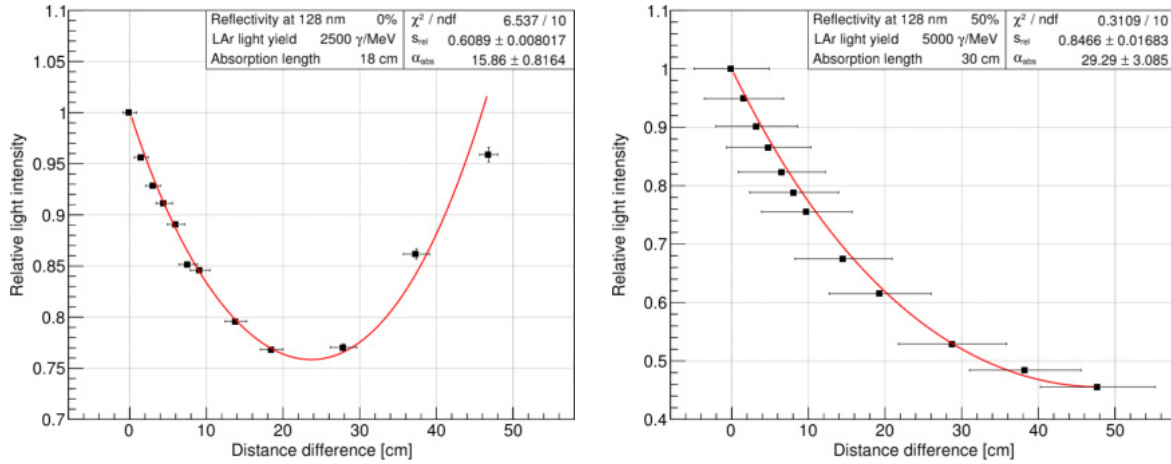


Figure 7.7: Relative light intensity observed in two simulation examples with various input parameters. For low light yields (left), the Cherenkov light is dominating at the larger distances and the relative light intensity grows. This effect cannot be observed for higher light yields (right). More examples are shown in figures A.12 and A.13. Originally published in [BDL⁺20].

The lower the light yield is, the stronger gets the contribution of the Cherenkov light and the relative light intensity rises sooner, i.e. already at smaller distances.

The larger uncertainties on the distance difference in figure 7.7 on the right side are a direct consequence of the applied solid angle correction, caused by the higher reflectivity leading to longer path lengths of the scintillation photons. This also leads to a much smaller χ^2 of the combined fit than for the low reflectivity example.

The parameter s_{rel} changes strongly with the different LAr light yields, but it is also influenced by the absorption length, i.e. larger values increase s_{rel} slightly. Depending on all the other parameters, the simulation input value for the absorption length can be retrieved very well, as it is the case in the example in figure 7.7 on the right side. In other cases the fit parameter has a small offset compared to the simulation input value. This happens especially when the light yield is high and the absorption length is small or the other way around. Since both are affected by impurities in LAr it is expected that both have either a low or high value.

More examples with various combinations of reflectivity, LAr light yield and absorption length can be found in appendix A.2, figures A.12 and A.13.

Measured data analysis

The same analysis technique evaluated for the simulation is applied to the measured data. The solid angle correction and the Cherenkov background are determined for each reflectivity assumption at 128 nm (see fig. 5.4). The data is then analyzed with each solid angle correction and the combined fit (eq. 7.4) is applied using the respective Cherenkov background fit of the corresponding simulation. The fits for all reflectivity assumptions are shown in the appendix, figures A.16 and A.17. The fit parameter results of the combined fit for the data are listed in table 7.1.

The parameter α_{abs} decreases clearly with larger reflectivities, while s_{rel} only shrinks slightly. This can be explained by a larger contribution of the Cherenkov light at higher reflectivities. Additionally, the uncertainties of both parameters grow with the reflectivity which is a direct consequence of the increasing distance uncertainties. The same behavior is observed for the simulations, which is discussed in section 7.3.4.

Table 7.1: Fit parameter results of the combined fit of the data with solid angle corrections of the various reflectivity assumptions at 128 nm.

reflectivity	s_{rel}	α_{abs} [cm]
0	0.6096 ± 0.0078	15.79 ± 0.70
0.01	0.6044 ± 0.0082	15.21 ± 0.85
0.05	0.6004 ± 0.0085	15.40 ± 0.83
0.1	0.6021 ± 0.0097	15.13 ± 0.89
0.2	0.5879 ± 0.0131	13.94 ± 1.12
0.3	0.5868 ± 0.0142	13.94 ± 1.37
0.4	0.5811 ± 0.0190	13.15 ± 1.74
0.5	0.5851 ± 0.0227	12.50 ± 2.08

Since the data fit results for the different reflectivity assumptions vary, the following analysis procedure is developed in order to determine one reflectivity assumption that sticks out, i.e. matches the acquired data better than the others. In order to achieve this, a combination of simulation input parameters is searched for that matches the behavior of the data when analyzing it with the solid angle corrections of each reflectivity assumption.

7.3.4 Determination of the best matching simulation input parameters

The best matching simulation is determined by generating simulations with different combinations of input parameters, i.e. iteratively varying the absorption length and light yield. The solid angle correction of the respective reflectivity assumption is used. The combined fit (eq. 7.4) is applied to these simulations and the fit parameters s_{rel} and α_{abs} are compared to the fit results of the data for the corresponding reflectivity assumption. This is done for each reflectivity assumption separately. The comparison is based on a χ^2 calculation for the two fit parameters as expressed in equation 7.6.

$$\chi^2 = \frac{(s_{\text{rel, sim}} - s_{\text{rel, data}})^2}{(\Delta s_{\text{rel, sim}})^2 + (\Delta s_{\text{rel, data}})^2} + \frac{(\alpha_{\text{abs, sim}} - \alpha_{\text{abs, data}})^2}{(\Delta \alpha_{\text{abs, sim}})^2 + (\Delta \alpha_{\text{abs, data}})^2} \quad (7.6)$$

Low values of χ^2 are interpreted as well matching, while higher values indicate a wider spread of the fit parameter results between simulation and data. An example of the fit parameter comparison for the reflectivity assumption of 0% at 128 nm is shown in figure 7.8. In this case, the χ^2 values indicate clearly the best matching simulation input parameters to be an absorption length of 18 cm and a LAr light yield of 2500 γ/MeV . The corresponding plots for the other reflectivity assumptions can be found in appendix A.2, figures A.14 and A.15. The respective best matching simulation input parameters are listed in table 7.2 for each reflectivity assumption. They are both decreasing with larger reflectivities as it is the case for the data.

Since the solid angle correction is dependent on the reflectivity assumption at 128 nm, the effect on the fit parameters s_{rel} and α_{abs} is studied by applying a solid angle correction determined with a certain reflectivity on a simulation using a different reflectivity assumption. Therefore the solid angle correction of every reflectivity assumption is applied to the best matching simulation of each reflectivity assumption.

The resulting values of the fit parameters s_{rel} and α_{abs} for each of these cases of simulations analyzed with different solid angle corrections are depicted in figure 7.9. The relative signal strength s_{rel} is correlated to the effective light yield observed in the simulation and decreases slightly if the reflectivity used in the applied solid angle correction increases.

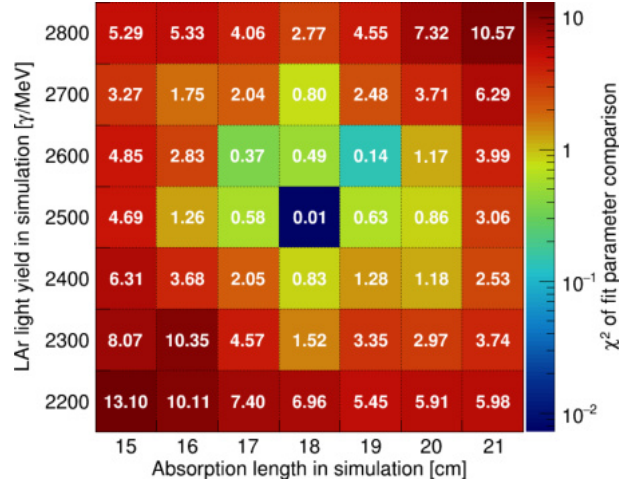


Figure 7.8: Results of the χ^2 comparison of the fit parameters s_{rel} and α_{abs} of data and simulation for the reflectivity assumption 0% at 128 nm. The lower the χ^2 value, the better are matching both fit parameters. In this case the simulation input parameters with an absorption length of 18 cm and a LAr light yield of 2500 γ/MeV are favored. The plots for the other reflectivity assumptions are depicted in figures A.14 and A.15.

Table 7.2: Best matching simulation input parameters determined by the comparison with the data for each reflectivity assumption. The corresponding simulations are analyzed with the solid angle corrections of each reflectivity assumption to determine which reflectivity assumption matches best to the data (see fig. 7.9).

reflectivity	LAr light yield [γ/MeV]	abs. length [cm]
0	2500	18
0.01	2400	17
0.05	2300	17
0.1	2150	17
0.2	1750	15
0.3	1550	14
0.4	1400	13
0.5	1300	12

The obtained value of α_{abs} tends to underestimate the corresponding simulation input value when analyzing the simulation with a solid angle correction using a low reflectivity. The fit value of α_{abs} gets closer to the input value for higher LAr light yields and higher reflectivities due to the decreasing influence of the Cherenkov effect.

In figure 7.9 black frames mark the fit parameter values of the simulation that match the fit results of the experimental data within their uncertainties. In the best case a horizontal line of black frames would mark the simulation generated with a certain reflectivity on the left axis that matches the data when analyzed with all different solid angle corrections.

Since the fit parameters s_{rel} and α_{abs} depicted in figure 7.9 are not considered individually, but both need to match the data, they are compared to the data fit results by using the χ^2 calculation in equation 7.6. The resulting χ^2 values for each case are shown on the left side and the projection of χ^2 on the left axis, i.e. the best matching simulation determined for each reflectivity assumption, is shown on the right side in figure 7.10. The projection of the χ^2 values clearly indicate that the simulations for low reflectivities up to 5% at 128 nm match the data much better than the other reflectivity assumptions.

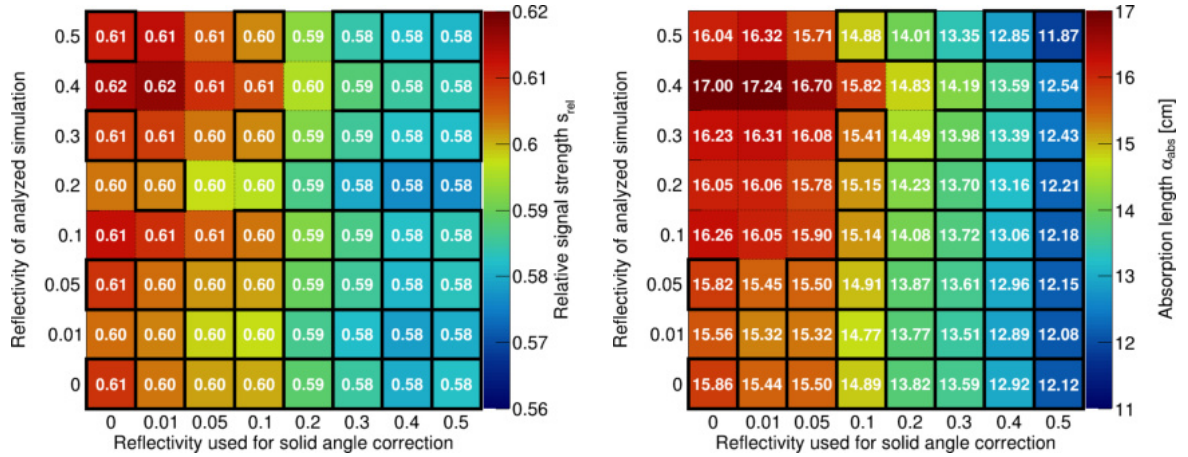


Figure 7.9: Values of the fit parameters s_{rel} (left) and α_{abs} (right) of the combined fit of the best matching simulations of each reflectivity assumption analyzed with each solid angle correction of all reflectivity assumptions. The black frames mark the values that match with the fit results of the experimental data within their uncertainties. Since the distance uncertainties in the solid angle correction propagate on the fit parameter values and they get larger for higher reflectivity assumptions, almost all simulations are marked as matching for the solid angle corrections generated with high reflectivities. A simulation (left axis) behaves like the experimental data when analyzed with all reflectivity assumptions (bottom axis) in the case, when there is a horizontal line of black marked frames. Originally published in [BDL⁺20].

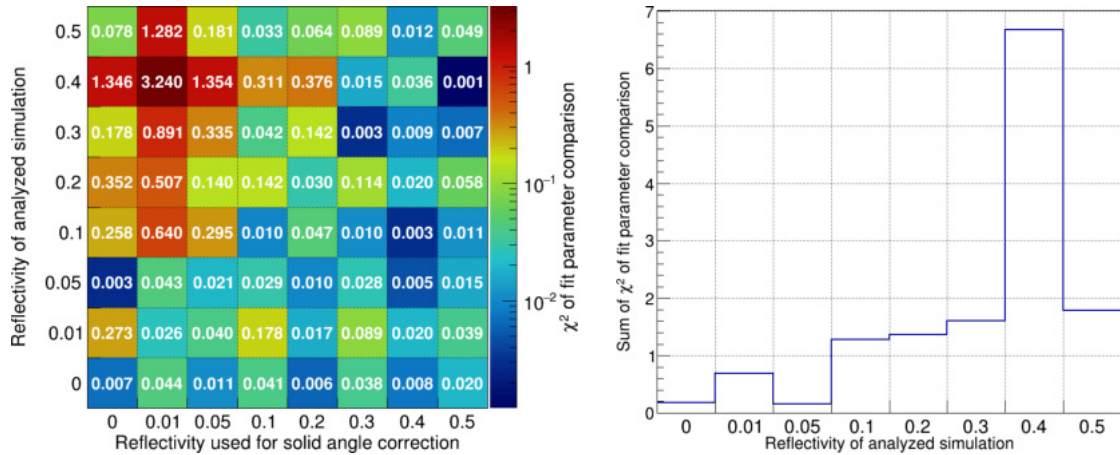


Figure 7.10: χ^2 values of the comparison of data and best matching simulation fit results when applying solid angle corrections of various reflectivities. Due to the larger uncertainties of the fit parameter values, χ^2 tends to be lower for the higher reflectivities. The projection on the left axis, i.e. the sum of the χ^2 values is depicted on the right side. The best matching simulations generated with 0% and 5% reflectivity at 128 nm describe the data much better than the other reflectivity assumptions.

7.3.5 Comparison of simulation and experimental data

The best matching reflectivities are determined with the help of the χ^2 values depicted in figure 7.10. While the 0% and 5% reflectivity at 128 nm describe the data very well, χ^2 is slightly lower for 0% reflectivity. Hence, the simulation that matches the data best is generated with an absorption of 18 cm, an LAr light yield of 2500 γ /MeV and a reflectivity assumption of 0% at 128 nm. The combined fit of this simulation in comparison with the data is shown in figure 7.11.

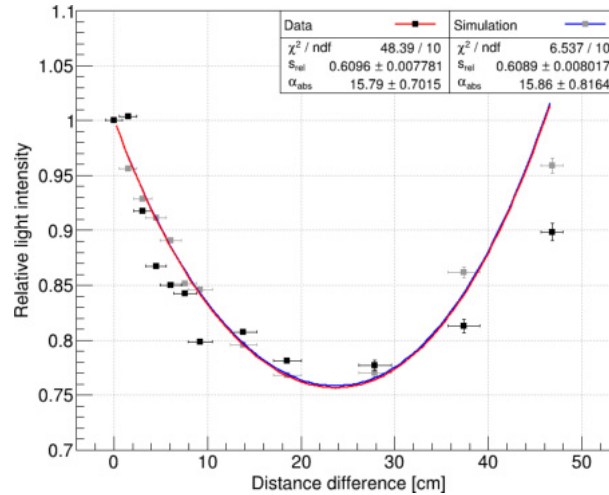


Figure 7.11: Comparison of the combined fits of the experimental data and the best matching simulation generated with an absorption of 18 cm, a LAr light yield of 2500 γ /MeV and a reflectivity assumption of 0% at 128 nm.

The fit parameter results of the best matching simulation and the measured data agree very well, although the experimental data points scatter much more, causing the reduced χ^2 to be much larger than for the simulation.

Nevertheless, the behavior of the data points clearly indicate that the Cherenkov light significantly contributes to the overall detected light, i.e. that the absorption length and LAr light yield are low as suggested by the fit results.

7.3.6 Systematic uncertainties

Systematic uncertainties of the absorption length retrieved from the measured data for an assumption of 0% reflectivity at 128 nm are investigated by generating the solid angle correction with different values of simulation input parameters and analyzing the data with the obtained solid angle correction. In the case the solid angle correction and the corresponding Cherenkov background are influenced by the various values of the simulation input parameters, the systematic uncertainty caused by this parameter is retrieved by calculating the difference of the resulting absorption length to original value. The simulation input parameters are varied within their systematic uncertainties as summarized in table 7.3.

As discussed in section 7.3.1 the solid angle correction and the Cherenkov background strongly change with the used reflectivity assumption at 128 nm (see also fig. A.4). Since the reflectivity assumptions of 0% and 5% at 128 nm both match well with the data, but the reflectivity of 0% fits the data slightly better, the data was analyzed with the reflectivity of 5% for the determination of the systematic uncertainty caused by the used reflectivity assumption.

The distance is conservatively changed according to its systematic uncertainty expressed in equation 6.1. The shrinking of the setup due to the operation in cryogenic temperatures causes the distance to get smaller, hence it is only taken into account for the systematic uncertainty corresponding to the minimum value of the distance. This leads to a systematic uncertainty of $\Delta d = {}^{+2.3}_{-2.4}$ mm for the closest measuring point and $\Delta d = {}^{+2.3}_{-3.9}$ mm for the farthest. As shown in figure A.5 the solid angle correction is affected by the distance uncertainty.

Table 7.3: List of simulation input parameters that were changed from their default values to a minimum and maximum value to investigate potential systematic uncertainties caused by a dependence of the solid angle correction on varying values of certain simulation input parameters. The solid angle correction is dependent on the simulation input parameters in the top rows, while this is only true for reflectivities larger than 0% for the middle row. The simulation parameters in the bottom row do not affect the solid angle correction. The corresponding plots are shown in figure A.4 – A.11.

parameter	default value	min. value	max. value
reflectivity at 128 nm	0%	–	5%
distance	d	$\Delta d = \pm 0.1 \text{ cm} \pm 0.127 \text{ cm} - 0.003 \cdot d[\text{cm}]$	
scattering length at 128 nm	70 cm	43 cm	104 cm
PMT diameter	64 mm	–	76 mm
WLS yield	1.2	–	1.5
reflectivity ratio at 100 nm	0.81	0.60	1.00
LAr light yield	5000 γ/MeV	1000 γ/MeV	10000 γ/MeV
PMT efficiency	Hamamatsu	LAr veto	WArP

The larger spread of the data points in figure 7.11 could be caused by the stepper motor responsible for the source movement. It has been tested at room temperature, hence the width of the step is expected to be smaller when operating in cryogenic temperatures. But since the step length at cryogenic temperatures could not be measured, the systematic uncertainty from this effect is unknown and not taken into account.

The scattering length significantly changes over the width of the scintillation peak as shown in figure 5.2. It is $\alpha_{\text{scat}}(122 \text{ nm}) = 43 \text{ cm}$ and increases to $\alpha_{\text{scat}}(134 \text{ nm}) = 104 \text{ cm}$. The scattering length is adapted to these values at 128 nm and its influence on the solid angle correction is investigated. As depicted in figure A.6 the solid angle correction and the Cherenkov background are changing greatly with the different values of the scattering length.

The PMT used for the attenuation measurement (see ch. 6.1.4) has a minimum active area with a diameter of 64 mm [Ham09]. However, the PMT itself has a diameter of 76 mm which is used as a maximum value of the possible active diameter of the PMT. This is a conservative estimation since it is expected that the efficiency of the PMT drops near the edge. The active PMT diameter influences the resulting solid angle correction and the corresponding Cherenkov background as shown in figure A.7.

The WLS yield is changed according to the measurements discussed in chapter 6.1.4. The different values of the WLS yield do not seem to affect the solid angle correction, but a small difference in the Cherenkov background can be observed (see fig. A.8).

Consequently, the influence of the systematic uncertainties of the reflectivity assumption, distance, scattering length, PMT diameter and the WLS yield on the solid angle correction are considered for the systematic uncertainty of the absorption length.

The reflectivity ratio of diffuse to total reflectivity is varied according to the curves shown in figure 5.4 and denoted by the respective value at 100 nm. As depicted in figure A.9 the solid angle correction and the Cherenkov background are obviously independent of the reflectivity ratio for a reflectivity of 0% at 128 nm, which is not the case for higher reflectivities. Since the best matching simulation was determined with a reflectivity of 0% at 128 nm, the reflectivity ratio is not considered further for the investigation of the systematic uncertainties.

The LAr light yield was arbitrarily changed to lower and higher values. The determination of the solid angle correction with MC simulations is purposely constructed in a way to be independent of the LAr light yield, since it is unknown at the time of the accomplishment of the attenuation measurement in the GERDA cryostat.

Since the LAr light yield does not affect the creation of Cherenkov light, the Cherenkov background is also independent of the LAr light yield as shown in figure A.10.

The PMT efficiency curve is changed to the ones obtained from the other measurements depicted in figure 5.6. Since it is the last instance an optical photon has to pass in the simulation, the detected light intensity in the simulation scales linearly with the PMT efficiency. Thus, it has no effect on the solid angle correction as shown in figure A.11 due to the relative analysis of the observed light intensity.

Accordingly, the LAr light yield and the PMT efficiency are not taken into account for the systematic uncertainty of the absorption length.

For all other investigated systematic uncertainties, the difference of the obtained absorption length compared to the default value is calculated. In some cases the resulting systematic uncertainty goes in only one direction. A complete list is given in table 7.4. Since the systematic uncertainties $\Delta\alpha_{\text{abs},i}$ retrieved from the respective simulation input parameters are uncorrelated, they are added as expressed in equation 7.7.

$$\Delta\alpha_{\text{abs}} = \sqrt{\sum_i (\Delta\alpha_{\text{abs},i})^2} \quad (7.7)$$

Table 7.4: List of simulation input parameters affecting the solid angle correction and the resulting impact on the systematic uncertainty of the absorption length.

simulation input parameter	syst. uncertainty
steel reflectivity	−0.4 cm
distance	+1.4 −1.4 cm
scattering length	+0.2 −0.5 cm
efficient area of the PMT	−2.7 cm
WLS yield	−1.5 cm

7.3.7 Result

The resulting absorption length retrieved with the reflectivity assumptions below 200 nm is given in equation 7.8. The attenuation length can be calculated according to equation 3.7. The values are obtained with the help of MC simulations with the assumption of a scattering length of 70 cm and a steel reflectivity of 0% at 128 nm.

$$\alpha_{\text{abs}} = 15.8 \pm 0.7(\text{stat.})_{-3.5}^{+1.4}(\text{syst.}) \text{ cm} \quad (7.8)$$

$$\alpha_{\text{att}} = 12.9 \pm 0.5(\text{stat.})_{-2.5}^{+1.0}(\text{syst.}) \text{ cm} \quad (7.9)$$

The statistical uncertainty is given by the uncertainty on the fit result of α_{abs} as shown in figure 7.11. The major contribution is caused by the uncertainty on the effective distance a scintillation photon travels from its origin until reaching the WLS on the PMT (relative uncertainty: 10.6% for the closest distance, 1.9% for the farthest distance).

Another contribution to the fit result uncertainty arises from the statistics of the simulations performed for the determination of the solid angle correction, which get poorer for the larger distances (relative uncertainty: 0.1% for the closest distance, 0.8% for the farthest distance).

The systematic uncertainty is derived from the investigations of the influence of varying simulation input parameters on the solid angle correction as discussed in section 7.3.6.

7.4 Simulation with the combined reflectivity

The combined reflectivity is implemented in the simulation between 120 nm and 800 nm as shown in figure 4.16. The following analysis procedure is very similar as described in section 7.3 for the implementation of the measured reflectivity by the IPF and the reflectivity assumptions below 200 nm. However, the analysis is much easier, since it is not dependent on the various reflectivity assumptions.

7.4.1 Solid angle correction, Cherenkov background and data analysis

The solid angle correction and the Cherenkov background are generated in the same way as for the IPF reflectivity as discussed in sections 7.3.1 and 7.3.2. The corresponding plots in appendix A.3, figures A.18 – A.20, show that the solid angle correction and the Cherenkov background behave extremely similar like for the reflectivity assumption of 25% at 128 nm for the IPF reflectivity shown in figures A.4 – A.11.

A set of simulations with varying combinations of input parameters of absorption length and LAr light yield is generated and analyzed with the solid angle correction of the combined reflectivity. The influence of the Cherenkov background looks similar as discussed before. The achieved fit results of the combined fit are reproducing the absorption length very well if absorption length and LAr light yield are both low or high as shown in figure A.21. For other combinations of absorption length and LAr light yield the behavior is similar as discussed for the reflectivity assumptions (see fig. A.16 and A.17).

The Cherenkov background is fit with the polynomial in equation 7.3 and the solid angle correction is applied to the data. The combined fit (eq. 7.4) of the data is shown in figure 7.13.

7.4.2 Determination of the best matching simulation input parameters

The best matching simulation input parameters are determined with the same procedure as described in section 7.3.4, however, here this is done solely for the combined reflectivity. The corresponding plot of the χ^2 values calculated with equation 7.6 is shown in figure 7.12.

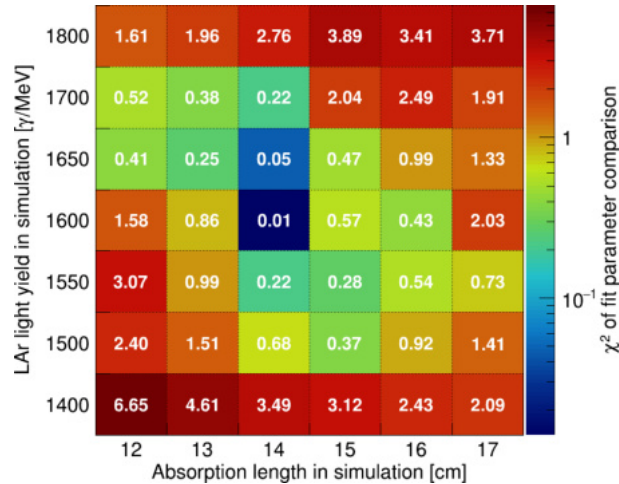


Figure 7.12: Results of the χ^2 comparison of the fit parameters s_{rel} and α_{abs} of data and simulation for the combined reflectivity. The simulation input parameters with an absorption length of 14 cm and a LAr light yield of 1600 γ/MeV are favored.

The resulting best matching simulation input parameters for the combined reflectivity are an absorption length of 14 cm and a LAr light yield of 1600 γ /MeV. These values are very near to the results derived from the reflectivity assumptions of 20% and 30% as listed in table 7.2. The combined reflectivity is 23% at 128 nm (see fig. 4.16). On the contrary, the reflectivity assumption of 0% at 128 nm yields different matching values of absorption length and light yield as shown in table 7.2.

This leads to the conclusion, that the shapes of the reflectivity curve assumptions depicted in figure 5.4 and the combined reflectivity shown in figure 4.16 are not important, but the reflectivity value at 128 nm is decisive.

7.4.3 Comparison of simulation and experimental data

The combined fits of the measured data and the best matching simulation with the applied solid angle correction obtained with the combined reflectivity are shown in figure 7.13. Both fits feature the same trend as the fit for the reflectivity assumption of 30% shown in figure A.17. The data points scatter more than the simulation points as discussed before, however, the effect is much smaller for the combined reflectivity. As a result, the reduced χ^2 of the fit of the experimental data is almost one.

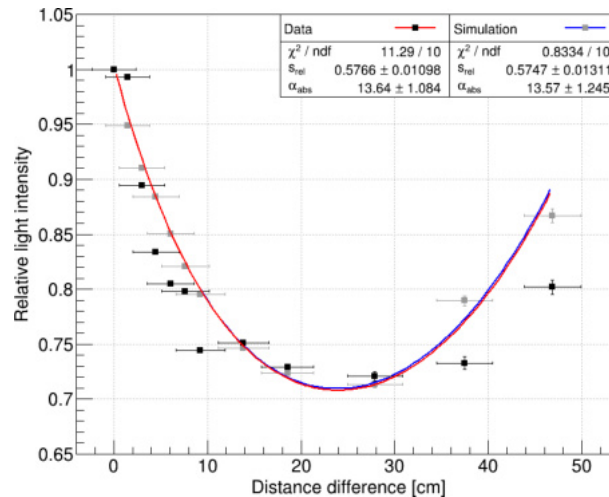


Figure 7.13: Comparison of the combined fits of the experimental data and the best matching simulation generated with an absorption length of 14 cm, a LAr light yield of 1600 γ /MeV for the combined reflectivity.

7.4.4 Systematic uncertainties

The systematic uncertainties of the absorption length are determined identically to the description given in section 7.3.6. The solid angle correction is calculated by changing the simulation input parameters within their systematic uncertainties listed in table 7.3 with exception of the reflectivity and the reflectivity ratio. These are compiled in table 7.5 for the combined reflectivity.

Since the simulation input parameters of reflectivity and reflectivity ratio at 128 nm both influence the solid angle correction as shown in figure A.18, they are taken into account for the determination of the systematic uncertainty of the absorption length. The dependence of the solid angle correction on the other investigated parameters is the same as described in section 7.3.6.

Table 7.5: Systematic uncertainties of simulation input parameters for the combined reflectivity. They are changed for the investigation of potential systematic uncertainties propagated on the solid angle correction. The other investigated parameters are listed in table 7.3. The solid angle correction is dependent on both, the reflectivity at 128 nm and the ratio of the diffuse versus the total reflectivity. The corresponding plots are shown in figure A.18 – A.20.

parameter	default value	min. value	max. value
reflectivity at 128 nm	23%	20%	25%
reflectivity ratio at 128 nm	0.63	0.35	0.77

The solid angle correction achieved with the combined reflectivity is applied to the data. The systematic uncertainty of the absorption length is determined by calculating the difference between the absorption length obtained with the solid angle correction generated with the default input parameters and their values changed to the minimum and maximum values given in table 7.3 and 7.5. The resulting systematic uncertainties of the absorption length are summarized in table 7.6 and added as expressed in equation 7.7 since they are uncorrelated.

Table 7.6: List of simulation input parameters affecting the solid angle correction of the combined reflectivity and the resulting impact on the systematic uncertainty of the absorption length.

simulation input parameter	syst. uncertainty
steel reflectivity	+0.4 -0.7 cm
reflectivity ratio	+0.1 -0.3 cm
distance	+1.3 -0.7 cm
scattering length	+3.6 -0.3 cm
efficient area of the PMT	-1.9 cm
WLS yield	-0.3 cm

7.4.5 Result

The determined absorption length with the combined reflectivity is given in equation 7.10. The attenuation length is calculated via the formula given in equation 3.7 under the assumption of a scattering length of 70 cm at 128 nm.

$$\alpha_{\text{abs}} = 13.6 \pm 1.1(\text{stat}) \begin{matrix} +3.8 \\ -2.2 \end{matrix}(\text{syst}) \text{ cm} \quad (7.10)$$

$$\alpha_{\text{att}} = 11.4 \pm 0.8(\text{stat}) \begin{matrix} +2.8 \\ -1.7 \end{matrix}(\text{syst}) \text{ cm} \quad (7.11)$$

The statistical uncertainty has the identical origin as discussed in section 7.3.7. The various contributions are in the same order of magnitude. The systematic uncertainty is calculated from the values given in table 7.6, which are achieved by varying the corresponding simulation input parameters used for the determination of the solid angle correction.

7.5 Discussion

The resulting absorption lengths achieved with the two different methods of implementing the steel reflectivity in the simulation agree with each other within their uncertainties. The first method with reflectivity assumptions below 200 nm leads to the conclusion that the reflectivity of 0% at 128 nm matches best the measured data. On contrary, the combined reflectivity is 23% at 128 nm.

One reason for this discrepancy could be that due to the different curve shapes of the reflectivities the real reflectivity at 128 nm could not be retrieved with the reflectivity assumptions shown in figure 5.4.

The best matching simulations in the two methods are generated with 2500 γ /MeV for 0% reflectivity at 128 nm and 1600 γ /MeV for the combined reflectivity. The observed light intensity is a combination of several efficiencies which includes the initial LAr light yield, the steel reflectivity, the WLS absorption and emission spectrum as well as the PMT efficiency. Consequently, the LAr light yield should not be compared autonomously, but treated as an effective light yield and only quoted together with the other relevant efficiencies. As a result the LAr light yield achieved here cannot be compared to other measurements, since the value is specific to the setup and the other simulation input parameters.

It has been observed in GERDA, that the triplet lifetime and the detected light intensity of the LAr veto dropped every time when a new part was submerged in the LAr cryostat. After several days the impurities on the surfaces of the new parts are dissolved completely in LAr and distributed evenly causing only a tiny effect on 64 m³ of LAr, hence the triplet lifetime and the light intensity usually return to their previous values.

The same effect has very likely occurred when submerging the attenuation setup in the LAr cryostat. It had time to outgas for approximately 12 hours. The LAr can flow into the setup through holes in the wall of the steel tube, however, they are probably not large enough to guarantee a continuous flow of LAr in the setup. Consequently, impurities dissolved in the LAr inside the setup could not flow outside effectively, but accumulated a higher concentration inside the setup. Since the attenuation measurement is not wavelength resolved, peaks created in the spectra by impurities like xenon or oxygen cannot be identified. Hence, the result corresponds to the absorption length of LAr in GERDA according to the impurity content inside the setup at the time of the measurement. Thus, the measured absorption length and the retrieved light yield can be much lower at the time of the accomplished measurement compared to the values actual present in GERDA.

In comparison to other measurements compiled in table 3.5 the achieved absorption length is significantly smaller, but lies at the same order of magnitude as quoted in [CCC⁺18]. However, in these measurements very pure argon was taken initially and doped with impurities for the investigation of the attenuation dependence on various impurities. In contrast to this, the LAr in the GERDA cryostat is not connected to a purification plant, but dwells in the cryostat since the filling in December 2009.

Despite the low values of the absorption length and the LAr light yield achieved in this measurement, the LAr veto of GERDA performs very well. One reason for this can be that the actual values in GERDA Phase II are much higher as discussed above. On the other hand, the attenuation measurement in GERDA triggered the collaboration to increase the efficiency of the LAr veto as much as possible, which is among other things the coating with WLS of all possible parts. This maximizes the conversion of scintillation photons into the visible region leading to a much longer range in LAr and therefore to a much higher detection probability.

Additionally, the attenuation measurement caused the awareness of more intensively cleaning new parts that are submerged in the cryostat to keep the LAr purity at its previous condition. Furthermore, a monitoring of the triplet life time of LAr has been developed for GERDA Phase II in order to get an overview of the current argon quality. It was also decided to run the successor experiment LEGEND with new very pure argon to maximize the veto efficiency from the beginning. An additional monitoring of the absorption length measured with an ^{241}Am source is currently under development and will be installed in LEGEND.

After Phase II of GERDA is finished and the detector array is removed from the LAr cryostat, the attenuation measurement could be redone to check whether the absorption length changed. However, this is not planned presently since the LAr properties in the monitoring during Phase II appear to be quite stable during the complete run time, hence a change in the absorption length is not expected.

In principle the setup developed for the attenuation measurement in GERDA can be also used in other experiments. Actually, the source and the PMT can be exchanged to satisfy other demands. For instance in LXe a PMT could be found, that is sensitive to the emitted scintillation light and a WLS would be unnecessary. Also, an ^{241}Am source could be used in order to eliminate the problem of Cherenkov light which would simplify the analysis of the measured data.

Chapter 8

Determination of the triplet lifetime of LAr in GERDA

The data acquired in the attenuation measurement can be analyzed with regard to the triplet lifetime of the LAr scintillation mechanism. A preliminary study with simulations performed with the IPF reflectivity (see ch. 7) has been discussed in [Kap18]. In this chapter, simulations are generated with the combined reflectivity and various input values of the triplet lifetimes in order to investigate the influence on the acquired data. Only the data taken at the shortest measuring point will be considered due to the higher statistics compared to the larger distances.

8.1 Event reconstruction

The event reconstruction for the attenuation analysis described in chapter 6.3.1 is optimized to find single pulses in order to integrate all light collected by the PMT. Single pulses are of no interest for the determination of the triplet lifetime, since they are treated as singlet events. Thus, the event reconstruction is adjusted to the needs of the triplet lifetime analysis.

A typical event with an initial singlet pulse and several triplet pulses forming a tail is shown in figure 8.1. While in the attenuation analysis it does not matter if these pulses are counted as one event or separately, it is important for the triplet lifetime analysis to reconstruct which pulse actually belongs to which event. For this the time between two pulses is calculated and in the case this time is larger than a certain value, the second pulse is treated as a new event. Otherwise the pulse is included in the previous event.

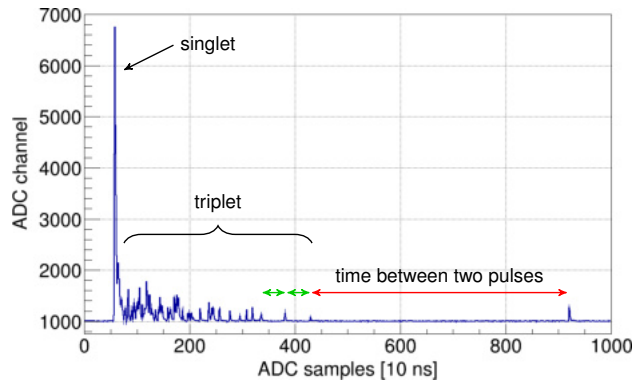


Figure 8.1: Typical scintillation event in LAr with a large initial singlet pulse and several pulses occurring afterwards due to the triplet lifetime. The time between two pulses is used in order to decide whether the second pulse still belongs to the regarded event. While the green arrows indicate that the respective second pulse is included in the event, the red arrow shows a time difference between pulses, where the second pulse will be treated as a new event.

The same flagging algorithm as described in chapter 6.3.1 is used, but the trigger condition is changed. Triggering on events that end up in the pedestal would greatly influence the optimum value of the time between pulses for the decision whether the pulse still belongs to the event. Hence, the trigger value has been increased to 400 ADC channel when comparing the sum of two samples with the two following samples. This is equal to the cut position at the minimum of the valley between pedestal and single p.e. peak depicted in figure 7.2. Consequently, single p.e. pulses can still be found by the software trigger. Cherenkov light is not problematic in this case, since it is created instantly and will occur simultaneously with the singlet peak.

With the help of MC simulations the maximum allowed event length t_{event} , as well as the maximum time between two pulses t_{pulse} for the determination of the event ending will be investigated and optimized for the analysis of the triplet lifetime.

8.2 Simulation studies of the triplet lifetime

For the dedicated simulations of the triplet lifetime studies, the half lives of ^{90}Sr and ^{90}Y have been set to zero in DECAY0 in order to prevent that the initial particle is emitted with a start time of several years while an accuracy of nanoseconds is needed for the determination of the detection time of the photons. In this way, the emission time of all initial β -particles is zero, i.e. the tracking of each event is started at 0 ns. MC simulations with various input values for the triplet lifetime are generated and for each photon that was observed by the PMT the hit time is saved.

In the next step, the start time of each event is chosen randomly with the probability density function for the next decay, which is expressed in equation 8.1.

$$p(t) = \lambda \cdot e^{-\lambda t} \quad (8.1)$$

The mean of this function is given by $1/\lambda$ which is equal to the inverse of the activity. The activity of the ^{90}Sr quoted by *Eckert & Ziegler* is 7.0 kBq (1.9.2011) with an uncertainty of 20%. Thus, at the time of the attenuation measurement in September 2014, the activity of the source was 6.5 ± 1.3 kBq. Due to the triplet lifetime, the lengths of the events can vary, leading to the possibility that pulses of an event are registered at the same time as the next event starts, creating an overlap, which makes the separation of such events very difficult.

The assignment of the hits to the respective event is known for the simulations (see fig. 8.1). Each event is shifted in such a way, that the first pulse is set to the first entry of a histogram, i.e. each event starts at the same time. All events are summed up to a histogram as depicted in figure 8.2. The simulated pulses are analyzed as it is done for the data, where the assignment to the related event is not accessible. Various combinations of the event length t_{event} and the time between two pulses t_{pulse} are used to find events and sum them up to create the histograms shown in figure 8.2. The goal is to reproduce the shape of the histograms generated with the known assignment between pulses and events.

In the case the maximum time between two pulses is chosen too small, the resulting histogram is dropping too fast since the events are chopped too early. On the other hand, if this time is too long, pulses of other events are included in events they do not actually belong to and the produced histogram has too many entries for the larger hit times.

The event length may not be selected to be too short, otherwise the created histogram has a significant cutoff at this time. With a long enough maximum event length and an optimized maximum time between two pulses, the histogram created with the original assignment of the hits to the events can be very well reproduced as shown in figure 8.2.

At this point, the maximum event length can be increased to very large values without affecting the resulting histogram. Consequently, the time between two pulses t_{pulse} has to be optimized, whereas for the event length t_{event} only the minimum matching time must be found.

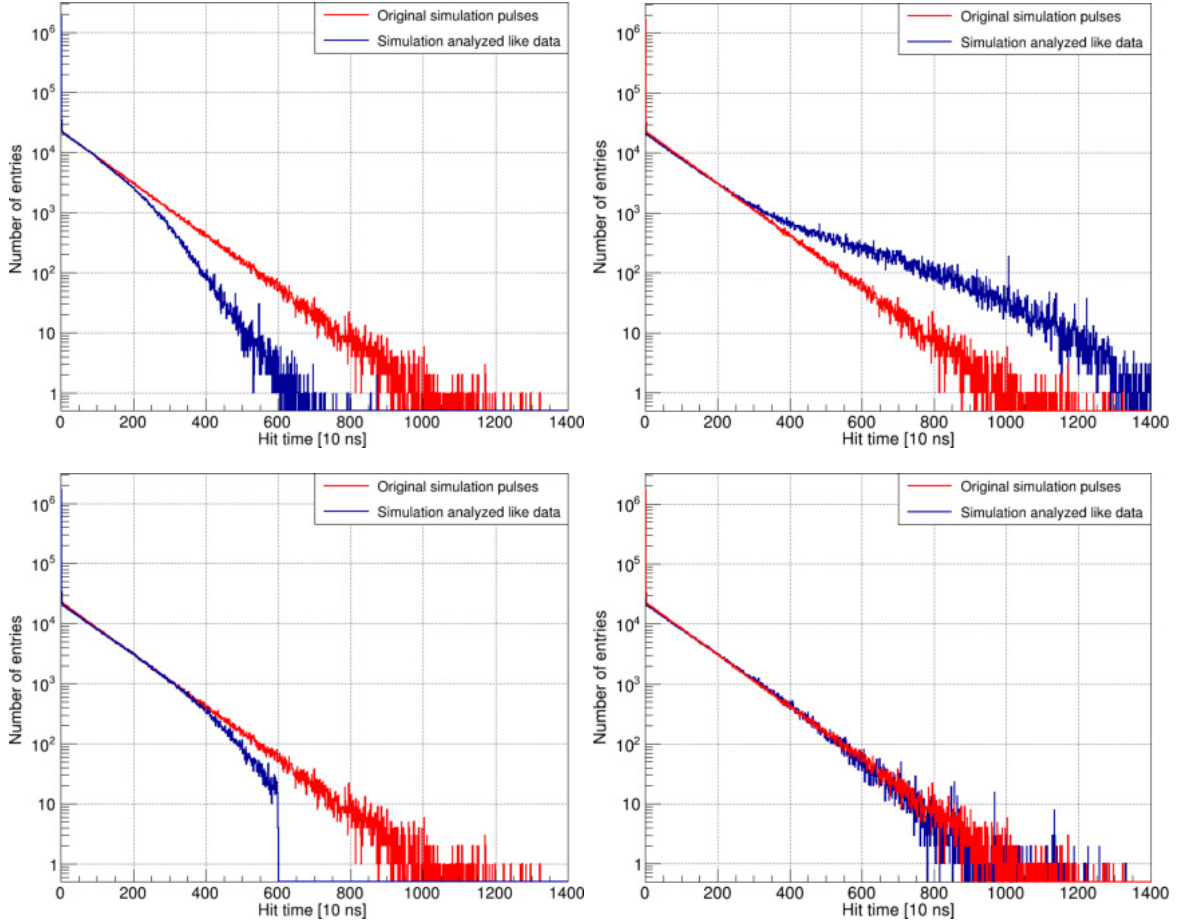


Figure 8.2: Summed up histograms of the hit times of all simulated events for a triplet lifetime of 1000 ns. The red line shows the histograms of the original simulated events with the known assignment of pulses to the respective event. The blue histograms on the top are created with $t_{\text{pulse}} = 1000$ ns (top left) and $t_{\text{pulse}} = 5000$ ns (top right) as well as $t_{\text{event}} = 15 \mu\text{s}$. On the bottom the blue histograms are generated with $t_{\text{event}} = 6 \mu\text{s}$ (bottom right) and $t_{\text{event}} = 15 \mu\text{s}$ (bottom left) with $t_{\text{pulse}} = 2100$ ns.

MC simulations with different values of the triplet lifetime are generated and analyzed with various combinations of t_{pulse} and t_{event} . The resulting histograms of the summed up pulses are compared via a χ^2 method with the histogram created with the known assignment of the pulses to the events. The reduced χ^2 is calculated by equation 8.2 with the number of entries $e_{1,i}$ and $e_{2,i}$ in the bin i of the respective histogram and the total number n of compared bins.

$$\chi^2 = \frac{1}{n} \sum_i \frac{(e_{1,i} - e_{2,i})^2}{e_{1,i} + e_{2,i}} \quad (8.2)$$

The comparison is constrained by excluding the singlet peak, i.e. starting at a hit time of 50 ns and stopping if in one histogram the bin entries are less than 5 to prevent comparing bins with low statistics. Figure 8.3 shows the resulting χ^2 values of the histogram comparison for the example of the triplet lifetime of 1000 ns.

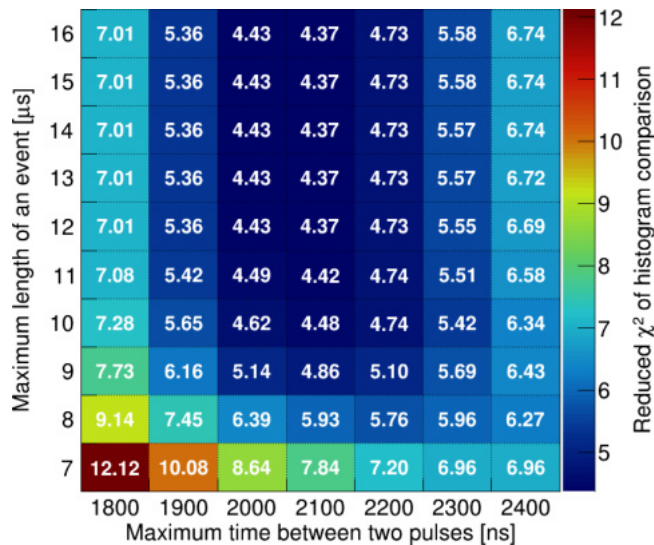


Figure 8.3: Reduced χ^2 values of the histogram comparison for a triplet lifetime of 1000 ns of the original simulation pulses and the simulation analyzed with various combinations of the maximum time between two pulses t_{pulse} and the maximum event length t_{event} . The best matching parameters are $t_{\text{pulse}} = 2100$ ns and $t_{\text{event}} \geq 12$ μs .

The histogram created with the best matching values of t_{pulse} and t_{event} is fit with the formula in equation 8.3 in order to retrieve the triplet lifetime that was used as an input parameter in the corresponding simulation. The sample width of 10 ns is included in the fit formula in order to get the resulting triplet lifetime, i.e. parameter p_1 in nanoseconds.

$$f(x) = p_0 \cdot e^{-10 \text{ ns} \cdot x / p_1} \quad (8.3)$$

The application of the fit expressed in equation 8.3 is depicted in figure 8.4. The fit starts at 100 ns to prevent the singlet lifetime to influence the fit and stops if the bin entries in the histogram are less than 100 in order to exclude bins with lower statistics.

The same optimization procedure and analysis is performed for simulations generated with triplet lifetimes in the range of 800–1500 ns, wherein the results of other measurements with very pure argon are populated (see tab. 3.2). The corresponding optimized values for t_{pulse} and t_{event} are listed in table 8.1.

Table 8.1: Simulation input value of the triplet lifetime $\tau_{\text{t,sim}}$, the respective optimized values of the maximum length of an event t_{event} and the maximum time between two pulses t_{pulse} as well as the fit result of the triplet lifetime $\tau_{\text{t,fit}}$. The last column is the calculated shift of the fit result to the simulation input value. On average, the fit result is 3% too large, which is used as a correction factor to better match the simulation input value.

$\tau_{\text{t,sim}}$ [ns]	t_{event} [μs]	t_{pulse} [ns]	$\tau_{\text{t,fit}}$ [ns]	$(\tau_{\text{t,fit}} - \tau_{\text{t,sim}}) / \tau_{\text{t,sim}}$
800	10	1800	822.0 ± 0.6	0.0275
900	13	1900	920.5 ± 0.7	0.0228
1000	12	2100	1032.2 ± 0.8	0.0322
1100	13	2200	1131.7 ± 0.9	0.0288
1200	13	2400	1238.4 ± 1.0	0.0320
1300	13	2500	1345.7 ± 1.0	0.0352
1400	15	2600	1440.8 ± 1.1	0.0291
1500	15	2700	1549.2 ± 1.2	0.0328

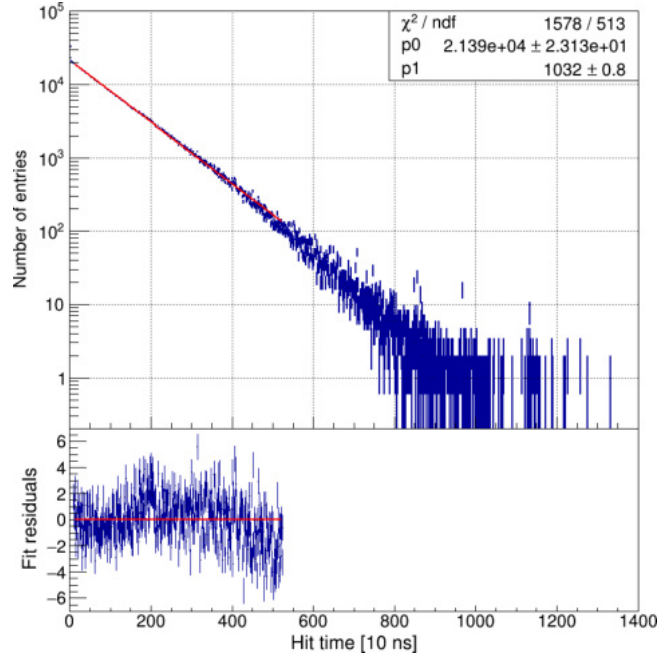


Figure 8.4: Fit of the histogram generated with the best matching values of t_{pulse} and t_{event} for a simulation performed with a triplet lifetime of 1000 ns. The fit parameter p_1 is the triplet lifetime in nanoseconds.

While the best matching value for t_{pulse} is increasing with the triplet lifetime, a maximum event length of $t_{\text{event}} \geq 15 \mu\text{s}$ is ideal for all cases. Thus, the histograms are created with the optimized value for t_{pulse} for each triplet lifetime and a fixed value of $t_{\text{event}} = 15 \mu\text{s}$ for all triplet lifetimes used to generate the simulations.

The retrieved fit results of the triplet lifetime are systematically overestimating the respective simulation input value by 3% on average. Hence, the resulting fit value is corrected by this systematic shift to better reflect the original simulation input value.

Since the triplet lifetime in the measured data is unknown, it is unclear which value of t_{pulse} should be used for the event reconstruction. Thus, an iterative method is applied, which is crosschecked with simulations. For this purpose, simulations with various triplet lifetimes as input parameters are analyzed using $t_{\text{event}} = 15 \mu\text{s}$ and a start value of $t_{\text{pulse}} = 2200 \text{ ns}$. The fit result of the triplet lifetime is farther away from the input value compared to the analysis with the optimized t_{pulse} , but it is still retrieving the input value by $\pm 50 \text{ ns}$. Consequently, in the second iteration the optimized t_{pulse} for the corresponding triplet lifetime can be used to redo the same steps and achieve a fit value that is much better matching the triplet lifetime input parameter. Additionally, the reduced χ^2 of the fit as well as the fit residuals indicate that the model is describing the histograms much better compared to the first iteration. In all investigated cases ($\tau_t = 800 - 1500 \text{ ns}$) the triplet lifetime input parameter was successfully retrieved within two iterative steps.

8.2.1 Systematic uncertainties

The optimized value of the time between two pulses t_{pulse} is dependent on the activity of the ^{90}Sr source. The activity of the source is varied to a minimum and maximum according to the quoted activity and uncertainty of $6.5 \pm 1.3 \text{ kBq}$. The analysis is repeated and the difference to the resulting triplet lifetime is calculated. The source activity causes on average a systematic uncertainty of $^{+1.6}_{-1.0}\%$ for the retrieved triplet lifetime.

8.3 Data analysis

The experimental data acquired in the attenuation measurement is analyzed with the described iterative method. The histogram of the summed up pulses and the fit of the final iteration are depicted in figure 8.5. The fit starts at $1 \mu\text{s}$ to prevent influences of a possible intermediate state, which is reported in some references (see ch. 3.2.1). The resulting fit value of the triplet lifetime is corrected by the systematic overestimation of 3% as discussed in section 8.2 leading to $\tau_t = 1087.5 \text{ ns}$.

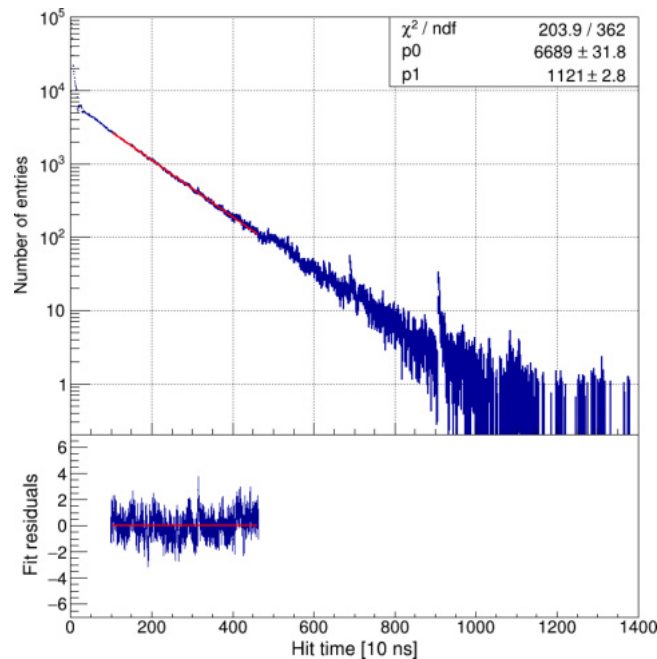


Figure 8.5: Histogram and fit of the summed up pulses for the experimental data. At a hit time of about $9 \mu\text{s}$ a small peak is visible, which indicates an overlap of two events. However, this is not problematic since this area is not included in the fit range.

8.3.1 Systematic uncertainties

The systematic uncertainty caused by the source activity is calculated as discussed in section 8.2.1 resulting in $^{+16.9}_{-11.3} \text{ ns}$. Furthermore, the value of t_{pulse} in the final iteration is varied by $\pm 100 \text{ ns}$ to determine the systematic uncertainty of the optimized time between two pulses for chopping an event. This leads to an additional uncertainty of $^{+6.7}_{-10.1} \text{ ns}$. Summarized, the analysis of the experimental data resulted in a triplet lifetime of:

$$\tau_t = 1087.5 \pm 2.8(\text{stat.})^{+18.2}_{-15.2}(\text{syst.}) \text{ ns} \quad (8.4)$$

8.4 Discussion

Comparing the triplet lifetime in equation 8.4 with the values compiled in table 3.2, the achieved result lies in the expected range in the lower area. Since the other measurements are performed in very pure argon, it is expected that the value in the LAr cryostat of GERDA is lower. This agrees also with the shorter absorption length since both values are expected to be smaller for a larger impurity concentration.

The triplet lifetime monitored during the operation of Phase II of GERDA is about $1 \mu\text{s}$, i.e. a bit lower. A possible reason is, that after the attenuation measurement was performed the impurity content of the LAr changed slightly due to the submerging of the LAr veto and the detector array.

Since the exact impurity composition is unknown, it is hard to speculate why the absorption length should be comparatively low while the triplet lifetime is in the range of the measurements done in very pure argon. But as discussed in chapter 3.2 various impurities can influence the LAr properties differently, which could justify uncommon combinations of absorption length and triplet lifetime achieved from the same measurement.

The singlet lifetime cannot be obtained from the acquired data due to the sampling rate of the FADC. A sample in the pulse trace has a width of 10 ns, which is almost two singlet lifetimes. A much higher sampling rate is necessary to be sensitive on the singlet lifetime. Consequently, also the ratio of singlet and triplet lifetime cannot be determined with the acquired data.

In the simulation only singlet and triplet lifetime are implemented, while some references report an additional intermediate state, which has an unclear origin (see ch. 3.2.1). Thus, the fit range is constrained to exclude the smaller hit times in which a possible intermediate state could affect the fit result. As shown in figure 8.5 the fit residuals scatter equally around the fit curve, clearly indicating that no intermediate state is visible in the fit range.

Chapter 9

$2\nu\beta\beta$ decay of ^{76}Ge into excited states of ^{76}Se

The search for the double beta decay of ^{76}Ge into excited states of ^{76}Se in the GERDA experiment has been started with Phase I data [GER15a] and further developed for Phase II [Leh16, Wes19]. In this work the analysis is continued for the data of Phase II that has been unblinded after the publishing of [Wes19] and for Phase II+.

The following sections are in strong connection to [Wes19]. The analysis steps including changes are pointed out in the individual sections, however, the statistical analysis method remains unchanged from the one discussed in detail in [Wes19]. The focus in this work lies on the implementation of the LAr veto for the excited states analysis.

9.1 Motivation

The half life $T_{1/2}^{0\nu}$ of the $0\nu\beta\beta$ decay is connected with the NME $M^{0\nu}$ as expressed in equation 1.21. The unknown Majorana neutrino mass $m_{\beta\beta}$ contained in this equation and also a potential quenching of the axial vector coupling constant g_A make a reliable prediction of the half life almost impossible. Indeed, while experimental limits on $T_{1/2}^{0\nu}$ increased over time, theoretical calculations of the NME have been adjusted to be compatible (see table 9.1).

For the $2\nu\beta\beta$ decay, the corresponding formula of the half life $T_{1/2}^{2\nu}$ is easier, since it is not dependent on the Majorana neutrino mass as expressed in equation 9.1 [BK18].

$$\left(T_{1/2}^{2\nu}\right)^{-1} = G^{2\nu} |M^{2\nu}|^2 \quad (9.1)$$

While the NMEs for the $0\nu\beta\beta$ decay and the $2\nu\beta\beta$ decay are numerically different, they rely on the same model assumptions. Thus, the observation of the $2\nu\beta\beta$ decay into excited states, together with the $2\nu\beta\beta$ decay into the ground state, cannot only further constrain the model parameters of the $2\nu\beta\beta$ NME, but also improve the predictions for the $0\nu\beta\beta$ decay.

The $2\nu\beta\beta$ decay into excited states has already been measured for two isotopes, ^{100}Mo and ^{150}Nd . Both have been observed for the transition into the first 0^+ excited state with half lives of $7.5 \cdot 10^{20}$ yr [NEM14] and $1.33 \cdot 10^{20}$ yr [KEFT14], respectively (compare also with $T_{1/2}^{2\nu}$ into the ground state of the corresponding transition in table 1.1). The most recent limit for the $2\nu\beta\beta$ decay of ^{76}Ge into the 0_1^+ state derived from GERDA data is $> 3.1 \cdot 10^{23}$ yr [Wes19]. The latest limit achieved by the MAJORANA collaboration for the same decay mode is $> 6.8 \cdot 10^{23}$ yr [MAJ20].

9.2 Decay modes

The Q -value of the $\beta\beta$ decay of ^{76}Ge into the ground state of ^{76}Se has been determined to be 2039.061 ± 0.007 keV [MRM10], allowing the population of the ten lowest nuclear states of ^{76}Se [IAE20]. However, the higher the energy level of the nuclear state, the less energy is available for the electrons and neutrinos emitted in the $\beta\beta$ decay. Since the phase space factor $G^{2\nu}$ scales with $Q_{\beta\beta}^5$ [DPR19], the decay rate into excited states decreases with the energy of the nuclear state (see eq. 9.1). Thus, only the decay into the three lowest excited states of ^{76}Se are investigated. The corresponding decay scheme of ^{76}Ge into ^{76}Se is depicted in figure 9.1. Furthermore, the nuclear spins of mother and daughter nuclei influence the decay rate, i.e. the transition of the $0_{\text{g.s.}}^+$ of ^{76}Ge into the $0_{\text{g.s.}}^+$ and 0_1^+ states of ^{76}Se is favored over the two 2^+ states.

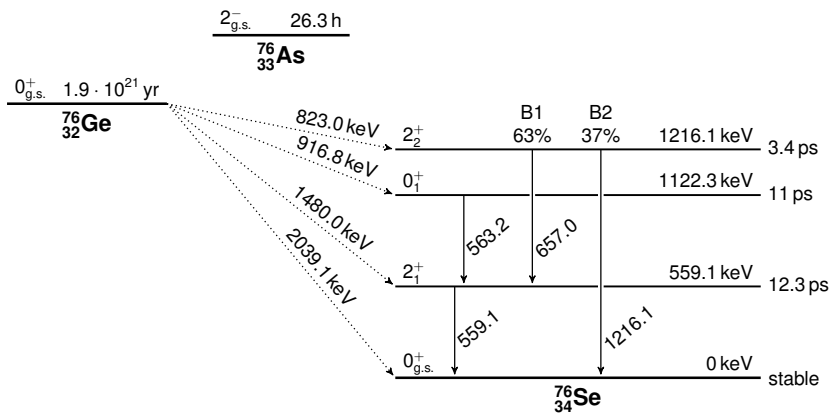


Figure 9.1: Decay scheme of the $\beta\beta$ decay of ^{76}Ge into ^{76}Se considering the ground state and the three lowest excited states. Higher excitation states of ^{76}Se are omitted. The energies available for the electrons and neutrinos of the corresponding decay modes are indicated on the respective dotted lines. The energies of the de-excitation γ rays are given in keV. The 2_2^+ state has two possible branches, B1 and B2, with two successive de-excitation γ 's or just one, respectively. Values are taken from [IAE20].

The two electrons of the $\beta\beta$ decay remain mainly in the source detector, but the de-excitation γ rays have a higher probability of leaving the source detector, enabling another detector to observe them. Thus, a distinct signal signature is the detection of the full energy of a de-excitation γ ray in one detector and at the same time another energy deposition compatible with the corresponding electron energy in a second detector. For the decay modes with a γ cascade, i.e. more than one de-excitation γ ray, it is sufficient to detect the full energy deposition of one of the γ rays.

Theoretical predictions for the half life of the investigated $2\nu\beta\beta$ decay modes of ^{76}Ge into excited states are calculated with different nuclear models. A compilation is listed in table 9.1. Additionally, the table shows half life limits achieved by various experiments. The half life limits for the $2\nu\beta\beta$ decay into the 2^+ states are well below the theoretical predictions, while for the 0_1^+ state several theoretical values have been already excluded by the more recent experiments. The 0_1^+ half life limit derived from GERDA Phase I data caused the adaption of nuclear model parameters and consequently the calculation of new theoretical half lives which are compatible with the experimental limit.

Table 9.1: Compilation of experimental limits and theoretical predictions for the half life of the $2\nu\beta\beta$ decay of ^{76}Ge into excited states of ^{76}Se . The lists are sorted by the publication year, respectively. The theoretical nuclear models are nuclear shell model (NSM), Hartree-Fock-Bogoliubov (HFB), Quasiparticle random-phase approximation (QRPA), multiple commutator method QRPA (MCM-QRPA), renormalized QRPA (RQRPA) and interacting boson model (IBM).

decay mode	$T_{1/2}^{2\nu}$ [yr]	model	year	ref.
$0_{\text{g.s.}}^+ \rightarrow 2_1^+$	$> 6.3 \cdot 10^{20}$ (68% C.L.)	exp.	1992	[BBE ⁺ 92]
	$> 1.1 \cdot 10^{21}$ (90% C.L.)	exp.	1995	[BDPU95]
	$> 1.6 \cdot 10^{23}$ (90% C.L.)	exp.	2015	[GER15a]
	$> 9.6 \cdot 10^{23}$ (90% C.L.)	exp.	2019	[MAJ20]
	$1.2 \cdot 10^{30}$	NSM	1984	[HS84]
	$5.8 \cdot 10^{23}$	HFB	1994	[DR94]
	$5.0 \cdot 10^{26}$	QRPA	1994	[CS94]
	$2.4 \cdot 10^{24}$	QRPA	1996	[SM96]
	$7.8 \cdot 10^{25}$	MCM-QRPA	1996	[AS96]
	$1.0 \cdot 10^{26}$	RQRPA	1997	[TS97]
	$(2.4 - 4.3) \cdot 10^{26}$	RQRPA	1998	[SSFK98]
	$2.0 \cdot 10^{27}$	RQRPA	2014	[Un14]
$0_{\text{g.s.}}^+ \rightarrow 0_1^+$	$> 6.3 \cdot 10^{20}$ (68% C.L.)	exp.	1992	[BBE ⁺ 92]
	$> 1.7 \cdot 10^{21}$ (90% C.L.)	exp.	1995	[BDPU95]
	$> 6.2 \cdot 10^{21}$ (90% C.L.)	exp.	2002	[KOSV02]
	$> 3.7 \cdot 10^{23}$ (90% C.L.)	exp.	2015	[GER15a]
	$> 6.8 \cdot 10^{23}$ (90% C.L.)	exp.	2019	[MAJ20]
	$4.0 \cdot 10^{22}$	QRPA	1994	[CS94]
	$4.5 \cdot 10^{22}$	QRPA	1996	[SM96]
	$7.5 \cdot 10^{21}$	MCM-QRPA	1996	[AS96]
	$(1.0 - 3.1) \cdot 10^{23}$	RQRPA	1997	[TS97]
	$(1.2 - 5.8) \cdot 10^{23}$	RQRPA	2014	[Suh14]
	$6.4 \cdot 10^{24}$	IBM-2	2014	[Iac14]
$(2.3 - 2.6) \cdot 10^{24}$	NSM	2014	[Men14]	
$0_{\text{g.s.}}^+ \rightarrow 2_2^+$	$> 1.4 \cdot 10^{21}$ (90% C.L.)	exp.	1995	[BDPU95]
	$> 2.3 \cdot 10^{23}$ (90% C.L.)	exp.	2015	[GER15a]
	$> 5.6 \cdot 10^{23}$ (90% C.L.)	exp.	2019	[MAJ20]
	$1.0 \cdot 10^{29}$	QRPA	1994	[CS94]
	$1.3 \cdot 10^{29}$	MCM-QRPA	1996	[AS96]
	$(0.7 - 2.2) \cdot 10^{28}$	RQRPA	1997	[TS97]

9.2.1 Angular correlation of de-excitation γ rays

The respective two de-excitation γ rays emitted in the cascades from the 0_1^+ and the 2_2^+ B1 states (see fig. 9.1) are angular correlated. Analytically, the correlation is described by the following formula [BD50, Eva55].

$$W(\vartheta)d\Omega = (1 + a_2 \cos^2 \vartheta + a_4 \cos^4 \vartheta)d\Omega \quad (9.2)$$

In some references, the formula is quoted with the corresponding Legendre polynomials, which results in different parameter values of a_2 and a_4 [Nag73, SMA⁺19, ZS89]. Both approaches can be easily translated into each other.

Theoretical predictions and the most recent measurement of the parameters a_2 and a_4 according to equation 9.2 are listed in table 9.2 for the γ cascades of the 0_1^+ and the 2_2^+ B1 states of ^{76}Se . Older measurements are reported in [Nag73, ZS89] for comparison.

Table 9.2: Parameter values of the angular correlation of the γ cascades from the 0_1^+ and the 2_2^+ B1 states of ^{76}Se derived from theoretical calculations and experimental data. I denotes the angular momenta of the initial (A), intermediate (B) and final (C) nuclear state and l stands for the angular momenta of the corresponding emitted γ ray. The theoretical values for the pure multipole γ rays are quoted, while the experimental values for the 2_2^+ B1 cascade are a mixture of the electric quadrupole ($l_1 = 2$) and the magnetic dipole ($l_1 = 1$) γ rays. The parameter values are quoted according to equation 9.2. Theoretical values are from [BD50, Eva55], experimental values from [ZS89].

γ cascade $I_A(l_1)I_B(l_2)I_C$	theoretical		experimental	
	a_2	a_4	a_2	a_4
0(2)2(2)0	-3	4	-2.930 ± 0.366	3.733 ± 0.416
2(2)2(2)0	-15/13	16/13	-1.218 ± 0.115	1.101 ± 0.131
2(1)2(2)0	3/7	0		

In the case, the γ cascade occurs for a spin sequence of nuclear states $2^+ \rightarrow 2^+ \rightarrow 0^+$, the first transition ($2^+ \rightarrow 2^+$) can be a mixture of the electric quadrupole (E2) and the magnetic dipole (M1) radiation, while the second transition ($2^+ \rightarrow 0^+$) must be a pure E2 radiation. Hence, the mixing ratio δ of M1 and E2 for the first transition can be determined very precisely [LM57]. This mixing ratio has been measured to be $\delta = 5.26 \pm 0.50$ for the $2_2^+ \rightarrow 2_1^+$ transition in ^{76}Se [ZS89]. The fraction Q of the respective multipole transition can be calculated from the mixing ratio as expressed in equation 9.3 [CW73].

$$Q_{\text{E2}} = \frac{\delta^2}{1 + \delta^2} \quad Q_{\text{M1}} = \frac{1}{1 + \delta^2} \quad (9.3)$$

The E2 radiation is dominating with 96.5% and the M1 contribution is measurable [LM57, ZS89]. The angular correlations including the mixing of the E2 and M1 radiations for the 2_2^+ B1 γ cascade for the measured parameters given in table 9.2 have been implemented in DECAY0, which generates the angular distribution of the de-excitation γ rays as shown in figure 9.2.

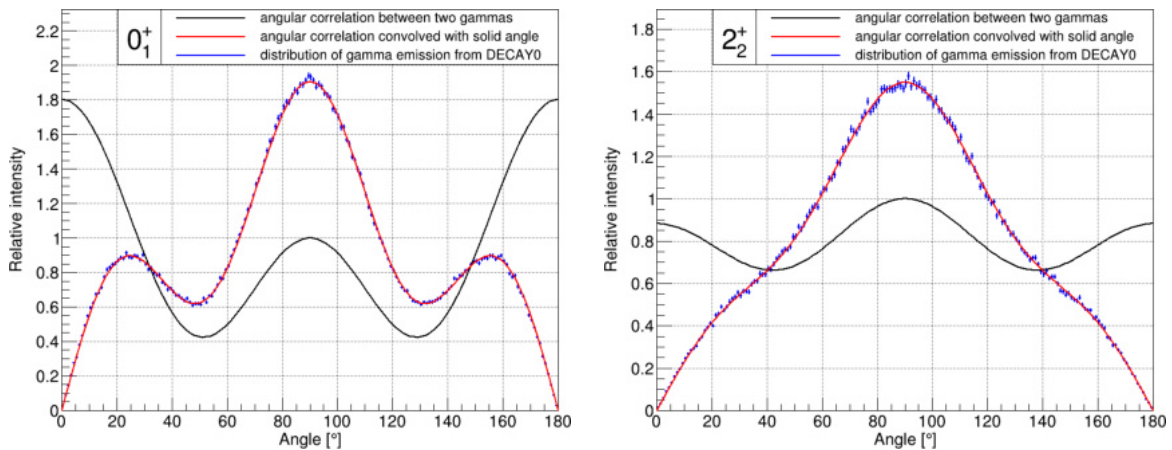


Figure 9.2: Angular correlation and convolution with the solid angle of the γ cascades with the experimental values quoted in table 9.2 for the 0_1^+ (left) and the 2_2^+ B1 (right) states of ^{76}Se . Also shown is the angular distribution generated with DECAY0 for 10^6 events.

9.3 Implementation of the LAr veto

For the $\beta\beta$ decay of ^{76}Ge into the ground state of ^{76}Se the LAr veto is used to suppress background events and therefore increase the signal to background ratio. Consequently, it is expected that the LAr veto can be applied to the excited states analysis as well. However, the search for excited states focuses on two-detector events.

For decays into excited states, where exactly one de-excitation γ ray is emitted and one of the detectors is required to observe the full energy of the γ ray while the other detector sees the energy deposited by the electrons, no energy is deposited in the LAr. Thus, the detection of scintillation light coincident to such an event signature would indicate a background event which can be rejected by the LAr veto.

On the contrary, decays with two de-excitation γ rays feature the same signal signature with the full energy of one of the γ rays while at the same time energy can be deposited in the LAr by the other γ ray. Hence, the LAr veto can be used to distinguish between the 0_1^+ and the 2_1^+ decay mode which share the same γ energy.

In order to determine the excited states signal efficiency sacrifice and background suppression factor caused by the application of the LAr veto, the LAr veto needs to be included in the excited states simulations. However, the simulation of the propagation of optical photons in a large volume such as the LAr surrounding the Ge detector array consumes an extremely high amount of computing power.

Moreover, the LAr absorption length and light yield directly affect the efficiency of the LAr veto. Although these optical parameters have been measured before the beginning of Phase II, it cannot be guaranteed that they are the same when Phase II started. At least the triplet lifetime has been constant during the whole data taking of Phase II (see fig. 2.5), which indicates that the optical parameters were stable within Phase II. However, the triplet lifetime dropped slightly shortly after the start of Phase II+, hence it is expected that also the absorption length and the light yield are affected. Additionally, the detection efficiencies of the SiPMs (see fig. 2.4) are unknown.

Consequently, a way has to be found to estimate the optical parameters and efficiencies for the simulations, determine the impact of the LAr veto on the excited states signal efficiencies and at the same time keep the computing power to a reasonable level. In order to achieve this, a photon detection probability map of the LAr veto has been produced, which allows to tune the optical parameters and efficiencies in the post processing of the MC simulations. In the following it is shortly denoted as LAr map.

The advantage of this approach is that the excited states simulations can be performed without photon tracking. The energy depositions in LAr are saved and can be folded in the post processing with the LAr map to determine if the event is LAr vetoed or not. The LAr light yield determines the number of produced photons for each energy deposition in the post processing. The other optical parameters affect the photon detection probability.

9.3.1 Creation of scintillation light in GEANT4

In order to explain the application of the LAr map, the creation process of scintillation light in GEANT4 has to be understood. Figure 9.3 shows a visualization of a γ ray and an electron propagating through LAr. γ rays have a comparatively long mean free path in LAr and deposit energy by Compton scattering or photo effect. The energy deposition happens only at the interaction point, thus also scintillation light is created at this location, which is denoted in GEANT4 as the post step point.

For electrons and other charged particles the situation is differently, since they lose energy continuously during their propagation through a medium. Consequently, scintillation light is created along the step, i.e. along the straight line between the pre and the post step point.

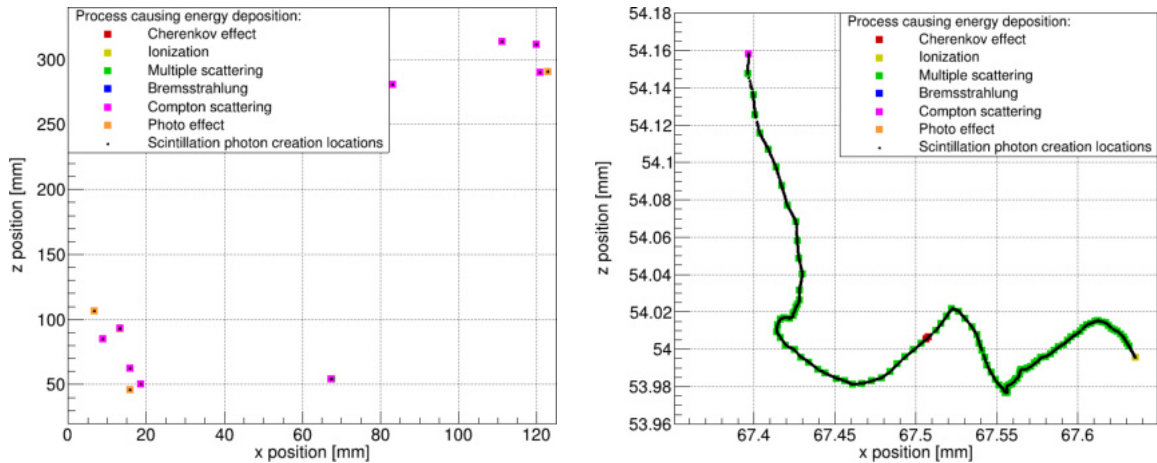


Figure 9.3: Positions of energy depositions of γ rays and electrons in LAr as well as creation locations of scintillation photons. The plot on the right is a zoom in on the plot on the left where a γ ray created an electron via Compton scattering. While γ particles have a long mean free path in LAr and scintillation light is created only at the post step point (left), electrons have a much shorter mean free path in LAr, but scintillation light is created along the step in GEANT4 (right).

In the simulations without photon tracking, the energy depositions in LAr are saved including the respective (x, y, z) position of the post step point. These points are used in the post processing to determine if the corresponding energy deposition lead to a photon detection, i.e. if the event is rejected by the LAr veto. As indicated in figure 9.3 an event can contain many energy depositions leading to a large amount of created scintillation photons at various locations in the LAr. If at least one photon triggers the LAr veto, the event is rejected.

This procedure shifts the origin point of scintillation light to the post step point only, which is true for photons, but not for electrons. Therefore, the mean free path of electrons in LAr in GEANT4 has been investigated with a simulation of ^{90}Y ($Q_\beta = 2280$ keV [CEF99]). Only electrons with an energy of more than 2 MeV have been taken into account. The mean free path has been determined to be 0.02 mm, while the maximum free path is 0.3 mm. Actually, the voxel size of the LAr map is much larger ($3.0 \times 3.0 \times 3.7$ mm³), making the mentioned shift to the post step point negligible.

9.3.2 LAr photon detection probability map

The LAr map has been developed in the work of [Per, Wie]. For the determination of the photon detection probabilities for each location where energy can be deposited in LAr, photons with a wavelength of 128 nm (see ch. 5.2.1) have been simulated. In order to keep the computing power at a reasonable amount, the volume where photons are started have been restricted to a radius of 38.5 cm and a height of 220 cm. This volume comprises the LAr veto (see fig. 2.4) featuring a radius of 23.5 cm and a height of 220 cm. Additionally, the LAr volume where photons are started has been partitioned into voxels of $3.0 \times 3.0 \times 3.7$ mm³. The voxel size has been optimized in order to achieve a sufficient resolution and large enough statistics while minimizing the simulation time.

In the simulations of the LAr map the efficiencies of the PMTs and SiPMs of the LAr veto have been set to 100% to achieve higher statistics with less simulation time. For each hit also the photon wavelength is saved allowing for an application of the actual PMT and SiPM efficiency curves in the post processing.

The scintillation fibers forming the fiber curtain are fixed in their positions by copper bars (see fig. 2.6). Due to the different thermal expansion coefficients of copper and scintillation fibers, it cannot be excluded that the careful arrangement of the scintillation fibers gets disturbed when submerging it into LAr. Thus, the fiber coverage is introduced as an additional free parameter in the simulation, which has to be determined by comparisons with real data.

The post processing of the MC simulations is done with the tier4izer, which is a software developed by the GERDA collaboration. The tier4izer converts the simulation data to the same structure as used for the measured data. While the data are processed from their raw format into tier4 via several steps, the tier4izer is directly applied to the MC simulations. Details of the tier structure of the GERDA data and the corresponding software tools can be found in [Wes19].

The post processing of the simulation data is done with the tier4izer, i.e. for each deposited energy in LAr, as shown in figure 9.4, the number of created scintillation photons is calculated with the LAr light yield and the number of detected photons is determined. Additionally, the user has the option to scale the PMT and SiPM efficiency curves as well as the LAr light yield, the absorption length and the fiber coverage. The resulting energy spectra of events rejected by the LAr veto and events surviving the LAr veto are then compared to calibration data. The optical properties are optimized in order to achieve a good match with the measured data. The best match for Phase II data has been obtained with an absorption length of 55 cm and a fiber coverage of 50%. The corresponding LAr map is depicted in figure 9.5.

For the validation of the scaling of the optical properties, LAr maps with varying values for the absorption length and fiber coverage are produced. Different volume partitions of the resulting LAr maps are compared individually in order to verify whether the scaling is homogeneous within the complete regarded volume of the LAr map. Unfortunately, none of the varied optical properties causes a homogeneous change of the LAr map. While it was found that the LAr map scales mainly linearly with the fiber coverage, the absorption length α_{abs} influences the detection probability p exponentially: $p \sim \exp(\alpha_{\text{abs}})$. In order to minimize the number of parameters used in the tier4izer, the fiber coverage absorbs the effects from other linear parameters, such as the surface reflectivities and the WLS efficiency.

The LAr map only accounts for the detection probability of scintillation photons created in LAr, but it does not regard photons produced by the Cherenkov effect. Since Cherenkov photons are also created in the visible region, they have a longer range in LAr than scintillation photons and therefore a higher detection probability. However, solely in the case that events are vetoed by Cherenkov light only, a difference to the number of events vetoed by the LAr map could be observed. The number of these cases have been determined with simulations to be 0.0002% for the investigated decay modes into excited states, thus the influence of Cherenkov light can be neglected.

It is important to note, that while the LAr vetoed data can be reproduced with the current LAr map very well already, verification and optimization steps are still work in progress and it is possible that changes are made to the LAr map in the future. The LAr map presented in figure 9.5 is only valid for Phase II of GERDA. For Phase II+ a new map has to be produced since the Ge detector array geometry changed due to the implementation of the IC detectors (see ch. 2.2.3). Additionally, the new inner fiber shroud enclosing the middle detector string (see fig. 2.6) has to be implemented in MaGe and the corresponding efficiencies of the new SiPM channels have to be determined. Moreover, it needs to be verified if one LAr map is sufficient for the complete run time of Phase II+ or if two maps are needed due to the contamination of the LAr during a valve exchange in the LAr cryostat that lead to a slightly shorter triplet lifetime (see fig. 2.5).

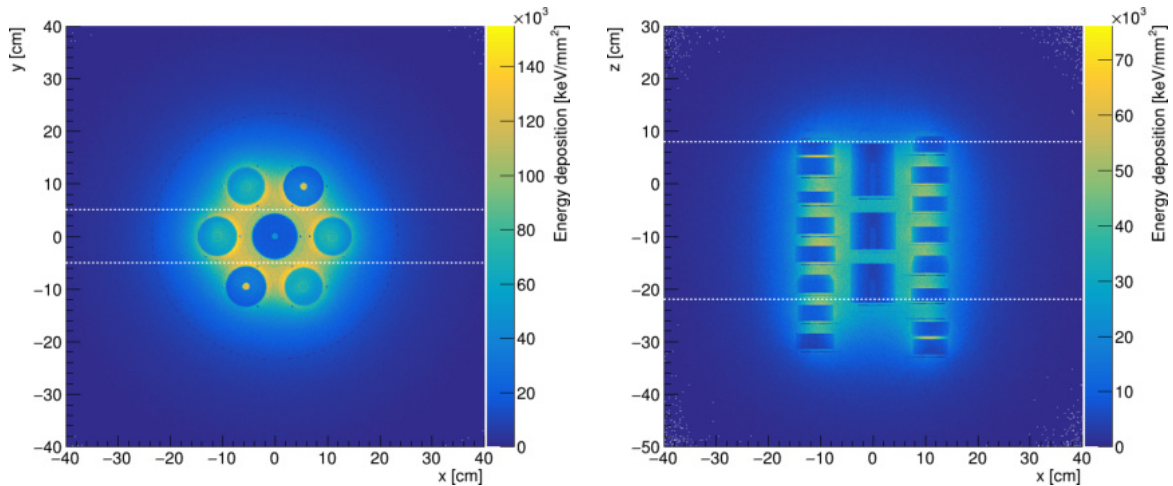


Figure 9.4: Simulation showing the energy depositions in LAr from 10^8 $2\nu\beta\beta$ decays of ^{76}Ge into the 0_1^+ state of ^{76}Se in Phase II of GERDA. The corresponding plots for Phase II+ are depicted in figure B.1. Solely the energy depositions in LAr from events that triggered exactly two different Ge detectors are shown. The voxel size is 1 mm^3 . The white dashed lines indicate the range used for the projection of the energy depositions for the respective other plot. In the view from the top of the Ge detector array (left) strings containing coaxial detectors can be identified by larger energy depositions in the LAr filling the bore holes in the middle of the detectors. Moreover, the position of the scintillation fiber curtain is visible as a dashed dark blue circular line with a radius of 23.5 cm. The nylon shrouds surrounding each detector string can also be seen as slightly darker circles. The darker dots positioned in a triangular symmetry around each detector string mark the locations of the copper bars of the detector holders (see fig. 2.8). In the view from the side (right) the detector strings 4, 7 and 1 (from left to right) can be identified (see also fig. 2.9). The slightly increased energy deposition within the bore holes of the coaxial detectors in string 7 are also visible in the side view. Additionally, the energy deposition is enhanced in the LAr between the BEGe pairs in the top of string 4 and in the bottom in string 1.

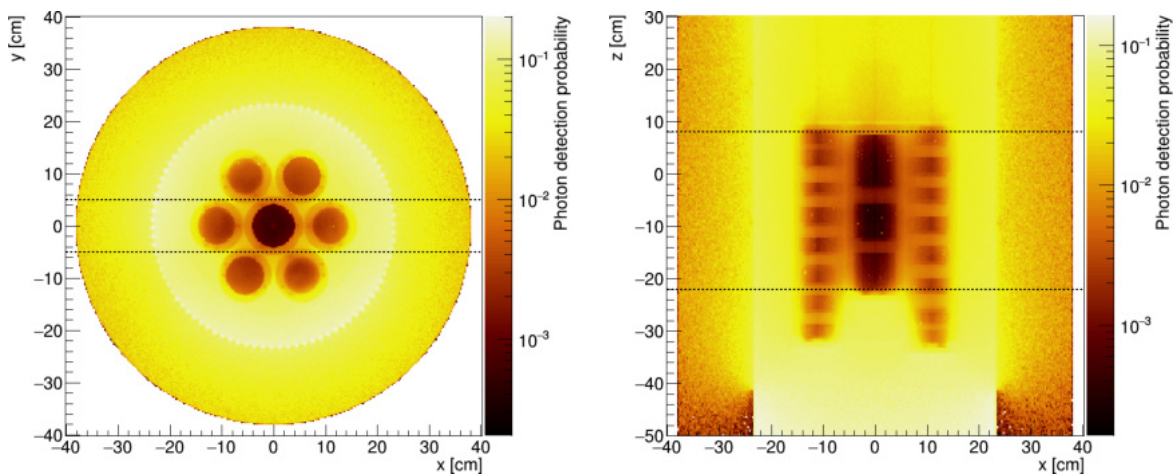


Figure 9.5: LAr photon detection probability map for Phase II of GERDA. It has been produced with simulations using an absorption length of 55 cm and a fiber coverage of 50%. The black dashed lines indicate the range used for the projection of the photon detection probability for the respective other plot. Due to the larger voxel size, geometrical features appear blurry in comparison to the energy deposition shown in figure 9.4. Still, the scintillation fiber curtain with a radius of 23.5 cm as well as the nylon shrouds surrounding each detector string are visible. The map has been produced by simulating the emission of photons in each voxel and determine the probability that a photon is detected by the LAr veto.

9.4 Monte Carlo simulation of the signal signature

The primary particles for the signal simulations are generated with DECAY0 taking into account the angular correlation between the de-excitation γ rays in the case of a γ cascade. In total 10^8 events have been simulated per decay mode. The number of primary particles started in each Ge detector is weighted with the enriched mass of the respective detector. The starting position of the primary particles is randomly chosen within the germanium detectors including the individual active volume and dead layer of each detector. The simulations are performed for the Phase II and the Phase II+ geometry separately.

For the further analysis solely events triggering exactly two different detectors are considered. These events are called M2 (Multiplicity = 2) events. Here, both energy depositions have to exceed a low energy threshold of 200 keV, which is near the optimized value for each decay mode (see sec. 9.6.2 and tab. 9.7).

9.4.1 Detector size and position in the array

The granularity of the detector array as well as the individual detector size and position affects the fraction of M2 events that each detector observes. Figure 9.6 shows the M2 fraction of each detector in Phase II and Phase II+ for the 0_1^+ decay mode. The corresponding plots for the other $2\nu\beta\beta$ decay modes are depicted in appendix B, figure B.2.

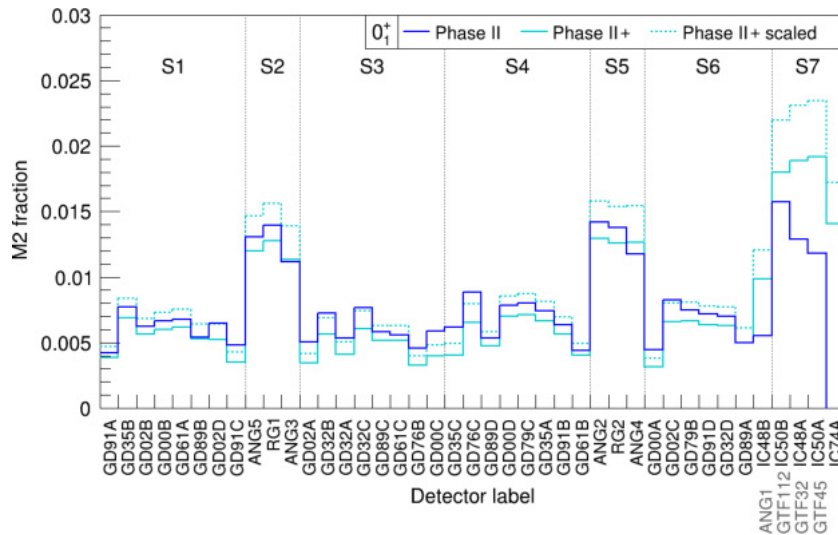


Figure 9.6: M2 fraction for each detector in Phase II and Phase II+ for the raw simulations. The detectors solely operated in Phase II are labeled in gray. These were exchanged by the IC detectors in Phase II+. The number of M2 events contributed by each detector is normalized on the total number of simulated events for all detectors, i.e. the exposures for the solid lines are the same. The M2 fraction for Phase II+ is also scaled with the relative increase of the enriched mass compared to Phase II to indicate the M2 fraction for an equal run time of both setups. Each M2 event triggers two detectors, hence it has two entries in the histogram. The coaxial detectors in string 2, 5 and 7 have a higher probability to absorb γ rays due to their larger size, thus they feature a higher M2 fraction. The natural GTF detectors in string 7 in Phase II have similar M2 fractions despite their low ^{76}Ge mass, which is due to the advanced geometrical position in the middle of the array. An increase of the M2 fraction for the IC detectors in the middle string in Phase II+ can be observed due to the larger enrichment factor.

Due to the large enriched mass of the IC detectors in Phase II+, the relative number of events started in the simulations is smaller for the BEGe and semi-coaxial detectors compared to Phase II. Thus, the fraction of M2 events is smaller for these detectors compared to Phase II for the same total number of simulated events.

However, the Phase II+ array has to run for a shorter time to accumulate the same exposure as in Phase II due to the larger ^{76}Ge mass. Hence, the M2 fraction for Phase II+ is also scaled with the ^{76}Ge mass increment relative to Phase II to get a comparison of the M2 fractions for the same run time, which is equal to comparing the total number of observed M2 events per time. In this case, the M2 fractions for the same run time are larger in Phase II+ for all semi-coaxial detectors and for more than half of the BEGes. The increase is more significant for the semi-coaxial detectors since they have a higher probability of absorbing a γ ray due to their larger mass.

More γ rays leave the detectors in the middle string in Phase II+ compared to Phase II since the IC detectors feature an enrichment of 87.7%, while the natural GTFs contain only 7.8% of ^{76}Ge . This also leads to a larger M2 fraction for all other detectors in Phase II+ serving as γ ray absorbers for the IC detectors. Despite the fact, that the degree of enrichment is 10 times larger for the IC detectors than for the GTFs, the increment of the M2 fraction for the IC detectors is not more than a factor of two, which is due to the large size of both detector types that causes a high self-absorption of γ rays. About 90% of the M2 events observed in the GTF detectors are caused by γ rays emitted by the other detectors, while only 10% are due to the $2\nu\beta\beta$ decay occurring within the GTF detectors. In comparison, the IC detectors feature an equal M2 fraction for absorbing γ rays, but a ten times larger M2 fraction acting as the source detector, leading to a respective contribution of 50% to the overall M2 events observed within an IC detector.

For a dedicated experiment focusing on the search for excited states, an ideal detector size should be utilized, which features an optimal balance between the probability of γ rays escaping a detector and the probability of a full energy deposition. The choice of the detector material and geometry, but also the energy of the de-excitation γ rays affect the ideal detector size.

The M2 fractions shown in figure 9.6 are integrated and listed in table 9.3 for all investigated decay modes. The integrals are already corrected for the double counting of each event. The $2\nu\beta\beta$ of ^{76}Ge is a negligible background for the search for excited states. The 2_1^+ state features a slightly lower M2 fraction compared to the other two excited states since only one de-excitation γ ray is emitted.

Table 9.3: Integrated M2 fractions for each decay mode in Phase II and Phase II+ with an energy threshold of 200 keV for the raw simulations. The values are already corrected for the fact that each event enters the integral twice. The contribution of the decay into the ground state is negligible. Since only one de-excitation γ ray is emitted from the 2_1^+ state, the M2 fraction is smaller than for the other excited states. For the same exposure, the M2 fraction increment in Phase II+ is very tiny compared to Phase II. For the same run time, the scaled M2 fraction is larger by a factor of 1.222 which is equal to the relative increase of the enriched mass from Phase II to Phase II+.

decay mode	Phase II	Phase II+	Phase II+ scaled
$0_{\text{g.s.}}^+ \rightarrow 0_{\text{g.s.}}^+$	0.0538%	0.0522%	0.0638%
$0_{\text{g.s.}}^+ \rightarrow 0_1^+$	15.65%	15.66%	19.13%
$0_{\text{g.s.}}^+ \rightarrow 2_1^+$	10.89%	10.94%	13.37%
$0_{\text{g.s.}}^+ \rightarrow 2_2^+$	15.50%	15.62%	19.09%

Figure 9.6 and table 9.3 only show the situation for the raw simulations, i.e. assuming that all detectors are running the whole time. Thus, in the next step the actual detector configuration and run selection will be taken into account.

Application of the LAr map

The raw simulations are processed with the tier4izer. This includes the smearing of the energy according to the respective energy resolution of the detector and applying an energy threshold of 40 – 150 keV, depending on the detector channel and considering the actual settings in the runs of the measured data. At least one of the energy depositions in a Ge detector has to exceed the given energy threshold, while the energy depositions in the other detectors are allowed to be lower, but need to be more than 40 keV.

The tier4izer also takes into account the run selection and the respective detector configuration. Additionally, the LAr veto cut is applied according to the LAr map and the selected optical parameter tuning. The M2 fractions for each detector in Phase II for a 200 keV energy threshold of both energy depositions is shown in figure 9.7 for all events, LAr vetoed events and events that survive the LAr veto for the decay into the 0_1^+ and the 2_1^+ state. The other decay modes are depicted in figure B.3.

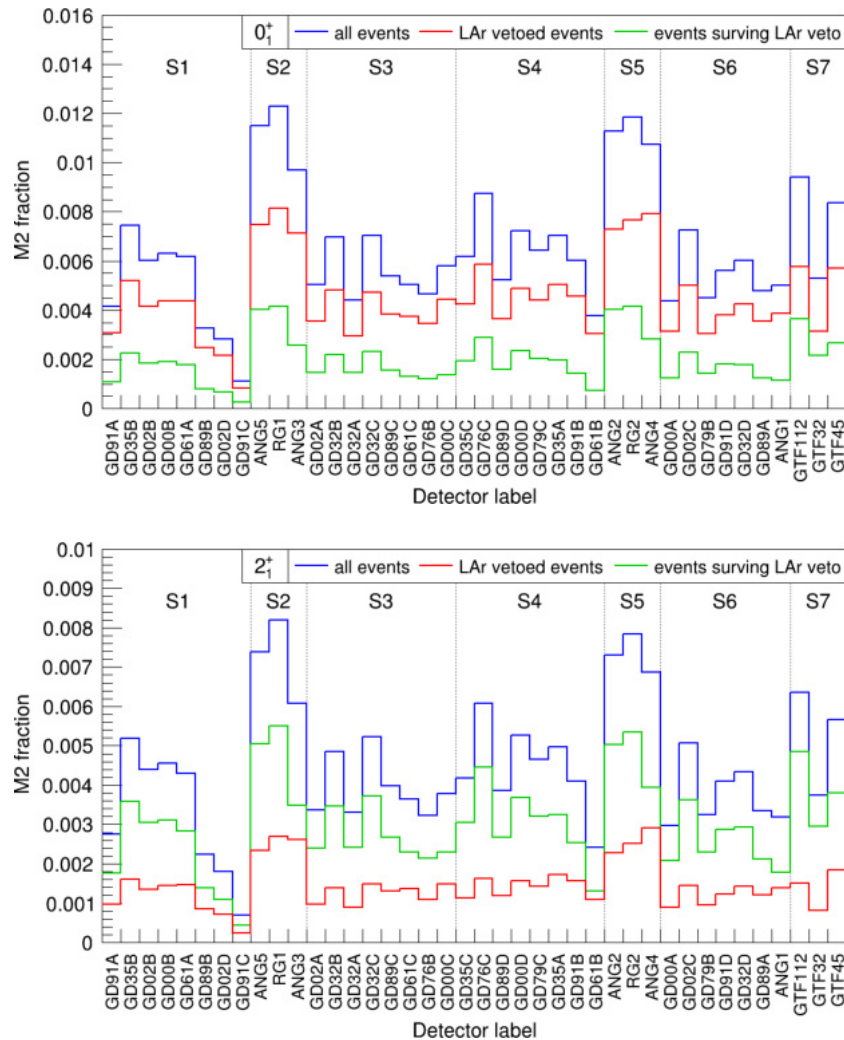


Figure 9.7: M2 fraction of each detector in Phase II for the tier4ized simulations for all events, LAr vetoed events and events surviving the LAr veto cut. Similar features as in figure 9.6 can be observed. Detectors that were switched off during some runs obviously contribute less to the M2 fraction compared to the raw simulations. This applies especially to the BEGes at the bottom of string 1. While for the 0_1^+ state (top) the fraction of LAr vetoed events is about a factor two larger than for the events surviving the LAr veto, the situation is the exact opposite for the 2_1^+ state (bottom). This behavior is caused by the fact, that the 0_1^+ state emits two de-excitation γ rays, but the 2_1^+ state only one, thus energy deposited in the LAr coincident with a M2 event is less likely for the 2_1^+ state. Consequently, less signal events are LAr vetoed for the 2_1^+ state.

While the general structure of the M2 fraction per detector for the tier4ized simulations in figure 9.7 is similar to the raw simulations in figure 9.6, detectors that were switched off during runs feature lower M2 fractions. Since from the 0_1^+ state two γ rays are emitted, while from the 2_1^+ state only one γ ray is released, it is more likely for the former than the latter that a M2 event is accompanied by an energy deposition in LAr. Thus, more signal events are vetoed by the LAr cut for the 0_1^+ state.

The integrated M2 fractions for the tier4ized simulations of Phase II are listed in table 9.4. For Phase II+ it is expected that the fraction of LAr vetoed events increases due to the larger LAr veto efficiency caused by the inner fiber shroud (see fig. 2.6).

Table 9.4: Integrated M2 fractions for each decay mode in Phase II with an energy threshold of 200 keV for the tier4ized simulations for all events, LAr vetoed events and events surviving the LAr veto cut. The $0_{\text{g.s.}}^+$ state is rarely vetoed since the two electrons remain almost every time in the detector. The 2_1^+ M2 events are less often vetoed since only one γ ray is emitted from this decay mode.

decay mode	all events	LAr vetoed	surviving LAr veto
$0_{\text{g.s.}}^+ \rightarrow 0_{\text{g.s.}}^+$	0.0428%	0.0057%	0.0372%
$0_{\text{g.s.}}^+ \rightarrow 0_1^+$	13.00%	9.03%	3.97%
$0_{\text{g.s.}}^+ \rightarrow 2_1^+$	8.92%	2.90%	6.02%
$0_{\text{g.s.}}^+ \rightarrow 2_2^+$	12.78%	8.63%	4.15%

Calorimetric cut for the LAr veto

Since for Phase II+ of GERDA a LAr map is not available at the time of writing, an alternative method is developed. For this, a simulation with photon tracking has been performed for the 0_1^+ state with a fiber coverage of 75% of the outer fiber shroud. This value is an estimate taking into account the number of new fibers installed compared to Phase II. However, the inner fiber shroud is not included in the simulation since it has an extremely complicated geometry and is not yet fully implemented in MaGe. Thus, the analysis of the data ignores the channels of the inner fiber shroud in order to be able to compare simulation and data sufficiently. The other optical parameters remain unchanged, although it is possible that the light yield and absorption length may have been dropped to lower values after a slight contamination of the LAr shortly after the start of Phase II+ (see fig. 2.5).

The simulation with photon tracking is tier4ized taking into account the events triggering the LAr veto. Additionally, the same simulation is tier4ized with a calorimetric cut, i.e. events depositing a certain amount of total energy in the LAr are treated as being vetoed. For Phase II it has been found that a calorimetric cut of 129 keV vetoes the same amount of events compared to the application of the LAr map. For Phase II+ the comparison of the simulation with photon tracking yields a calorimetric cut value of 94.5 keV. Since the LAr veto is more effective in Phase II+ due to more scintillation fibers and a denser arrangement of the fiber shroud, also more events should be LAr vetoed. Thus, the energy of the calorimetric cut is lower.

The integrated multiplicity fractions are listed in table 9.5 and the individual contributions of each detector are shown in appendix B, figure B.4.

Table 9.5: Integrated M2 fractions for each decay mode in Phase II+ with an energy threshold of 200 keV for the tier4ized simulations for all events, LAr vetoed events and events surviving the LAr veto cut. The LAr veto is applied with a calorimetric cut for the total energy of 94.5 keV that an event deposited in LAr.

decay mode	all events	LAr vetoed	surviving LAr veto
$0_{\text{g.s.}}^+ \rightarrow 0_1^+$	13.02%	9.18%	3.85%
$0_{\text{g.s.}}^+ \rightarrow 2_1^+$	9.14%	3.20%	5.93%
$0_{\text{g.s.}}^+ \rightarrow 2_2^+$	12.89%	8.92%	3.98%

9.4.2 Signal signature of the decay modes

The signal signature of each decay mode is investigated with simulations to define the ROI for each decay mode. The signal cuts and their efficiencies are determined with the tier4ized simulations for the analysis which is based on a cut and count method (see sec. 9.6.2 and 9.6.3). The simulations shown in this section reflect the Phase II run selection. The counts are scaled to the Phase II exposure and the half life limits achieved in [Wes19].

$0_{\text{g.s.}}^+ \rightarrow 0_1^+$

The deposited energies of the M2 events are depicted in two-dimensional plots in figure 9.8 for all events, LAr vetoed events and events surviving the LAr veto. The signal has been scaled to a half life of $3.1 \cdot 10^{23}$ yr [Wes19].

The horizontal and vertical lines forming a cross in the two-dimensional spectra are equal to the respective full energy deposition of one of the two de-excitation γ rays. The energy resolution is sufficient to distinguish the two γ lines at 559.1 keV and 563.2 keV (see fig. 9.1), although only one line can be observed at this energy in the visualization. Along these lines, the energy in the other detector corresponds to the energy of the two electrons of up to 916.8 keV and it can also include a part or the full energy of the other γ ray. Thus, the γ line can be accompanied by an energy deposition of up to 1480 keV.

One-dimensional depictions of the M2 events are shown in figure 9.9. The single spectra show the energy deposited per detector and the sum spectra the sum of the two energies. Lines in the single spectra correspond to horizontal and vertical lines in the two-dimensional spectra and lines in the sum spectra are equal to diagonal lines in figure 9.8. The latter are hard to see in the two-dimensional depiction.

In the single spectra a line at the sum energy of both γ rays can be seen at 1122.3 keV. This line is hardly visible in the two-dimensional plot since it is very unlikely that both γ rays deposit their energy in the same detector, while another detector observes the electrons. Thus, this line has a low efficiency contribution and is neglected for the analysis. The same is true for the lines in the sum spectra, which feature a much lower count rate compared to the lines at 559.1 keV and 563.2 keV in the single spectra. Thus, the signal cut condition for the 0_1^+ state requires that one of two energy depositions equals the energy of one of the γ rays with respect to a certain energy window width which is defined by the energy resolution.

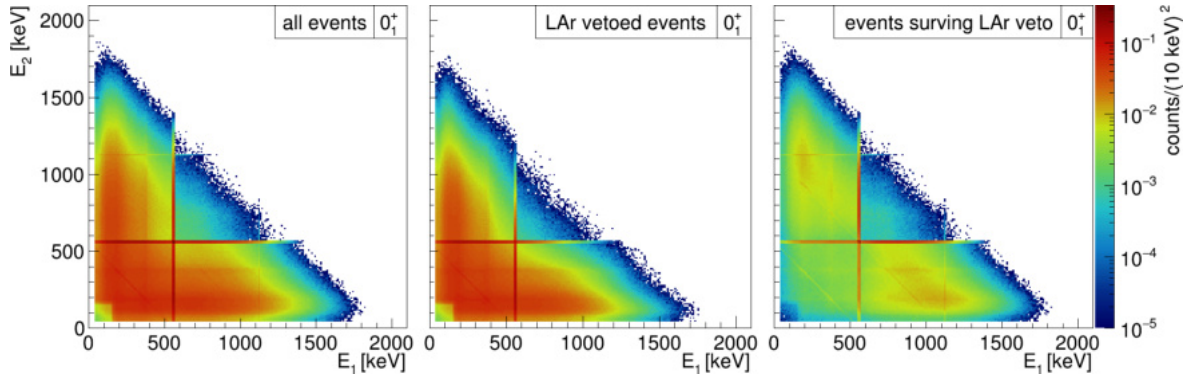


Figure 9.8: Two-dimensional plot of the energy depositions of M2 events for the 0_1^+ state. The energy deposition of the detector with the lower ID number is depicted on the bottom axis. The horizontal and vertical lines correspond to the full energy deposition of one of the two de-excitation γ rays (see fig. 9.1). While these are also LAR vetoed (middle), the lines stick out more clearly in the plot of the events surviving the LAR veto (right).

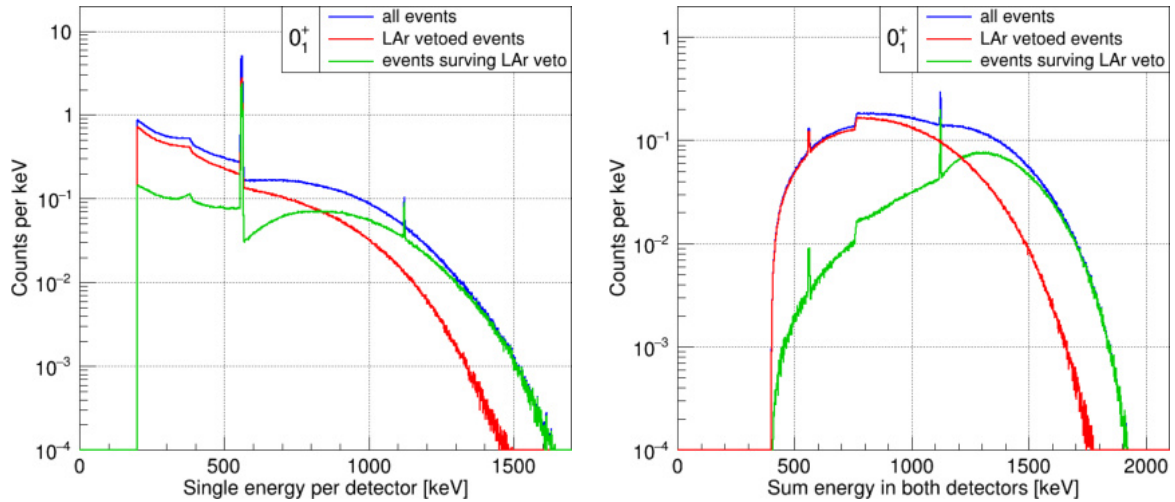


Figure 9.9: Single detector spectra (left) and sum spectra (right) of M2 events for the 0_1^+ state. In the single spectra the respective energy deposited per detector is plotted and in the sum spectra the sum of these two energies is shown. The single spectra for all events and events surviving the LAR veto feature lines at the γ energy and their sum. The sum energy line in the single spectrum is not LAR vetoed since the corresponding spectrum does not show a line at this energy. The lines in the sum energy spectrum match the energies of diagonal lines in the 2D spectrum in figure 9.1. The sum energy line of the both γ rays is not LAR vetoed in the sum spectra. Both, single and sum spectra, show that the continuous regions in the low energy part are suppressed significantly by the LAR veto.

$0_{\text{g.s.}}^+ \rightarrow 2_1^+$

The two- and one-dimensional spectra for the 2_1^+ state are shown in figures 9.10 and 9.11, respectively. The signal is scaled to a half life of $3.4 \cdot 10^{23}$ yr [Wes19].

The spectra look very similar compared to the 0_1^+ state, but the 2_1^+ state emits only one de-excitation γ ray at 559.1 keV. The full energy deposition of this γ ray in one detector is accompanied by the energy deposition of the two electrons in another detector.

Since it is very unlikely, that the electrons or the produced bremsstrahlung leave the source detector, events that enter the γ peak are extremely rarely LAR vetoed. Thus, the intensity of the γ line is almost the same for the events surviving the LAR compared to all events.

Although the 559.1 keV line in the sum spectra is more prominent, the intensity is much lower compared to the single spectra. Consequently, the signal cut requires that one of the two energy depositions equals the full energy of the γ ray.

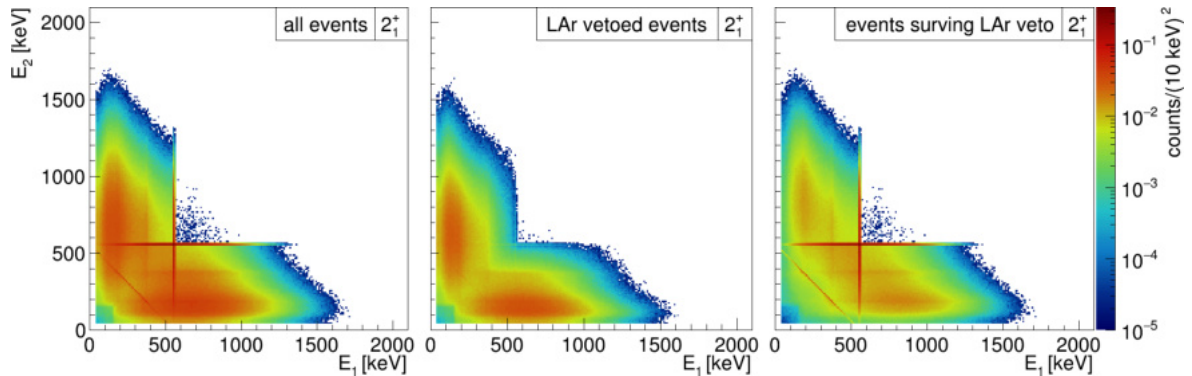


Figure 9.10: Two-dimensional plot of the energy depositions of M2 events for the 2_1^+ state. The full energy deposition of the γ ray is rarely LAR vetoed, thus it is more prominent in the spectra of the events surviving the LAR veto. The diagonal line represents the γ ray depositing part of its energy in one detector and the remaining energy in another, while the electrons are not observed. This can happen, when the $\beta\beta$ decay occurs in the dead layer of the detector or when the electrons convert their energy into bremsstrahlung which leaves the detector unseen. The former case likely survives the LAR veto cut, while the latter has a large probability to be vetoed. Since the diagonal line is more prominent in the spectra of events surviving the LAR veto and almost invisible in the LAR vetoed events, the former case occurs dominantly.

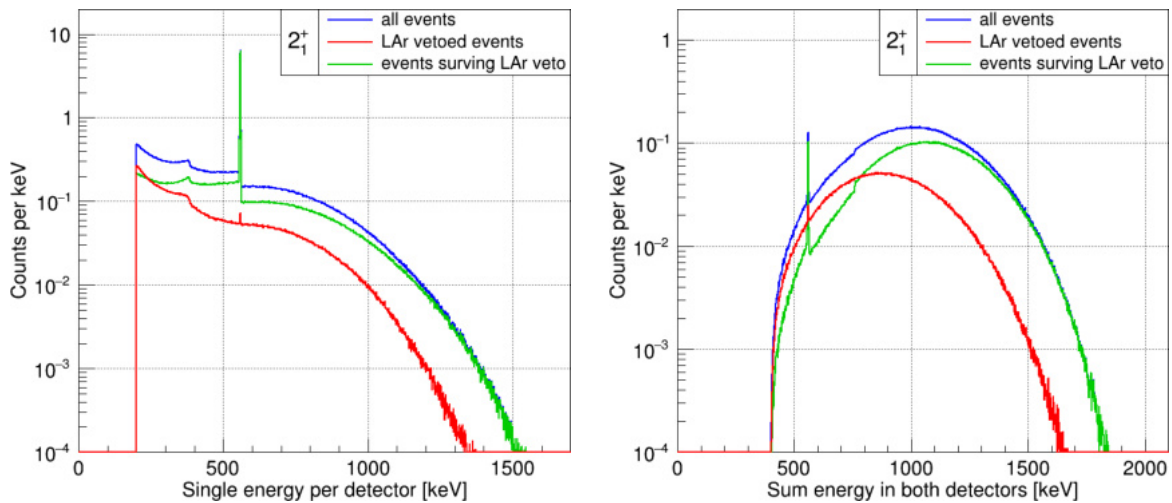


Figure 9.11: Single detector spectra (left) and sum spectra (right) of M2 events for the 2_1^+ state. In both spectra, the γ line is very rarely LAR vetoed. Although the γ line in the sum spectra is very prominent, its intensity is very small compared to the line in the single spectra. Thus, it is not further taken into account.

$$0_{\text{g.s.}}^+ \rightarrow 2_2^+$$

The corresponding plots of the two- and one-dimensional spectra for the 2_2^+ state are depicted in figure 9.12 and 9.13. The spectra have been scaled to match a half life of $2.5 \cdot 10^{23}$ yr [Wes19].

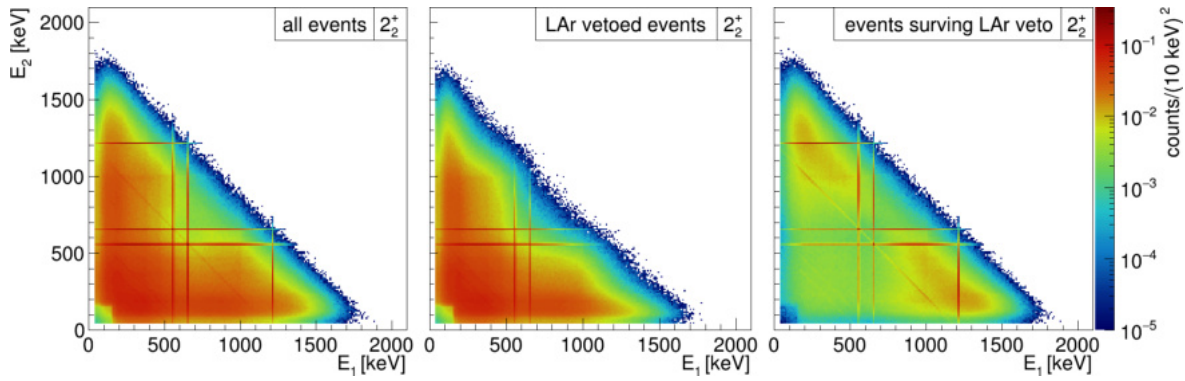


Figure 9.12: Two-dimensional plot of the energy depositions of M2 events for the 2_2^+ state. The two lower energy lines correspond to B1, while the high energy line is emitted by B2 (see fig. 9.1). Since only the two electrons and neutrinos are emitted along the γ ray from B2, no energy is deposited in LAr and this line does not occur in the LAr vetoed spectrum.

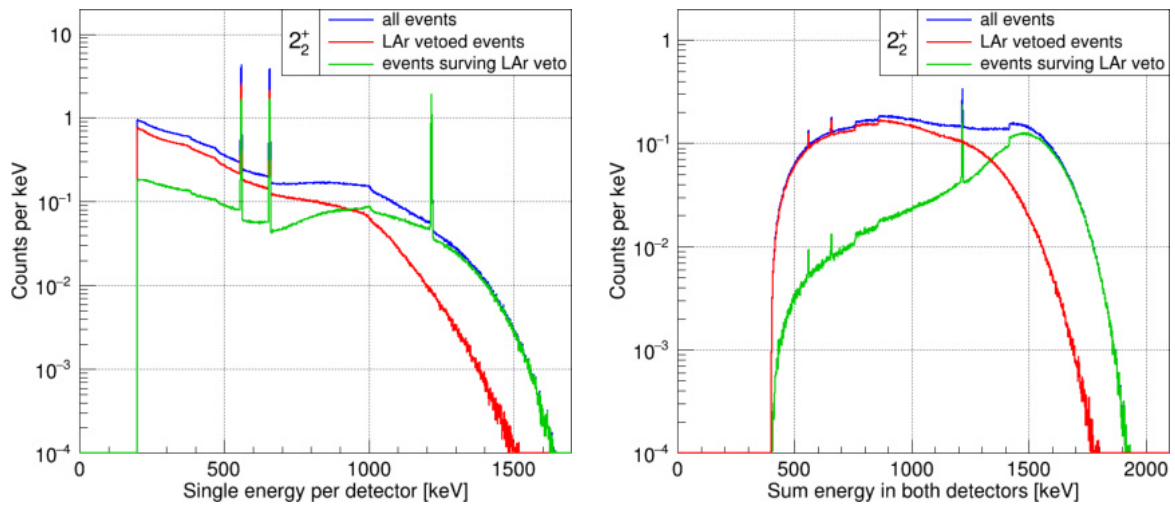


Figure 9.13: Single detector spectra (left) and sum spectra (right) of M2 events for the 2_2^+ state. While the lower energy lines of B1 lose some of their intensity due to the LAr veto, the 1216.1 keV line from B2 is not visible in the LAr vetoed spectra.

Due to the two de-excitation branches with two and one emitted γ ray, respectively, the spectra of the 2_2^+ combines features of the 0_1^+ and 2_1^+ states. In contrast to the 0_1^+ state, the two γ energies of the 2_2^+ B1 state (see fig. 9.1) are distinguishable in the visualization, creating a double cross pattern in the two-dimensional plot.

The γ line at 559.1 keV can be accompanied by the energy deposition of the electrons and the other γ ray reaching an energy deposition in the other detector up to 1480 keV. Along the 657.0 keV γ line an energy up to 1382.1 keV can be observed in the other detector. Since the respective other γ ray can leave the Ge detectors unseen or deposit only a part of its energy, the remaining energy can be released in the LAr. Thus, these lines occur in the LAr vetoed spectra very prominently.

The γ line at 1216.1 keV from the 2_2^+ B2 state is accompanied by an energy deposition of the electrons of up to 823.0 keV in the other detector. Since the energy available for the electrons is lower compared to the 2_1^+ state, they rarely produce bremsstrahlung, which could deposit energy in LAr. Thus, this γ line is almost never LAr vetoed and occurs in the same intensity in the events surviving the LAr veto as observed in all events.

The intensity of the γ lines in the sum spectra are much lower than in the single spectra, thus they are not further considered in the analysis. The signal cut for B1 is divided in two ROIs demanding one of the two energy deposition to be equal to one of the two γ ray energies, while for B2 one ROI is defined to match the energy of the corresponding γ ray.

9.5 Data sets

The search for the decay into excited states is performed for Phase II and Phase II+ data of GERDA. Solely M2 events are taken into account, since higher multiplicities have a comparatively tiny sensitivity. Table 9.6 lists important parameters of the data sets used for the analysis. Run periods where the setup did not perform perfectly stable, are not considered in the analysis. This applies to run 66 where the muon Cherenkov veto was switched off, run 68 when the test pulser did not work, runs 80 – 82 where the water tank was empty or partly filled due to a valve failure and run 102 which was a special ^{226}Ra calibration run.

Each individual run reflects constant settings regarding detectors that were fully operational, switched off or only used in anti-coincidence mode. The latter are not considered for triggering on an event and the energy is not reconstructed for those detectors. The run settings also include the trigger thresholds, which were around 150 keV until run 86 and lowered since run 87 to about 25 keV depending on the detector and run. For the offline analysis an energy threshold of 40 keV is used for all detectors. According to the run selection and detector configuration, the live time and exposure of the data sets are calculated.

Table 9.6: Important parameters of the Phase II and Phase II+ data sets used for the analysis. Runs with unstable conditions are rejected for the analysis. The natural detectors in Phase II were replaced by almost the same total mass of new enriched detectors in Phase II+, leading to a larger overall ^{76}Ge mass.

parameter	Phase II	Phase II+
start date	20.12.2015	25.05.2018
end date	03.04.2018	11.11.2019
run selection	53 – 92	95 – 114
rejected runs	66, 68, 80 – 82	102
live time [d]	683.3	428.6
detector mass [kg]	43.2	44.5
^{76}Ge mass [kg]	31.7	38.8
exposure [kg · yr]	60.1	43.6

The tier4 data is already corrected for cross-talk effects as described in [Wes19]. The energy is reconstructed using the Zero Area Cusp (ZAC) signal shaping filter [GER15b]. An individual calibration curve for each detector is extracted from a combination of all calibration measurements taken during Phase II and Phase II+, respectively. The calibration curve is described by the following formula.

$$\text{FWHM}(E) = 2.35482 \cdot \sqrt{p_0 + p_1 \cdot E} \quad (9.4)$$

The corresponding fit parameters vary between the detectors for Phase II in the range of $0.20 < p_0 < 2.45$ and $0.00033 < p_1 < 0.00095$ and for Phase II+ within $0.18 < p_0 < 1.50$ and $0.00029 < p_1 < 0.0055$. Instead of extracting the resolution curves from the M2 data as discussed in [Wes19], the same resolution curves as for the M1 data is used here since the difference between both approaches is not significant anymore due to an improved cross-talk correction.

9.6 Analysis

In the following, the signal cuts are optimized in order to improve the signal to background ratio. For that, the underlying background model is explained first and prominent background lines are considered for exclusion cuts. In a second step the signal cuts and their optimization are discussed. The goal is to maximize the sensitivity for each decay mode. The resulting signal efficiencies are calculated with the corresponding signal MC simulations for each decay mode. For a background model independent analysis, sideband (SB) regions are positioned close to the ROI in order to determine the number of background counts expected in the ROI.

9.6.1 Background model

The background model has been developed for Phase II M1 and M2 data as described in [GER20]. For that, the decay of all relevant radioactive contaminations inside GERDA have been simulated for each part according to expectations from preceding screening measurements and observed γ lines. The considered parts are the Ge detectors themselves, holders, cables, mini-shrouds, fiber shroud, copper shrouds, PMTs, SiPMs and the LAr volume surrounding the detector array. In a global fit all these components are combined to match the measured spectrum. In this step, the corresponding activity of each nuclide is determined for every part.

Figure 9.14 shows the two-dimensional depiction of the background model for the Phase II M2 data and in figure 9.15 are the corresponding projections of the single and the sum energy spectra. The spectra are scaled to reflect the Phase II exposure, i.e. the counts are the expected background counts for the considered Phase II data set as described in section 9.5.

Vertical and horizontal lines in the two-dimensional spectra correspond to γ lines in the single detector spectra, while diagonal lines refer to γ lines in the sum spectra. The most prominent γ lines are caused by ^{40}K at 1460.8 keV and ^{42}K at 1524.6 keV [IAE20]. While ^{40}K is contained in all parts close to the Ge detectors, ^{42}K is a daughter nuclide of ^{42}Ar , which is, according to the background model, distributed inhomogeneously within the LAr surrounding the detector array.

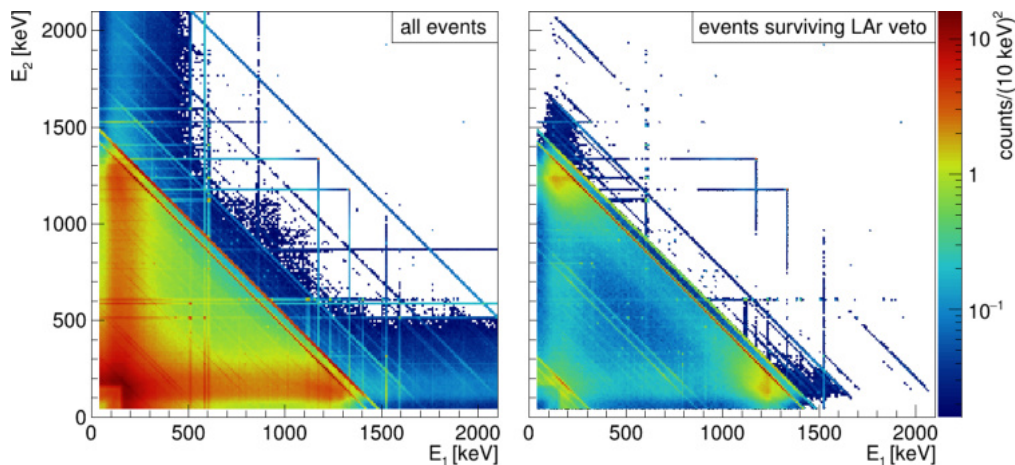


Figure 9.14: Two-dimensional depiction of the background model for Phase II for all events (left) and events that survived the LAr veto cut (right). The model including the LAr veto is preliminary and can change with an improved LAr map. The two most prominent diagonal lines are from ^{40}K and ^{42}K , which are also visible in the sum energy spectra in figure 9.15. The ^{42}K γ line gets effectively LAr vetoed due to the accompanying electron depositing energy in the LAr, which is not the case for the EC of ^{40}K . Also, the γ lines of ^{228}Ac get more prominent in the spectra of the events surviving the LAr veto cut.

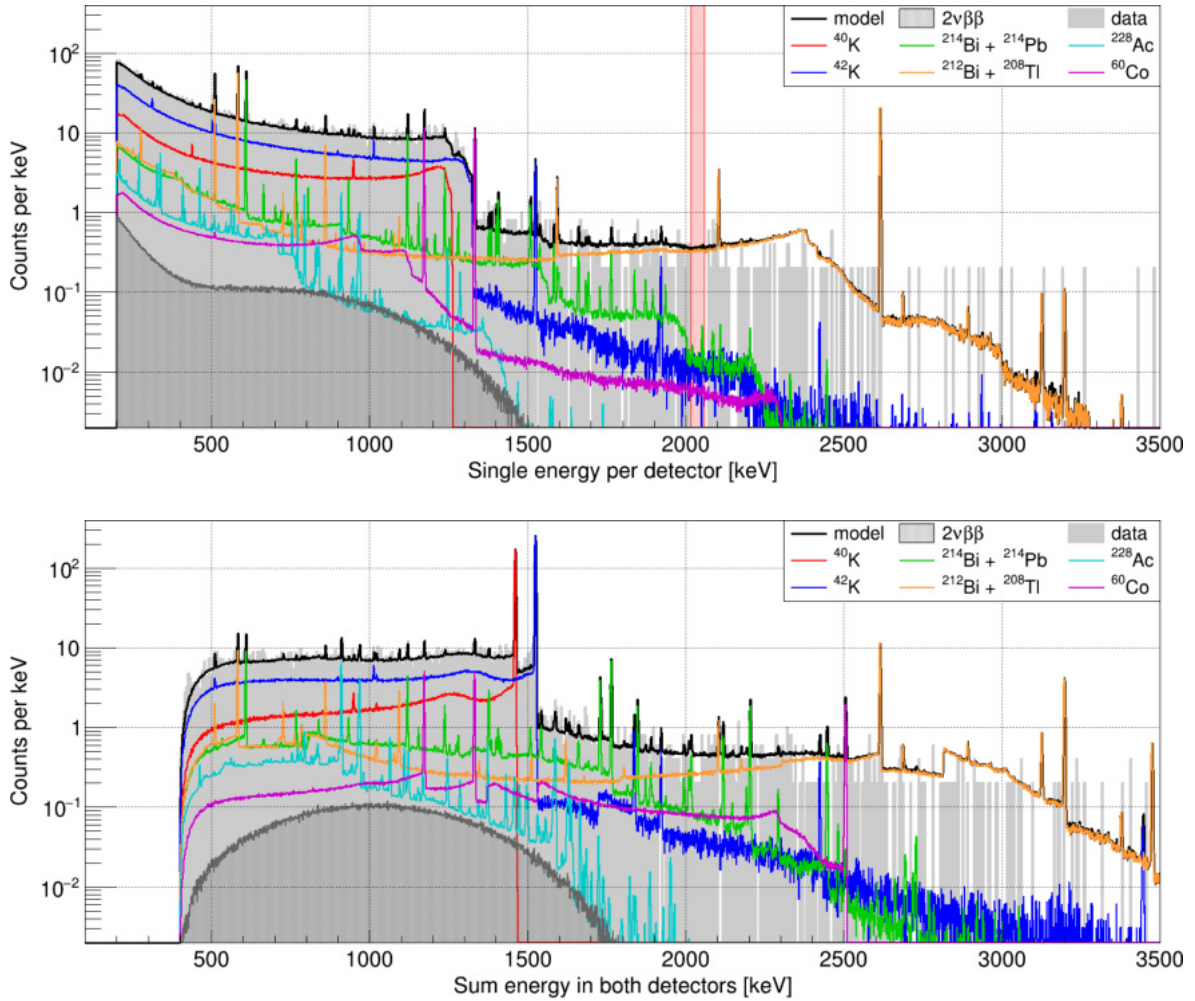


Figure 9.15: Single detector spectra (top) and sum spectra (bottom) of the background model for M2 events for Phase II with a threshold of 200 keV for both energy depositions. The edges in the sum spectra 200 keV above several γ lines are due to this energy threshold. The respective spectra with an energy threshold of 40 keV are depicted in figure B.5. The sum energy spectra are also published with an energy threshold of 40 keV in [GER20]. The contribution of the $2\nu\beta\beta$ decay of ^{76}Ge into the ground state of ^{76}Se to the background for the excited states analysis is negligible compared to the radioactive contaminations in the setup. The single detector spectrum of the $2\nu\beta\beta$ decay in the low energy region is dominated by bremsstrahlung escaping the source detector. This effect is not visible in the sum spectra, since the sum of the energies of the electrons remaining in the source detector and the bremsstrahlung photon observed by another detector is plotted. The corresponding spectra for the events surviving the LAr veto cut are shown in figure B.6 and B.7. The data are plotted with a bin width of 5 keV and scaled accordingly in order to reflect the counts per keV. The data are blinded at $Q_{\beta\beta} \pm 25$ keV indicated by the light red band in the single detector spectra.

Consequently, the electron emitted in the β^- decay of ^{42}K deposits almost always energy in LAr which can be detected by the LAr veto. Hence, the ^{42}K γ line can be effectively suppressed by the LAr veto. On the contrary, the γ line from ^{40}K is the follow-up of an EC, thus no energy is deposited in LAr and the γ line survives the LAr veto cut. Both effects are visible in the two-dimensional spectra in figure 9.14 as well as in the single and sum spectra in appendix B, figures B.6 and B.7.

However, the ^{40}K and ^{42}K lines are only dominant in the sum spectra. In the two-dimensional depiction these diagonal lines cross the vertical and horizontal signal lines, thus they need to be removed for the analysis. This is done by excluding energy depositions that are in sum in a ± 5 keV window around the ^{40}K and ^{42}K γ energies.

Additionally, the γ lines of ^{228}Ac at 911.2 keV, 964.8 keV and 969.0 keV [IAE20] are barely visible in the spectra of all events, but get much more prominent after applying the LAr veto cut. However, their intensities are negligible compared to the ^{40}K and ^{42}K lines.

The background model also serves for the verification that the background near the ROI is flat or linear. For that, SBs are located symmetrically around the ROI. With the aid of the background model, the SBs are positioned in order to avoid locations of known γ lines. Due to the better energy resolutions caused by the ZAC filter, the optimized widths of the ROI windows are smaller compared to [Wes19]. Thus, the positions of the SBs are reevaluated for Phase II data.

The background behaves equally for Phase II+ with the exception of a new ^{65}Zn contamination on the IC detectors. However, as this occurs only in the M1 data set, it is not relevant for the M2 data analysis. Thus, for Phase II+ the same window width and SB positions are used as for Phase II and no new background model is developed. As a consequence, sensitivities cannot be calculated from the MC background expectation as it was done in [Wes19].

9.6.2 Signal cuts and optimization

The data is processed in a tier structure, where several basic cuts are applied. This includes quality cuts and the rejection of muon vetoed events. For the excited states analysis only M2 events with both energy depositions above 40 keV are taken into account. The analysis is performed for all events without considering the LAr veto cut and also for events that survive the LAr veto cut. Both approaches are discussed together in the following. However, the signal cuts are independent of the LAr veto cut application.

Signal cut optimization

The optimization has the goal to maximize the sensitivity and is performed using a Feldman-Cousins approach as described in [Wes19].

One of the two energy depositions needs to be equal to the energy of the de-excitation γ ray of the regarded decay mode. The other energy deposition is very likely caused by the electrons of the $\beta\beta$ decay and the partly or fully contribution of the other de-excitation γ ray, if applicable. Thus, constraining the low and high energy threshold of this second energy deposition is equal to selecting the part of the $\beta\beta$ spectra with a sufficiently large emission probability. Consequently, the low and high energy threshold are optimized per decay mode due to the varying energies available for the electrons. The low energy threshold is varied between 50 keV and 500 keV in steps of 10 keV and the high energy threshold is investigated between 800 keV and 1500 keV in steps of 50 keV. Due to the lower electron energy, the ranges are different for the 2_2^+ state, i.e. the low energy threshold is changed within 100 keV and 400 keV and the high energy threshold between 500 keV and 850 keV.

The optimization of the window width of each ROI is dependent on the energy resolution. It is investigated in steps of 0.1 keV within 0.7 keV and 2.5 keV for all decay modes. For the 0_1^+ state, the ROIs for the two γ lines overlap for values of the window width that are larger than 2.05 keV. The optimized value is found to be smaller. The resulting optimized window width for each decay mode as well as the low and high energy thresholds are summarized in table 9.7. All three parameters are used for Phase II and Phase II+.

In Phase II the middle string is composed of natural detectors which feature a much lower rate of $\beta\beta$ decays compared to the enriched detectors. However, they are very good γ ray absorbers as shown in figure 9.6. Thus, they are considered in the analysis as potential γ ray detectors, where the energy is equal to the ROI, but excluded as source detectors.

An individual detector pair selection as described in [Wes19] is not performed because the sensitivity gain is comparatively small when the natural detectors are already excluded as source detectors. Since in Phase II+ solely enriched detectors are operated and also because there exists no background model yet, a detection pair selection is not applied.

$0_{g.s.}^+ \rightarrow 0_1^+$ signal cut

The ROI is divided in two regions next to each other due to the two γ lines at 559.1 keV and 563.2 keV. One of the two energy depositions has to be equal to one of those energies within ± 1.4 keV. SBs are arranged symmetrically around the mean of the two ROIs avoiding background lines as shown in figure 9.16. The energy in the other detector needs to be between 210 keV and 1250 keV which corresponds to the $\beta\beta$ decay of a maximum energy of 916.8 keV and the potential contribution of the other γ ray.

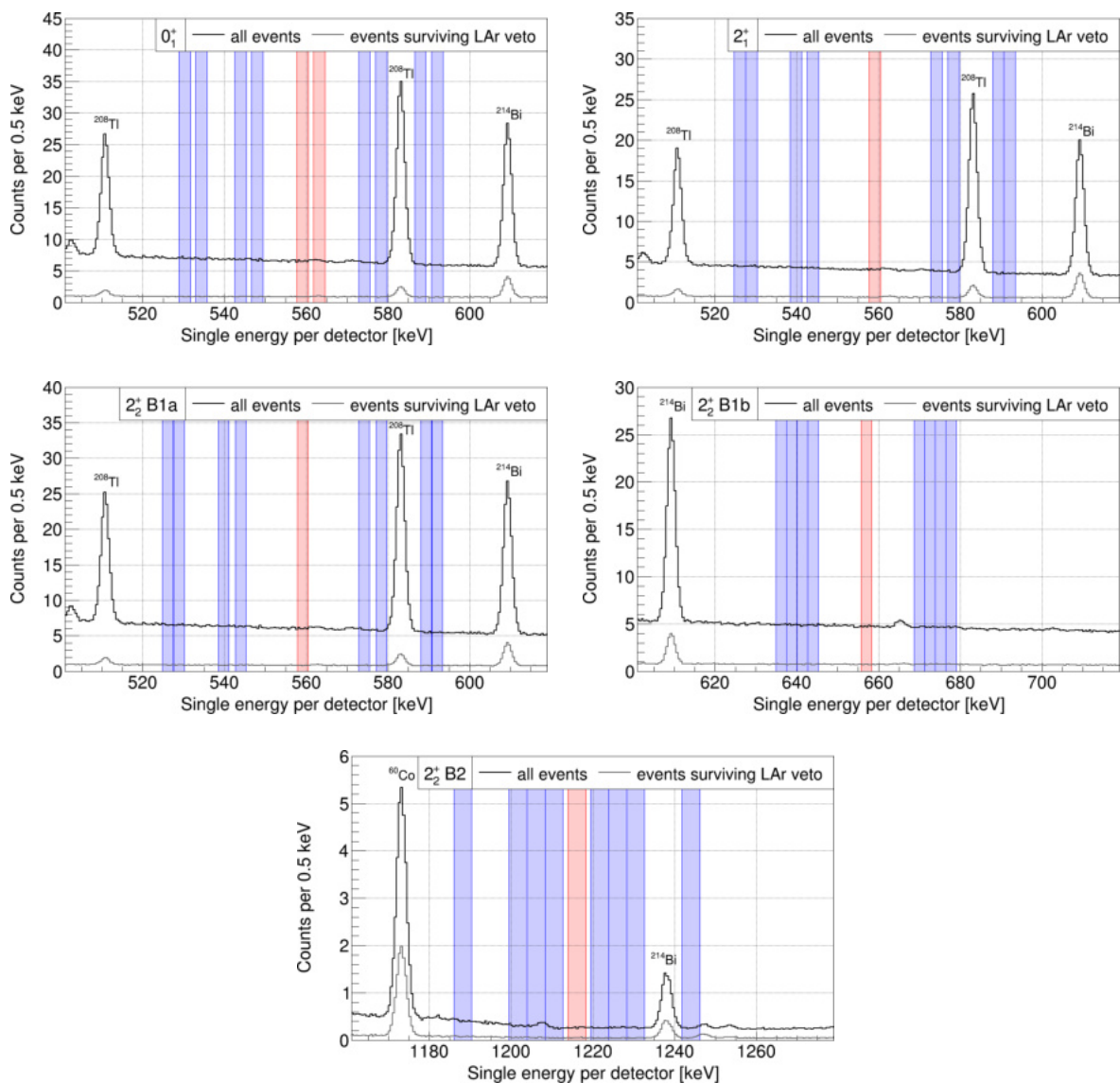


Figure 9.16: ROI (red) and SB (blue) positions for all three decay modes. The background model with an energy threshold of 200 keV for all events and events surviving the LAr veto cut indicates the locations of considered γ lines near the ROIs. A list of the center energies of the ROI and SB positions is compiled in table B.1.

$0_{\text{g.s.}}^+ \rightarrow 2_1^+$ signal cut

One ROI is defined with a width of ± 1.4 keV around 559.1 keV. The other energy deposition needs to be within 360 keV and 1150 keV corresponding to the electrons that can receive a maximum energy of 1480 keV.

 $0_{\text{g.s.}}^+ \rightarrow 2_2^+$ signal cut

For the first decay branch (B1) two ROIs are defined with ± 1.3 keV at 559.1 keV and 657.0 keV, respectively. For each ROI, SBs are assigned separately as shown in figure 9.16. The other energy deposition is restricted to not overlap with the ROI of the second branch and needs to be within 230 keV and 1180 keV which reflects the maximum electron energy of 823.0 keV overlaid with the energy deposition of the other γ ray.

The second decay branch (B2) features only one ROI which is ± 2.2 keV at 1216.1 keV. The other energy deposition has to be between 310 keV and 600 keV corresponding to the preceding $\beta\beta$ decay that distributes a maximum energy of 823 keV to the electrons.

After applying the signal cut, events can occur where one of the two energy depositions is in a ROI and the other in a SB. For such an event an unambiguous assignment to either ROI or SB cannot be made. Such events are not taken into account in order to avoid double counting.

9.6.3 Signal cut efficiencies

In total 10^8 decays were simulated per investigated decay mode in all detectors with regard to their respective enrichment fraction. The simulations are tier4ized taking into account the run configurations in Phase II and Phase II+ as discussed in section 9.5. With the help of the MC simulations, the efficiency is determined per decay mode as the ratio of counts that survive all described cuts. A list of the calculated efficiencies for Phase II and Phase II+ with and without the application of the LAr veto is given in table 9.7.

Table 9.7: Summary of the optimized values for the low and high energy thresholds and the window width of the ROI and SBs, which are equal to $\pm w$. Also listed are the efficiencies for Phase II and Phase II+ for all events (ε) and events that survive the LAr veto cut (ε_{LAr}). The decay modes emitting only one de-excitation γ ray deposit almost never energy in the LAr when the full energy of the γ ray is detected, thus the efficiency is almost equal for all events and LAr veto applied. The efficiencies for Phase II+ are in general larger due to the larger enriched detector mass. The efficiency determination for Phase II+ with LAr is done omitting the inner fiber shroud. When including it, the corresponding efficiencies are expected to decrease since more events will be vetoed.

decay mode	E_{low} [keV]	E_{high} [keV]	w [keV]	Phase II		Phase II+	
				ε [%]	ε_{LAr} [%]	ε [%]	ε_{LAr} [%]
$0_{\text{g.s.}}^+ \rightarrow 0_1^+$	210	1250	1.4	1.784	0.835	2.030	0.925
$0_{\text{g.s.}}^+ \rightarrow 2_1^+$	360	1150	1.4	1.118	1.115	1.265	1.262
$0_{\text{g.s.}}^+ \rightarrow 2_2^+$	B1	230	1180	1.078	0.468	1.227	0.521
	B2	310	600	0.217	0.217	0.242	0.242

Several parameters used for the efficiency calculation introduce various systematic uncertainties. In order to account for that, these parameters are changed within a minimum and maximum value and the efficiency is recalculated.

Active volume and dead layer thickness of each detector

A larger active volume (smaller dead layer) increases the detection probability for the electrons and γ rays and vice versa. More decays are occurring within a thicker dead layer, resulting in less electrons that get detected. The dead layer of each detector is varied within $\pm 3\sigma$ in the tier4izer and the MC simulations are reprocessed to determine the change in the efficiency. The dead layer uncertainty introduces a systematic uncertainty of about 1 – 5% for the efficiency [Wes19].

Energy resolution and energy scale

The window width of the ROI is dependent on the energy resolution. If the energy resolution gets worse, a smaller fraction of the signal peak is covered by the ROI and the other way around. Additionally, a shift in the energy scale would cause the signal peak to move away from the center of the ROI, decreasing the efficiency in any case. The energy resolution and scale result in a systematic uncertainty of 1 – 4% for the efficiency [Wes19].

MC simulations

A systematic uncertainty of 4% is assumed to be introduced by the implementation of the physics processes in GEANT4 [GER15a]. The statistical uncertainty of the MC simulations is negligible.

9.7 Data count results

The data in the tier4 structure already includes a threshold of 40 keV for each energy deposition. By applying an energy threshold, the multiplicity of an event can be altered. In the case one of the energy depositions of a M2 event is below the energy threshold, the event changes to M1 and is not considered any further. M3 events, that feature two energy depositions above the threshold and one below, are treated as M2 events after applying the energy threshold. An equivalent behavior can occur for higher multiplicity events. However, the number of events with higher multiplicities is only about 5% compared to M2 events, thus the fraction of events counting as M2 with an initially higher multiplicity is negligible.

Figure 9.17 shows the two-dimensional depiction of the M2 data events with an energy threshold of 40 keV for Phase II and Phase II+ with and without the application of the LAr veto cut.

Due to the larger exposure in Phase II, more events are registered than for Phase II+. The LAr veto cut suppresses the ^{42}K line effectively, while the ^{40}K line is still very well visible in the events surviving the LAr veto. Events with a sum energy equal to the γ lines of ^{40}K and ^{42}K are removed from the data for the analysis.

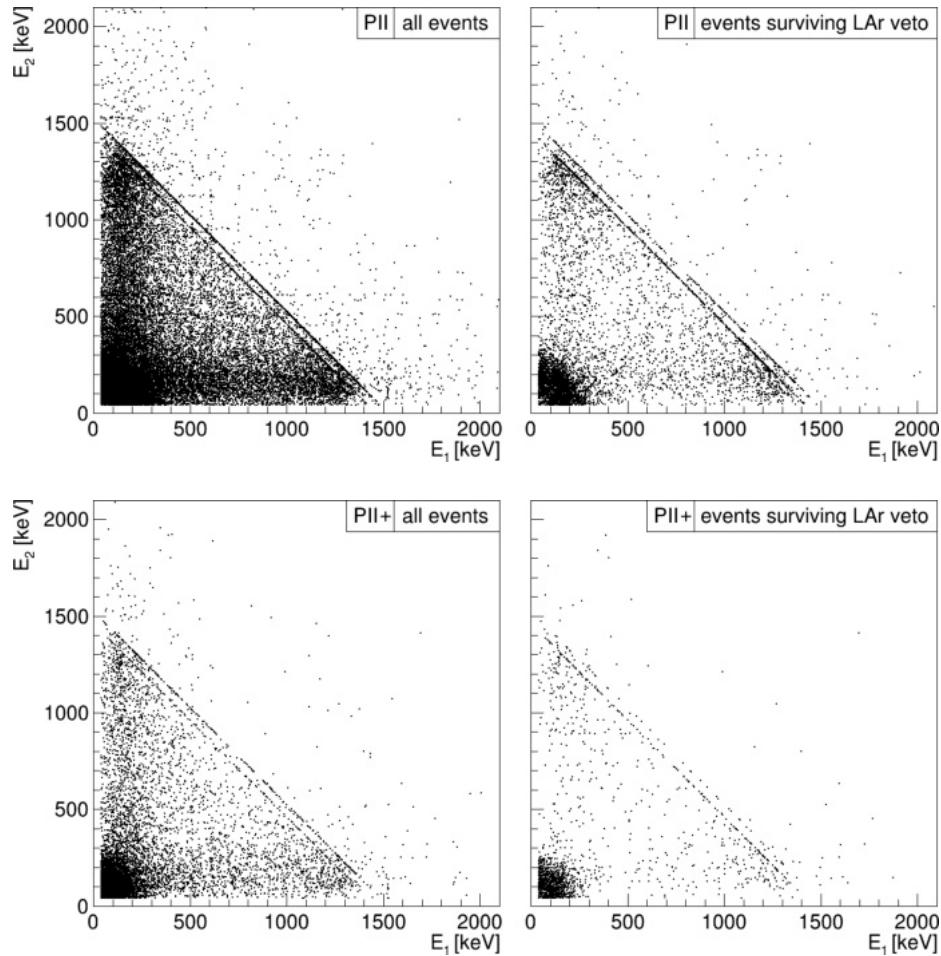


Figure 9.17: Two-dimensional depiction of the M2 data with an energy threshold of 40 keV for Phase II (top) and Phase II+ (bottom) without (left) and with (right) applying the LAr veto cut, but ignoring the inner fiber shroud. The diagonal lines are from ^{40}K and ^{42}K causing the main background and are therefore removed for the excited states analysis.

The optimized signal cuts (see tab. 9.7) are applied to the data and the respective number of counts surviving all cuts for each decay mode is determined. This is not only done for each ROI, but also for the corresponding SBs in order to calculate the expected number of background counts for the ROI. Figure 9.18 shows the respective surviving counts in the ROI and SBs for each decay mode. A detailed list of the obtained counts with and without applying the LAr veto for Phase II and Phase II+ is given in table 9.8.

Since the exposure in Phase II+ is lower and the efficiency only slightly larger in comparison to Phase II, in general less counts are expected in Phase II+. An excess of the counts in the ROI with respect to the expected counts derived from the SBs is observed for all decay modes in Phase II, but not in Phase II+. The 559.1 keV γ ray occurs in the decay modes 0_1^+ , 2_1^+ and 2_2^+ B1 and consequently the corresponding ROI is shared among these decay modes. Thus, an excess of events in this ROI affects all three decay modes.

Since the branching ratio of the $2\nu\beta\beta$ decay of ^{76}Ge into the excited states of ^{76}Se is still unknown, the contribution of each decay mode to the signal counts in the shared ROI cannot be determined. Consequently, each decay mode is evaluated under the assumption that the contribution of the other decay modes is negligible. If no signal is observed this assumption is sufficient.

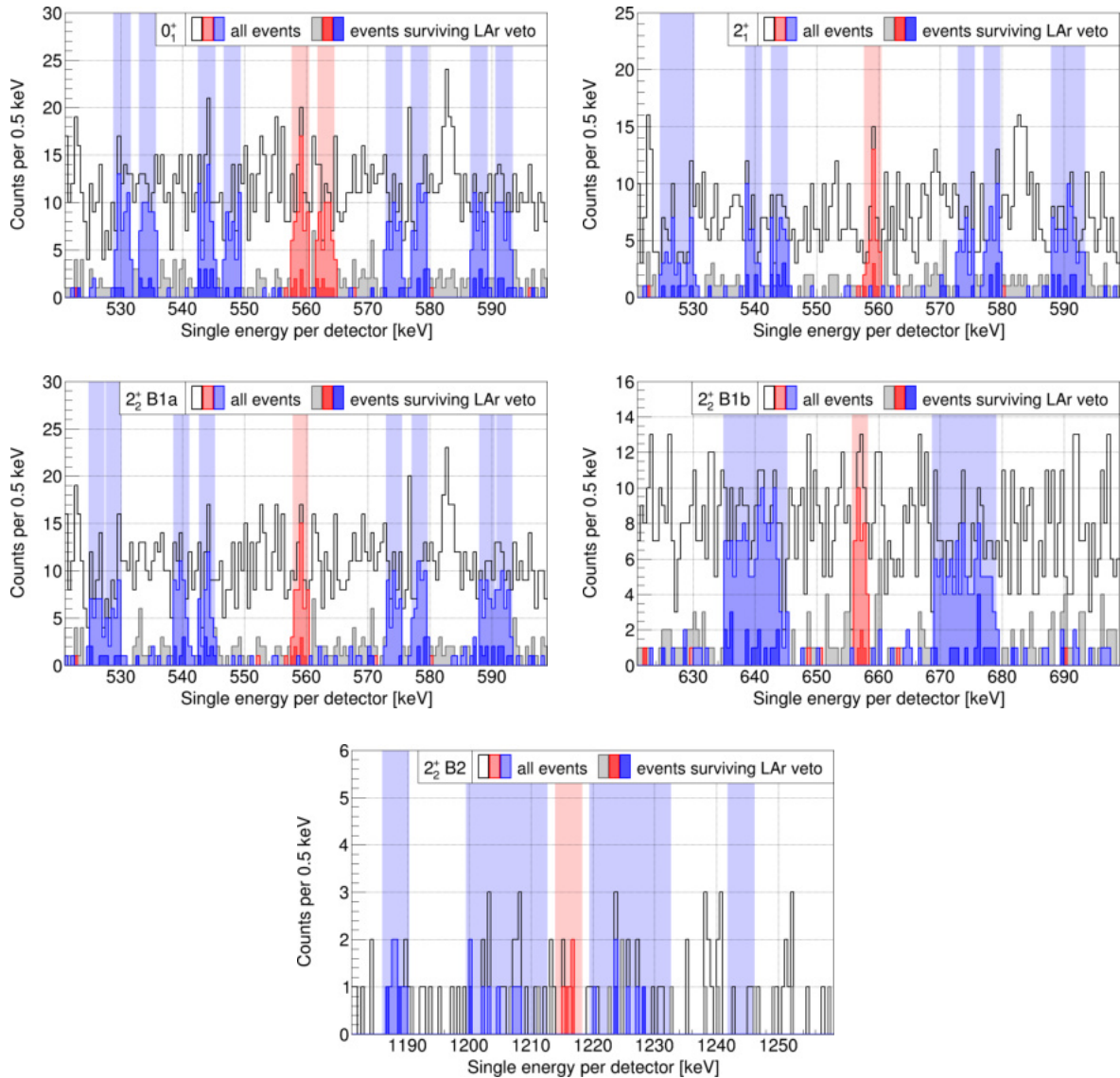


Figure 9.18: Number of counts surviving all cuts for each decay mode. The counts are summed up for Phase II and Phase II+. A separate depiction can be found in figures B.8 and B.9. The black and gray histograms show the respective data counts after removing events with a sum energy equal to the ^{40}K and ^{42}K γ lines. Also, the optimized low energy threshold per decay mode (see tab. 9.7) are taken into account. Thus, the data histograms differ for the various decay modes. The red and blue colors indicate in shades from light to dark the ROI and SB positions, the counts surviving all cuts without applying the LAr veto and the counts also surviving the LAr veto cut. Here, counts that are solely vetoed by the inner fiber shroud in Phase II+ are treated as surviving the LAr veto. While one of the energy depositions must be within the ROI or SBs, the corresponding other energy deposition can be located anywhere within the low and high energy threshold, which is indicated by the red and blue counts outside the ROI and SBs. The SB count within the ROIs in 2_1^+ and in 2_2^+ B1a is accompanied by an energy deposition in a natural GTF located in a SB. Since the GTF detectors are excluded as source detectors, this event is treated as background and covered as a SB event.

However, in the case a signal is measured in either of the ROIs, the individual contribution of each decay mode must be identified. A discrimination via the occurrence of a second de-excitation γ ray or the application of the LAr veto may help to distinguish between the decay modes. According to the half life predictions (see tab. 9.1), it is expected that the decay into the 0_1^+ state has the lowest half life compared to the other decay modes into excited states. Thus, a signal observation of this decay mode would also influence the results for the 2_1^+ and 2_2^+ B1 states.

Table 9.8: Compilation of counts in the ROI (N^{ROI}) and in each SB (N^{SB}) surviving all cuts with and without applying the LAr veto for Phase II and Phase II+. Also given are the average counts \bar{N}^{SB} expected in the ROI derived from the SB counts. Since the 0_1^+ state has two ROIs close to each other, the SBs are combined accordingly, resulting effectively in 4 SBs. All other decay modes feature 8 SBs for each ROI. In Phase II N^{ROI} exceeds the expected counts from \bar{N}^{SB} for all decay modes, which is not the case for Phase II+. Since the inner fiber shroud of Phase II+ is not fully implemented in MaGe yet, the related signal efficiencies cannot be calculated. Hence, the counts without using the inner fiber shroud are used for the further analysis. The counts surviving the LAr veto including the inner fiber shroud are shown for comparison.

decay mode	N^{ROI}	N^{SB}	\bar{N}^{SB}
Phase II			
$0_{\text{g.s.}}^+ \rightarrow 0_1^+$	65	54,57,51,45	51.8
$0_{\text{g.s.}}^+ \rightarrow 2_1^+$	20	10,7,19,16,16,17,13,13	13.8
$0_{\text{g.s.}}^+ \rightarrow 2_2^+$ B1	45	30,36,48,37,38,37,34,31	36.4
B2	4	7,1,4,0,1,0,1,0	1.75
Phase II with LAr veto			
$0_{\text{g.s.}}^+ \rightarrow 0_1^+$	11	8,12,1,6	6.8
$0_{\text{g.s.}}^+ \rightarrow 2_1^+$	5	1,2,2,7,1,1,4,2	2.5
$0_{\text{g.s.}}^+ \rightarrow 2_2^+$ B1	7	4,4,6,7,1,2,9,4	4.6
B2	2	2,0,0,0,1,0,1,0	0.5
Phase II+			
$0_{\text{g.s.}}^+ \rightarrow 0_1^+$	40	48,36,42,51	44.25
$0_{\text{g.s.}}^+ \rightarrow 2_1^+$	12	10,10,9,14,12,19,16,19	13.625
$0_{\text{g.s.}}^+ \rightarrow 2_2^+$ B1	39	32,25,36,28,25,36,30,35	30.875
B2	1	2,3,0,0,2,2,0,0	1.125
Phase II+ with LAr veto without inner fiber shroud			
$0_{\text{g.s.}}^+ \rightarrow 0_1^+$	4	2,3,7,7	4.75
$0_{\text{g.s.}}^+ \rightarrow 2_1^+$	0	1,0,2,2,1,4,1,3	1.75
$0_{\text{g.s.}}^+ \rightarrow 2_2^+$ B1	4	6,1,4,5,1,6,4,6	4.125
B2	0	0,1,0,0,0,0,0,0	0.125
Phase II+ with LAr veto with inner fiber shroud			
$0_{\text{g.s.}}^+ \rightarrow 0_1^+$	2	2,3,6,5	4.0
$0_{\text{g.s.}}^+ \rightarrow 2_1^+$	0	1,0,2,2,1,4,0,3	1.625
$0_{\text{g.s.}}^+ \rightarrow 2_2^+$ B1	3	6,1,3,4,1,6,2,6	3.625
B2	0	0,1,0,0,0,0,0,0	0.125

Time distribution of surviving events

Figure 9.19 shows the time distribution of the events surviving all cuts for the 0_1^+ decay mode. While the count rate is slightly higher in Phase II+ due to the larger enriched detector mass, it is in general stable over the complete measuring time. The time distributions of the other decay modes are shown in figure B.10.

Detailed lists of the surviving events can be found in tables B.2 – B.9. The selected events differ from [Wes19] due to the changed energy resolution and scale, the reprocessing of the data and the smaller window width of the ROI.

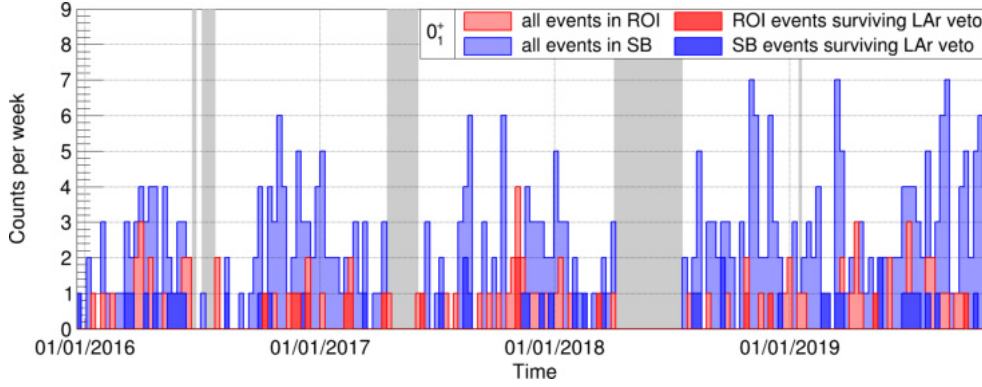


Figure 9.19: Time distribution of the events in the ROI and SBs surviving all cuts with and without applying the LAr veto for the 0_1^+ decay mode. Here, events which are solely vetoed by the inner fiber shroud in Phase II+ are treated as events surviving the LAr veto cut. The gray bands indicate the rejected run periods (see also tab. 9.6). Events overlapping with the beginning or end of the gray marked bands occur in the case that an omitted run stops and an accepted run starts within the same week or vice versa.

9.8 Statistical analysis

The analysis procedure remains unchanged from the descriptions given in [Wes19] and is summarized in the following sections. A Bayesian approach is used in order to obtain results for the half lives of the investigated decay modes. For this, a likelihood function is constructed which is converted into a posterior probability density distribution of the inverse half life $T_{1/2}^{-1}$ using the Bayes theorem and the Bayesian Analysis Toolkit (BAT).

9.8.1 Likelihood function

The likelihood function is composed of two Poisson distributions for the respective counts in the ROI and in the SBs as expressed in equation 9.5 [Wes19]. The Poisson distribution for the ROI gives the probability for the observation of the counts in the ROI assuming a number of expected signal and background events. The Poisson distribution for the SBs yields the probability for obtaining the counts in the SBs with the assumption of the expected background events. The likelihood combines multiple data sets d , i.e. Phase I, Phase II and Phase II+ or Phase II with LAr and Phase II+ with LAr. If a decay mode features several decay branches r , as it is the case for the 2_2^+ state, all branches are combined in the likelihood for the regarded decay mode.

$$\mathcal{L}(\mathbf{n}, \mathbf{m} | \mathbf{s}, \mathbf{b}) = \prod_{d,r} \left[\frac{(s_{d,r} + b_{d,r}/\tau_{d,r})^{n_{d,r}}}{n_{d,r}!} \cdot e^{-(s_{d,r} + b_{d,r}/\tau_{d,r})} \right] \cdot \left[\frac{b_{d,r}^{m_{d,r}}}{m_{d,r}!} \cdot e^{-b_{d,r}} \right] \quad (9.5)$$

The number of observed events in the ROI is given by $n_{d,r} = N_{d,r}^{\text{ROI}}$, and the number of observed events in the SBs is $m_{d,r} = \sum_i N_{d,r,i}^{\text{SB}}$ for each data set d and decay branch r . The expected signal counts in the ROI are $s_{d,r}$ and the expected background counts in the SBs are $b_{d,r}$ for the respective data set d and decay branch r . In general, $\tau_{d,r}$ is the ratio between $b_{d,r}$ and the expected background counts in the ROI. If the background is flat and each SB has the same width as the ROI, which is the case here, then $\tau_{d,r}$ is equal to the number of SBs.

In the Likelihood, the $n_{d,r}$ are combined to $\mathbf{n} = (n_{\text{PI},B1}, n_{\text{PII},B1}, \dots)$ considering all desired data sets and decay branches. This is equivalent for \mathbf{m} , \mathbf{s} and \mathbf{b} . The expected signal counts are calculated assuming a certain half life $T_{1/2}$ for the investigated decay mode as expressed in equation 9.6 [Wes19].

$$s_{d,r} = T_{1/2}^{-1} \cdot \varepsilon_{d,r} \cdot \ln 2 \cdot N_A \cdot \mathcal{E}_{76,d} \quad (9.6)$$

The signal efficiency of branch r in the data set d is given by $\varepsilon_{d,r}$ (see tab. 9.7). The Avogadro constant is N_A and the ^{76}Ge exposure of data set d is given by $\mathcal{E}_{76,d}$ (see tab. 9.6).

9.8.2 Prior and posterior probability density distribution

The prior probability density distribution, in the following shortly called prior, is defined as a flat distribution for the respective free parameter. The prior for the inverse half life $T_{1/2}^{-1}$ is limited in the range of $[0, 2] \cdot 10^{-23} \text{ yr}^{-1}$ taking into account previously achieved limits [GER15a]. The prior for the background expectation $b_{d,r}$ is constrained to $\pm 5\sqrt{m_{d,r}}$, but minimum 0 and maximum 10.

With the Bayes theorem, the likelihood multiplied with the priors yields a multi-dimensional posterior probability density distribution, which is in the following shortly called posterior.

9.8.3 Systematical uncertainties

For the efficiency $\varepsilon_{d,r}$ the systematical uncertainties caused by the uncertainty of the MC processes, the dead layer uncertainty as well as the energy resolution and energy scale are taken into account as discussed in section 9.6.3. The uncertainty contributions are equal to the ones reported in [Wes19] for Phase II, because the detector array has not been changed. For Phase II+ the same values are assumed since the energy resolution and scale are almost equal and with the exception of the new IC detectors, all other detectors remain unchanged, thus also featuring the same dead layer uncertainties as before the upgrade. Since the uncertainties are the same as in [Wes19], their effect on the limit calculation is also in the same order of magnitude, i.e. about 1%.

The systematical uncertainties on the efficiency introduced by the LAr map or the calorimetric cut have not been determined since both are not finalized yet and their uncertainties still have to be investigated. The inclusion of these uncertainties has only a small impact on the efficiency and therefore would just slightly weaken the derived limits on the half life for each decay mode. In the case of a measurement, the uncertainty of the efficiency has a significant impact on the uncertainty of the obtained half life.

The systematical uncertainty of the exposure is taken into account considering the isotopic enrichment uncertainties of the detectors. It results in an uncertainty of 1.1% on the exposure [Wes19].

The systematical uncertainties are considered in the likelihood by the product of one standard deviation with a free parameter a . The prior for a is a Gaussian distribution with a mean of 0 and a standard deviation of 1 defined in the range $[-5, 5]$.

9.8.4 Limit extraction

Given the priors and the likelihood function, BAT returns the multi-dimensional posteriors, which are marginalized for obtaining the one-dimensional posteriors $p(T_{1/2}^{-1} | \mathbf{n}, \mathbf{m})$. These are shown in figure 9.20 for a combination of the data sets of Phase I, Phase II and Phase II+. The posteriors including only Phase I and Phase II with and without applying the LAr veto can be found in figure B.11.

The best fit value is defined as the maximum of the posterior. For all decay modes and data sets a non-zero best fit value has been obtained for the inverse half life $T_{1/2}^{-1}$. However, in all cases $T_{1/2}^{-1} = 0$ is within the 68%, 95% or 99.7% interval, thus no signal is observed.

Consequently, a 90% credibility limit on the inverse half life is derived from the posterior $p(T_{1/2}^{-1}|\mathbf{n}, \mathbf{m})$.

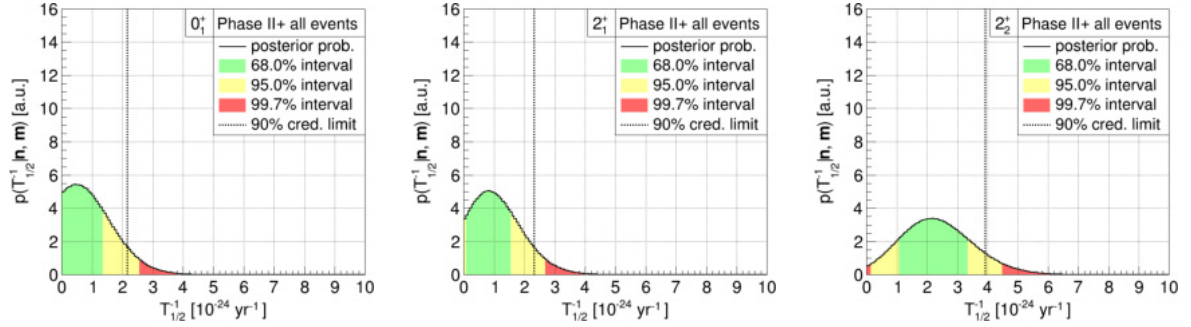


Figure 9.20: Marginalized posteriors for $T_{1/2}^{-1}$ for Phase II+ without applying the LAr veto. The posteriors are all compatible with $T_{1/2}^{-1} = 0$ within the 68%, 95% or 99.7% interval. Thus, a 90% credibility limit is derived.

The obtained limits for all investigated decay modes are compiled in table 9.9. The limits derived for Phase II are a combination of Phase I and Phase II, while Phase II+ includes both, Phase I and Phase II. The same combination pattern is used for the limits calculated with the LAr veto, although the LAr veto did not exist in Phase I, i.e. the Phase I data set stays unchanged while applying the LAr veto for Phase II and Phase II+.

Table 9.9: 90% credibility limits on the half life of each investigated decay mode for Phase II and Phase II+ considering all events and events that survived the LAr veto cut. The limits are derived for a combination with the respective previous data sets dividing the data sets in ignoring and applying the LAr veto. Phase I is included in both categories without any LAr veto cut.

decay mode	Phase II		Phase II+	
	$T_{1/2}^{\text{all}} [10^{23} \text{ yr}]$	$T_{1/2}^{\text{LAr}} [10^{23} \text{ yr}]$	$T_{1/2}^{\text{all}} [10^{23} \text{ yr}]$	$T_{1/2}^{\text{LAr}} [10^{23} \text{ yr}]$
$0_{\text{g.s.}}^+ \rightarrow 0_1^+$	> 3.03	> 3.47	> 4.63	> 5.61
$0_{\text{g.s.}}^+ \rightarrow 2_1^+$	> 2.85	> 5.37	> 4.33	> 11.25
$0_{\text{g.s.}}^+ \rightarrow 2_2^+$	> 2.17	> 2.66	> 2.55	> 3.65

9.9 Discussion

New limits have been derived for the $2\nu\beta\beta$ decay of ^{76}Ge into the first three excited states of ^{76}Se with the combination of 22 kg · yr Phase I data, 60.1 kg · yr Phase II data and 43.6 kg · yr Phase II+ data of GERDA. Solely M2 events, i.e. two detector hits are taken into account for the analysis. The analysis procedure described in [Wes19] is the base for this work and has been adapted in order to include the LAr veto and switch to using the tier4izer to handle simulation data.

While in Phase II the middle string consisted of natural detectors, this position advantage has been utilized in Phase II+ by exchanging these detectors with enriched ones. This results in a higher probability that emitted γ rays are detected by the surrounding detectors, yielding a higher sensitivity rate in Phase II+.

A non-significant excess of events has been observed in Phase II, but not in Phase II+ (see tab. 9.8). The achieved limits summarized in table 9.9 are in general stronger when applying the LAr veto.

Furthermore, the limits for all three investigated decay modes have been improved for the combination of all three data sets compared to the previous limits in [Wes19]. With the achieved limits for the combination of all three data sets with applying the LAr veto some additional theoretical predictions of the half lives are disfavored, which are [TS97] and [Suh14] for the 0_1^+ decay mode and [DR94] for the 2_1^+ decay mode (compare tab. 9.1 and tab. 9.9).

After reaching its design goal of $100\text{ kg}\cdot\text{yr}$ the physics data taking of GERDA has been stopped in November 2019 and several special calibration runs have been performed since then. This also includes special calibrations with fixed source positions for the LAr veto. This is important in order to determine the efficiencies of the PMTs and SiPMs. The uncertainties derived for these efficiencies as well as the uncertainties of the absorption length, light yield and fiber coverage determine the systematic uncertainty introduced by using the LAr map for the excited states analysis. Additionally, this is needed for the development of a LAr map for Phase II+. Changes in the LAr map can affect the signal efficiencies of the excited states decay modes and therefore also the derived limits when applying the LAr veto cut. Thus, the analysis should be redone after the LAr maps for Phase II and Phase II+ and their systematic uncertainties are fixed.

The successor experiment LEGEND will continue to search for the $0\nu\beta\beta$ decay of ^{76}Ge with the existing infrastructure of GERDA. More enriched detectors will be added to the already existing ones. However, the detector strings will be arranged differently with the goal to maximize the LAr detection efficiency by improving the light propagation in the LAr (see fig. 2.12). This detector positioning is not optimal for coincidence events resulting in a potential smaller sensitivity for the excited states search compared to the densely packed detector array of GERDA Phase II+. Nevertheless, the search for excited states will be continued in LEGEND utilizing the optimized LAr veto and the larger enriched detector mass.

Chapter 10

Conclusions

This work has been developed in the context of the GERDA experiment which searches for the $0\nu\beta\beta$ decay of ^{76}Ge in germanium detectors operated in LAr. So far no signal has been observed.

The first part of this work addresses the optical properties of LAr which serves as an additional background veto. It utilizes the fact that LAr creates scintillation light when energy is deposited in it. For the optimization of the LAr veto a dedicated setup has been developed in order to measure the attenuation of the scintillation light in LAr which depends strongly on the LAr impurity content and concentration.

This includes the determination of the steel reflectivity with a combination of two measuring approaches in the visible as well as in the UV region where LAr scintillates. Since no publications are available yet concerning the steel reflectivity below 200 nm, the measurements performed for this work can be useful for other experiments that use scintillation light created by argon or xenon and have steel components in their setup which can affect the light propagation by reflections.

During the upgrade between Phase I and Phase II of GERDA the attenuation measurement has been performed for the optimization of the LAr veto instrumentation. The analysis of the acquired data required intense MC simulations in order to understand the background originated by Cherenkov light. In this context, the optical properties of LAr and all relevant surfaces in MaGe have been reviewed and updated to the current scientific knowledge. It is assumed, that a larger impurity concentration inside LAr in the setup during the attenuation measurement caused the absorption length and light yield to be very small.

Due to the attenuation measurement more attention was gained within the collaboration concerning the importance of keeping the LAr as clean as possible. Furthermore, the measurement triggered the realization of a constant monitoring of the triplet lifetime in Phase II of GERDA which serves as an indication of the LAr purity. An additional outcome of the attenuation measurement is the determination of the triplet lifetime at the time of the measurement. The achieved result is consistent with the monitoring of the triplet lifetime in GERDA Phase II. Additionally, it was decided for the successor experiment LEGEND to buy new very pure LAr and to develop a monitoring of the absorption length and light yield of LAr.

With the improved characterization of the optical parameters in MaGe it was possible to develop a LAr detection probability map to determine the efficiency of the LAr veto depending on the amount and location of the energy deposited in LAr.

The second part of this work focuses on the search for the $2\nu\beta\beta$ decay of ^{76}Ge into excited states of ^{76}Se . The analysis has been carried out combining the data sets of Phase I, Phase II and Phase II+ of GERDA. In contrast to the $0\nu\beta\beta$ search, where solely M1 events are taken into account, the excited states analysis considers M2 events.

For the determination of the background, SBs were positioned around the ROI. While the positioning of the SBs was verified with the background model developed for M1 and M2 data, the actual background expectation was obtained from measuring data and is therefore independent of the MC background model.

The LAr veto has been included in the excited states analysis by using the LAr map for the determination of the signal efficiencies in Phase II when applying the LAr veto. Once a LAr map containing the inner fiber shroud is available for Phase II+, the corresponding signal efficiencies will be updated. New limits have been calculated for the data sets with and without LAr veto. Especially with the stronger limits derived from the data with applying the LAr veto, some theoretical predictions can be disfavored. This helps to further constrain the corresponding nuclear models and their internal assumptions which can also improve the calculations for the half life predictions of the $0\nu\beta\beta$ decay into the ground state. So far no signal has been observed, however, the search for excited states will continue in the successor experiment LEGEND with more detectors, i.e. a larger ^{76}Ge mass and an enhanced LAr veto.

In general, LEGEND will naturally focus on the search for the $0\nu\beta\beta$ decay in ^{76}Ge combining the detectors of GERDA and MAJORANA with the successfully proved techniques developed by both collaborations.

Appendix A

Simulation and analysis of the scintillation light attenuation in LAr

A.1 Low energy fits of the attenuation spectra

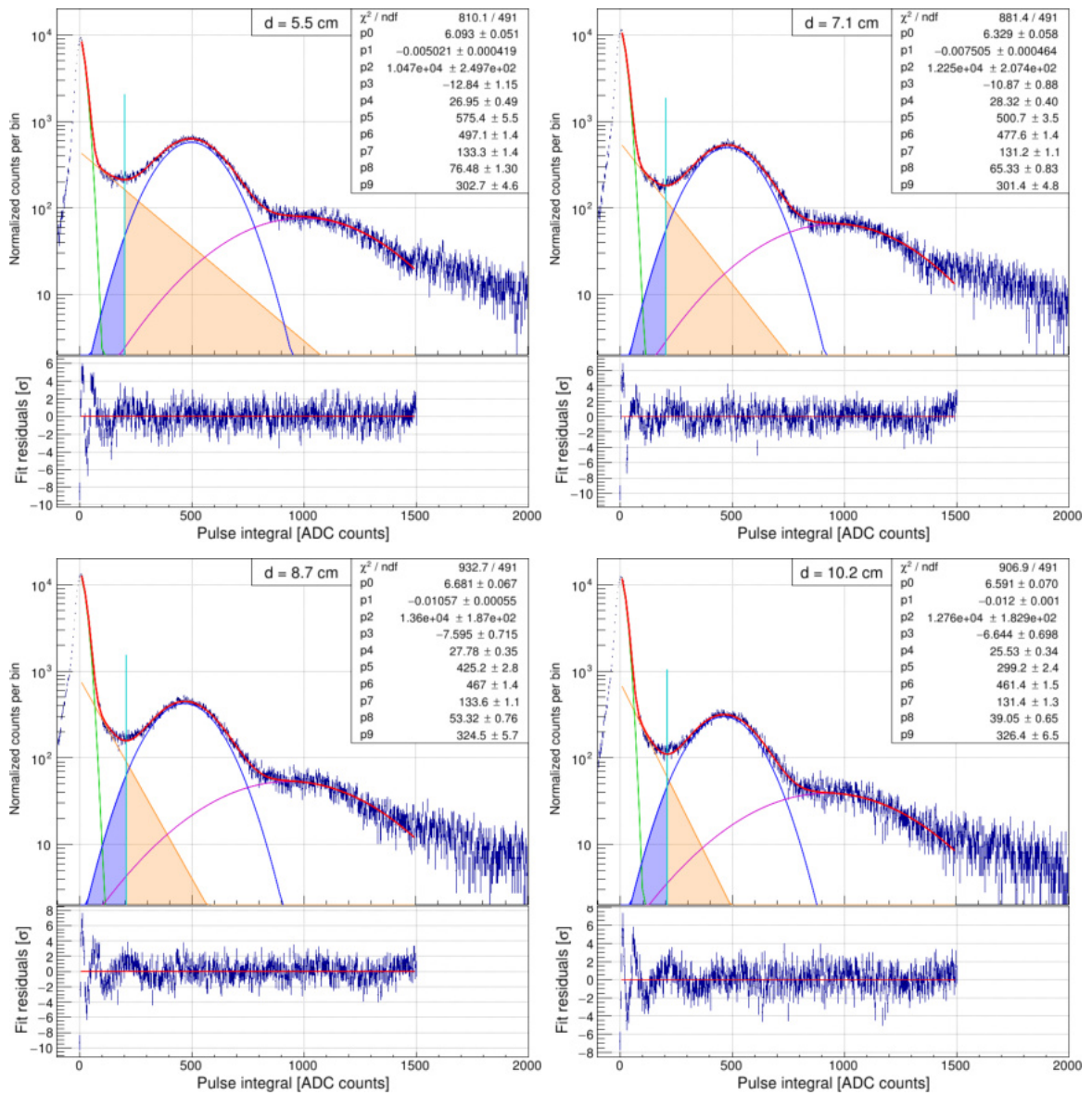


Figure A.1: Fits of the low energy part of the spectra acquired in the attenuation measurement for various measuring distances between source and PMT.

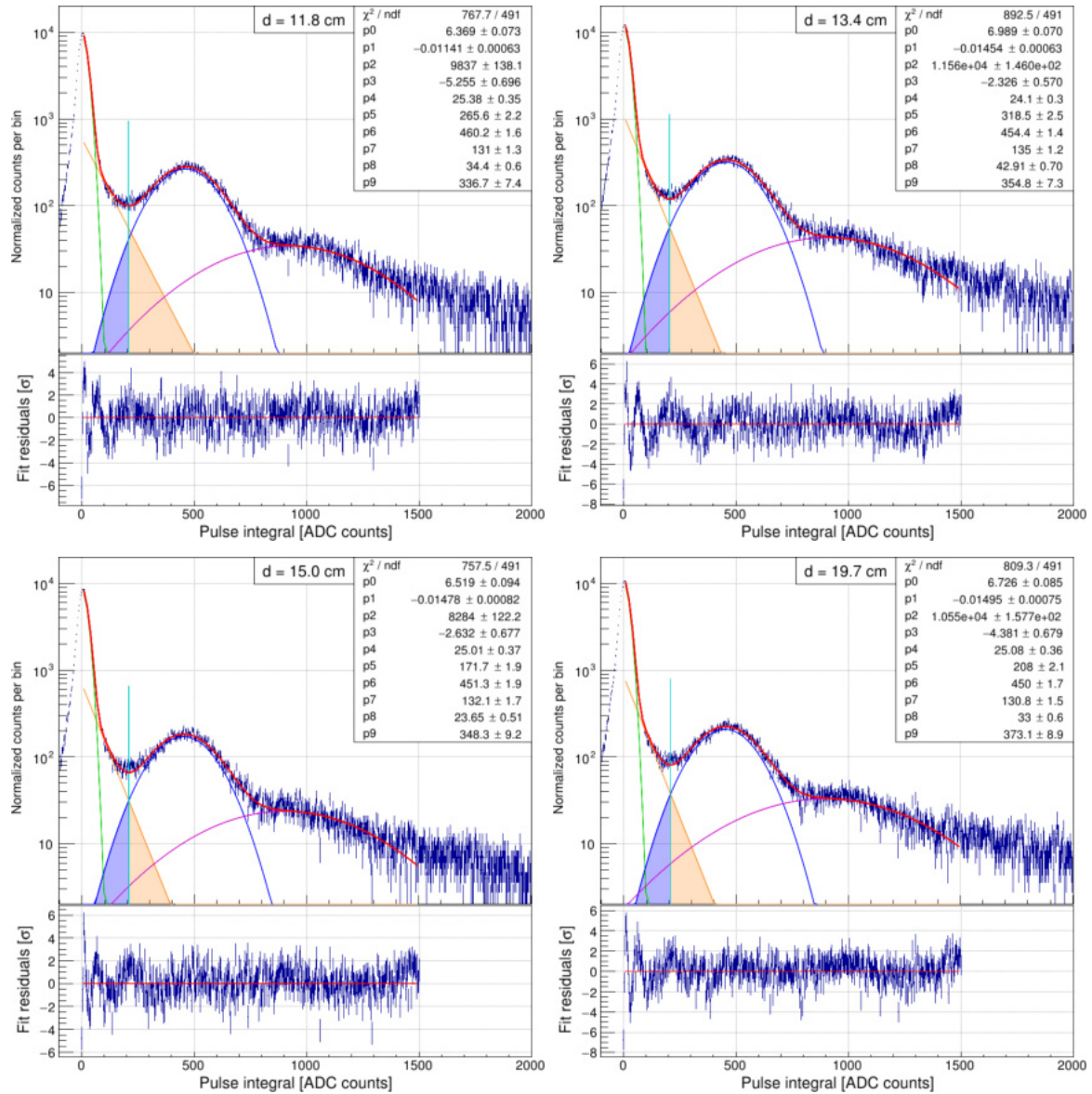


Figure A.2: Fits of the low energy part of the spectra acquired in the attenuation measurement for various measuring distances between source and PMT.

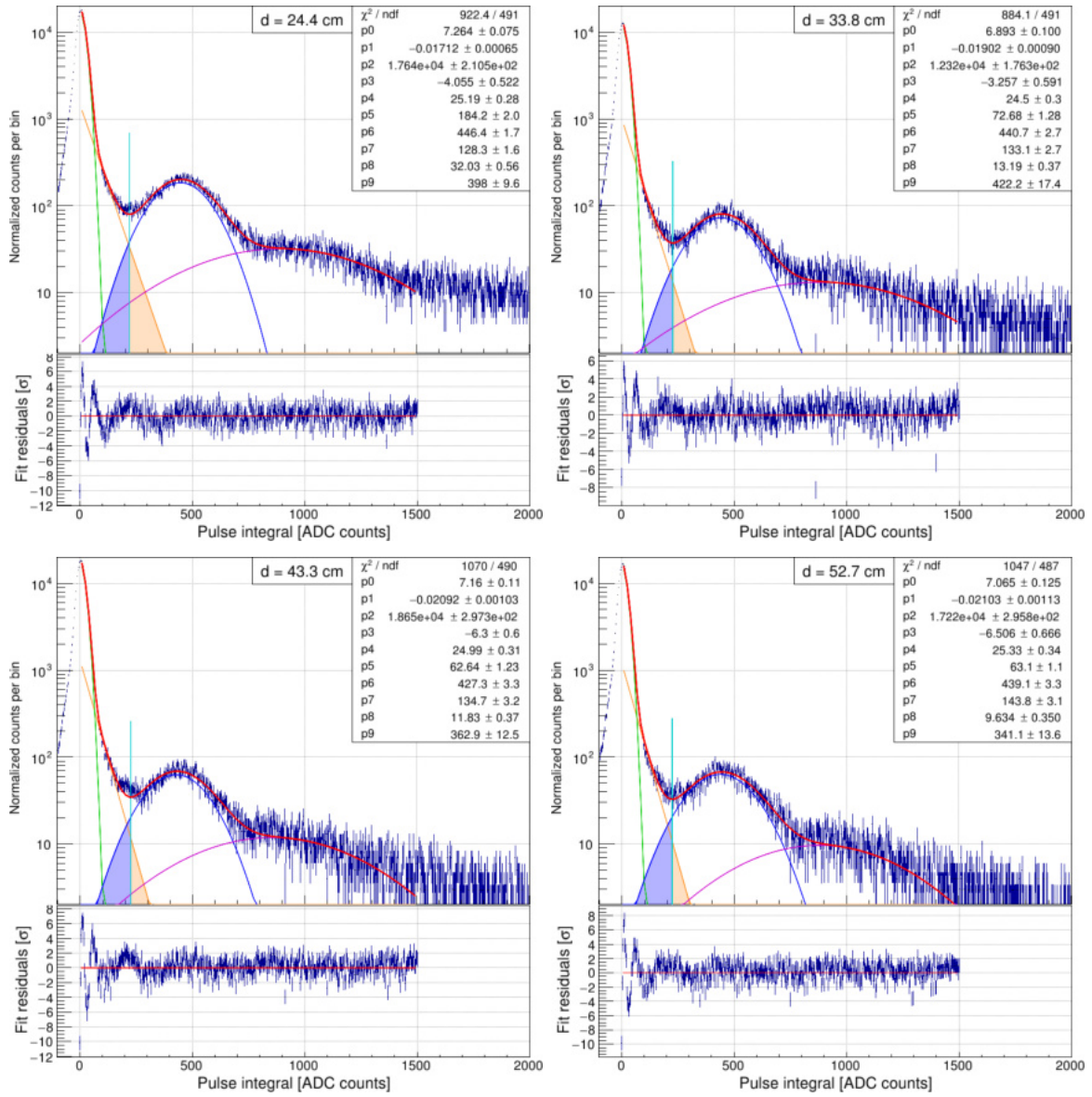


Figure A.3: Fits of the low energy part of the spectra acquired in the attenuation measurement for various measuring distances between source and PMT.

A.2 Attenuation simulation and analysis with IPF reflectivity

The default simulation parameters for the determination of the solid angle correction factor and the Cherenkov background are listed in table 7.3. In the following plots one parameter is changed to various values as stated in the legend.

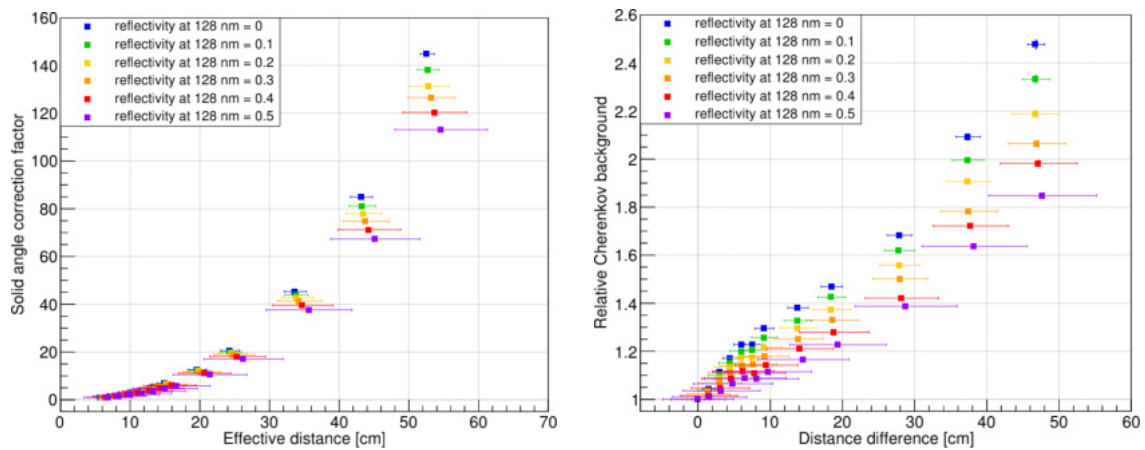


Figure A.4: (Left) Solid angle correction factor. (Right) Cherenkov background corrected by the solid angle.

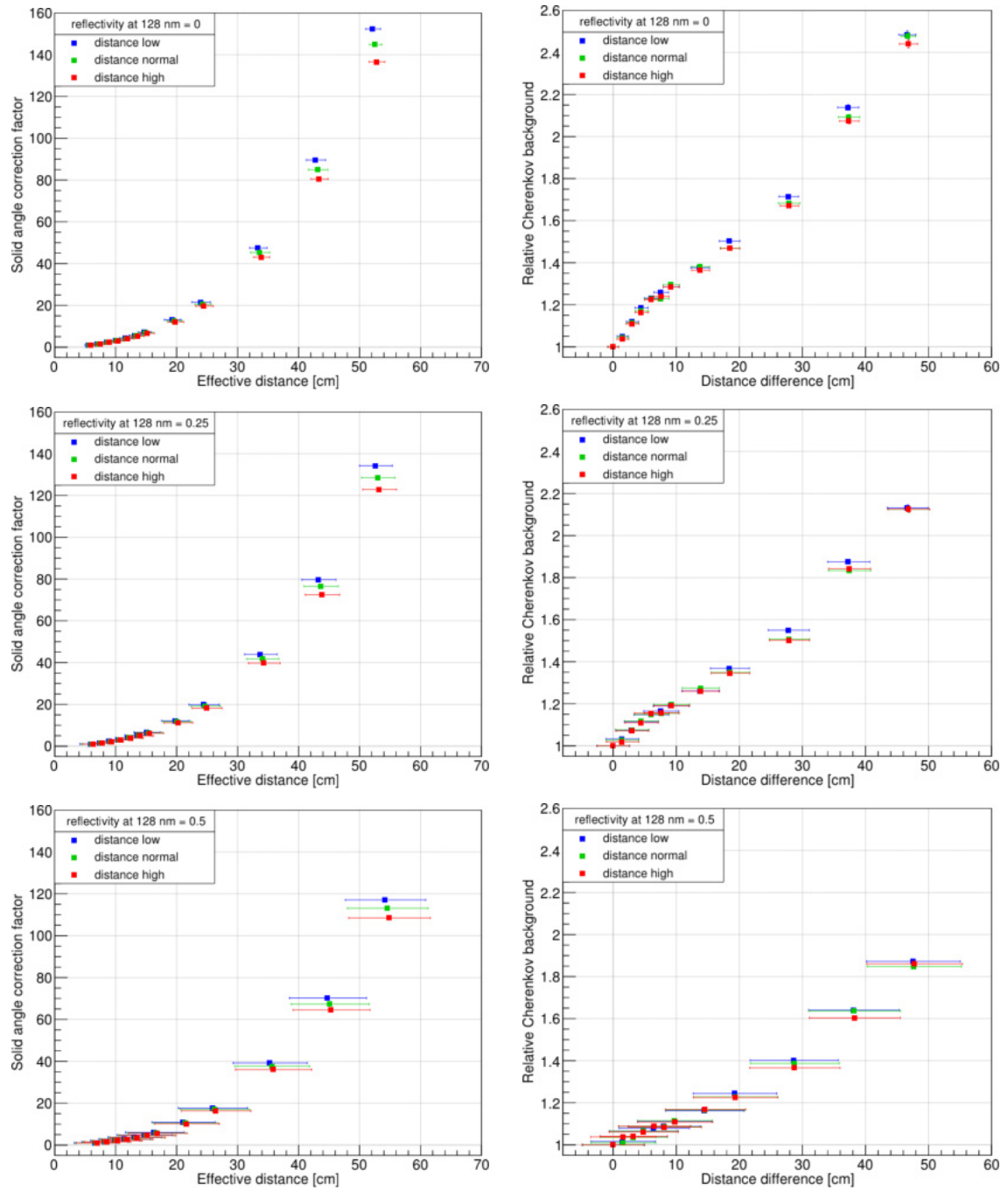


Figure A.5: (Left) Solid angle correction factor. (Right) Cherenkov background corrected by the solid angle.

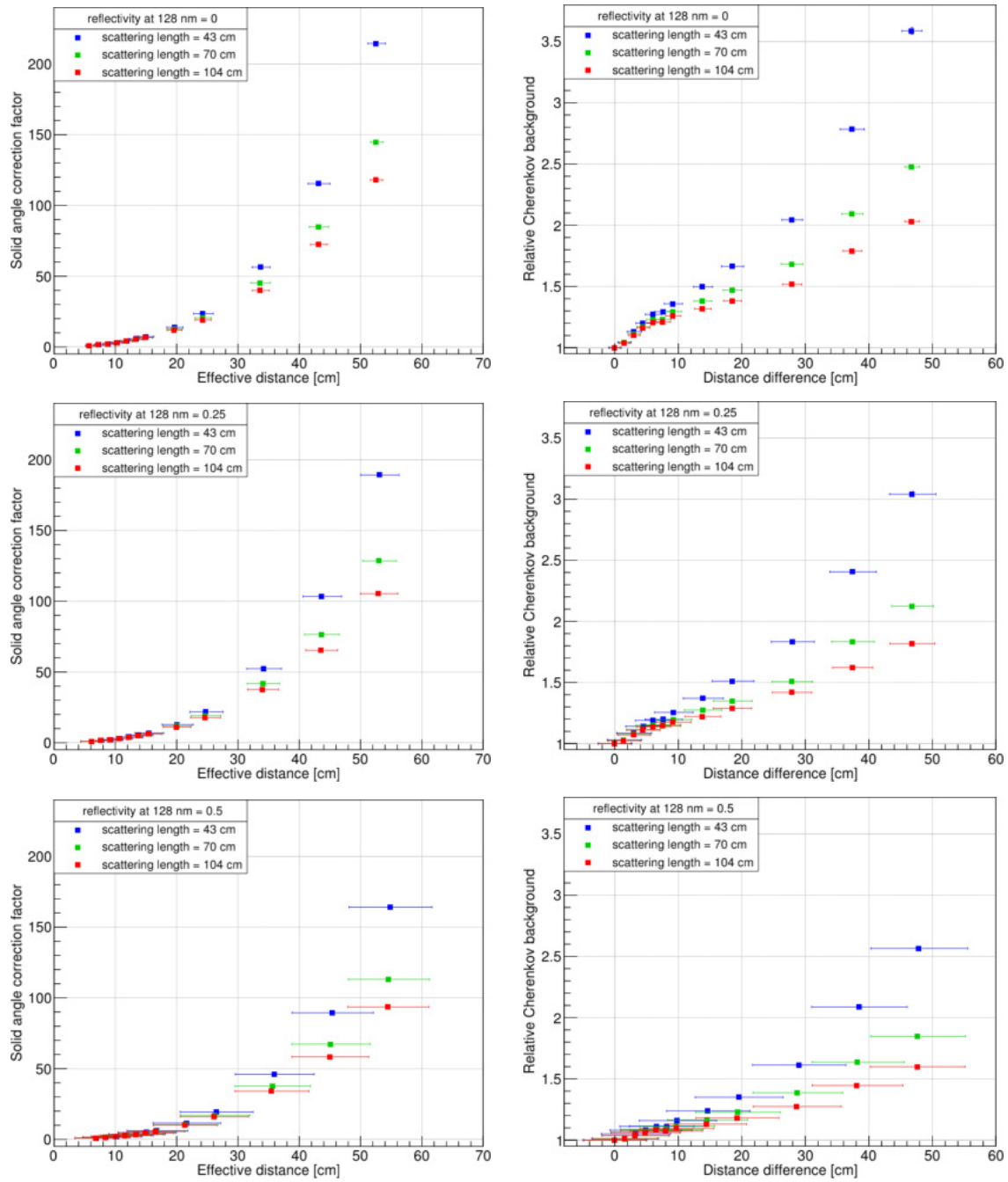


Figure A.6: (Left) Solid angle correction factor. (Right) Cherenkov background corrected by the solid angle.

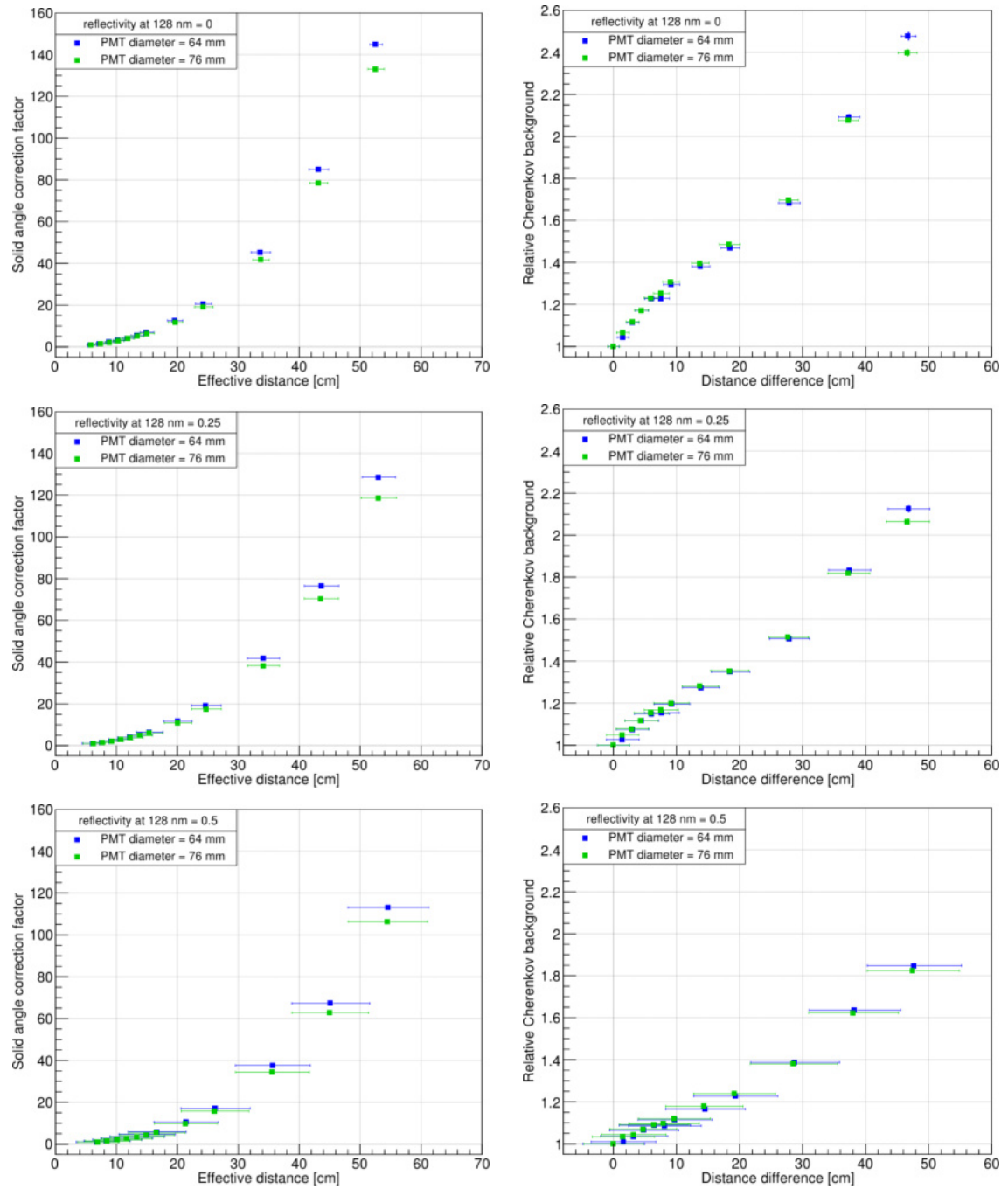


Figure A.7: (Left) Solid angle correction factor. (Right) Cherenkov background corrected by the solid angle.

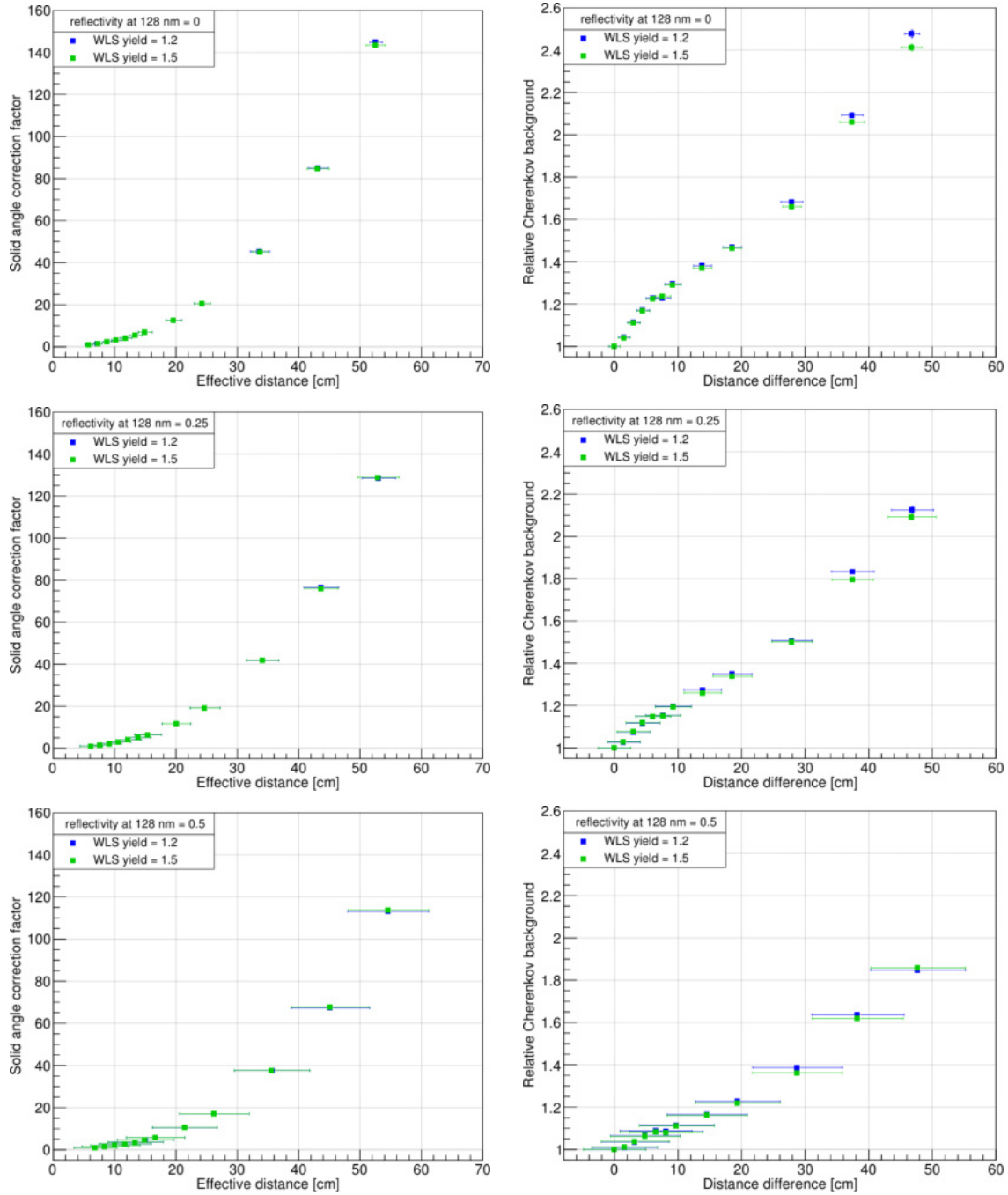


Figure A.8: (Left) Solid angle correction factor. (Right) Cherenkov background corrected by the solid angle.

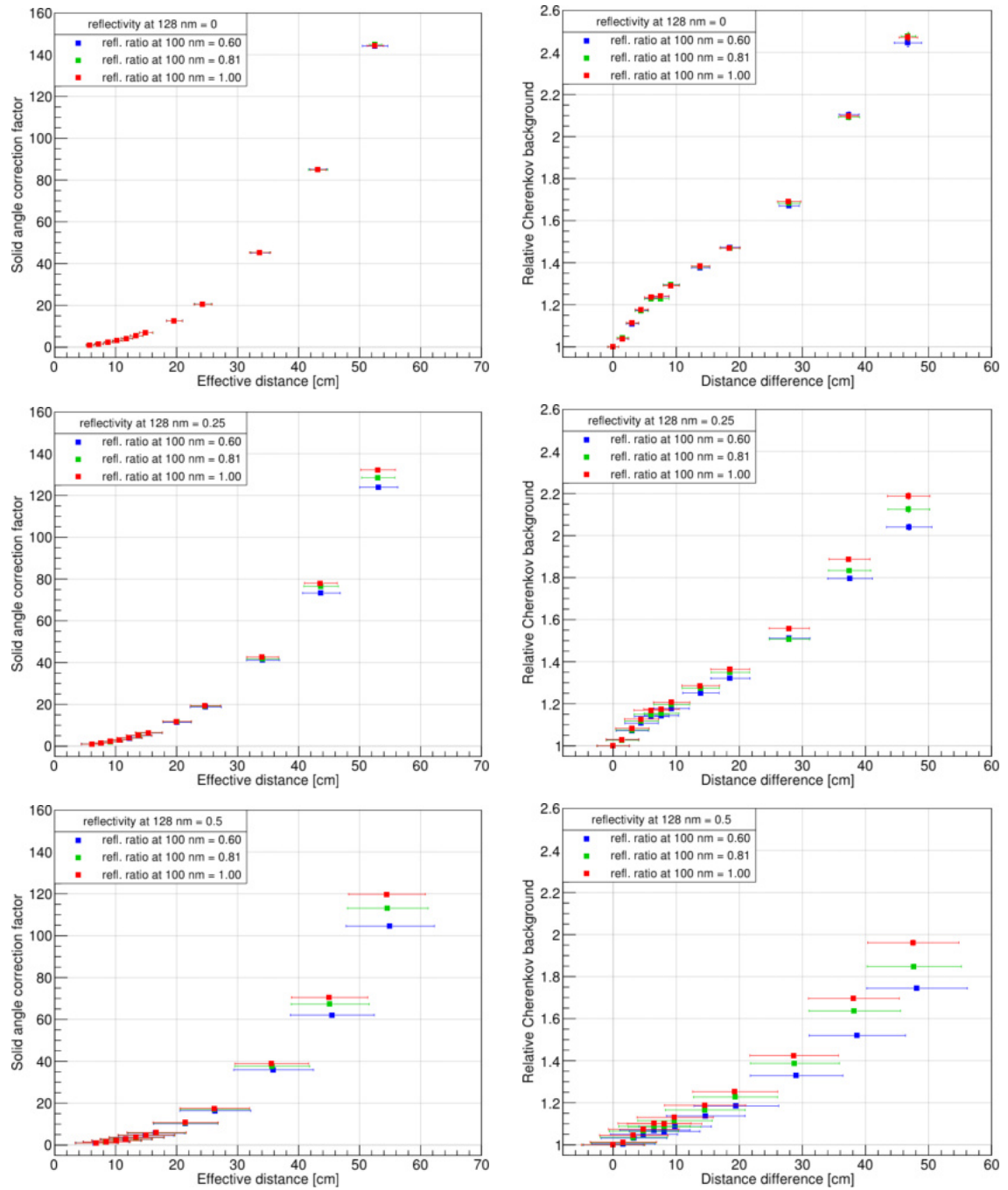


Figure A.9: (Left) Solid angle correction factor. (Right) Cherenkov background corrected by the solid angle.

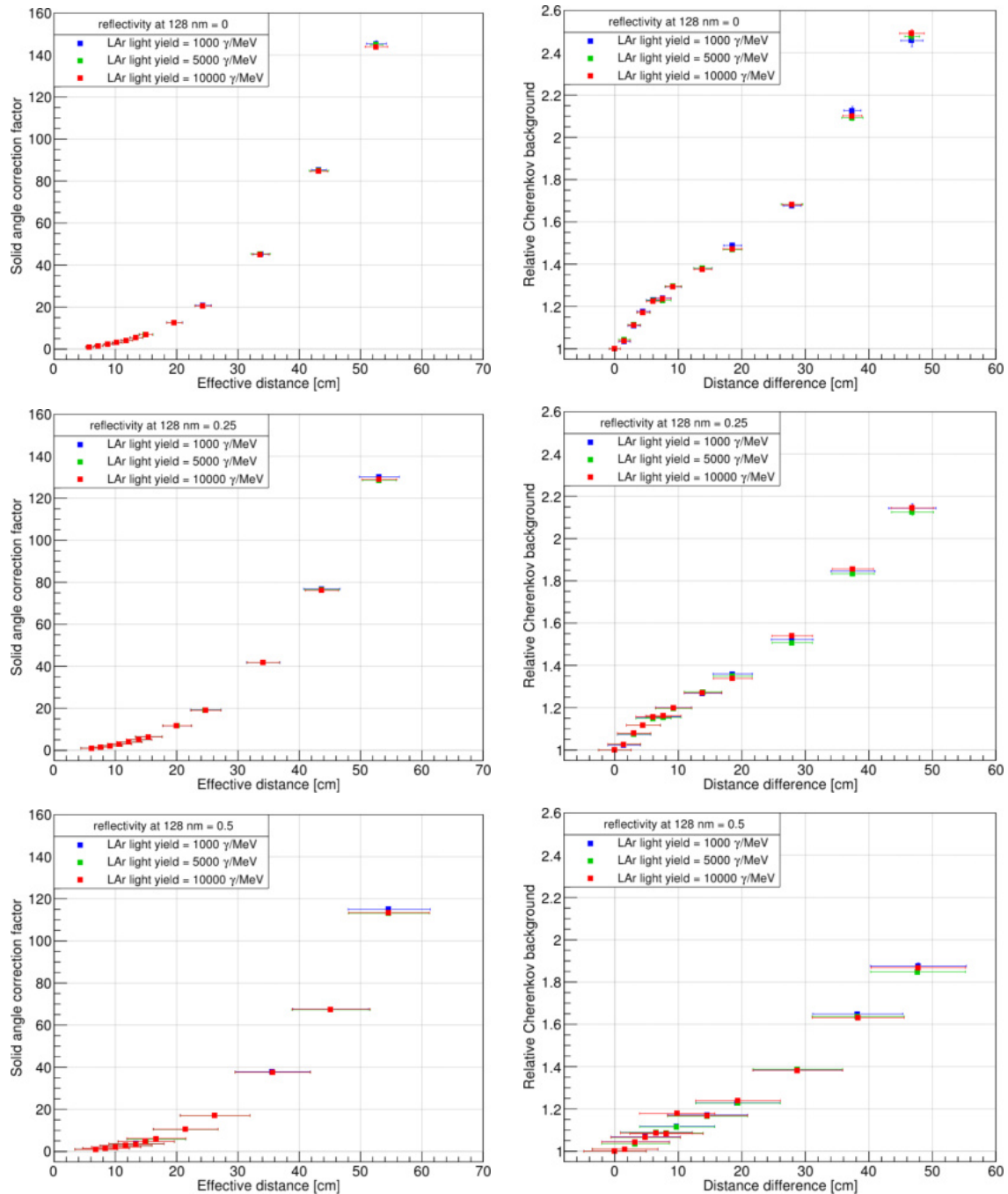


Figure A.10: (Left) Solid angle correction factor. (Right) Cherenkov background corrected by the solid angle.

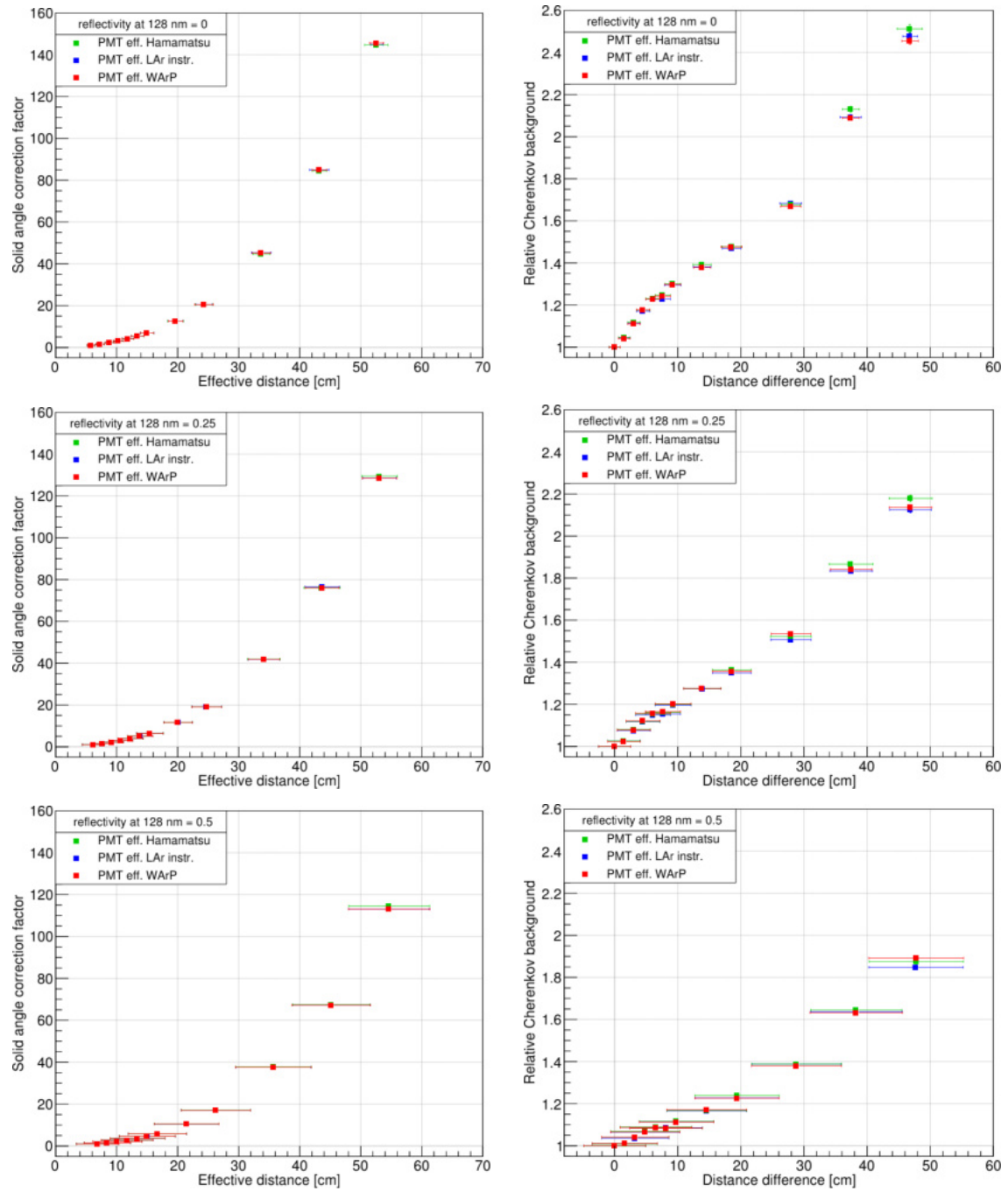


Figure A.11: (Left) Solid angle correction factor. (Right) Cherenkov background corrected by the solid angle.

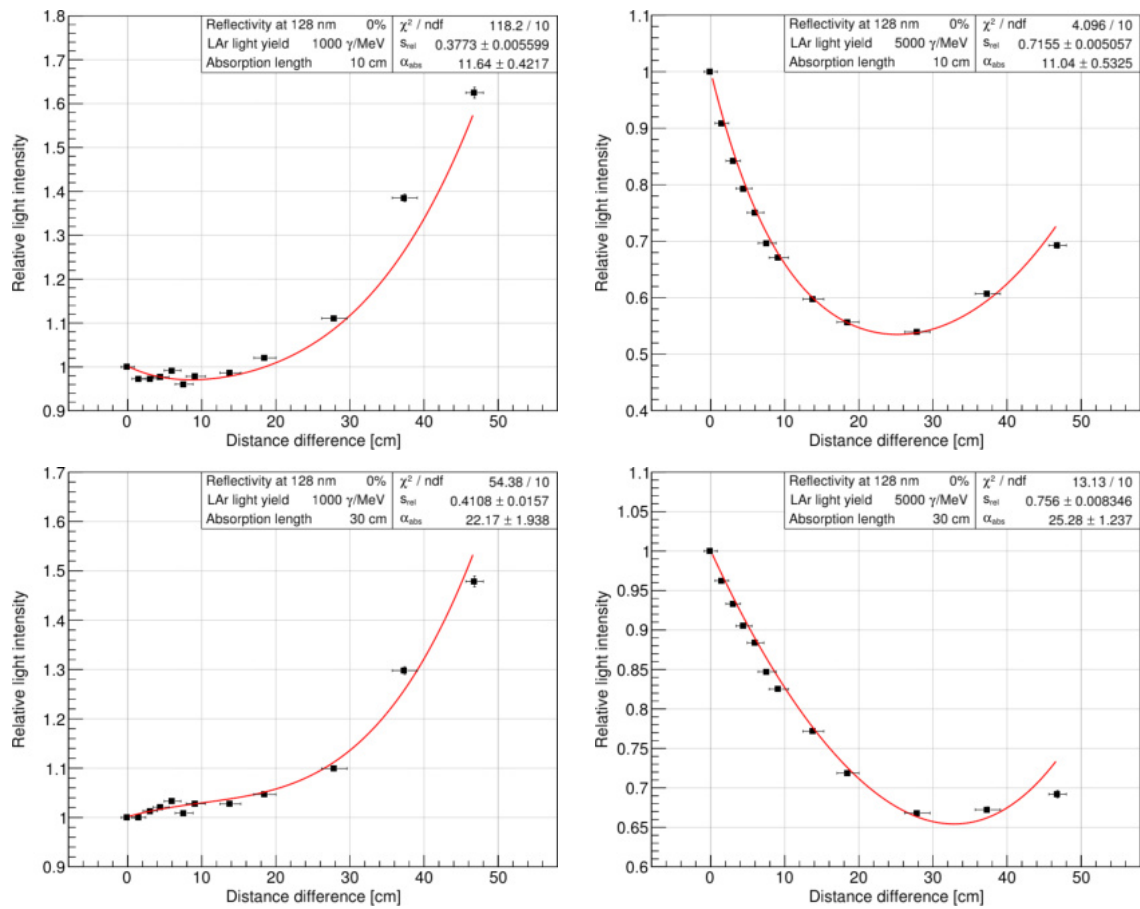


Figure A.12: Fit results of simulations produced with various parameter combinations.

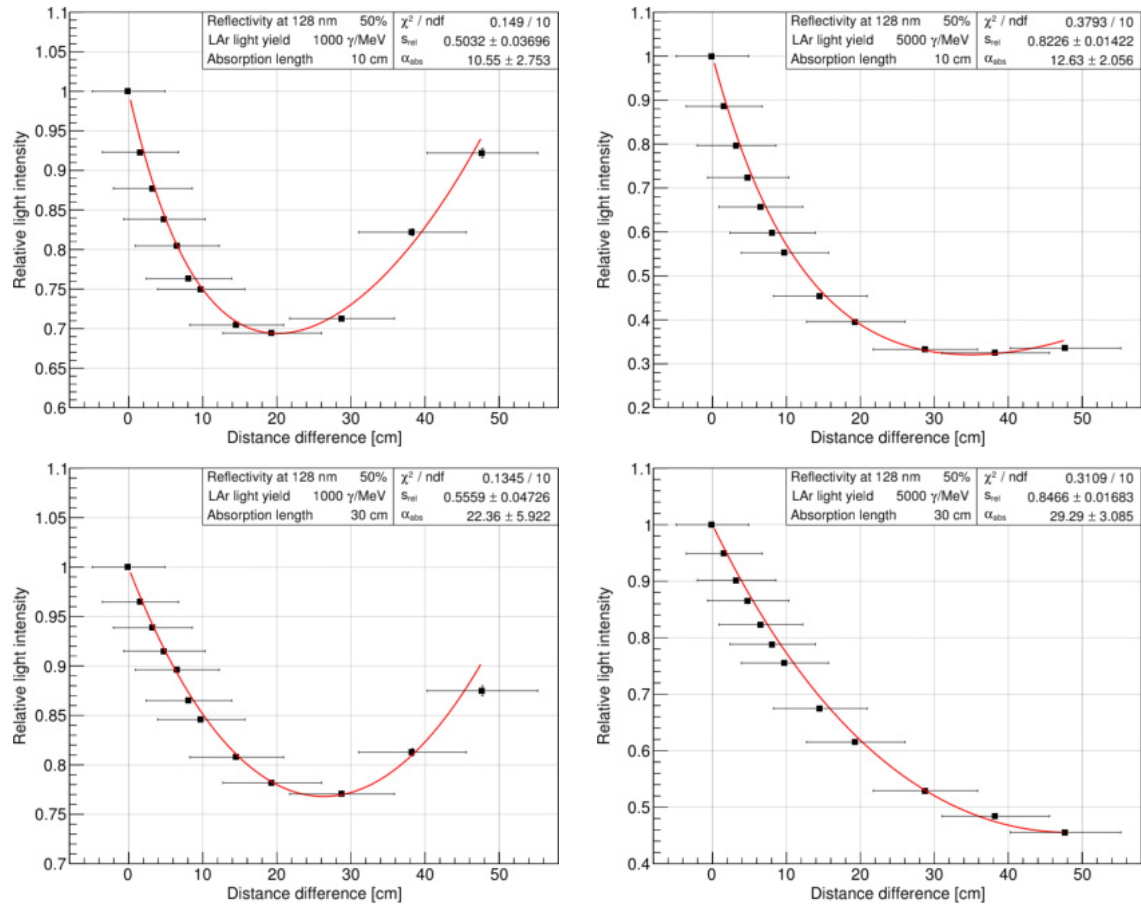


Figure A.13: Fit results of simulations produced with various parameter combinations.

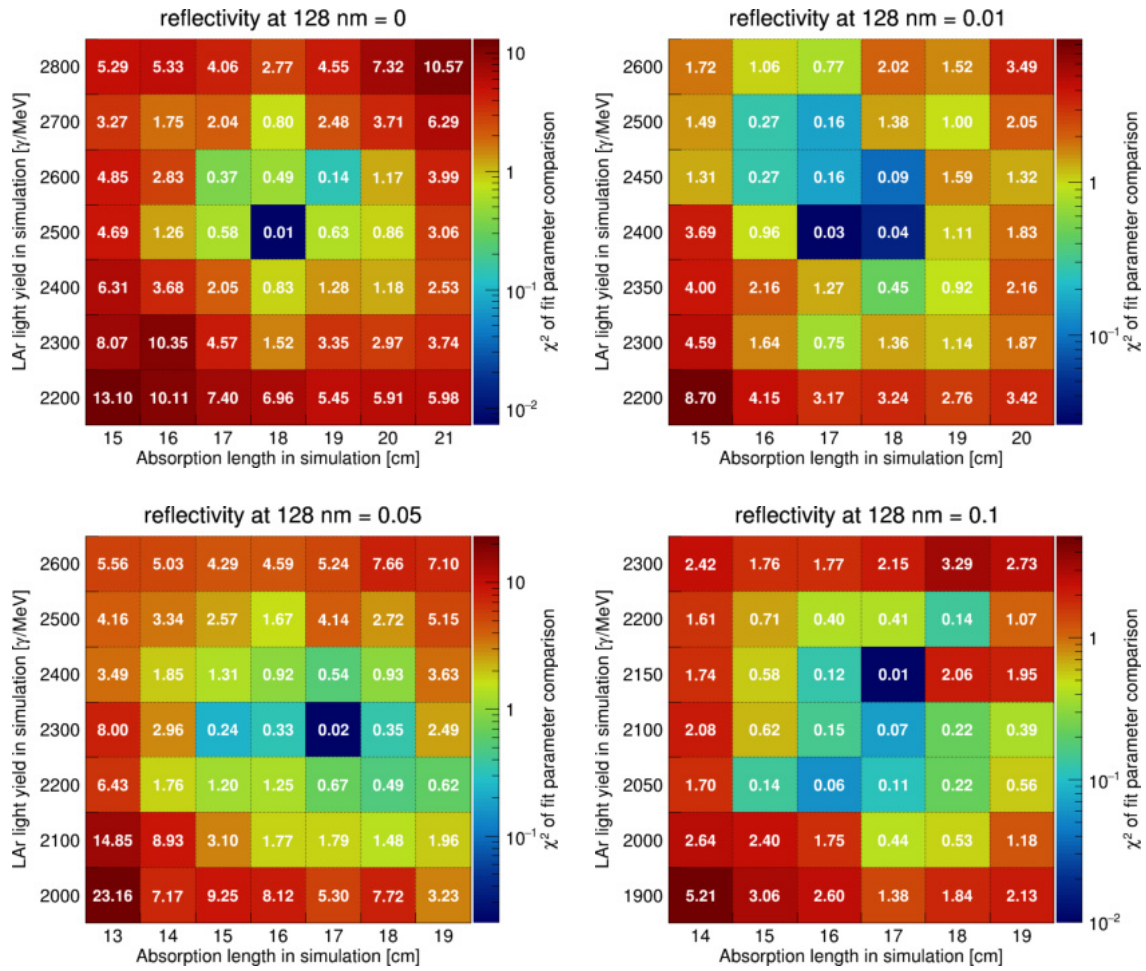


Figure A.14: Results of the χ^2 comparison of simulation and data fit parameter for the determination of the best matching simulation input parameters, i.e. the combination of light yield and absorption length. The reflectivity assumption at 128 nm used for the solid angle correction and the generation of the corresponding simulations is denoted above each plot.

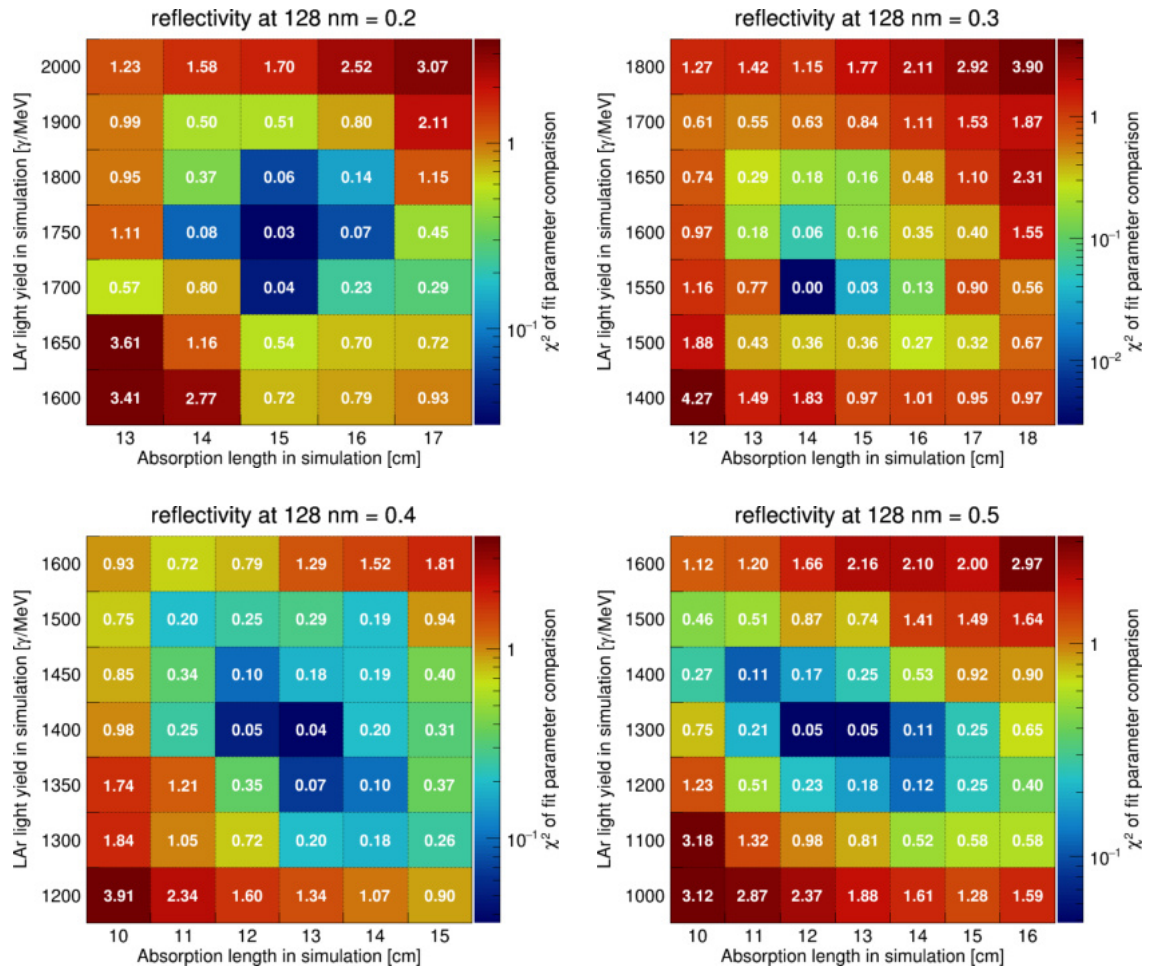


Figure A.15: Results of the χ^2 comparison of simulation and data fit parameter for the determination of the best matching simulation input parameters, i.e. the combination of light yield and absorption length. The reflectivity assumption at 128 nm used for the solid angle correction and the generation of the corresponding simulations is denoted above each plot.

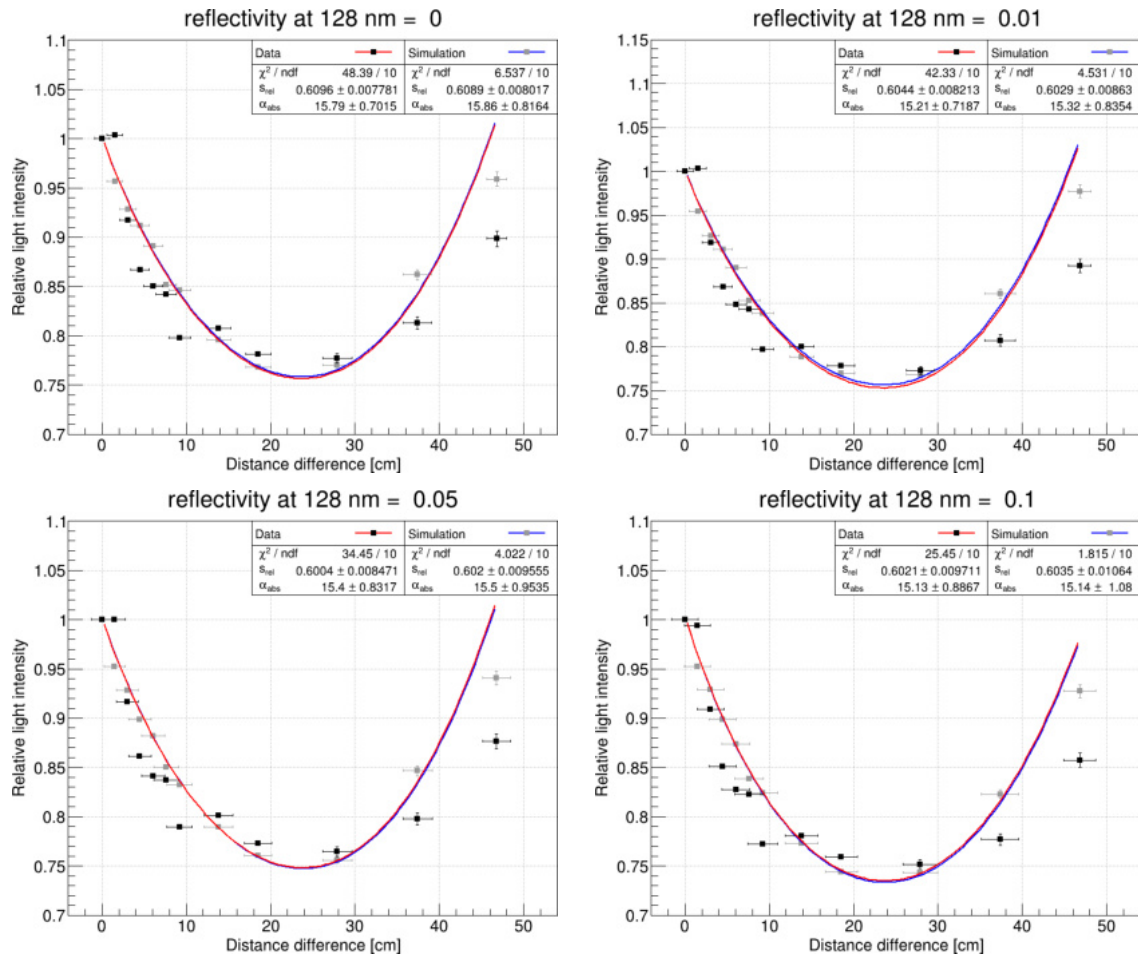


Figure A.16: Combined fit of data and respective best matching simulation for each reflectivity assumption at 128 nm, which is used for the solid angle correction and the generation of the corresponding simulations and denoted above each plot. The simulation input values of LAr light yield and absorption length of the best matching simulations are listed in table 7.2.

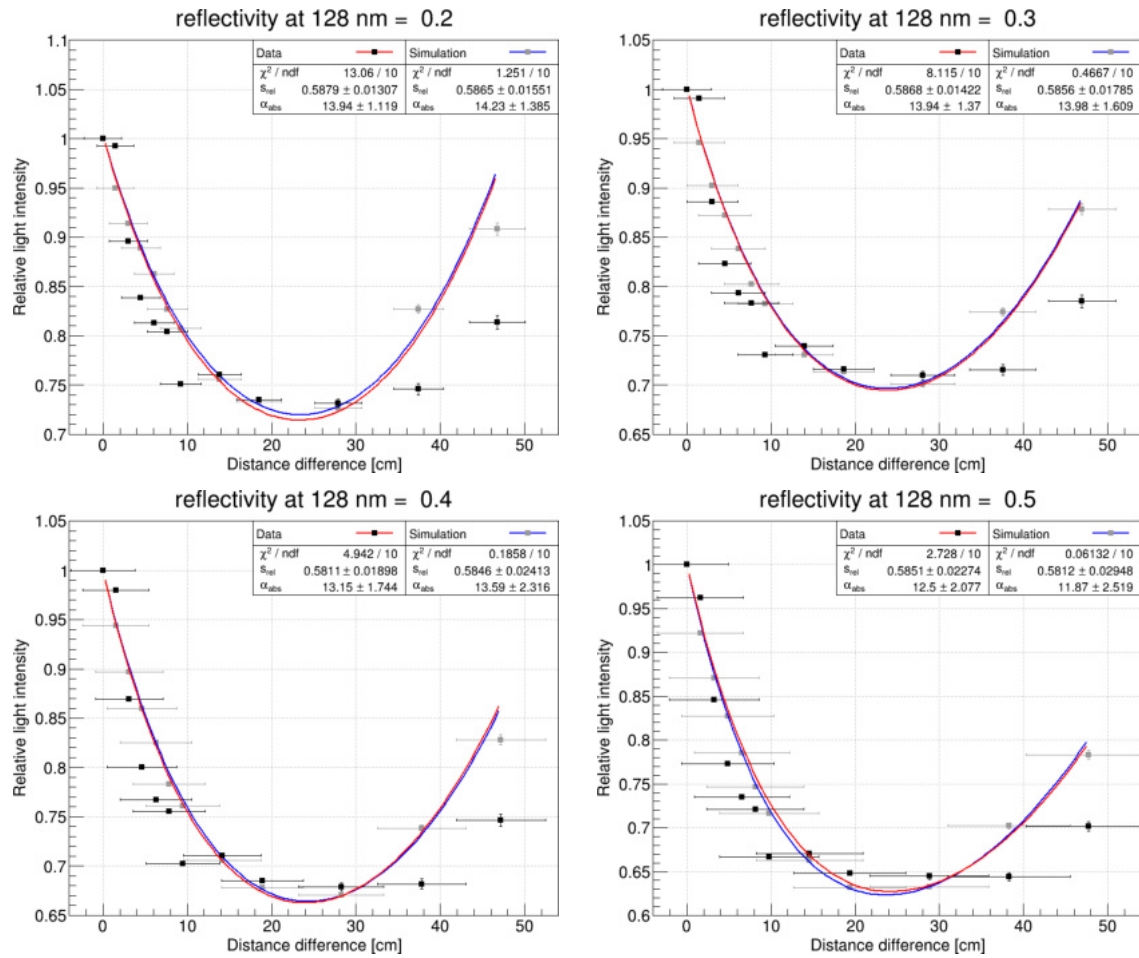


Figure A.17: Combined fit of data and respective best matching simulation for each reflectivity assumption at 128 nm, which is used for the solid angle correction and the generation of the corresponding simulations and denoted above each plot. The simulation input values of LAr light yield and absorption length of the best matching simulations are listed in table 7.2.

A.3 Attenuation simulation and analysis with the combined reflectivity

The default simulation parameters for the determination of the solid angle correction factor and the Cherenkov background are listed in table 7.3 and 7.5. In the following plots one parameter is changed to various values as stated in the legend.

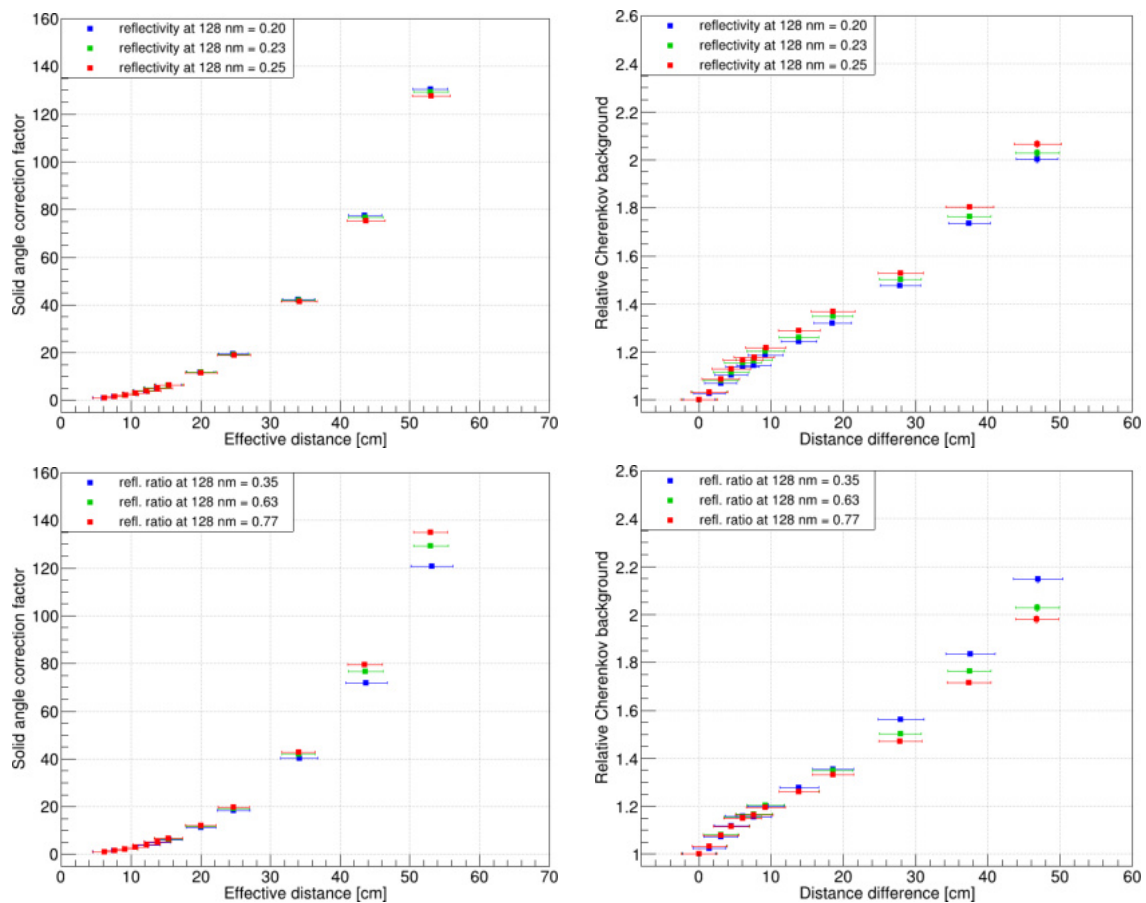


Figure A.18: (Left) Solid angle correction factor. (Right) Cherenkov background corrected by the solid angle.

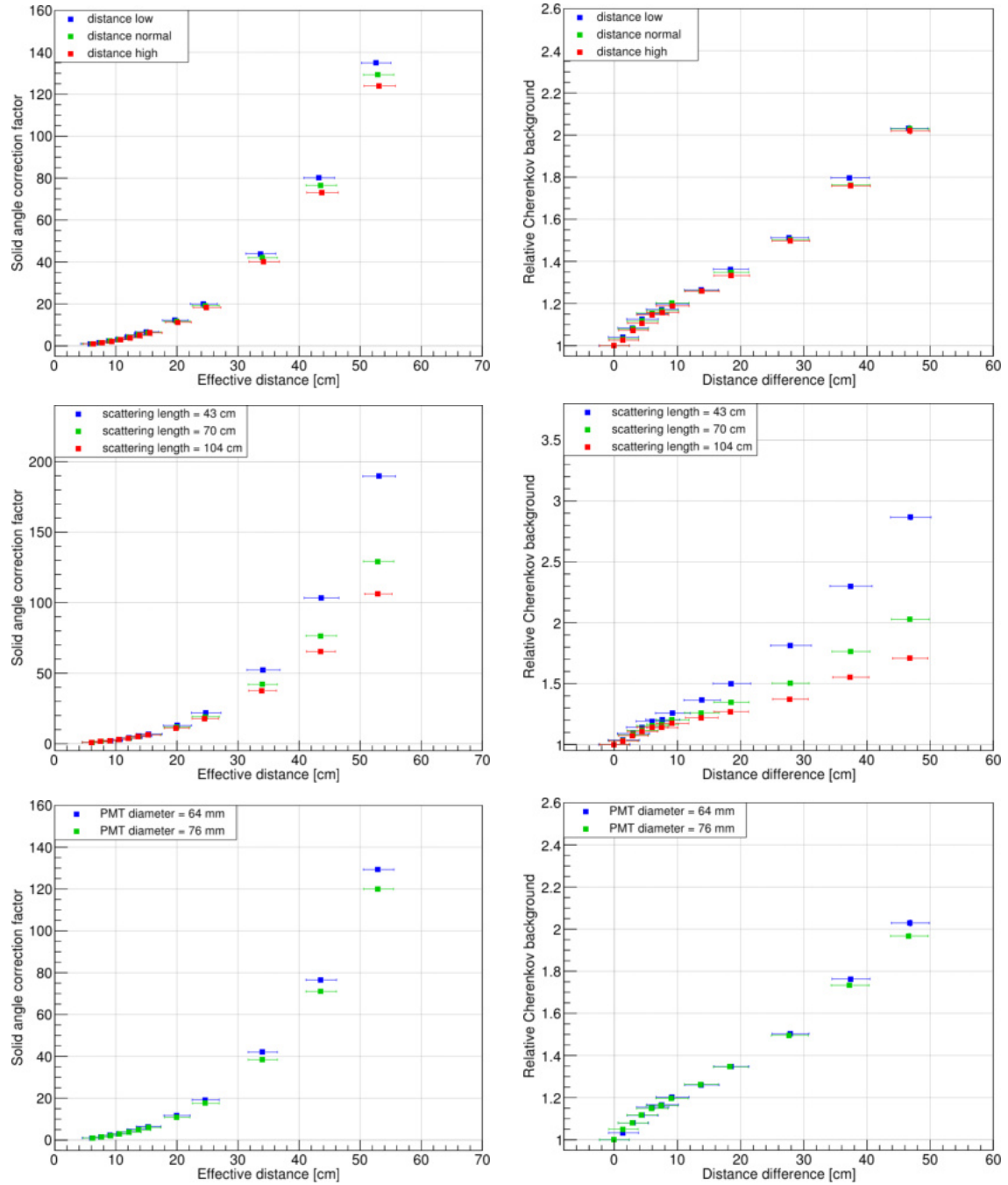


Figure A.19: (Left) Solid angle correction factor. (Right) Cherenkov background corrected by the solid angle.

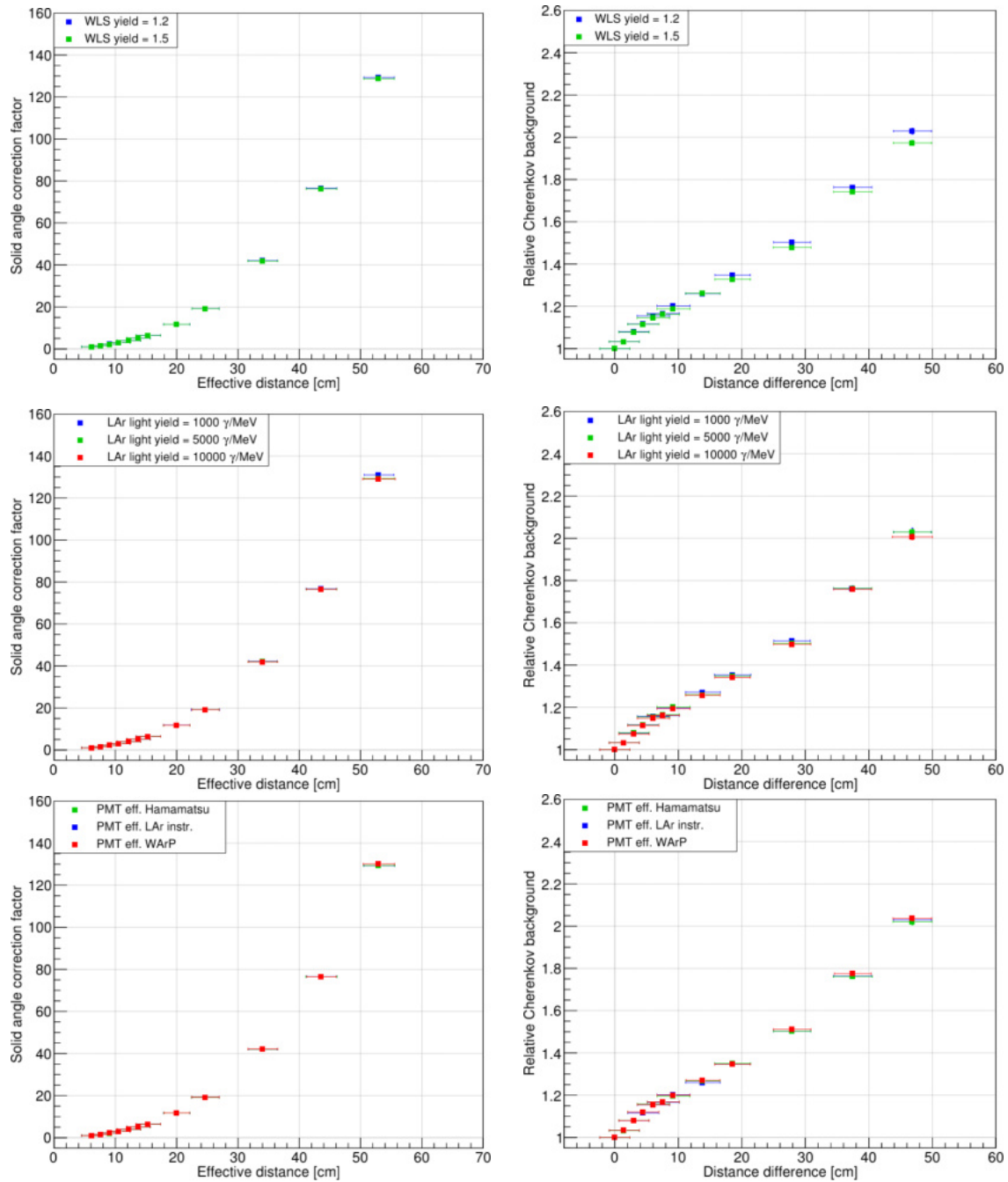


Figure A.20: (Left) Solid angle correction factor. (Right) Cherenkov background corrected by the solid angle.

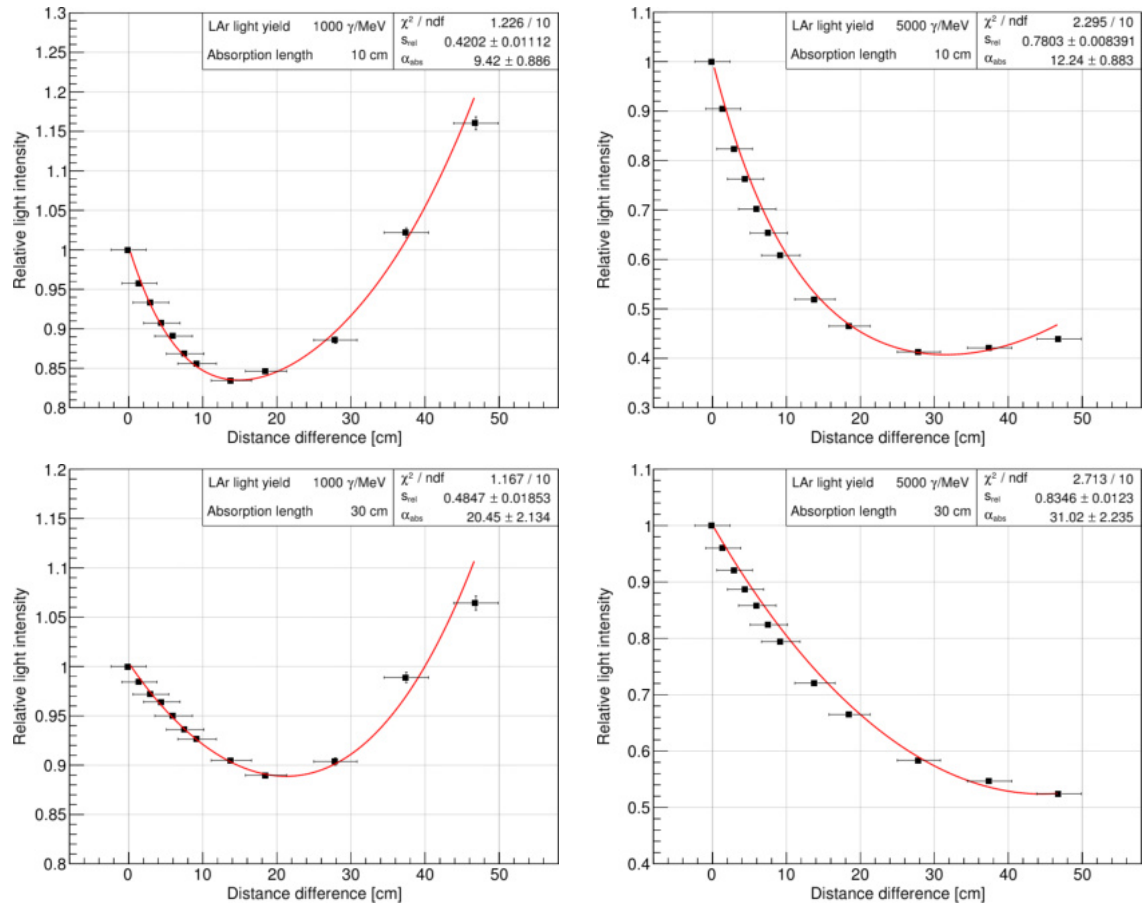


Figure A.21: Fit results of simulations produced with various parameter combinations.

Appendix B

Simulation and analysis of the $2\nu\beta\beta$ decay into excited states

B.1 Energy depositions in LAr

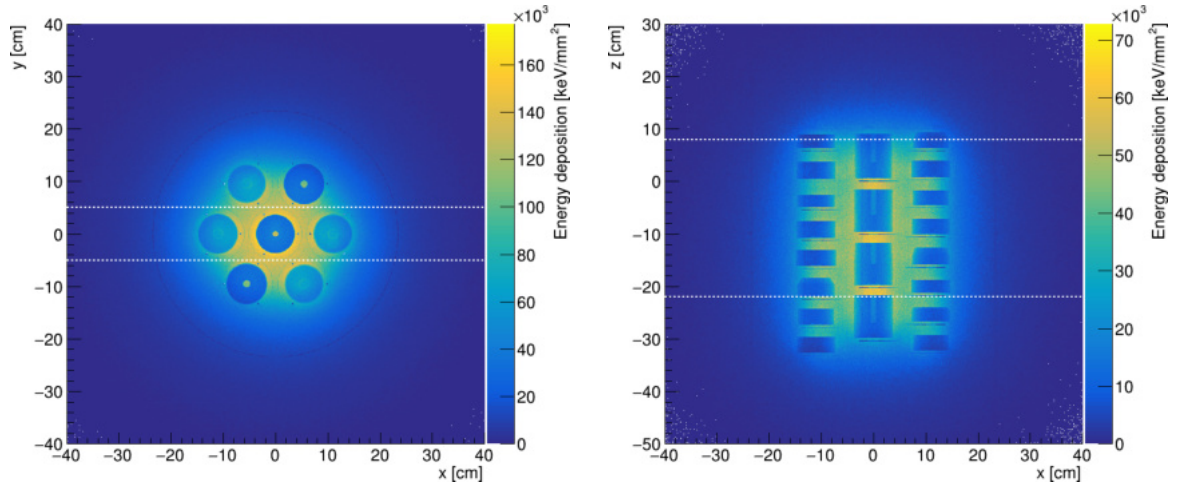


Figure B.1: Simulation of 10^8 events showing the energy depositions in LAr from the $2\nu\beta\beta$ decay of ^{76}Ge into the 0_1^+ state of ^{76}Se in Phase II+ of GERDA. See figure 9.4 for detailed explanations.

B.2 M2 fractions of each detector

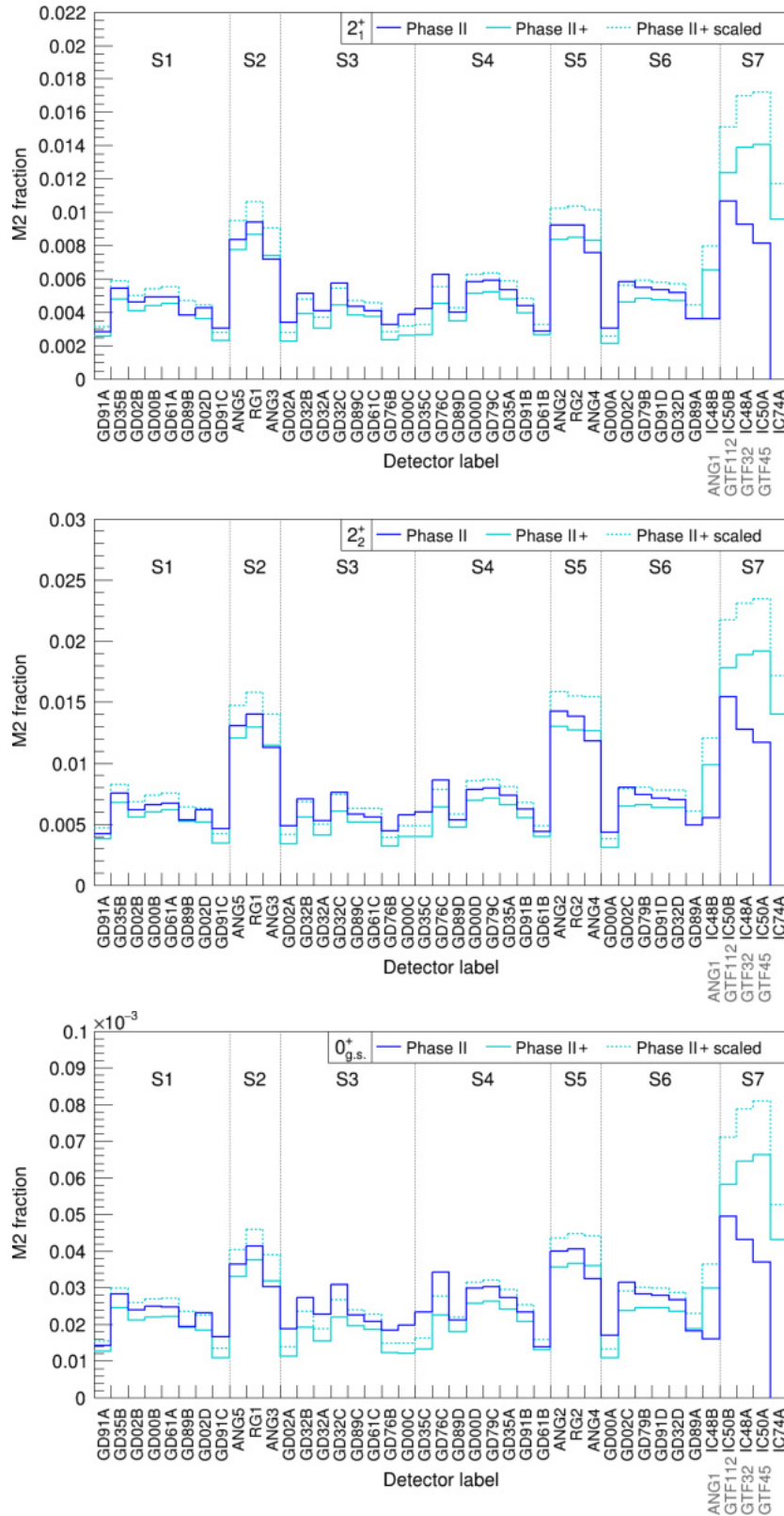


Figure B.2: M2 fraction of each detector in Phase II and Phase II+ for the raw simulations for the decay into the 2_1^+ , 2_2^+ and $0_{g.s.}^+$ states. See figure 9.6 for the 0_1^+ decay mode and detailed explanations.

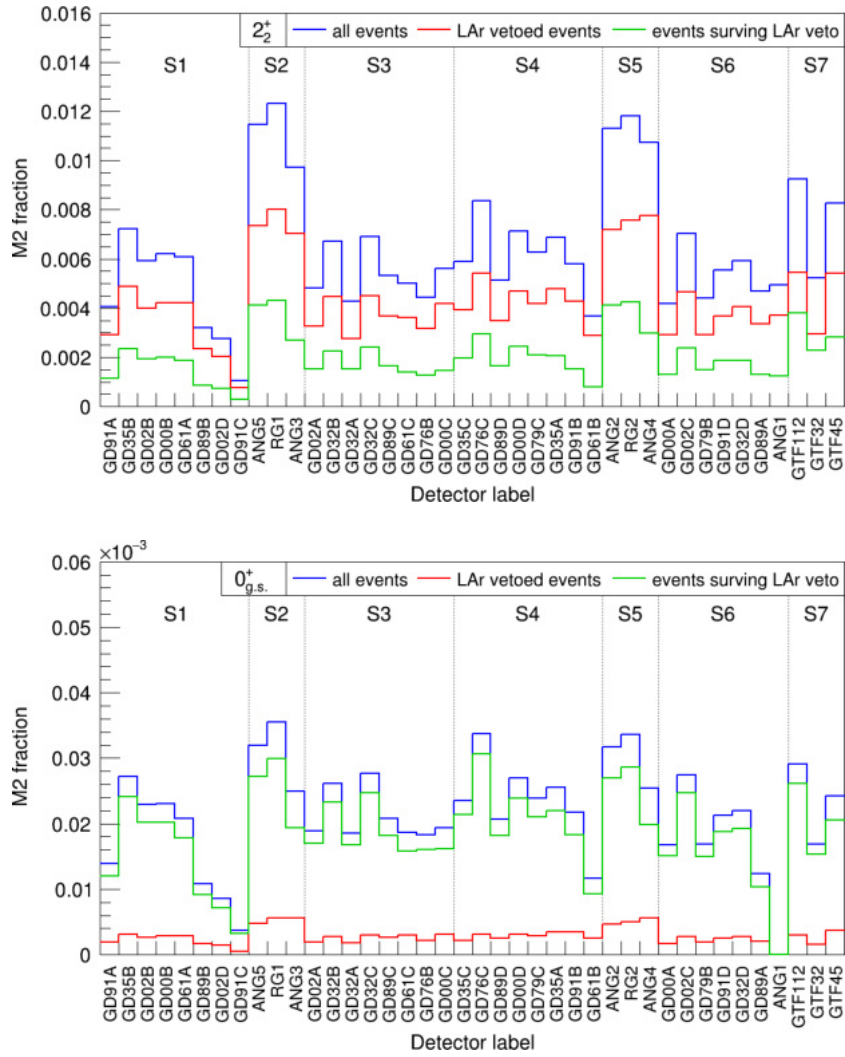


Figure B.3: M2 fraction of each detector in Phase II for the tier4ized simulations for all events, LAR vetoed events and events surviving the LAR veto cut for the decay into the 2_2^+ and the $0_{g.s.}^+$ states. See figure 9.7 for the other decay modes and detailed explanations.

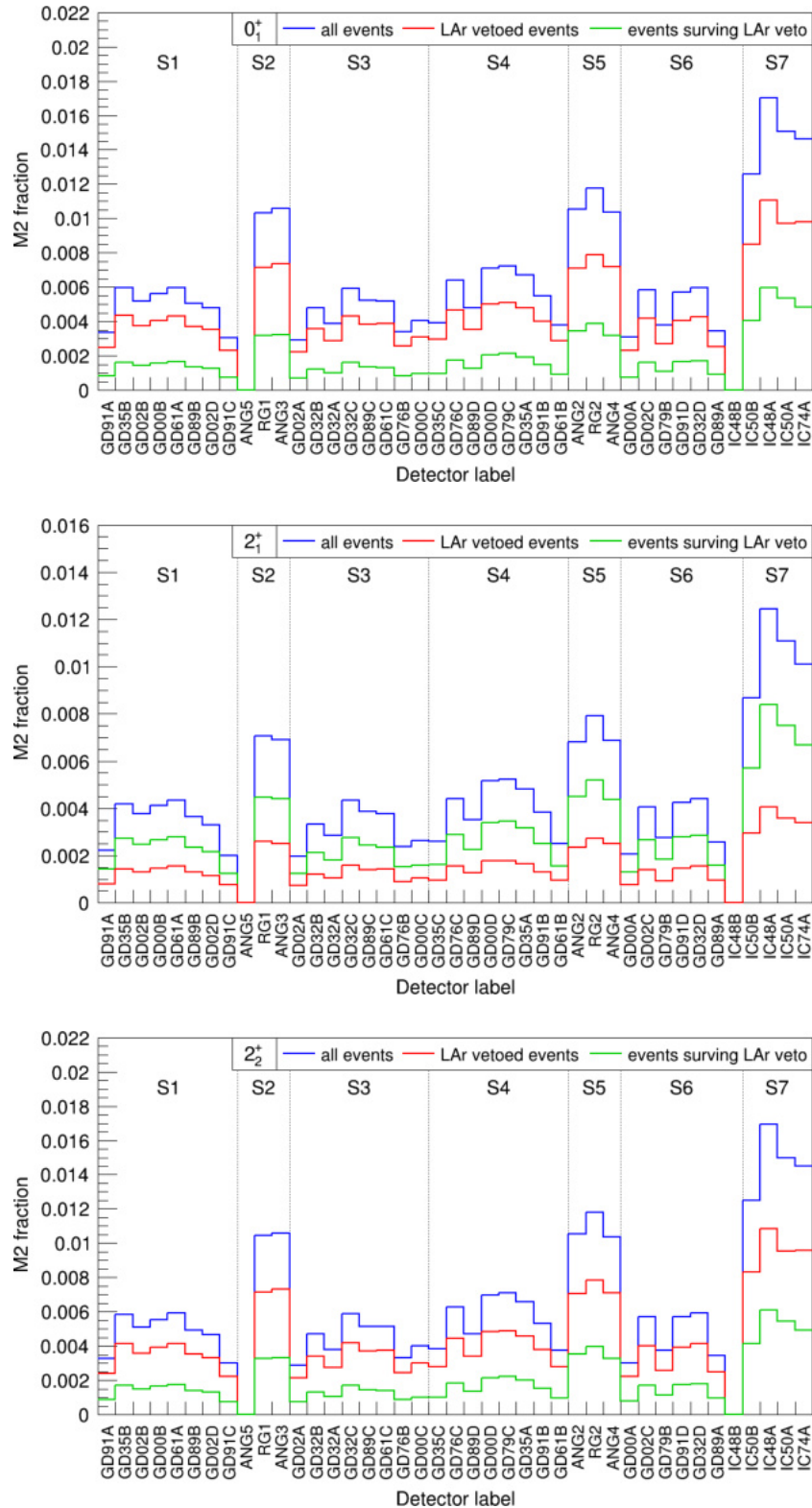


Figure B.4: M2 fraction of each detector in Phase II+ for the tier4-tized simulations for all events, LAr vetoed events and events surviving the LAr veto cut for all investigated decay modes. See figure 9.7 for detailed explanations.

B.3 Background model for M2 data in Phase II

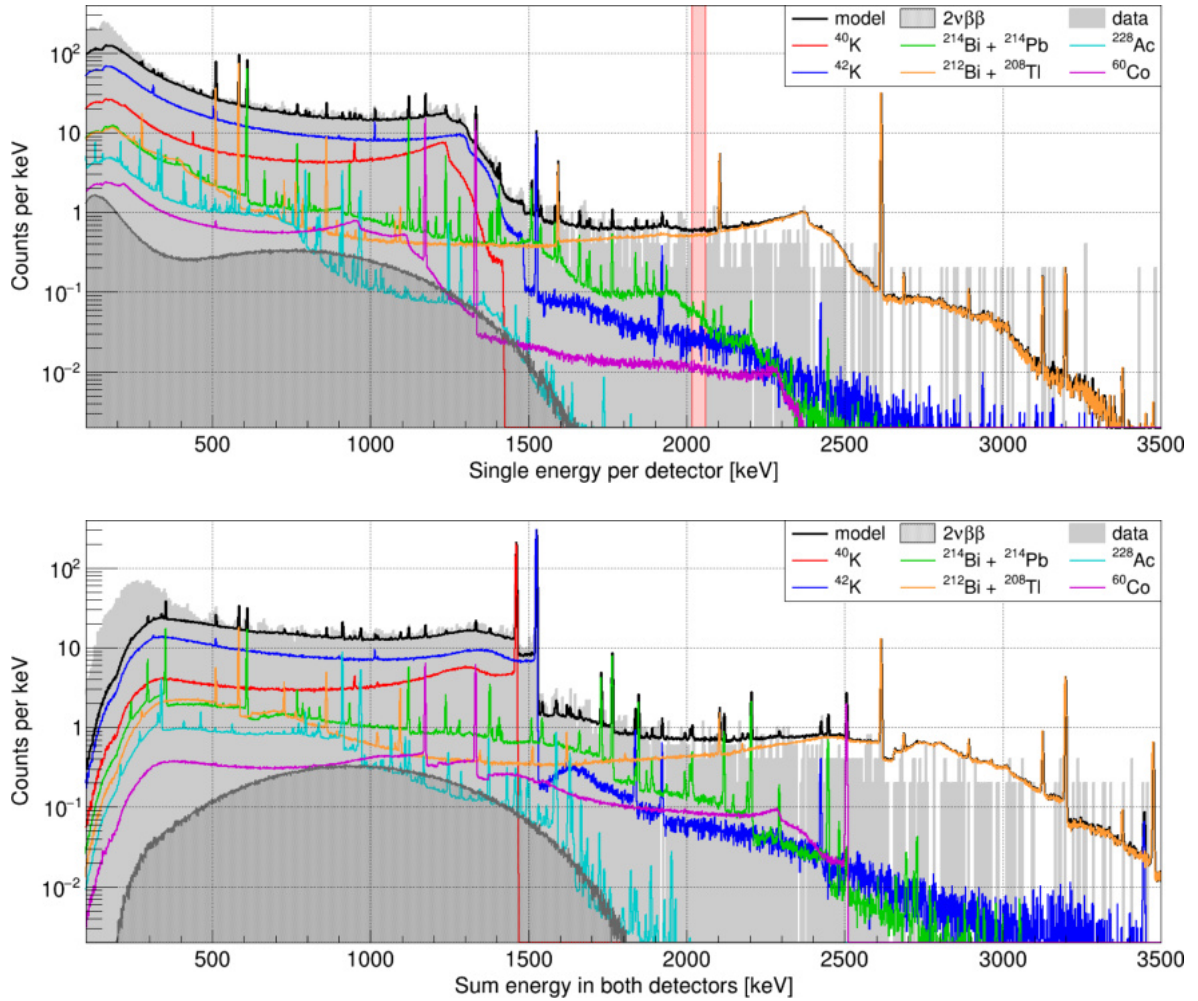


Figure B.5: Single detector spectra (top) and sum spectra (bottom) of the background model for M2 events for Phase II with an energy threshold of 40 keV for both energy depositions in the Ge detectors. In the low energy region, the data is dominated by ^{39}Ar ($Q_\beta = 565$ keV [IAE20]) events, which is not contained by the background model since only significant contributions above 500 keV are taken into account. ^{39}Ar is therefore neither relevant for the $0\nu\beta\beta$ search nor for the excited states analysis.

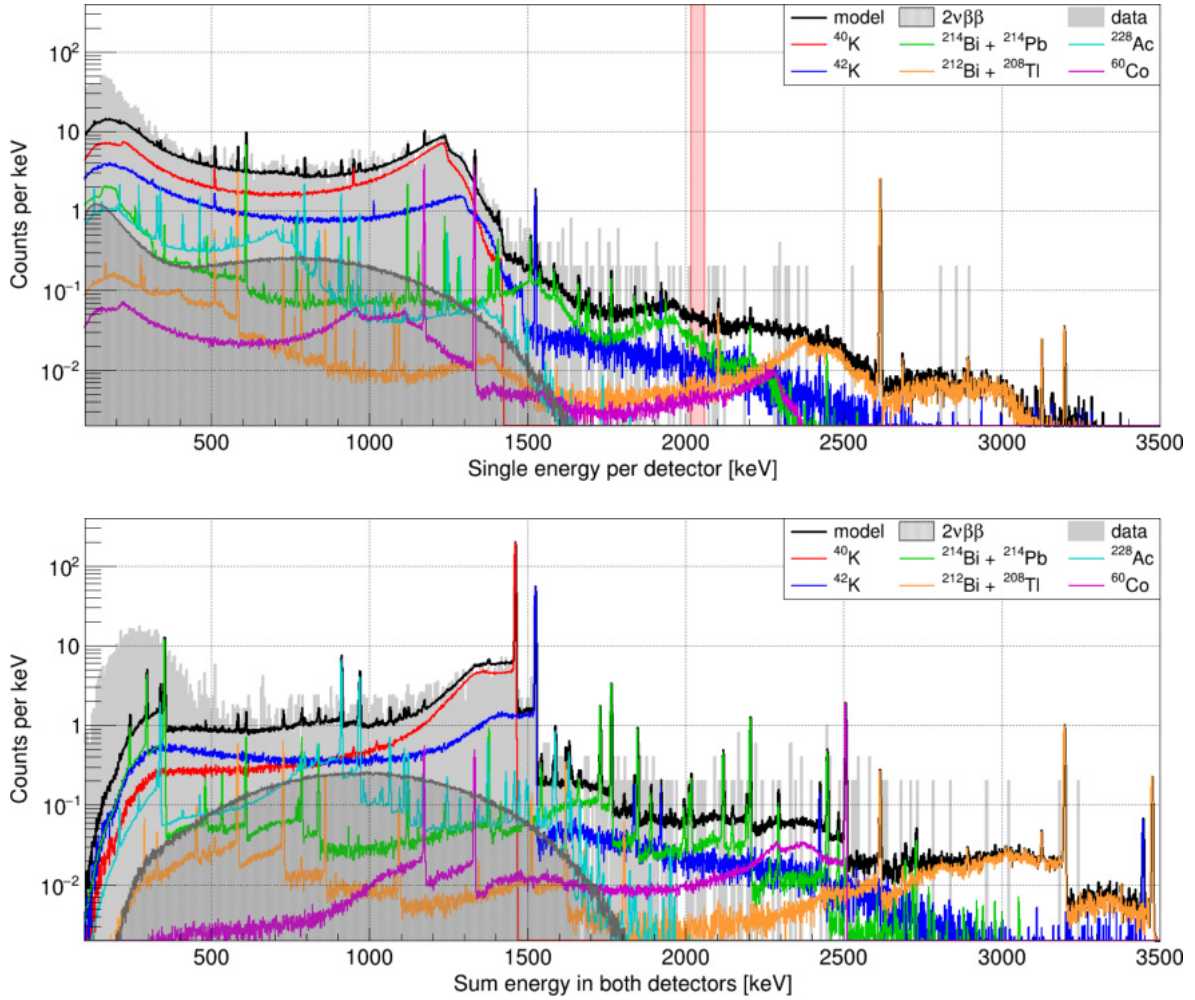


Figure B.6: Single detector spectra (top) and sum spectra (bottom) of the background model for Phase II M2 events that survived the LAr veto cut with an energy threshold of 40 keV for both energy depositions in the Ge detectors. In the low energy region, the data is dominated by ^{39}Ar ($Q_\beta = 565$ keV [IAE20]) events, which is not contained by the background model since only significant contributions above 500 keV are taken into account. ^{39}Ar is therefore neither relevant for the $0\nu\beta\beta$ search nor for the excited states analysis.

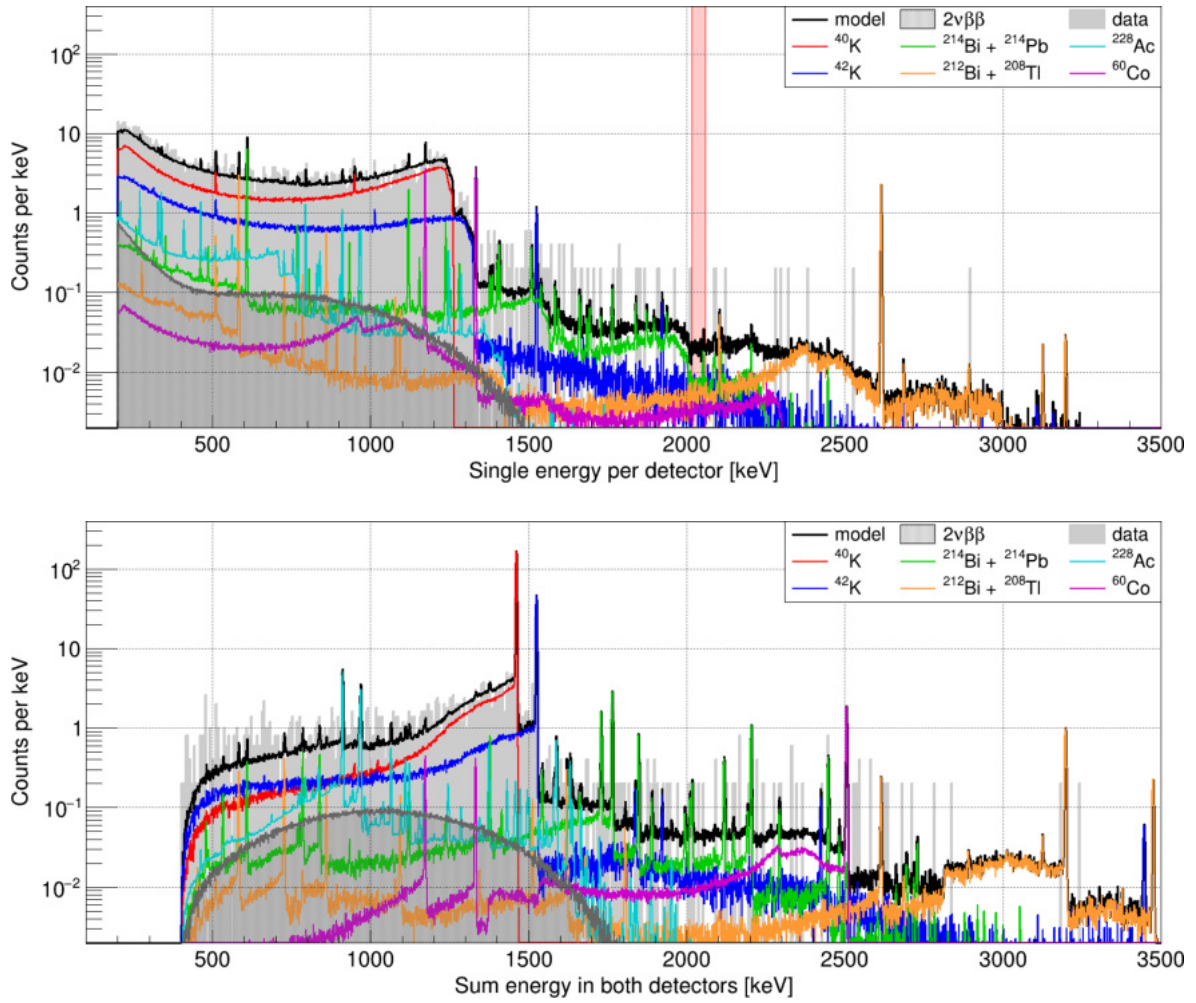


Figure B.7: Single detector spectra (top) and sum spectra (bottom) of the background model for Phase II M2 events that survived the LAr veto cut with an energy threshold of 200 keV for both energy depositions in the Ge detectors.

B.4 Events in ROI and SBs surviving all cuts

Table B.1: Center energies of the ROI and SB positions for all three decay modes for Phase II and Phase II+.

E_{center} [keV]	$0_{\text{g.s.}}^+ \rightarrow 0_1^+$	$0_{\text{g.s.}}^+ \rightarrow 2_1^+$	$0_{\text{g.s.}}^+ \rightarrow 2_2^+$ B1a	$0_{\text{g.s.}}^+ \rightarrow 2_2^+$ B1b	$0_{\text{g.s.}}^+ \rightarrow 2_2^+$ B2
ROI	559.1, 563.2	559.1	559.1	657.0	1216.1
SB 1	530.25	526.1	526.1	636.2	1188.2
SB 2	534.35	528.9	528.9	638.8	1201.7
SB 3	543.95	539.8	539.8	641.4	1206.1
SB 4	548.05	544.0	544.0	644.0	1210.5
SB 5	574.25	574.2	574.2	670.0	1221.7
SB 6	578.35	578.4	578.4	672.6	1226.1
SB 7	587.95	589.3	589.3	675.2	1230.5
SB 8	592.05	592.1	592.1	677.8	1244.0

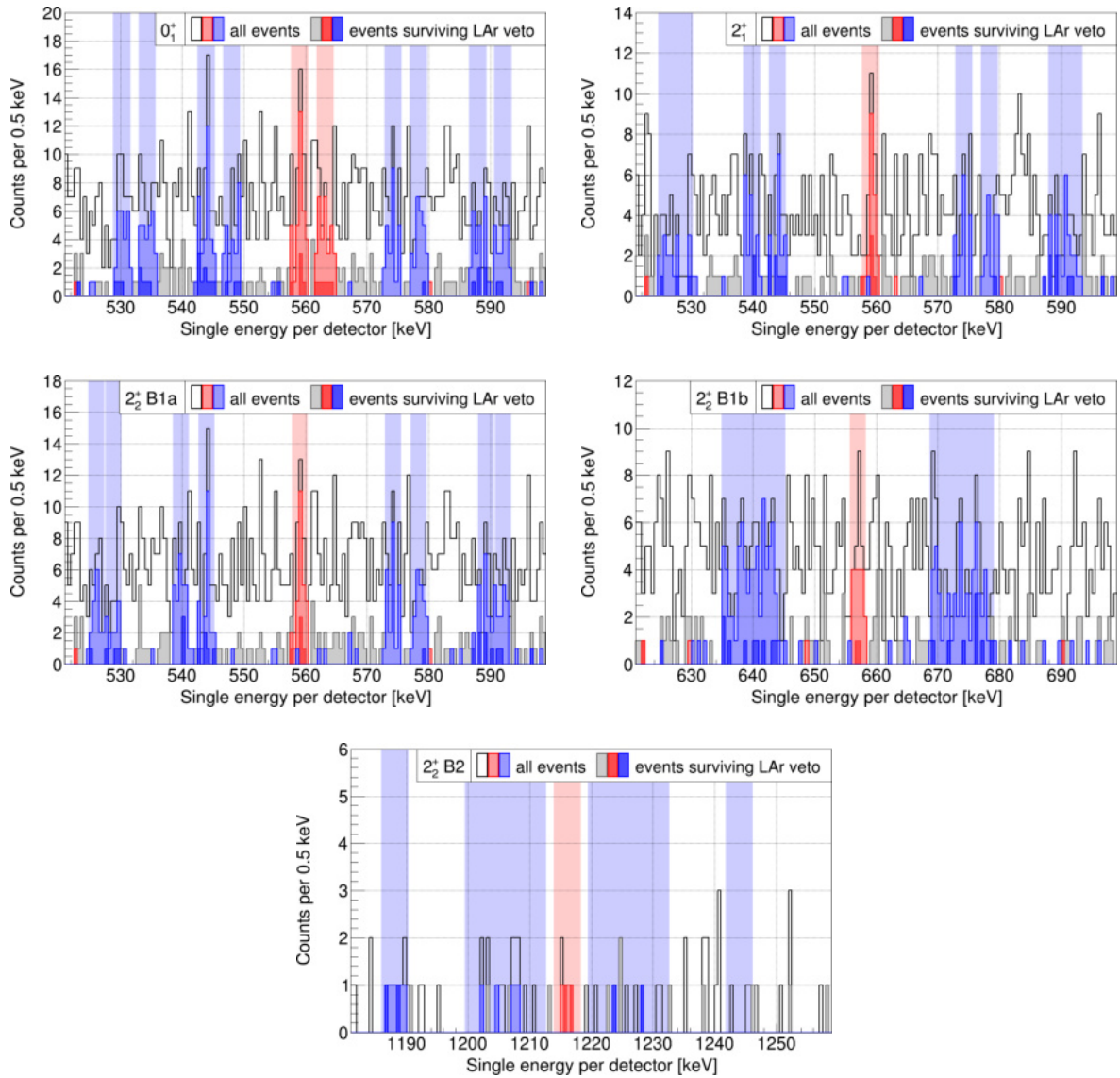


Figure B.8: Number of counts surviving all cuts for each decay mode for Phase II. See figure 9.18 for more details.

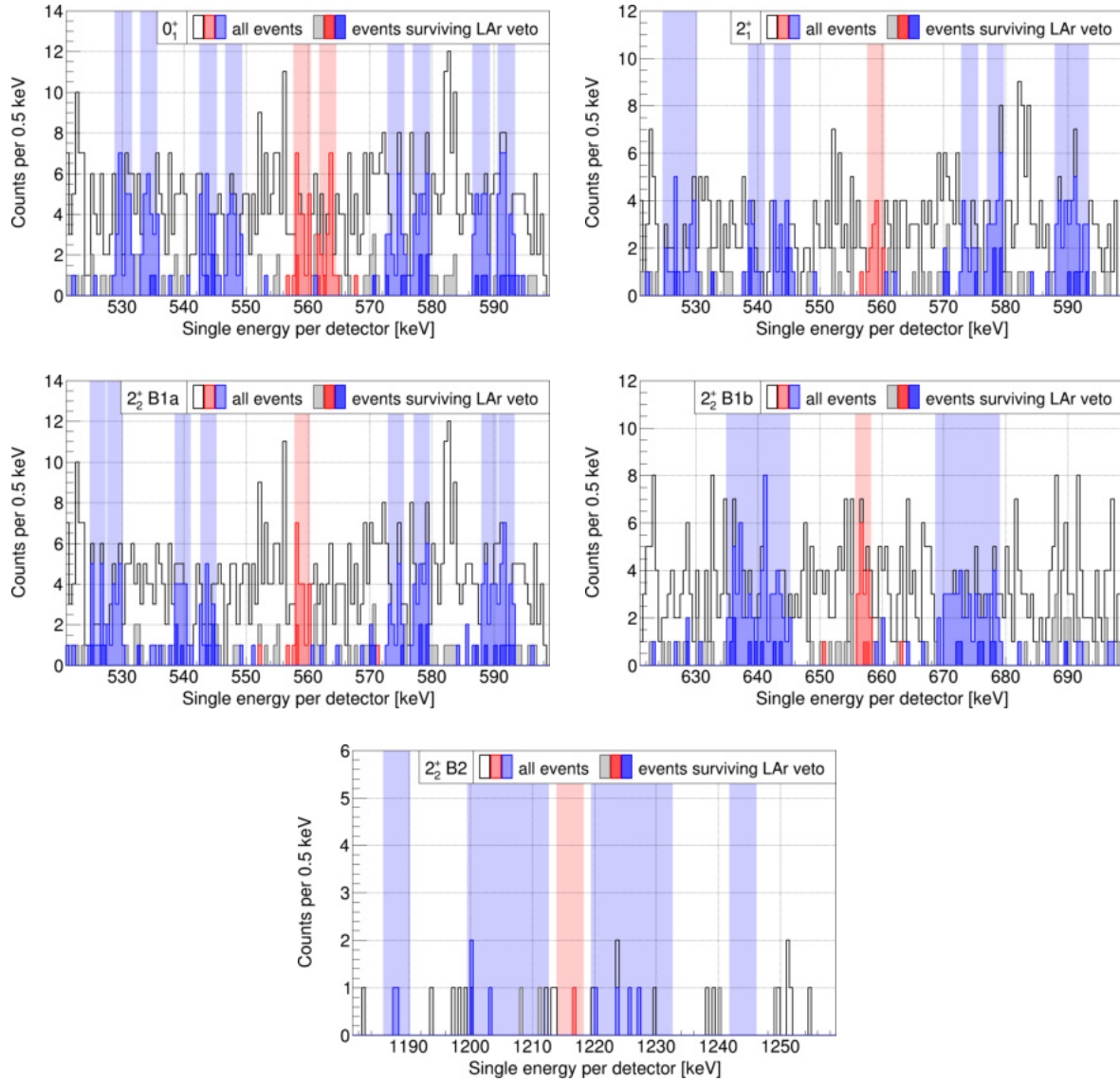


Figure B.9: Number of counts surviving all cuts for each decay mode for Phase II+. See figure 9.18 for more details.

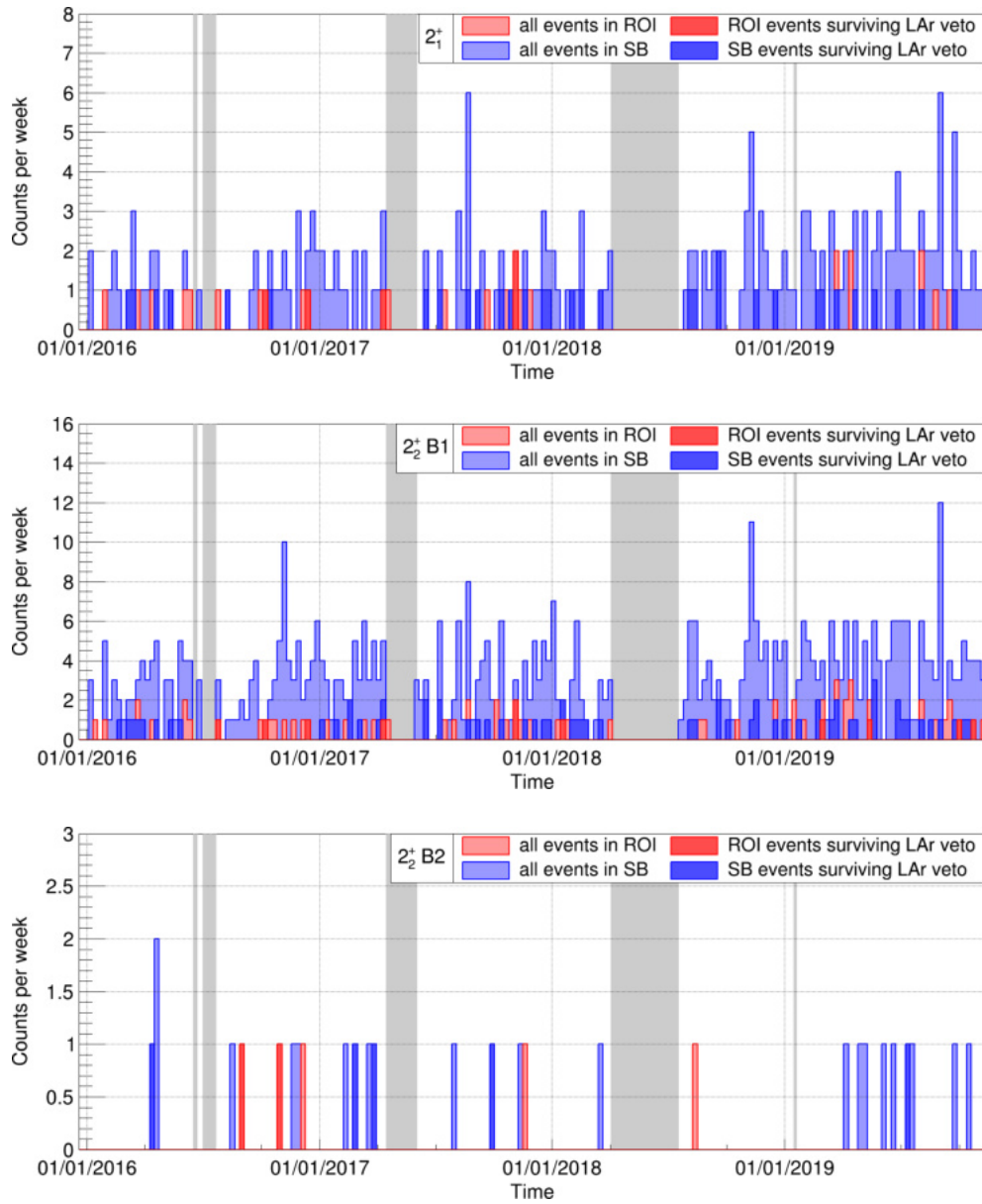


Figure B.10: Time distribution of the events in the ROI and SBs surviving all cuts with and without applying the LAr veto for the 2_1^+ and the two branches of the 2_2^+ decay mode. The inner fiber shroud is not included in the LAr veto here. The gray bands indicate the rejected run periods (see also table 9.6).

B.5 List of events in ROI surviving all cuts

Table B.2: List of events in the ROI that survive all cuts for the 0_1^+ decay mode in Phase II. The events are sorted by their run number and timestamp. The deposited energy and corresponding detector is given and the sum energy of both events is calculated. The LAr cut indicates whether the event survives the LAr veto cut (0) or not (1).

run	timestamp	E_1 [keV]	ID ₁	E_2 [keV]	ID ₂	E_{sum} [keV]	LAr cut
53	1452514402	359.8	GD32A	559.0	GD35A	918.8	1
55	1454162376	559.8	GD76B	618.2	GD00C	1178.1	1
56	1455066967	677.8	GD35C	562.0	GD76C	1239.8	1
58	1457214111	561.9	GD35B	285.7	GD02C	847.6	1
60	1458448615	557.8	GD00D	223.5	GD35A	781.3	1
60	1458564607	558.1	ANG5	580.1	GD02A	1138.2	1
60	1459188901	559.1	ANG2	269.3	RG2	828.4	1
60	1459273501	344.8	ANG5	562.8	RG1	907.6	1
60	1459328926	212.9	GD76B	562.2	GD00C	775.1	1
61	1459945891	561.8	GD35C	236.1	GD76C	798.0	1
61	1460412357	559.5	GD00A	610.6	GD02C	1170.0	1
62	1460549741	723.1	GD76C	564.5	ANG2	1287.6	1
63	1462404678	564.6	RG2	867.4	ANG4	1432.0	1
63	1462810379	562.4	GD02A	702.5	GD32B	1264.8	1
64	1464532001	560.4	GD91A	308.8	GD91C	869.2	1
65	1464966755	323.5	GD35B	564.6	GD00C	888.1	1
65	1465097655	608.9	GD32C	560.3	GD89C	1169.2	1
65	1465613823	283.5	GD02C	564.3	GTF112	847.8	1
65	1465677253	559.7	GD02A	445.9	GD89D	1005.6	1
69	1469299852	669.2	GD76B	558.6	GD00C	1227.8	1
69	1469413764	559.4	GD00B	223.6	RG1	783.0	1
73	1475310606	559.1	GD61A	480.5	GD32D	1039.6	1
73	1475626060	518.2	GD35B	559.2	GD02B	1077.4	0
73	1476804729	558.6	GD35B	354.6	GD00A	913.2	1
73	1476983241	558.7	ANG5	311.4	GD32C	870.1	1
74	1479205186	404.9	GD79B	564.0	GTF112	968.9	1
74	1479930011	564.2	GD35C	936.6	GD76C	1500.9	0
74	1480247332	563.7	GD35B	267.7	GD02B	831.4	0
75	1480688657	1035.3	ANG1	559.2	GTF45	1594.5	1
75	1481341171	897.2	ANG5	557.8	RG1	1455.0	0
75	1481655499	596.2	GD61A	563.8	GD89B	1160.0	1
75	1483475924	300.5	ANG5	563.0	GD32C	863.5	1
77	1487042219	782.8	GD89D	561.9	GTF112	1344.6	0
77	1487276122	562.5	ANG2	240.8	RG2	803.3	0
77	1487325253	736.6	GD02C	563.4	GTF112	1300.0	1
79	1492182476	559.6	GD00B	690.4	ANG3	1250.1	0
79	1492213134	559.1	GD02A	648.5	GD32B	1207.6	1
83	1496581190	711.1	GD00A	563.1	GD02C	1274.2	1
83	1496937009	697.9	RG2	563.5	ANG4	1261.4	0

continued on next page

run	timestamp	E_1 [keV]	ID ₁	E_2 [keV]	ID ₂	E_{sum} [keV]	LAr cut
<i>continued from previous page</i>							
84	1500265032	559.2	GD91B	512.7	GD61B	1072.0	1
84	1501553751	563.2	GD79C	675.8	GD35A	1239.0	1
85	1504526163	421.3	GD35C	559.6	GD76C	980.9	1
86	1505641907	558.7	ANG3	563.2	GD61C	1121.9	1
86	1507474457	236.9	GD32B	559.0	ANG2	796.0	1
87	1508806753	732.9	GD89C	559.6	GD61C	1292.5	1
87	1509358024	557.8	GD79C	214.1	GD35A	771.8	1
87	1509472530	562.3	GD35A	294.6	ANG4	856.9	1
87	1509749342	559.3	GD02B	622.0	GD00B	1181.3	0
87	1509999140	603.1	ANG5	563.2	RG1	1166.4	1
87	1510047111	224.4	RG1	559.2	GD89C	783.6	1
87	1510055512	523.0	GD89C	559.1	GD35A	1082.1	0
87	1510444704	603.5	GD02B	564.3	GD91D	1167.8	1
87	1510453287	609.0	GD89C	559.4	GD61C	1168.4	1
88	1511998182	752.9	ANG5	560.1	GTF112	1313.0	1
88	1512168381	562.7	GD35C	358.4	GD76C	921.2	1
88	1512799572	562.8	RG2	710.1	ANG4	1272.9	1
89	1513348496	228.4	GD79C	559.9	RG2	788.3	1
90	1514927437	562.5	GD89C	260.9	GD35A	823.4	1
90	1515583802	311.0	GD89C	558.0	GD61C	869.0	1
90	1515671297	228.7	GD35B	557.8	GTF112	786.5	1
91	1517006770	211.4	ANG2	562.4	RG2	773.8	1
91	1517287415	563.5	GD35C	688.4	GD76C	1252.0	1
92	1520928073	562.5	GD79B	267.1	GD91D	829.6	0
92	1521202243	305.1	GD02A	564.1	GD32B	869.2	1
92	1522631854	560.1	GD02B	349.4	GD32D	909.5	1

Table B.3: List of events in the ROI that survive all cuts for the 0_1^+ decay mode in Phase II+. The events are sorted by their run number and timestamp. The deposited energy and corresponding detector is given and the sum energy of both events is calculated. The LAr cut indicates whether the event survives the LAr veto cut (0) or not (1) or if the event is solely LAr vetoed by the inner fiber shroud (2).

run	timestamp	E_1 [keV]	ID ₁	E_2 [keV]	ID ₂	E_{sum} [keV]	LAr cut
95	1532879794	243.1	GD89C	563.9	GD61C	807.0	1
95	1533587285	567.9	RG1	563.3	IC48A	1131.3	1
97	1535571336	559.9	GD32B	248.4	GD89C	808.3	1
97	1537123038	283.2	ANG4	558.1	IC48A	841.3	1
97	1537698458	563.8	IC50B	308.2	IC48A	872.0	1
98	1540333090	791.5	GD61A	563.7	GD89C	1355.3	1
98	1540830067	246.0	GD89C	561.9	IC50A	807.9	2
99	1542337417	1043.0	ANG3	558.6	GD61C	1601.6	1
99	1544026488	271.5	GD91A	562.9	ANG2	834.4	0
99	1545161741	559.3	GD02B	556.9	IC50B	1116.2	1
100	1545942071	563.7	ANG4	223.1	IC74A	786.8	1
100	1546406775	238.9	GD91D	558.4	GD32D	797.3	1
100	1546587778	704.9	GD35B	562.2	GD32D	1267.2	1
101	1547482256	291.2	ANG4	559.0	IC74A	850.1	1
103	1548528097	392.7	GD76C	563.5	GD89D	956.2	1
105	1552443683	563.5	RG1	368.9	IC48A	932.4	1
106	1553248706	559.1	ANG4	759.4	IC74A	1318.5	1
106	1553333235	765.5	GD02B	560.2	ANG3	1325.7	1
106	1554632269	558.2	RG1	233.5	IC48A	791.6	1
106	1555086110	498.3	GD89D	559.0	GD00D	1057.3	1
106	1555231189	351.9	GD00D	560.2	IC50A	912.1	1
106	1555424057	558.7	GD32B	412.1	GD76C	970.9	1
107	1555924956	358.2	ANG3	561.9	IC50A	920.1	1
108	1557866034	292.9	RG2	558.4	GD91D	851.3	0
108	1558275179	379.0	GD02B	564.0	GD00B	943.0	1
109	1558653495	514.1	ANG3	559.0	GD79C	1073.1	1
109	1559538965	278.4	ANG2	564.5	IC50B	843.0	1
109	1560047038	216.8	GD61C	562.0	IC74A	778.8	1
110	1562043183	561.9	GD79C	602.7	GD35A	1164.6	1
110	1562441390	563.7	IC50A	414.0	IC74A	977.7	1
110	1562537140	560.0	GD32B	325.6	ANG2	885.6	1
111	1564793751	512.2	GD02A	558.5	GD32B	1070.7	1
111	1564907098	558.4	ANG4	825.3	IC74A	1383.6	1
111	1565487428	221.4	RG1	560.5	IC50A	781.9	1
111	1565744326	482.0	GD91A	563.3	GD35B	1045.4	1
111	1566699390	560.1	RG2	835.3	IC48A	1395.4	1
112	1567698843	498.5	GD00B	564.4	IC50B	1062.9	1
112	1568483024	387.6	ANG4	558.0	IC50A	945.6	1
112	1569581158	558.1	ANG4	399.8	IC48A	957.9	1
112	1570026820	558.2	GD32B	252.3	GD32C	810.6	2

Table B.4: List of events in the ROI that survive all cuts for the 2_1^+ decay mode in Phase II. The events are sorted by their run number and timestamp. The deposited energy and corresponding detector is given and the sum energy of both events is calculated. The LAr cut indicates whether the event survives the LAr veto cut (0) or not (1).

run	timestamp	E_1 [keV]	ID ₁	E_2 [keV]	ID ₂	E_{sum} [keV]	LAr cut
55	1454162376	559.8	GD76B	618.2	GD00C	1178.1	1
60	1458564607	558.1	ANG5	580.1	GD02A	1138.2	1
61	1460412357	559.5	GD00A	610.6	GD02C	1170.0	1
65	1465097655	608.9	GD32C	560.3	GD89C	1169.2	1
65	1465677253	559.7	GD02A	445.9	GD89D	1005.6	1
69	1469299852	669.2	GD76B	558.6	GD00C	1227.8	1
73	1475310606	559.1	GD61A	480.5	GD32D	1039.6	1
73	1475626060	518.2	GD35B	559.2	GD02B	1077.4	0
75	1480688657	1035.3	ANG1	559.2	GTF45	1594.5	1
75	1481341171	897.2	ANG5	557.8	RG1	1455.0	0
79	1492182476	559.6	GD00B	690.4	ANG3	1250.1	0
79	1492213134	559.1	GD02A	648.5	GD32B	1207.6	1
84	1500265032	559.2	GD91B	512.7	GD61B	1072.0	1
85	1504526163	421.3	GD35C	559.6	GD76C	980.9	1
86	1505641907	558.7	ANG3	563.2	GD61C	1121.9	1
87	1508806753	732.9	GD89C	559.6	GD61C	1292.5	1
87	1509749342	559.3	GD02B	622.0	GD00B	1181.3	0
87	1510055512	523.0	GD89C	559.1	GD35A	1082.1	0
87	1510453287	609.0	GD89C	559.4	GD61C	1168.4	1
88	1511998182	752.9	ANG5	560.1	GTF112	1313.0	1

Table B.5: List of events in the ROI that survive all cuts for the 2_1^+ decay mode in Phase II+. The events are sorted by their run number and timestamp. The deposited energy and corresponding detector is given and the sum energy of both events is calculated. The LAr cut indicates whether the event survives the LAr veto cut (0) or not (1) or if the event is solely LAr vetoed by the inner fiber shroud (2).

run	timestamp	E_1 [keV]	ID ₁	E_2 [keV]	ID ₂	E_{sum} [keV]	LAr cut
99	1542337417	1043.0	ANG3	558.6	GD61C	1601.6	1
99	1545161741	559.3	GD02B	556.9	IC50B	1116.2	1
106	1553248706	559.1	ANG4	759.4	IC74A	1318.5	1
106	1553333235	765.5	GD02B	560.2	ANG3	1325.7	1
106	1555086110	498.3	GD89D	559.0	GD00D	1057.3	1
106	1555424057	558.7	GD32B	412.1	GD76C	970.9	1
109	1558653495	514.1	ANG3	559.0	GD79C	1073.1	1
111	1564793751	512.2	GD02A	558.5	GD32B	1070.7	1
111	1564907098	558.4	ANG4	825.3	IC74A	1383.6	1
111	1566699390	560.1	RG2	835.3	IC48A	1395.4	1
112	1568483024	387.6	ANG4	558.0	IC50A	945.6	1
112	1569581158	558.1	ANG4	399.8	IC48A	957.9	1

Table B.6: List of events in the ROI that survive all cuts for the first branch (B1) of the $2\nu\beta\beta$ decay mode in Phase II. The events are sorted by their run number and timestamp. The deposited energy and corresponding detector is given and the sum energy of both events is calculated. The LAr cut indicates whether the event survives the LAr veto cut (0) or not (1).

run	timestamp	E_1 [keV]	ID ₁	E_2 [keV]	ID ₂	E_{sum} [keV]	LAr cut
53	1452514402	359.8	GD32A	559.0	GD35A	918.8	1
55	1454162376	559.8	GD76B	618.2	GD00C	1178.1	1
58	1457012878	657.1	GD91D	475.5	GD32D	1132.6	1
60	1458564607	558.1	ANG5	580.1	GD02A	1138.2	1
60	1458694122	342.3	GD02B	657.8	GTF112	1000.1	1
60	1459188901	559.1	ANG2	269.3	RG2	828.4	1
61	1460412357	559.5	GD00A	610.6	GD02C	1170.0	1
64	1464532001	560.4	GD91A	308.8	GD91C	869.2	1
65	1465097655	608.9	GD32C	560.3	GD89C	1169.2	1
65	1465170488	658.2	GD00A	516.7	GD02C	1174.9	1
65	1465677253	559.7	GD02A	445.9	GD89D	1005.6	1
69	1469540827	253.3	GD32A	657.2	GD32C	910.5	0
73	1475310606	559.1	GD61A	480.5	GD32D	1039.6	1
73	1475626060	518.2	GD35B	559.2	GD02B	1077.4	0
73	1476804729	558.6	GD35B	354.6	GD00A	913.2	1
73	1476983241	558.7	ANG5	311.4	GD32C	870.1	1
74	1478719150	392.8	GD02C	656.1	GD79B	1048.9	1
74	1479467784	656.1	RG1	248.1	GD89C	904.2	1
75	1480688657	1035.3	ANG1	559.2	GTF45	1594.5	1
75	1481341171	897.2	ANG5	557.8	RG1	1455.0	0
76	1484023544	656.9	GD32A	629.8	GD35C	1286.7	1
76	1485568483	657.5	GD00A	319.7	GD02C	977.2	1
77	1487009572	658.3	ANG3	264.2	GD00C	922.4	1
78	1489587915	656.3	GD91A	231.3	ANG5	887.6	1
78	1490367414	609.1	ANG5	657.2	GD32B	1266.3	1
79	1492182476	559.6	GD00B	690.4	ANG3	1250.1	0
79	1492213134	559.1	GD02A	648.5	GD32B	1207.6	1
84	1500265032	559.2	GD91B	512.7	GD61B	1072.0	1
84	1501519994	475.8	RG1	656.4	GD89D	1132.2	1
85	1503355078	657.7	RG1	272.8	GD89C	930.4	1
85	1503697061	316.6	GD00D	657.8	RG2	974.3	1
85	1504526163	421.3	GD35C	559.6	GD76C	980.9	1
86	1505641907	558.7	ANG3	563.2	GD61C	1121.9	1
86	1507287928	246.7	GD32C	656.7	GD89C	903.4	1
86	1507474457	236.9	GD32B	559.0	ANG2	796.0	1
87	1508806753	732.9	GD89C	559.6	GD61C	1292.5	1
87	1509749342	559.3	GD02B	622.0	GD00B	1181.3	0
87	1510055512	523.0	GD89C	559.1	GD35A	1082.1	0
87	1510453287	609.0	GD89C	559.4	GD61C	1168.4	1
88	1511998182	752.9	ANG5	560.1	GTF112	1313.0	1
90	1515583802	311.0	GD89C	558.0	GD61C	869.0	1
90	1516248500	656.8	GD76C	245.4	ANG2	902.2	0
91	1517058973	458.2	ANG3	656.9	GTF45	1115.1	1
91	1517927794	391.3	ANG5	657.6	GTF112	1048.9	1
92	1522631854	560.1	GD02B	349.4	GD32D	909.5	1

Table B.7: List of events in the ROI that survive all cuts for the first branch (B1) of the 2_2^+ decay mode in Phase II+. The events are sorted by their run number and timestamp. The deposited energy and corresponding detector is given and the sum energy of both events is calculated. The LAr cut indicates whether the event survives the LAr veto cut (0) or not (1) or if the event is solely LAr vetoed by the inner fiber shroud (2).

run	timestamp	E_1 [keV]	ID ₁	E_2 [keV]	ID ₂	E_{sum} [keV]	LAr cut
95	1533533166	401.4	GD35C	656.8	GD76C	1058.1	1
96	1534871906	657.9	RG1	378.2	GD89D	1036.1	1
97	1535571336	559.9	GD32B	248.4	GD89C	808.3	1
97	1537123038	283.2	ANG4	558.1	IC48A	841.3	1
97	1537551961	239.0	IC50B	657.4	IC48A	896.4	1
98	1539627693	386.7	ANG2	658.1	RG2	1044.8	1
99	1542337417	1043.0	ANG3	558.6	GD61C	1601.6	1
99	1544999828	657.0	GD89B	552.3	IC74A	1209.3	1
99	1545161741	559.3	GD02B	556.9	IC50B	1116.2	1
100	1546406775	238.9	GD91D	558.4	GD32D	797.3	1
101	1547316389	418.6	GD91A	657.3	GD35B	1075.9	1
101	1547482256	291.2	ANG4	559.0	IC74A	850.1	1
103	1548598015	306.2	IC50A	657.8	IC74A	964.0	1
104	1551575482	777.3	ANG3	657.7	IC74A	1435.0	0
104	1551700939	571.1	GD00D	656.0	ANG2	1227.1	1
106	1553248706	559.1	ANG4	759.4	IC74A	1318.5	1
106	1553333235	765.5	GD02B	560.2	ANG3	1325.7	1
106	1553414033	656.8	GD35A	1092.1	ANG4	1748.9	1
106	1554546630	657.0	GD32C	295.8	GD76C	952.8	1
106	1554632269	558.2	RG1	233.5	IC48A	791.6	1
106	1555086110	498.3	GD89D	559.0	GD00D	1057.3	1
106	1555231189	351.9	GD00D	560.2	IC50A	912.1	1
106	1555424057	558.7	GD32B	412.1	GD76C	970.9	1
108	1557585587	336.6	GD79C	658.0	GD35A	994.7	1
108	1557866034	292.9	RG2	558.4	GD91D	851.3	0
109	1558653495	514.1	ANG3	559.0	GD79C	1073.1	1
110	1562537140	560.0	GD32B	325.6	ANG2	885.6	1
111	1564793751	512.2	GD02A	558.5	GD32B	1070.7	1
111	1564907098	558.4	ANG4	825.3	IC74A	1383.6	1
111	1566699390	560.1	RG2	835.3	IC48A	1395.4	1
112	1567482111	663.4	ANG3	656.3	IC74A	1319.7	1
112	1567797023	243.6	ANG2	656.6	RG2	900.2	1
112	1568459402	657.6	GD00A	650.9	GD02C	1308.5	1
112	1568483024	387.6	ANG4	558.0	IC50A	945.6	1
112	1569581158	558.1	ANG4	399.8	IC48A	957.9	1
112	1570026820	558.2	GD32B	252.3	GD32C	810.6	2
113	1571125568	656.7	GD00A	489.0	GD02C	1145.7	1
113	1571634494	657.0	IC50B	242.9	IC48A	899.9	0
114	1573405321	607.1	GD91D	656.1	GD32D	1263.3	1

Table B.8: List of events in the ROI that survive all cuts for the second branch (B2) of the 2_2^+ decay mode in Phase II. The events are sorted by their run number and timestamp. The deposited energy and corresponding detector is given and the sum energy of both events is calculated. The LAr cut indicates whether the event survives the LAr veto cut (0) or not (1).

run	timestamp	E_1 [keV]	ID ₁	E_2 [keV]	ID ₂	E_{sum} [keV]	LAr cut
71	1472915677	551.5	ANG5	1216.0	GD89C	1767.5	0
74	1477840989	313.1	GD00A	1216.9	GTF112	1529.9	0
75	1480959366	1215.3	GD35B	320.5	GD02B	1535.7	1
88	1511021389	525.2	ANG2	1216.4	GTF112	1741.7	1

Table B.9: List of events in the ROI that survive all cuts for the second branch (B2) of the 2_2^+ decay mode in Phase II+. The events are sorted by their run number and timestamp. The deposited energy and corresponding detector is given and the sum energy of both events is calculated. The LAr cut indicates whether the event survives the LAr veto cut (0) or not (1) or if the event is solely LAr vetoed by the inner fiber shroud (2).

run	timestamp	E_1 [keV]	ID ₁	E_2 [keV]	ID ₂	E_{sum} [keV]	LAr cut
96	1534384772	1217.0	RG2	412.2	IC48A	1629.2	1

B.6 Marginalized posterior probability density distributions

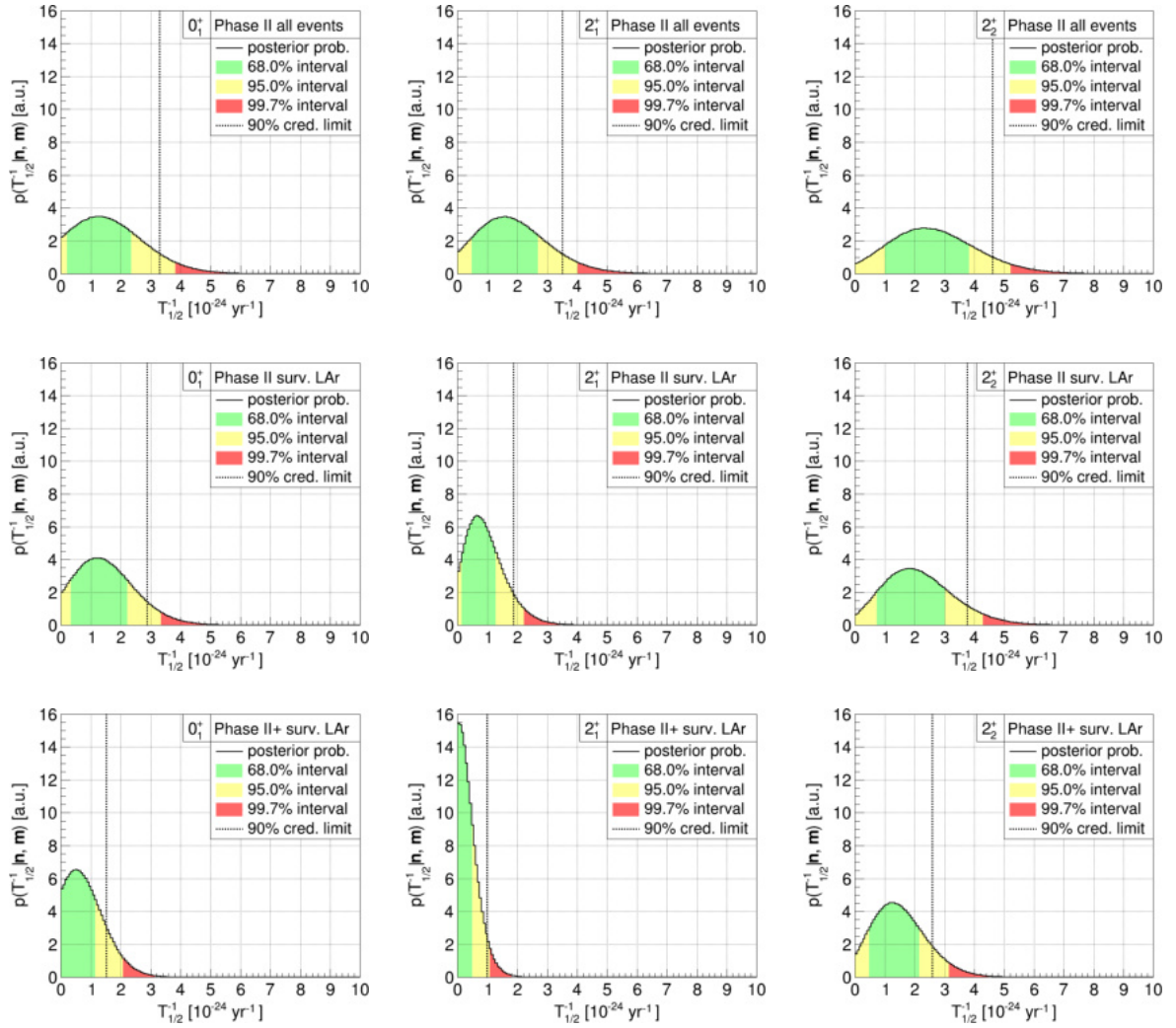


Figure B.11: Marginalized posteriors for $T_{1/2}^{-1}$ for Phase II and Phase II+ with and without applying the LAr veto. The posteriors are all compatible with $T_{1/2}^{-1} = 0$ within the 68%, 95% or 99.7% interval. Thus, a 90% credibility limit is derived (see tab. 9.9).

List of Figures

1.1	Normal and inverted neutrino mass ordering	13
1.2	Fermion masses of quarks and charged leptons and allowed regions of neutrino masses	16
1.3	Constraints on the parameter space of the effective Majorana neutrino mass	17
1.4	Masses of nuclei and the respective mass parabolas	18
1.5	Feynman graphs of the $2\nu\beta\beta$ -decay and $0\nu\beta\beta$ -decay	19
1.6	Compilation of NMEs calculated with various models assuming for nuclides of different mass numbers	20
1.7	Typical spectral shape of a $\beta\beta$ -decay	22
2.1	Muon flux depending on the depth of several underground laboratories	25
2.2	Sketch of the LNGS underground laboratory with the three main halls	26
2.3	The setup of the GERDA experiment in phase II	27
2.4	LAr veto for Phase II of GERDA	28
2.5	Monitoring of the survival probability of ^{39}Ar events and triplet lifetime of LAr in GERDA Phase II	29
2.6	View on the bottom of the 7 germanium detector strings hanging in the lock	29
2.7	Sketch of the detector array for Phase II and II+	30
2.8	Detector holder structure in Phase II and II+ of GERDA	31
2.9	String configuration in Phase II	31
2.10	String configuration in Phase II+	32
2.11	Energy spectra of GERDA Phase II	33
2.12	Lock design for the LAr cryostat and LAr veto for the LEGEND experiment	34
3.1	Sketch of the LAr scintillation mechanism	35
3.2	LAr energy scheme of the four lowest excited states	36
3.3	Argon scintillation emission spectrum	38
3.4	Time constants of the LAr scintillation mechanism with various concentrations of N_2 and O_2	40
3.5	Dependence of the quenching factor Q_F and surviving fraction S_F of the scintillation light in LAr for N_2 and O_2	41
3.6	Wavelength-dependent attenuation length and redshift of the scintillation peak in LAr	42
4.1	Schematical depiction of the specular and diffuse reflection at a surface	45
4.2	Measurements of the specular reflectance of stainless steel and aluminum	46
4.3	Reflectance of aluminum, gold and silver, which are typically used as mirror coatings	46
4.4	Reflectivity measuring device in Münster	47

4.5	Emission spectrum of the deuterium lamp McPherson Model 632	48
4.6	Transmission spectrum of fused silica	49
4.7	Sketch of the spectrophotometer Cary 5000 of Agilent	50
4.8	Reflectance of PTFE	50
4.9	Reflectivity measurements in the visible region	51
4.10	Reflectivity dependence on the chosen spot of the steel sample	52
4.11	Average steel reflectivity of the measurement performed in the IPF.	53
4.12	Absorption cross section of oxygen	53
4.13	Reflectometer of the PTB	54
4.14	Measurements of the homogeneity of the steel reflectance	55
4.15	Angular measurement of the reflectivity and unfolding of the data	56
4.16	Combination of the reflectivity measurements	57
5.1	Absorption length and scintillation peak of LAr as implemented in the simulation	61
5.2	Refractive index and scattering length of LAr as implemented in MaGe	62
5.3	Schematic visualization of the possible reflection processes in GEANT4	64
5.4	Average steel reflectivities measured in the IPF and assumptions below 200 nm for the simulations	65
5.5	Absorption length measurements of TPB	66
5.6	PMT efficiencies measured for the model R11065	67
5.7	Compilation of the LAr scintillation peak, the Cherenkov emission spectrum, the WLS emission spectrum and the quantum efficiency of the PMT	68
6.1	CAD drawing of the setup for the attenuation measurement	70
6.2	CAD drawing and picture of the stepper motor	70
6.3	Decay scheme of ^{210}Po	72
6.4	Decay chain of ^{90}Sr	73
6.5	With DECAV0 generated electron emission spectrum of ^{90}Sr and ^{90}Y	73
6.6	Decay scheme of ^{241}Am	74
6.7	Origin positions of scintillation photons created in LAr	74
6.8	Pulse trace with flagged samples	77
6.9	Examples of physical events that can be identified by the software trigger	78
7.1	Pulse integral spectra of the attenuation measurement for various measuring points	81
7.2	Example of a pulse integral spectrum with the combined fit	83
7.3	Schematic drawing of the setup as it is implemented in MaGe	84
7.4	Solid angle correction factors for various reflectivity assumptions and LAr light yields	85
7.5	Relative Cherenkov background for various reflectivity assumptions and LAr light yields	86
7.6	Polynomial fit of the relative Cherenkov background	87
7.7	Relative light intensity observed in two simulation examples with various input parameters and application of the combined fit	88
7.8	Results of the χ^2 comparison of the fit parameters of data and simulation	90
7.9	Values of the fit parameters of the combined fit of the best matching simulations of each reflectivity assumption analyzed with each solid angle correction	91
7.10	χ^2 values of the comparison of data and best matching simulation fit results for various reflectivities	91
7.11	Comparison of the combined fits of the experimental data and the best matching simulation	92

7.12	Results of the χ^2 comparison of the fit parameters of data and simulation for the combined reflectivity	95
7.13	Comparison of the combined fits of the experimental data and the best matching simulation for the combined reflectivity	96
8.1	Typical scintillation event in LAr	101
8.2	Summed up histograms of the hit times of all simulated events	103
8.3	Reduced χ^2 values of the histogram comparison for a triplet lifetime of 1000 ns	104
8.4	Fit of the histogram generated with the best matching values of t_{pulse} and t_{event} for a simulation performed with a triplet lifetime of 1000 ns	105
8.5	Histogram and fit of the summed up pulses for the experimental data	106
9.1	Decay scheme of the $\beta\beta$ decay of ^{76}Ge into ^{76}Se	110
9.2	Angular correlation and distribution of γ ray cascades from the 0_1^+ and the 2_2^+ states of ^{76}Se	112
9.3	Positions of energy depositions of γ rays and electrons in LAr as well as creation locations of scintillation photons	114
9.4	Energy depositions in LAr from the $2\nu\beta\beta$ decay of ^{76}Ge into the 0_1^+ state of ^{76}Se	116
9.5	LAr photon detection probability map for Phase II of GERDA	116
9.6	M2 fraction for each detector in Phase II and Phase II+	117
9.7	M2 fraction of each detector in Phase II for the tier4ized simulations for all events, LAr vetoed events and events surviving the LAr veto cut	119
9.8	Two-dimensional plot of the energy depositions of M2 events for the 0_1^+ state	122
9.9	Single detector spectra and sum spectra of M2 events for the 0_1^+ state	122
9.10	Two-dimensional plot of the energy depositions of M2 events for the 2_1^+ state	123
9.11	Single detector spectra and sum spectra of M2 events for the 2_1^+ state	123
9.12	Two-dimensional plot of the energy depositions of M2 events for the 2_2^+ state	124
9.13	Single detector spectra and sum spectra of M2 events for the 2_2^+ state	124
9.14	Two-dimensional depiction of the background model for Phase II	126
9.15	Single detector spectra and sum spectra of the background model for M2 events for Phase II	127
9.16	ROI and SB positions for all three decay modes	129
9.17	Two-dimensional depiction of the M2 data for Phase II and Phase II+ with and without applying the LAr veto cut	132
9.18	Number of counts surviving all cuts for each decay mode summed up for Phase II and Phase II+	133
9.19	Time distribution of the events in the ROI and SBs surviving all cuts for the 0_1^+ decay mode	135
9.20	Marginalized posteriors for $T_{1/2}^{-1}$ for Phase II+ without applying the LAr veto	137

List of Tables

1.1	List of $\beta\beta$ -isotopes with natural abundance, $Q_{\beta\beta}$, $T_{1/2}^{2\nu}$ and $T_{1/2}^{0\nu}$	23
3.1	Production times of the excimer molecules for different particle beams depositing energy in LAr.	36
3.2	Compilation of selected measurements of singlet τ_s and triplet τ_t lifetimes and singlet to triplet intensity ratio I_s/I_t in pure LAr.	37
3.3	Measurements of the peak position of the 2nd excimer continuum in LAr.	38
3.4	The rate constant k_Q of the light quenching process of the triplet state derived from doping LAr with various impurities	40
3.5	Compilation of attenuation length measurements performed in very pure LAr and for known impurity compositions	43
3.6	Measurements of the absorption coefficient k_A for various impurities in LAr investigated in different concentration ranges	43
5.1	Optical surface settings for the surface boundary of steel and LAr	63
5.2	Optical surface properties of the steel surface in LAr and the implemented measured data sets of the steel reflectivity.	64
5.3	Optical property settings of the WLS TPB and the implemented values in MaGe.	65
6.1	Compilation of relevant possible intrinsic impurities in stainless steel and their relevant types of decays	71
6.2	Number of detected events estimated with MC simulations	75
6.3	List of efficiencies of the data processing	79
7.1	Fit parameter results of the combined fit of the data	89
7.2	Best matching simulation input parameters for each reflectivity assumption	90
7.3	List of simulation input parameters for investigating potential systematic uncertainties	93
7.4	List of simulation input parameters affecting the solid angle correction and the resulting impact on the systematic uncertainty of the absorption length	94
7.5	Systematic uncertainties of simulation input parameters for the combined reflectivity	97
7.6	List of simulation input parameters affecting the solid angle correction of the combined reflectivity and the resulting impact on the systematic uncertainty of the absorption length	97
8.1	Optimized parameters and fit results for the triplet lifetime simulations	104
9.1	Compilation of experimental limits and theoretical predictions for the half life of the $2\nu\beta\beta$ decay of ^{76}Ge into excited states of ^{76}Se	111
9.2	Parameter values of the angular correlation of the γ cascades from the 0_1^+ and the 2_2^+ B1 states of ^{76}Se	112

9.3	Integrated M2 fractions for each decay mode in Phase II and Phase II+ for the raw simulations	118
9.4	Integrated M2 fractions for each decay mode in Phase II for the tier4ized simulations for all events, LAr vetoed events and events surviving the LAr veto cut	120
9.5	Integrated M2 fractions for each decay mode in Phase II+ for the tier4ized simulations for all events, LAr vetoed events and events surviving the LAr veto cut	121
9.6	Important parameters of the Phase II and Phase II+ data sets used for the analysis	125
9.7	Summary of the optimized values for the low and high energy thresholds, window width of ROI and SBs as well as efficiencies for Phase II and Phase II+	130
9.8	Compilation of counts in the ROI and SBs surviving all cuts with and without applying the LAr veto for Phase II and Phase II+	134
9.9	90% credibility limits on the half life of each investigated decay mode for Phase II and Phase II+	137

List of Acronyms

$0\nu\beta\beta$	Neutrinoless double beta decay
$2\nu\beta\beta$	Neutrino accompanied double beta decay
$\beta\beta$	Double beta decay
$\beta^-\beta^-$	Double beta minus decay
$\beta^+\beta^+$	Double beta minus decay
ASCII	American Standard Code for Information Interchange
BAT	Bayesian Analysis Toolkit
BEGe	Broad Energy Germanium detector
BI	Background index
CAD	Computer-aided design
CC	Charged current
CSDA	Continuous-slowing-down approximation
C.L.	Confidence level
COBRA	Cadmium Zinc Telluride 0-Neutrino Double-Beta Research Apparatus
CP	Charge conjugation parity symmetry
CUORE	Cryogenic Underground Laboratory for Rare Events
CUPID	CUORE Upgrade with Particle Identification
DAQ	Data acquisition
EC	Electron capture
ECHo	Electron Capture ^{163}Ho Experiment
EDF	Energy density functional theory
EPDL	Photon Interaction Data
EADL	Atomic Relaxation Data
EEDL	Electron Interaction Data
ENSDF	Evaluated Nuclear Structure Data File
EC	Electron capture
ECEC	Double electron capture
FADC	Fast Analog to Digital Converter
Fortran	FORmula TRANslation

f.f.	Fission fragments
FWHM	Full width at half maximum
GAr	Gaseous argon
GEANT4	GEometry ANd Tracking toolkit
GERDA	Germanium Detector Array
g.s.	Ground state
GTF	Genius test facility
h.c.	Hermitian conjugate
HOLMES	Holmium-163 electron-capture spectroscopy
HPGe	High Purity Germanium detector
IBM	Interacting boson model
IC	Inverted coaxial detector
IGEX	International Germanium experiment
IMO	Inverted mass ordering
INFN	Istituto Nazionale di Fisica Nucleare
IPF	Leibniz Institute of Polymer Research Dresden
KATRIN	Karlsruhe Tritium Neutrino experiment
LAr	Liquid argon
LEGEND	Large Enriched Germanium Experiment for $0\nu\beta\beta$ Decay
LXe	Liquid xenon
LNGS	Laboratori Nazionali del Gran Sasso
M1	Multiplicity = 1, data with the energy deposition in one single detector
M2	Multiplicity = 2, data with energy depositions in two different detectors
MaGe	MAJORANA/GERDA simulation framework
MC	Monte Carlo
m.w.e.	Meters of water equivalent
NC	Neutral current
NIR	Near infrared light
NIST	National Institute of Standards and Technology
NME	Nuclear matrix element
NMO	Normal mass ordering
NSM	Nuclear shell model
NuMECS	Neutrino Mass via Electron Capture Spectroscopy
p.e.	Photoelectron
PMNS	Pontecorvo-Maki-Nakagawa-Sakata matrix
PMT	Photomultiplier tube
PS	Polystyrene
PSD	Pulse shape discrimination

PTB	Physikalisch-Technische Bundesanstalt
PTFE	Polytetrafluorethylen
QFT	Quantum field theory
QRPA	Quasiparticle random-phase approximation
ROI	Region of interest
SB	Sideband
SiPM	Silicon photomultiplier
SM	Standard Model of particle physics
SNO	Sudbury Neutrino Observatory
TPB	Tetraphenyl butadiene
TPC	Time projection chamber
UV	Ultraviolet light
VD	Voltage divider
VUV	Vacuum ultraviolet light
WArP	WIMP Argon Programme
WIMP	Weakly interacting massive particle
WLS	Wavelength shifter
XRF	X-ray fluorescence
XRR	X-ray reflectometry
ZAC	Zero Area Cusp signal shaping filter

Bibliography

- [ABB⁺08] C. Amsler, V. Boccone, A. Büchler et al., *Luminescence quenching of the triplet excimer state by air traces in gaseous argon*, *J. Instrum.* **3**(02):02001, 2008.
- [Agi16] Agilent Technologies, Cary 100/300/4000/5000/6000i/7000 Spectrophotometers User's Guide, https://www.agilent.com/cs/library/usermanuals/public/1972_7000.pdf [last accessed on 27.12.2019], 2016.
- [Agi19] Agilent Technologies, diffuse reflectance accessories for the Cary 4000/5000/6000i UV-VIS-NIR spectrophotometers, https://www.agilent.com/cs/library/flyers/public/5991-1717EN_PromoFlyer_UV_DRA.pdf [last accessed on 18.12.2019], 2019.
- [App14] Appec, <https://www.appec.org/news/hands-on-experimental-underground-physics-at-lngs> [last accessed on 22.07.2019], 2014.
- [AS96] M. Aunola and J. Suhonen, *Systematic study of beta and double beta decay to excited final states*, *Nucl. Phys. A* **602**(2):133, 1996.
- [Bar19] A. S. Barabash, *Average and recommended half-life values for two-neutrino double beta decay: Upgrade-2019*, *AIP Conf. Proc.* **2165**(1):020002, 2019.
- [BBB⁺87] R. M. Bionta, G. Blewitt, C. B. Bratton et al., *Observation of a neutrino burst in coincidence with supernova 1987A in the Large Magellanic Cloud*, *Phys. Rev. Lett.* **58**:1494, 1987.
- [BBB⁺94] E. Bellamy, G. Bellettini, J. Budagov et al., *Absolute calibration and monitoring of a spectrometric channel using a photomultiplier*, *Nuclear Instruments and Methods in Physics Research Section A: Accelerators, Spectrometers, Detectors and Associated Equipment* **339**(3):468, 1994.
- [BBB⁺18] A. S. Barabash, P. Belli, R. Bernabei et al., *Final results of the Aurora experiment to study 2β decay of ^{116}Cd with enriched $^{116}\text{CdWO}_4$ crystal scintillators*, *Phys. Rev. D* **98**:092007, 2018.
- [BBD⁺15] L. Baudis, G. Benato, R. Dressler et al., *Enhancement of light yield and stability of radio-pure tetraphenyl-butadiene based coatings for VUV light detection in cryogenic environments*, *Journal of Instrumentation* **10**(09):09009, 2015.
- [BBE⁺92] M. Beck, J. Bockholt, J. Echternach et al., *New half life limits for the $\beta\beta_{2\nu+0\nu}$ decay of ^{76}Ge to the excited states of ^{76}Se from the Heidelberg-Moscow $\beta\beta$ experiment*, *Z. Physik A - Hadrons and Nuclei* **343**:397, 1992.
- [BCC⁺07] P. Benetti, F. Calaprice, E. Calligarich et al., *Measurement of the specific activity of ^{39}Ar in natural argon*, *Nucl. Instr. Meth. A* **574**(1):83, 2007.

- [BCD⁺11] M. Boswell, Y. Chan, J. A. Detwiler et al., *MaGe-a GEANT4-Based Monte Carlo Application Framework for Low-Background Germanium Experiments*, *IEEE Trans. Nucl. Sci.* **58**(3):1212, 2011.
- [BCD19] C. Brofferio, O. Cremonesi and S. Dell’Oro, *Neutrinoless Double Beta Decay Experiments With TeO₂ Low-Temperature Detectors*, *Frontiers in Physics* **7**:86, 2019.
- [BD50] E. L. Brady and M. Deutsch, *Angular Correlation of Successive Gamma-Rays*, *Phys. Rev.* **78**:558, 1950.
- [BDL⁺20] N. Barros, A. Domula, B. Lehnert, B. Zatschler and K. Zuber, *In-situ measurement of the scintillation light attenuation in liquid argon in the GERDA experiment*, *Nucl. Instr. Meth. A* **953**:163059, 2020.
- [BDPU95] A. S. Barabash, A. V. Derbin, L. A. Popeko and V. I. Umatov, *Search for $\beta\beta$ decay of ⁷⁶Ge to the excited states in ⁷⁶Se*, *Z. Physik A - Hadrons and Nuclei* **352**:231, 1995.
- [BGAJ81] A. Bideau-Mehu, Y. Guern, R. Abjean and A. Johannin-Gilles, *Measurement of refractive indices of neon, argon, krypton and xenon in the 253.7 – 140.4 nm wavelength range. Dispersion relations and estimated oscillator strengths of the resonance lines*, *J. Quant. Spectrosc. Radiat. Transfer* **25**(5):395, 1981.
- [BK18] A. B. Balantekin and B. Kayser, *On the Properties of Neutrinos*, *Annu. Rev. Nucl. Part. S.* **68**(1):313, 2018.
- [BOG18] C. Benson, G. D. Orebi Gann and V. Gehman, *Measurements of the intrinsic quantum efficiency and absorption length of tetraphenyl butadiene thin films in the vacuum ultraviolet regime*, *Eur. Phys. J. C* **78**(4):329, 2018.
- [CBPJ14] V. Cuplov, I. Buvat, F. Pain and S. Jan, *Extension of the GATE Monte-Carlo simulation package to model bioluminescence and fluorescence imaging*, *J. Biomed. Opt.* **19**(2):1, 2014.
- [CCC⁺18] J. Calvo, C. Cantini, P. Crivelli et al., *Measurement of the attenuation length of argon scintillation light in the ArDM LAr TPC*, *Astrop. Phys.* **97**:186, 2018.
- [CEF99] S. Chu, L. Ekström and R. Firestone, *The Lund/LBNL Nuclear Data Search* [last accessed on 08.08.2019], 1999.
- [CK79] M. J. Carvalho and G. Klein, *Luminescence decay in condensed argon under high energy excitation*, *J. Lumin.* **18-19**:487–490, 1979.
- [CS94] O. Civitarese and J. Suhonen, *Two-neutrino double-beta decay to excited one- and two-phonon states*, *Nucl. Phys. A* **575**(2):251, 1994.
- [CUO18] CUORE Collaboration, *First Results from CUORE: A Search for Lepton Number Violation via $0\nu\beta\beta$ Decay of ¹³⁰Te*, *Phys. Rev. Lett.* **120**:132501, 2018.
- [CUP18] CUPID-0 collaboration, *First Result on the Neutrinoless Double- β Decay of ⁸²Se with CUPID-0*, *Phys. Rev. Lett.* **120**:232502, 2018.
- [CW73] G. Chow and M. Wiedenbeck, *Determination of mixing ratios from the gamma-gamma directional correlations in a triple cascade*, *Nucl. Instrum. Methods* **109**(3):597, 1973.

- [Dar18] DarkSide collaboration, *Low-Mass Dark Matter Search with the DarkSide-50 Experiment*, *Phys. Rev. Lett.* 121:081307, 2018.
- [DEA19] DEAP collaboration, *Search for dark matter with a 231-day exposure of liquid argon using DEAP-3600 at SNOLAB*, *Phys. Rev. D* 100:022004, 2019.
- [DHK⁺02] T. Doke, A. Hitachi, J. Kikuchi et al., *Absolute Scintillation Yields in Liquid Argon and Xenon for Various Particles*, *Jpn. J. Appl. Phys.* 41(Part 1, No. 3A):1538, 2002.
- [Die16] E. Dietz-Laursonn, *Peculiarities in the Simulation of Optical Physics with GEANT4*, [arXiv:1612.05162](https://arxiv.org/abs/1612.05162) 2016.
- [DMS90] T. Doke, K. Masuda and E. Shibamura, *Estimation of absolute photon yields in liquid argon and xenon for relativistic (1 MeV) electrons*, *Nucl. Instr. Meth. A* 291(3):617, 1990.
- [DMVV16] S. Dell’Oro, S. Marcocci, M. Viel and F. Vissani, *Neutrinoless Double Beta Decay: 2015 Review*, *Adv. High Energy Phys.* 2016, 2016.
- [DPR19] M. J. Dolinski, A. W. Poon and W. Rodejohann, *Neutrinoless Double-Beta Decay: Status and Prospects*, *Annu. Rev. Nucl. Part. Sci.* 69(1):219, 2019.
- [DR94] S. K. Dhiman and P. K. Raina, *Two-neutrino double-beta decay matrix elements for ground and excited states of ^{76}Ge and ^{82}Se nuclei*, *Phys. Rev. C* 50:R2660, 1994.
- [ECH14] ECHo Collaboration, *The Electron Capture ^{163}Ho Experiment ECHo*, *J. Low Temp. Phys.* 176:876, 2014.
- [EM17] J. Engel and J. Menéndez, *Status and future of nuclear matrix elements for neutrinoless double-beta decay: a review*, *Rep. Prog. Phys.* 80(4):046301, 2017.
- [Eva55] R. D. Evans, *The atomic nucleus*, McGraw Hill Book Company, 1955.
- [EXO18] EXO-200 Collaboration, *Search for Neutrinoless Double-Beta Decay with the Upgraded EXO-200 Detector*, *Phys. Rev. Lett.* 120:072701, 2018.
- [Fer34] E. Fermi, *Versuch einer Theorie der β -Strahlen*, *Zeitschrift für Physik* 88(3):161, 1934.
- [FMN⁺13] R. Francini, R. M. Montoreali, E. Nichelatti et al., *VUV-Vis optical characterization of Tetraphenyl-butadiene films on glass and specular reflector substrates from room to liquid Argon temperature*, *Journal of Instrumentation* 8(09):09006, 2013.
- [GA02] P. Gumplinger and J. Apostolakis, *Optical Photon Processes in GEANT4, TRIUMF/GEANT4 Users’ Workshop at CERN 2002*.
- [GBMN17] E. Grace, A. Butcher, J. Monroe and J. A. Nikkel, *Index of refraction, Rayleigh scattering length, and Sellmeier coefficients in solid and liquid argon and xenon*, *Nucl. Instrum. Meth. A* 867:204, 2017.
- [Gea19] <https://geant4.web.cern.ch/> [last accessed on 03.01.2020], 2019.
- [GER15a] GERDA collaboration, *$2\nu\beta\beta$ decay of ^{76}Ge into excited states with GERDA Phase I*, *J. Phys. G: Nucl. Partic.* 42(11):115201, 2015.

- [GER15b] GERDA collaboration, *Improvement of the energy resolution via an optimized digital signal processing in GERDA Phase I*, *Eur. Phys. J. C* 75(255), 2015.
- [GER18a] GERDA collaboration, *Improved Limit on Neutrinoless Double- β Decay of ^{76}Ge from GERDA Phase II*, *Phys. Rev. Lett.* 120:132503, 2018.
- [GER18b] GERDA collaboration, *Upgrade for Phase II of the GERDA experiment*, *Eur. Phys. J. C* 78:388, 2018.
- [GER19] GERDA collaboration, *Probing Majorana neutrinos with double- β decay*, *Science* 365:1445, 2019.
- [GER20] GERDA collaboration, *Modeling of GERDA Phase II data*, *J. High Energ. Phys.* 139, 2020.
- [Gia10] GianniG46, <https://commons.wikimedia.org/wiki/File:Lambert2.gif> [last accessed on 17.12.2019], 2010.
- [GJR⁺72] A. Gedanken, J. Jortner, B. Raz, and A. Szöke, *Electronic Energy Transfer Phenomena in Rare Gases*, *J. Chem. Phys.* 57(8):3456, 1972.
- [Gou16] A. de Gouvêa, *Neutrino Mass Models*, *Annu. Rev. Nucl. Part. Sci.* 66(1):197, 2016.
- [GSR⁺11] V. Gehman, S. Seibert, K. Rielage et al., *Fluorescence efficiency and visible re-emission spectrum of tetraphenyl butadiene films at extreme ultraviolet wavelengths*, *Nucl. Instr. Meth. A* 654(1):116, 2011.
- [Gus18] K. Gusev, *Internal report*, 2018.
- [GVBB97] D. E. Grosjean, R. A. Vidal, R. A. Baragiola and W. L. Brown, *Absolute luminescence efficiency of ion-bombarded solid argon*, *Phys. Rev. B* 56:6975, 1997.
- [Ham09] Hamamatsu, tentative data sheet, Photomultiplier tube R11065, http://lartpc-docdb.fnal.gov/0004/000441/001/R11065_data_sheet_0903-1.pdf, 2009.
- [Ham15] Hamamatsu, *Photonic Devices – Electron Tube Devices and Applied Products*, 2015.
- [HDH⁺10] T. Heindl, T. Dandl, M. Hofmann et al., *The scintillation of liquid argon*, *Europhys. Lett.* 91(6):62002, 2010.
- [HDH⁺13] M. Hofmann, T. Dandl, T. Heindl et al., *Ion-beam excitation of liquid argon*, *Eur. Phys. J. C* 73(10):2618, 2013.
- [Hei11] T. Heindl, *Die Szintillation von flüssigem Argon*, PhD thesis, TU München, 2011.
- [HKK⁺87] K. Hirata, T. Kajita, M. Koshiba et al., *Observation of a neutrino burst from the supernova SN1987A*, *Phys. Rev. Lett.* 58:1490, 1987.
- [HOL15] HOLMES Collaboration, *HOLMES - The Electron Capture Decay of ^{163}Ho to Measure the Electron Neutrino Mass with sub-eV sensitivity*, *Eur. Phys. J. C* 74:112, 2015.
- [HS84] W. Haxton and G. Stephenson, *Double beta decay*, *Prog. Part. Nucl. Phys.* 12:409, 1984.

- [HTF⁺83] A. Hitachi, T. Takahashi, N. Funayama et al., *Effect of ionization density on the time dependence of luminescence from liquid argon and xenon*, *Phys. Rev. B* 27:5279, 1983.
- [Iac14] F. Iachello, personal communication in [Leh16], 2014.
- [IAE20] IAEA, live Chart of Nuclides, <https://www-nds.iaea.org/relnsd/vcharthtml/VChartHTML.html> [last accessed on 17.01.2020], 2020.
- [ICD⁺97] N. Ishida, M. Chen, T. Doke et al., *Attenuation length measurements of scintillation light in liquid rare gases and their mixtures using an improved reflection suppresser*, *Nucl. Instr. Meth. A* 384(2):380, 1997.
- [JAB⁺13] B. J. P. Jones, T. Alexander, H. O. Back et al., *The effects of dissolved methane upon liquid argon scintillation light*, *J. Instrum.* 8(12):12015, 2013.
- [JCC⁺13] B. J. P. Jones, C. S. Chiu, J. M. Conrad et al., *A measurement of the absorption of liquid argon scintillation light by dissolved nitrogen at the part-per-million level*, *J. Instrum.* 8(07):07011, 2013.
- [JMRW65] J. Jortner, L. Meyer, S. A. Rice and E. G. Wilson, *Localized Excitations in Condensed Ne, Ar, Kr, and Xe*, *J. Chem. Phys.* 42(12):4250, 1965.
- [JSV⁺00] G. Jeyasree, A. Subramanian, T. Vasudevan, S. Mohan and R. Venkatachalam, *Electropolishing of stainless steel*, *Bull. Electrochem.* 16(9):338, 2000.
- [Kap18] F. Kaps, *Untersuchung des Einflusses von verschiedenen Algorithmen zur Ereignisselektion auf die Triplett Lebensdauer von Argon*, Bachelor thesis, TU Dresden, 2018.
- [KAT19] KATRIN Collaboration, *Improved Upper Limit on the Neutrino Mass from a Direct Kinematic Method by KATRIN*, *Phys. Rev. Lett.* 123:221802, 2019.
- [KCF⁺14] M. Krumrey, L. Cibik, A. Fischer et al., *Reflektometrie mit Synchrotronstrahlung*, *PTB-Mitteilungen* 124(3/4), 2014.
- [KEFT14] M. F. Kidd, J. H. Esterline, S. W. Finch and W. Tornow, *Two-neutrino double- β decay of ^{150}Nd to excited final states in ^{150}Sm* , *Phys. Rev. C* 90:055501, 2014.
- [KGS79] J. W. Keto, R. E. Gleason and F. K. Soley, *Exciton lifetimes in electron beam excited condensed phases of argon and xenon*, *J. Chem. Phys.* 71(6):2676, 1979.
- [KHR78] S. Kubota, M. Hishida and J. Raun, *Evidence for a triplet state of the self-trapped exciton states in liquid argon, krypton and xenon*, *J. Phys. C* 11(12):2645, 1978.
- [KHSR82] S. Kubota, M. Hishida, M. Suzuki and J. Ruan, *Liquid and solid argon, krypton and xenon scintillators*, *Nucl. Instr. Meth.* 196(1):101, 1982.
- [KLZ16] KamLAND-Zen Collaboration, *Search for Majorana Neutrinos Near the Inverted Mass Hierarchy Region with KamLAND-Zen*, *Phys. Rev. Lett.* 117:082503, 2016.
- [KOSV02] A. Klimenko, S. Osetrov, A. Smolnikov and S. Vasiliev, *Double-Beta Decay of ^{150}Nd and ^{76}Ge to Excited States*, *Czech. J. Phys.* 52:589, 2002.

- [LCC⁺16] J. Loach, J. Cooley, G. Cox et al., *A database for storing the results of material radiopurity measurements*, *Nucl. Instr. Meth. A* 839:6, <http://www.radiopurity.org>, 2016.
- [LEG17] LEGEND collaboration, *The large enriched germanium experiment for neutrinoless double beta decay (LEGEND)*, *AIP Conf. Proc.* 1894(1):020027, 2017.
- [Leh16] B. Lehnert, *Search for $2\nu\beta\beta$ Excited State Transitions and HPGe Characterization for Surface Events in GERDA Phase II*, PhD thesis, TU Dresden, 2016.
- [Lev14] C. Levy, *Light Propagation and Reflection off Teflon in Liquid Xenon Detectors for the XENON100 and XENON1T Dark Matter Experiment*, PhD thesis, WWU Münster, 2014.
- [LM57] T. Lindqvist and I. Marklund, *Mixing ratios of $2+ \rightarrow 2+$ transitions in some even nuclei*, *Nuclear Physics* 4:189, 1957.
- [LNG20] LNGS, <https://www.lngs.infn.it> [last accessed on 10.01.2020], 2020.
- [MAB⁺04] R. Mohapatra, S. Antusch, K. Babu et al., *Theory of Neutrinos*, [arXiv:hep-ph/0412099](https://arxiv.org/abs/hep-ph/0412099) 2004.
- [MAJ19a] MAJORANA Collaboration, *Search for neutrinoless double- β decay in ^{76}Ge with 26 kg yr of exposure from the MAJORANA Demonstrator*, *Phys. Rev. C* 100:025501, 2019.
- [MAJ20] MAJORANA Collaboration, *Results of the MAJORANA DEMONSTRATOR's Search for Double-Beta Decay of ^{76}Ge to Excited States of ^{76}Se* , *J. Phys. Conf. Ser.* 1468:012115, 2020.
- [McP17] McPherson http://www.tokyoinst.co.jp/product_file/file/MC04_cat02_ja.pdf [last accessed on 18.12.2019], 2017.
- [Mel05] B. Mellish, <https://commons.wikimedia.org/wiki/File:Image-Metal-reflectance.png> [last accessed on 17.12.2019], 2005.
- [Men14] J. Menéndez, personal communication in [Leh16], 2014.
- [Mol20] <http://www.molbase.com> [last accessed on 10.01.2020], 2020.
- [MRM10] B. J. Mount, M. Redshaw and E. G. Myers, *Double- β -decay Q values of ^{74}Se and ^{76}Ge* , *Phys. Rev. C* 81:032501, 2010.
- [MS06] R. Mohapatra and A. Smirnov, *Neutrino Mass and New Physics*, *Annu. Rev. Nucl. Part. Sci.* 56(1):569, 2006.
- [Nag73] T. Nagahara, *Energy Levels in ^{76}Se from the Decay of ^{76}As* , *J. Phys. Soc. Japan* 34(3):579, 1973.
- [NDH⁺15] A. Neumeier, T. Dandl, A. Himpl et al., *Attenuation of vacuum ultraviolet light in pure and xenon-doped liquid argon – An approach to an assignment of the near-infrared emission from the mixture*, *Europhys. Lett.* 111(1):12001, 2015.
- [NEM11] NEMO-3 collaboration, *Investigation of double-beta decay with the NEMO-3 detector*, *Phys. Atom. Nuclei* 74:312, 2011.

- [NEM14] NEMO-3 collaboration, *Investigation of double beta decay of ^{100}Mo to excited states of ^{100}Ru* , *Nuclear Physics A* 925:25, 2014.
- [NEM16] NEMO-3 Collaboration, *Measurement of the $2\nu\beta\beta$ decay half-life of ^{150}Nd and a search for $0\nu\beta\beta$ decay processes with the full exposure from the NEMO-3 detector*, *Phys. Rev. D* 94:072003, 2016.
- [NHO⁺12] A. Neumeier, M. Hofmann, L. Oberauer et al., *Attenuation of vacuum ultraviolet light in liquid argon*, *Eur. Phys. J. C* 72(10):2190, 2012.
- [NIST19a] NIST, ASTAR program, <https://physics.nist.gov/PhysRefData/Star/Text/ASTAR.html> [last accessed on 20.01.2020], 2019.
- [NIST19b] NIST, ESTAR program, <https://physics.nist.gov/PhysRefData/Star/Text/ESTAR.html> [last accessed on 20.01.2020], 2019.
- [NIST20] NIST, material properties: 304 Stainless, https://trc.nist.gov/cryogenics/materials/304Stainless/304Stainless_rev.htm [last accessed on 17.01.2020], 2020.
- [NOv19] NOvA Collaboration, *First measurement of neutrino oscillation parameters using neutrinos and antineutrinos by NOvA*, *Phys. Rev. Lett.* 123:151803, 2019.
- [NuM16] NuMECS Collaboration, *Development of Holmium-163 Electron-Capture Spectroscopy with Transition-Edge Sensors*, *J. Low Temp. Phys.* 184:958, 2016.
- [PDG19] Particle Data Group, *Review of Particle Physics: 14. Neutrino Masses, Mixing, and Oscillations*, *Phys. Rev. D* 98:030001, <http://pdg.lbl.gov/index.html>, 2018.
- [Per] L. Pertoldi, PhD thesis, in preparation, Università degli Studi di Padova.
- [PGO19] Präzisions Glas & Optik <https://www.pgo-online.com/intl/curves/quartz-glass-transmission.html> [last accessed on 18.12.2019], 2019.
- [Phy20] Phytron GmbH, <https://www.phytron.de/produkte/motoren-aktuatoren/vss-vsh/> [last accessed on 16.01.2020], 2020.
- [Pom09] F. Di Pompeo, *Complete Monte Carlo simulation of the optical response of the WARP detector for Dark Matter search, 14th GEANT4 Users and Collaboration Workshop*, 2009.
- [PPS⁺08] P. Peiffer, T. Pollmann, S. Schönert, A. Smolnikov and S. Vasiliev, *Pulse shape analysis of scintillation signals from pure and xenon-doped liquid argon for radioactive background identification*, *J. Instrum.* 3(08):08007, 2008.
- [Pro17] Project 8 Collaboration, *Determining the neutrino mass with cyclotron radiation emission spectroscopy—Project 8*, *J. Phys. G* 44(5):054004, 2017.
- [PTZ00] O. Ponkratenko, V. Tretyak and Y. Zdesenko, *Event Generator DECAY4 for Simulating Double-Beta Processes and Decays of Radioactive Nuclei*, *Phys. Atom. Nucl.* 63:1282, 2000.
- [RC56] F. Reines and C. Cowan, *The Neutrino*, *Nature* 178:446, <http://pdg.lbl.gov/index.html>, 1956.

- [Sch14] B. Schneider, *Development of a setup for an in-situ measurement of the light attenuation of liquid argon for the GERDA experiment*, Diploma thesis, TU Dresden, 2014.
- [SK02] Super-Kamiokande Collaboration, *Determination of solar neutrino oscillation parameters using 1496 days of Super-Kamiokande-I data*, *Physics Letters B* 539(3):179, 2002.
- [SLY02] G. Seidel, R. Lanou and W. Yao, *Rayleigh scattering in rare-gas liquids*, *Nucl. Instr. Meth. A* 489(1):189, 2002.
- [SM96] S. Stoica and I. Mihut, *Nuclear structure calculations of two-neutrino double-beta decay transitions to excited final states*, *Nucl. Phys. A* 602(2):197 – 210, 1996.
- [SMA⁺19] J. Smith, A. MacLean, W. Ashfield et al., *Gamma-gamma angular correlation analysis techniques with the GRIFFIN spectrometer*, *Nucl. Instrum. Meth. A* 922:47, 2019.
- [SNO02] SNO Collaboration, *Direct Evidence for Neutrino Flavor Transformation from Neutral-Current Interactions in the Sudbury Neutrino Observatory*, *Phys. Rev. Lett.* 89:011301, 2002.
- [SP06] J. H. Seinfeld and S. N. Pandis, *Atmospheric Chemistry and Physics*, Hoboken, NJ: John Wiley & Sons, 2006.
- [Spe19] Spectrecology, <https://www.spectrecology.com/reflection/> [last accessed on 17.12.2019], 2019.
- [SPP⁺10] C. Silva, J. Pinto da Cunha, A. Pereira et al., *Reflectance of polytetrafluoroethylene for xenon scintillation light*, *J. Appl. Phys.* 107(6):064902, 2010.
- [SSFK98] J. Schwieger, F. Šimkovic, A. Faessler and W. A. Kamiński, *Double β decay to excited states of several medium-heavy nuclei within the renormalized quasiparticle random phase approximation*, *Phys. Rev. C* 57:1738, 1998.
- [Suh14] J. Suhonen, personal communication in [Leh16], 2014.
- [SV82] J. Schechter and J. W. F. Valle, *Neutrinoless double- β decay in $SU(2)\times U(1)$ theories*, *Phys. Rev. D* 25:2951, 1982.
- [TS97] J. Toivanen and J. Suhonen, *Study of several double-beta-decaying nuclei using the renormalized proton-neutron quasiparticle random-phase approximation*, *Phys. Rev. C* 55:2314, 1997.
- [UKO⁺08] S. Umehara, T. Kishimoto, I. Ogawa et al., *Neutrino-less double- β decay of ^{48}Ca studied by $\text{CaF}_2(\text{Eu})$ scintillators*, *Phys. Rev. C* 78:058501, 2008.
- [Unl14] S. Unlu, *Quasi Random Phase Approximation Predictions on Two-Neutrino Double Beta Decay Half-Lives to the First 2^+ State*, *Chin. Phys. Lett.* 31(4):042101, 2014.
- [UR16] T. M. Undagoitia and L. Rauch, *Dark matter direct-detection experiments*, *J. Phys. G* 43(1):013001, 2016.
- [WAr10a] WArP collaboration, *Effects of Nitrogen contamination in liquid Argon*, *J. Instrum.* 5(06):06003, 2010.

- [WAr10b] WArP collaboration, *Oxygen contamination in liquid Argon: combined effects on ionization electron charge and scintillation light*, *J. Instrum.* 5(05):05003, 2010.
- [WAr12] WArP collaboration, *Demonstration and comparison of photomultiplier tubes at liquid Argon temperature*, *Journal of Instrumentation* 7(01):01016, 2012.
- [Weg17] A. Wegmann, *Characterization of the liquid argon veto of the GERDA experiment and its application for the measurement of the Ge-76 half-life*, PhD thesis, University of Heidelberg, 2017.
- [Wes19] T. Wester, *Characterisation of Coincidence Data of the GERDA Experiment to Search for Double Beta Decays to Excited States*, PhD thesis, TU Dresden, 2019.
- [Wie] C. Wiesinger, PhD thesis, in preparation, Technische Universität München.
- [Wie19] C. Wiesinger, *Results and post-upgrade performance of GERDA Phase II*, *TAUP 2019*, 2019.
- [XEN17] XENON collaboration, *First Dark Matter Search Results from the XENON1T Experiment*, *Phys. Rev. Lett.* 119:181301, 2017.
- [XZ17] Z. zhong Xing and J. yu Zhu, *Neutrino mass ordering and μ - τ reflection symmetry breaking*, *Chinese Phys.* 41(12):123103, 2017.
- [ZND94] J. C. Zwinkels, M. Noël and C. X. Dodd, *Procedures and standards for accurate spectrophotometric measurements of specular reflectance*, *Appl. Opt.* 33(34):7933, 1994.
- [ZS89] C. B. Zamboni and R. N. Saxena, *Gamma-gamma angular correlations in the decay of ^{76}As* , *Phys. Rev. C* 39:2379, 1989.
- [Zsi19] A. J. Zsigmond, *LEGEND: The future of neutrinoless double-beta decay search with germanium detectors*, *TAUP 2019*, 2019.

Acknowledgements

Initially, I like to thank my supervisor and first referee Prof. Kai Zuber for offering me the possibility to do my PhD in the nuclear physics group of the TU Dresden. Thank you for letting me choose my topics freely, for reviewing my paper drafts and contributing to all of my work with constructive criticism. I also thank Prof. Stefan Schönert for agreeing to be the second referee for my thesis and for a lot of fruitful discussions concerning LAr.

I thank the GERDA collaboration in general and specifically several former and current collaboration members. This includes Nuno Fiuza de Barros for coming up with the idea to measure the attenuation length of LAr inside GERDA and programming the initial simulation for a feasibility study as well as for reading my paper drafts. Then I like to thank Alexander Domula for designing the setup for the attenuation measurement and participating in the follow-up tests as well as the measurement itself and the workshop of the TU Dresden, especially Martin Siegel, for building the setup. I also want to thank the workshop and GERDA collaboration members in Heidelberg for giving us the possibility to test the attenuation setup inside their liquid nitrogen cryostat. For participating in the accomplishment of the attenuation measurement, I want to thank Bernhard Schwingenheuer, Jan Thurn and Björn Lehnert, who additionally gave me a lot of feedback concerning the analysis of the data and the corresponding paper drafts.

Furthermore, I like to thank Roman Hiller from the GERDA collaboration for reading and commenting my GSTR and paper drafts. I thank Luigi Pertoldi and Christoph Wiesinger for the idea and realization of the LAr map as well as Katharina von Sturm, Ann-Kathrin Schütz, Luigi Pertoldi and Thomas Wester for the background model development for GERDA.

Big thanks go to Thomas Wester for reading my complete thesis and contributing with very constructive feedback. Thank you for updating the excited states analysis and answering all my questions, and especially for keeping up the communication via regular calls during the stay-at-home order due to COVID-19.

Moreover, I thank Anja Marie Steiner from the IPF in Dresden for the steel reflectivity measurement in the visible region as well as Alexander Gottwald and Udo Kroth from the PTB for the steel reflectivity measurement in the UV region.

Then, I also like to thank the referees from Elsevier for their constructive feedback to the LAr scintillation light attenuation paper.

Additionally, I acknowledge the ZIH and HPC at TU Dresden for providing the computing power on the HRSK-II used for the simulations and analyses of my work.

I thank the nuclear physics group in Dresden in general, particularly Andreas Jansen, Steffen Turkat and Heinrich Wilsenach for their continuous feedback to my group meeting talks and especially Heinrich Wilsenach for his support in the preparation of the attenuation measurement.

Finally, I like to thank my husband Stefan for his continuous and strong support at all times as well as countless fruitful discussions concerning my work, physics in general and all other topics not related to physics.

Zum Schluss möchte ich noch meinen Eltern und Schwiegereltern für ihre Unterstützung danken. Das betrifft insbesondere das entgegengebrachte Verständnis dafür, dass Stefan und ich immer sehr wenig Zeit für allerlei soziale Aktivitäten hatten und auch die vielen Fahrten zum Flughafen zu unsäglichen Uhrzeiten.

Versicherung

Hiermit versichere ich, dass ich die vorliegende Arbeit ohne unzulässige Hilfe Dritter und ohne Benutzung anderer als der angegebenen Hilfsmittel angefertigt habe; die aus fremden Quellen direkt oder indirekt übernommenen Gedanken sind als solche kenntlich gemacht. Die Arbeit wurde bisher weder im Inland noch im Ausland in gleicher oder ähnlicher Form einer anderen Prüfungsbehörde vorgelegt.

Die Promotion wurde an der Technischen Universität Dresden, am Institut für Kern- und Teilchenphysik unter der wissenschaftlichen Betreuung von Prof. Dr. Kai Zuber durchgeführt.

Ich erkenne die Promotionsordnung des Bereichs Mathematik und Naturwissenschaften der TU Dresden vom 23.02.2011 an.

Birgit Zatschler
Dresden, 29. Juni 2020